THE UNIVERSITY OF MANITOBA

Molecular Collisions: Effect on the HD Infrared Spectrum and Development of a Moyal Quantum Mechanical Description

by

Barry R. McQuarrie

A THESIS SUBMITTED TO
THE FACULTY OF GRADUATE STUDIES OF
THE UNIVERSITY OF MANITOBA
IN PARTIAL FULFILLMENT OF THE REQUIREMENTS OF
THE DEGREE OF DOCTOR OF PHILOSOPHY

DEPARTMENT OF PHYSICS
WINNIPEG, MANITOBA
November 1997

0-612-32007-3

THE UNIVERSITY OF MANITOBA

FACULTY OF GRADUATE STUDIES
*****
COPYRIGHT PERMISSION PAGE

MOLECULAR COLLISIONS: EFFECT ON THE HD INFRARED SPECTRUM AND DEVELOPMENT OF A MOYAL QUANTUM MECHANICAL DESCRIPTION

BY

BARRY R. McQUARRIE

A Thesis/Practicum submitted to the Faculty of Graduate Studies of The University

of Manitoba in partial fulfillment of the requirements of the degree

of

DOCTOR OF PHILOSOPHY

Abstract

Interference is possible between the allowed dipole moment of the molecule HD and the pair dipole moment induced by collision with a foreign gas atom. The resulting line shape can be described by the sum of a Lorentzian and an asymmetric profile. Parameters which determine the line intensity and asymmetry can be calculated. The mixing of rotational levels by an anisotropic interaction potential can permit components of the induced dipole moment that do not have the same symmetry of the allowed moment to interfere with it. For the rotational spectrum of HD-He and HD-Ar the effect of each component of the induced dipole moment on the line shape parameters is determined for various temperatures and transitions. For line intensity, the component with the same symmetry as the allowed moment always dominates, but the effect of the other components is shown to be significant.

The line shape parameters for the vibrorotational spectrum of HD-He are calculated for $P_1(1)$, $R_1(0)$, $R_1(1)$ transitions at 77, 195, and 295 K. To model molecular vibrations, the intermolecular potential is assumed to have a vibrational state dependence. Line asymmetry is found to be sensitive to this dependence.

Moyal quantum mechanics is an alternative to Heisenberg or Schrödinger quantum mechanics. The method yields a semiclassical expansion of phase space trajectories in terms of Planck's constant, $\hbar$. The ***Moyal correction*** to the classical part of the solution is found to $O(\hbar^2)$.

The first computational version of Moyal quantum mechanics to calculate average values for three dimensional systems with physically relevant parameters is developed. The system treated is the scattering of a Gaussian wave packet by the helium, neon, and argon interaction potentials. The Gaussian is squeezed in momentum so that the momentum average can be done analytically. This introduces a *momentum correction* and the Gaussian is taken to have a single initial velocity. We examine scattering at velocites of 300-1200 m/s.

Sensitive areas of the phase space average are identified. Integrals over coordinate phase space (impact parameter and displacement y) are examined in detail. The region of phase space which produces rainbow scattering is determined to result in the largest quantum effects. The Moyal correction is found to be small for impact parameters greater than $2b_{rainbow} - b_{glory}$.

The corrections to average values are examined in detail for helium at a velocity of 300 m/s. It is shown that the Moyal corrections have an asymptotic time behaviour which is the same as that of the classical part of the average, but that they may grow as $t \rightarrow \infty$ to dominate the total average.

The corrections to the average value are examined as functions of mass and velocity. The Moyal correction is seen to change sign relative to the classical part of the average in both cases. The momentum correction is shown to have a mass^{-2} dependence. More complex asymptotic behaviour of the Moyal correction is examined for both the mass and the velocity.

Comparison between the size of the correction for the systems consisting of two helium, neon, and argon atoms is performed. Helium is found to exhibit the largest corrections. Although argon has a mass twice that of neon, and thus might be expected to have relatively small quantum corrections, the corrections for argon and neon are found to be comparable. This is due to the stronger interaction in the argon potential.

Acknowledgements

I am greatly indebted to my both of my advisors. Prof. George Tabisz's enthusiasm is a constant source of inspiration. From the HD problem through Moyal, his patience, trust and high spirits made (almost!) every day exciting. The steady guidance he provided through the sometimes rocky waters that a Ph.D. candidate must navigate has made all the difference. Prof. Tom Osborn's incredible drive and work ethic were at times astounding. His sense of humour when things seemed almost unworkable was always appreciated. I feel fortunate to have had the opportunity to work with two people of such character and skill.

I would like to thank my external examiner Prof. Lothar Frommhold who was able to attend my defence and has offered many words of encouragement and support over the past year.

My committee, Profs. Wallace and Zetner, for their suggestions and improvements to the thesis, and guidance over the course of my time here.

I would like to thank Guy Durocher for his substantial computer assistance over the years.

On a personal level, I would like to thank my Mother for patiently listening to all my computer ills and subsequent solutions; Steve and Kim for their friendship, care, laughter - and sometimes anger! - over many great years; Darlene for assistance with the ever changing Meaning of Life; Phil and Angie for being there whenever I needed them; and Jeff, Ed, and Moe for putting some much needed tradition back into my life. "To All My Friends!"

The financial support of the National Science and Engineering Research Council in the form of a PGS-B scholarship and the Department of Physics is gratefully acknowledged.

Contents

List of Tables

List of Figures

Chapter 1

Introduction

Classical collision dynamics are generally well understood, especially for elastic collisions. However, in many physical situations quantum effects can radically alter the relative translational motion and the internal degrees of freedom of a molecule. In the past, this quantum nature has been dealt with in a number of ways. In some instances it is valid to treat the collision partners as moving along straight lines. This essentially assumes the interaction potential is negligible as far as collision dynamics are concerned, and this *straight line approximation* ignores even the classical deviation from a free particle. The *classical path approximation* assumes the collision partners follow trajectories which are determined entirely classically. This approximation is used frequently in line shape theories, and will be used in Chapters 1-4 of this thesis to calculate line shape parameters for collision-induced line shapes of HD. If the classical path approximation is not appropriate for the system being studied (usually determined by a de Broglie wavelength comparable to the interaction distance), one can look for *semi-classical approximations* to incorporate quantum effects. A semi-classical approach is often desirable since it is not as complex as a fully quantal treatment, and lessons learned from the classical result can be applied. In Chapters 5-6, a semi-classical approach based on Moyal quantum mechanics will be developed to treat scattering problems. The classical path approximation will be recovered from the leading $O(\hbar^0)$ term, and the first Moyal quantum correction will result from the $O(\hbar^2)$ term. The results for single trajectories or average values can then be examined directly to see when the Moyal correction is small compared to the classical part, and the classical path approximation is invalid. The Moyal correction is based on the Jacobi fields and higher derivatives of the classical trajectories. As such it is a phase space based semi-classical formalism built around classical quantities. The ability to recover the classical path approximation and its dependence on classical quantities make the Moyal formalism a particularly suitable semi-classical extension. We begin, however, with the HD collision-induced line shape problem.

The molecule HD, as one of the simplest heteronuclear molecules, serves an important role in physics. Both theoretically and experimentally tractable, it often serves as the first bridge between theory and experiment. Its small allowed dipole moment is a result of a breakdown of the Born Oppenheimer approximation - an approximation which works very well for most systems. This small allowed dipole moment also allows an almost unique opportunity to study intracollisional interference - interference between optical transitions involving the allowed and collision-induced dipole moment. For most molecules these two processes can be treated as entirely independent and mutually exclusive, either due to no allowed dipole being present (for homonuclear molecules), or to an allowed dipole moment which is much larger than the collision-induced dipole.

The HD molecule makes an important contribution to cosmology. The D/H ratio in the solar system soon after its formation would have affected the evolution of solar nebula and the formation of planets. As well, this ratio would be a function of the mechanism which formed the solar system [Geiss and Reeves, 1972; Gautier and Owen, 1983]. The present D/H ratios in the atmospheres of Jupiter and Saturn are likely to be the same as at the time of the solar system's formation [Trauger *et al.*, 1973; Trafton,1978; Bézard *et al.*, 1986]. They can be determined by examining the ratio of HD/H_2 ($D/H = \frac{1}{2}HD/H_2$) [Trauger *et al.*, 1973; Bézard *et al.*, 1986]. Various HD lines have been detected in the atmospheres of the giant planets, for example, the $P_4(1)$ line [on Jupiter by Trauger *et al.*, 1973; on Uranus by Trafton, 1978] and the $R_0(0)$ and $R_0(1)$ lines [on Jupiter, Saturn, Uranus and Neptune by Bézard *et al.*, 1986]. To be able to convert these observed spectra into abundances of HD, one requires a theoretical model for HD line shapes which is capable of accurately predicting line shape parameters at temperatures and pressures which are found in the atmospheres of the gas giants.

The allowed pure rotational dipole moment of HD was first postulated by Wick [Wick, 1935]. He realized that due to its mass asymmetry, the HD molecule should possess a dipole moment that would not exist within the Born Oppenheimer approximation. Since the dipole moment is due entirely to the coupling of nuclear and electronic motion it is very small, on the order of 10^{-4} Debye for the fundamental band. Experimental verification of the existence of the HD dipole moment had to wait until 1949 when Herzberg [Herzberg, 1949] detected the 2-0 and 3-0 bands.

In the early 1970's McKellar investigated the spectrum of gaseous HD at a temperature of 77K for the fundamental and first overtone bands for densities from 1 to 60 amagat (1 amagat = density of perfect gas at 0° C and 1 atmosphere) [McKellar, 1973]. The line shapes he found could be represented by a Fano profile - the sum of a Lorentzian and an asymmetric dispersion line shape. At low densities the profile was Lorentzian (symmetric), but became more asymmetric at high densities. He tentatively ascribed the asymmetry to the interference of continuum (collision-induced dipole) and discrete (allowed dipole) transitions. His estimates of the allowed dipole moment for HD for the $R_1(0)$ transition, 0.49×10^{-4} D [McKellar, 1973] and 0.515×10^{-4} D [McKellar, 1974], agreed well with the experimental value of Bejar and Gush, 0.42×10^{-4} D [Bejar and Gush, 1974], but did not agree with the theoretical values, 0.80×10^{-4} D [Poll and Karl, 1973], 1.106×10^{-4} D [Wolniewicz and Kowalski, 1973].

In the following years, more accurate theoretical estimates of the allowed dipole matrix elements were made. Wolniewicz [Wolniewicz, 1976] obtained values which agreed with the experimentally obtained ones for the fundamental and overtones bands, but disagreed for the pure rotational band. Similar results were found by Ford and Browne [Ford and Browne, 1977]. Theoretical estimates of the allowed dipole moment for the $R_0(0)$ transition were -8.36×10^{-4} D [Wolniewicz, 1976], -8.31×10^{-4} D [Ford and Browne, 1977], and -8.65×10^{-4} D [Bishop and Cheung, 1978]. As is plainly evident, the theoretical estimates agree quite well. The experimental value was lower, -5.85×10^{-4} D [Trefler and Gush, 1968]. This disagreement between theory and experiment for the pure rotation band of HD was puzzling.

Interference between collision-induced dipoles and allowed dipoles can be present in systems with an allowed dipole [McKellar, 1973], but is usually masked because of the large size of the allowed dipole. For HD, with its small allowed dipole moment, this is not the case. This effect (known as *intracollisional interference* since it only occurs during a collision) was observed experimentally and first interpreted theoretically in the spectrum of HD-Kr in 1976 by Poll, Tipping, Prasad and Reddy [Poll *et al.*, 1976]. They found that intracollisional interference can be either constructive or destructive, that the spectral profile has a width that is the same order of magnitude as the allowed line, and that the effect is more important at high density.

Tipping, Poll and McKellar [Tipping *et al.*, 1978] later investigated the intracollisional interference effect for pure HD. Their theory used adiabatic separation of the relative translational motion from internal degrees of freedom and the non-mixing of rotational levels. They postulated that the descrepancy between theoretical and experimental values for the permanent allowed dipole moment of HD was due to destructive intracollisional interference, an effect which must be taken into account in determining allowed dipoles from experiment. As well, they obtained excellent agreement with experiment for the $R_1(1)$ line, but not very good agreement for the $R_1(0)$ line. Due to the asymmetrical line shape for $R_1(0)$ they concluded that rotational level mixing was important and should be included in the calculation. By the late 1970's, with the papers by Herman [Herman, 1979] and Herman, Tipping and Poll [Herman, *et al.*, 1979], the theory of intracollisional interference within the classical path impact formalism with the approximation that no rotational level mixing occurs and including intercollisional interference (interference of collision-induced dipoles in successive collisions [Van Kranendonk, 1968]) was formed. This theory of intracollisional interference was able to improve the agreement between theory and experiment for the allowed dipole moment in the pure rotation band, but was not as successful in determining the interference parameters of the Fano profile.

The early 1980's saw considerable work in experimental intracollisional interference in HD systems. Nelson and Tabisz [Nelson and Tabisz, 1982; 1983] performed detailed experimental work on the pure rotational spectrum of HD and HD-rare gas mixtures. Rich and McKellar [Rich and McKellar, 1983] examined the fundamental spectrum of HD and HD-X (X=He, Ne, Ar) at 77K, while McKellar, Johns, Majewski and Rich [McKellar *et al.*, 1984] observed the pure rotational spectra for HD and HD-Ne at 77K.

The theoretical understanding of intracollisional interference was improved in the mid 1980's by Tabisz and Nelson [Tabisz and Nelson, 1985], who made the first attempt to include rotational level mixing. Their method included rotational level mixing through the anisotropic part of the interaction potential at the time when the induced dipoles act. This inclusion of mixing improved the agreement between theoretical and experimental estimates of the interference parameter for $R_1(1)$ [Ma *et al.*, 1988]. There followed again a series of experimental work, most notably the pure rotational spectrum of HD and HD-X (X=H_2, He, Ne, Ar, Kr, Xe, N_2) at 295K by Drakopoulos and Tabisz [Drakopoulos and Tabisz, 1987a; 1987b]; McKellar [McKellar, 1986] on the pure rotational spectrum of HD at 295K; and Ulivi, Lu and Tabisz [Ulivi *et al.*, 1989] for the pure rotational spectrum of HD. Although improved, there still existed a descrepancy between theoretical and experimental line shape parameters.

In the early 1990's the theory of intracollisional interference for the pure rotational spectrum was improved by Gao, Tabisz, Trippenbach and Cooper [Gao *et al.*, 1991]. This treatment is notable since it included rotational level mixing at any time during the collision, ie. ***propagation***. The theory also reduced to the previous theories of Tabisz and Nelson [Tabisz and Nelson, 1985] and Herman, Tipping Poll [Herman *et al.*, 1979] as limiting cases. The theory was applied to HD-X (X=He, Ar) systems by Gao, Cooper and Tabisz [Gao *et al.*, 1992] and agreement with experiment was improved over that of the previous theories. An experimentally evident J dependence of the line shape parameters for a fixed temperature was present in the results, a feature not reproduced in earlier theories. This theory forms the basis for the research which is carried out in this thesis.

This thesis will advance the theory of intracollisional interference on a number of fronts. It has already been established that inelastic collisions and collisional propagation are important contributions to the interference effect [Gao *et. al.* 1992]. Inelastic collisions enable induced dipole components which do not have the same symmetry as the allowed moment to contribute to the interference effect. We will look at the role of the individual induced dipole moment components in collisional interference in detail for the pure rotational spectrum of HD-He and HD-Ar. As well, the theory of Gao *et al.* will be extended to treat the vibration-rotation spectrum of HD-He mixtures.

There are features in the experimental data which are not fully explained by the present theory of intracollisional interference. One method of improving the theory is obvious. The collision-induced dipoles and interaction potentials are largest at closest approach along any single trajectory. The classical path approximation is least valid in precisely this region, where interactions are the strongest. A method of incorporating quantum effects into the collisional average should improve the results. As a step to this end, a computational form of Moyal quantum mechanics is developed to treat scattering problems.

Moyal quantum mechanics is a formulation of quantum theory set in classical phase space and based on classical flow. Equations of motion that must be solved are similar to the classical Hamiltonian equations, and the time evolution operator is found in terms of an $\hbar$-expansion.

In 1927, Weyl [Weyl, 1927] presented a procedure which maps the classical function A to an integral operator $\hat{A}$ on the Hilbert space $H = L^2(\mathbb{R}^3)$ [Voros, 1978]. In 1932, Wigner [Wigner, 1932] introduced a transform which was the inverse of the Weyl transform, mapping operators from the Hilbert space H to functions on the classical phase space [Carruthers and Zachariasen, 1983]. With the development of the star ($*$, or *twisted*, or *Weyl*) product for symbols by Groenewold [Groenwald, 1946] which gave a method for finding the Weyl symbol for products of operators, the stage was set for the development by Moyal of a quantization procedure based on the Wigner-Weyl correspondence [Moyal, 1949].

Traditionally, time evolution of the system has been determined by the Poisson bracket method [Prosser, 1983; Estrada *et al.*, 1989]. Due to the complexity of the equations for time evolution found from the Poisson bracket method, the emphasis has been on developing the algebra of Moyal quantum mechanics and not on solution of physical systems. Treatment is usually restricted to one dimensional systems with simple potential interactions [Braunss and Rompf, 1993].

In 1995, however, Osborn and Molzahn [Osborn and Molzahn, 1995] developed an alternate to the Poisson bracket method, the *cluster-graph expansion*. This resulted in simplified equations of motion to be solved.

In this thesis we begin with the results from the cluster-graph expansion and develop a formulation of Moyal quantum mechanics which is capable of treating three dimensional dynamical evolution. Average values for the scattering of a three dimensional Gaussian under helium, neon, and argon interaction potentials will be calculated. The tools and computer code which are developed can be used in the future to treat collisional problems in a semiclassical manner for any theories which requires such, including line shape theories and dipole moment expectation values.

Chapter 2

Theory of Collisional Interference

2.1 Allowed Dipole Moment of HD

The allowed (sometimes referred to as *permanent*) dipole moment of HD was first postulated, and a theoretical estimate of its strength made, by Wick [Wick, 1935]. His estimate of the dipole moment for the fundamental band involved treating the nonadiabatic contribution as a perturbation. Although he neglected some contributions which turned out to be important, he was able to identify the HD permanent dipole as a purely nonadiabatic effect.

A calculation for the allowed dipole moment is presented which employs the Born-Oppenheimer approximation - involving separating the electronic and nuclear motions of the molecule - to obtain adiabatic wavefunctions. These wavefunctions are used in a second order perturbation approximation to estimate the allowed dipole moment. The only nonvanishing contribution is from a term in the Hamiltonian which mixes electric and nuclear components, i.e. from a breakdown in the Born-Oppenheimer approximation.

An overview of this calculation follows. The Schrödinger equation for the system, after the separation of the center of mass coordinates, is [Bunker, 1968; Tipping and Poll, 1985]:

$$H\Psi(\vec{x};\vec{r}) = E\Psi(\vec{x};\vec{r}) , \tag{2.1}$$

where

$$\begin{aligned}
H &= H_0 + H' , &(2.2)\\
H_0 &= -\frac{\hbar^2}{2m_e}(\nabla_1^2 + \nabla_2^2) + V , &(2.3)\\
H' &= H_1' + H_2' + H_3' , &(2.4)\\
H_1' &= -\frac{\hbar^2}{8\mu}(\nabla_1 + \nabla_2)^2 , &(2.5)\\
H_2' &= -\frac{\hbar^2}{2\mu}\nabla_r^2 , &(2.6)\\
H_3' &= -\frac{\hbar^2}{2\mu_a}\vec{\nabla}_r \cdot (\vec{\nabla}_1 + \vec{\nabla}_2) , &(2.7)
\end{aligned}$$

where

$$\begin{aligned}
\mu &= \frac{M_A M_B}{M_A + M_B} , &(2.8)\\
\mu_a &= \frac{M_A M_B}{M_A - M_B} , &(2.9)
\end{aligned}$$

where $\vec{x} = (1,2)$ are the electronic coordinates, $\vec{r}$ are the nuclear coordinates, m_e is the electron mass, M_A and M_B are the nuclear masses, μ is the reduced mass, μ_a is the mass asymmetry, and V is the total potential.

The Born-Oppenheimer, or *clamped nuclei*, Hamiltonian H_0 satisfies

$$H_0\phi_{n\Lambda}(\vec{x};\vec{r}) = \epsilon_{n\Lambda}(r)\phi_{n\Lambda}(\vec{x};\vec{r}) , \tag{2.10}$$

where $\phi_{n\Lambda}$ is the electronic part of the total wavefunction, and $n\Lambda$ are electronic quantum numbers.

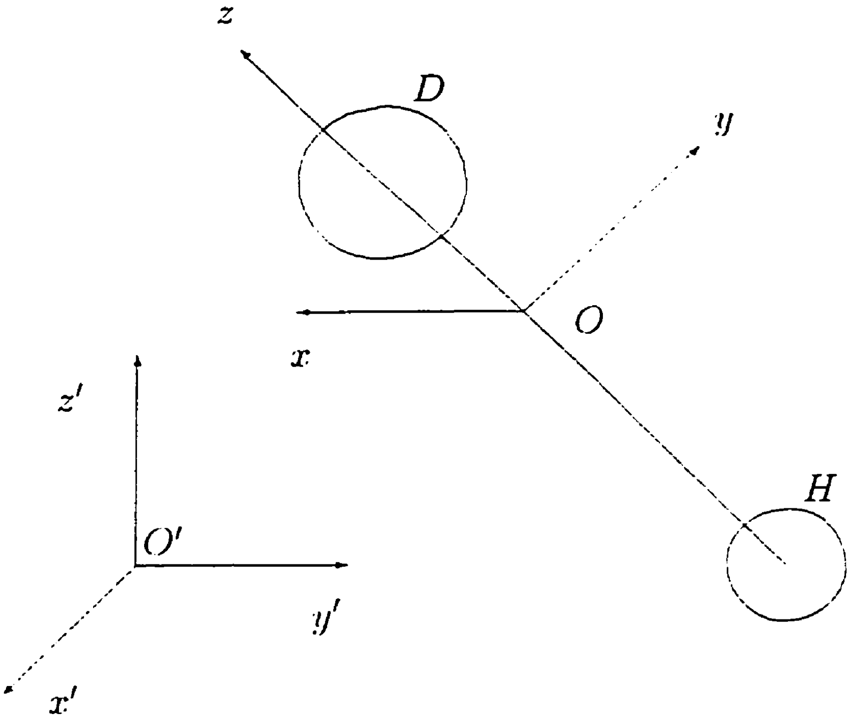

Figure 2.1:

Coordinate systems for the allowed dipole moment of the HD molecule.

O' : space fixed frame

O : molecular frame located at center of mass, z-axis along HD axis

To separate the rotational motion one may transform the Hamiltonian to the angular momentum representation by assuming [Kolos, 1973; Kolos and Wolniewicz, 1963]

$$\Psi = \sum_{\Lambda=-J}^{J} \Omega^J_{M\Lambda} u^J_\Lambda \, . \tag{2.11}$$

where the u^J_Λ depend only on the relative positions of the particles, and $\Omega^J_{M\Lambda}$ are eigenfunctions of the operator of the total angular momentum $\hat{J}^2$ (quantum number J), of its component in the direction of a space fixed axis $\hat{J}_{z'}$ (quantum number M), and a component of the electronic angular momentum in the direction of the molecular axis $\hat{L}_z$ (quantum number Λ) (Figure 2.1). Since $\hat{L}_z$ does not commute with H', the Hamiltonian in this representation will be nondiagonal. The adiabatic approximation neglects the off diagonal terms. The total wavefunction is written as [Tipping and Poll, 1985]

$$\begin{aligned} \Psi^{AD} &= \left[\frac{2J+1}{4\pi}\right]^{\frac{1}{2}} \Omega^J_{M\Lambda} \phi_{n\Lambda} \chi^{(n\Lambda)}_{vJ} \, . \\ &= |n\Lambda vJM\rangle \, . \qquad (2.12) \\ & \qquad (2.13) \end{aligned}$$

where $\chi^{(n\Lambda)}_{vJ}$ are nuclear adiabatic wavefunctions, vJ are nuclear quantum numbers. The adiabatic wavefunctions are used as a basis to determine the nonadiabatic corrections via perturbation theory.

In a constant electric field, $\vec{F}$, the Hamiltonian is modified to:

$$H = H_0 + H' - \vec{\mu} \cdot \vec{F} \, . \tag{2.14}$$

where $\vec{\mu}$ is the dipole moment operator of the molecule. The dipole moment operator is given by:

$$\vec{\mu} = - \lim_{\vec{F} \to 0} \frac{\partial H}{\partial \vec{F}} \, . \tag{2.15}$$

Second order perturbation theory allows the expansion of the energy of the molecule, and application of Equation (2.15) yields the result:

$$\begin{aligned}\langle i|\vec{\mu}|f\rangle &= \sum_{n'\Lambda'v'J'M'}{}' \frac{\langle n_i\Lambda_iv_iJ_iM_i|H'|n'\Lambda'v'J'M'\rangle\langle n'\Lambda'v'J'M'|\vec{\mu}|n_f\Lambda_fv_fJ_fM_f\rangle}{E_{n'\Lambda'v'J'M'}-E_i} \\ &+ \sum_{n'\Lambda'v'J'M'}{}' \frac{\langle n_i\Lambda_iv_iJ_iM_i|\vec{\mu}|n'\Lambda'v'J'M'\rangle\langle n'\Lambda'v'J'M'|H'|n_f\Lambda_fv_fJ_fM_f\rangle}{E_{n'\Lambda'v'J'M'}-E_f}.\end{aligned} \tag{2.16}$$

where the prime on the summation indicates that states which yield a zero denominator are not included. The vibrorotational band of HD involves transitions within the ground electronic state ($n = \Lambda = 0$). Equation (2.16) simplifies to:

$$\begin{aligned}\langle i|\vec{\mu}|f\rangle &= \sum_{n'\Lambda'v'J'M'}{}' \frac{\langle 00v_iJ_iM_i|H'|n'\Lambda'v'J'M'\rangle\langle n'\Lambda'v'J'M'|\vec{\mu}|00v_fJ_fM_f\rangle}{E_{n'\Lambda'v'J'M'}-E_i} \\ &+ \sum_{n'\Lambda'v'J'M'}{}' \frac{\langle 00v_iJ_iM_i|\vec{\mu}|n'\Lambda'v'J'M'\rangle\langle n'\Lambda'v'J'M'|H'|00v_fJ_fM_f\rangle}{E_{n'\Lambda'v'J'M'}-E_f}.\end{aligned} \tag{2.17}$$

For the dipole to be nonzero we require the matrix elements in Equation (2.17) to be nonzero. The ground electronic state of HD is $X^1\Sigma_g^+$ which has an even inversion symmetry. The intermediate states in Equation (2.17) therefore must have an odd inversion symmetry, since the dipole connects states of different parity. The only term in Equation (2.4) for H' that has odd symmetry is the term H'_3. This term couples the electronic and nuclear motion and as such would be ignored in the Born-Oppenheimer approximation. Notice that for symmetric molecules (like H_2) we have $M_A = M_B$ and the mass asymmetry is infinite. This leads to $H'_3 = 0$, and no permanent dipole moment. The fact that the allowed dipole moment of HD is due purely to nonadiabatic effects is unlike the usual case for polar molecules where the permanent dipole moment exists within the Born-Oppenheimer approximation. The smallness of HD's allowed moment ($\sim 10^{-3} - 10^{-4}$ Debye) can be traced to this fact.

The dipoles used in this research (Table 2.1) are from Ford and Browne [Ford and Browne, 1977], who employed a sum over states technique to obtain numerical estimates of the dipole moments of HD. Since the molecular z axis points from H to D (Figure 2.1), a negative allowed moment implies H^+D^-.

Band	Line		
	$P(1)$	$R(0)$	$R(1)$
$0-0$	-8.306	-8.306	-8.297
$1-0$	$+0.485$	$+0.560$	$+0.594$

Table 2.1:

Allowed dipole moments of HD. Taken from [Ford and Browne, 1977].

Units: 10^{-4} Debye.

2.2 Collision-induced Dipole Moment

Induced dipoles are created from distortions of the electronic charge distributions of colliding molecules. These distortions are small, and hence the induced dipoles are small, on the order of 10^{-1}-10^{-3} Debye at 1.5 Å separation, and drop off rapidly with increasing distance. These distortions arise from three types of phenomena: multipolar induction, electron exchange, and dispersion interaction [Buckingham, 1967].

Long range multipolar induction is due to permanent multipoles of the colliding molecules. The presence of the multipole moment on one molecule distorts the electron charge distribution of the other molecule and polarizes it. The induced dipole is given by:

$$\vec{\mu} = \vec{\alpha} \cdot \vec{E} \ . \tag{2.18}$$

where $\vec{E}$ is the multipole field of the first molecule, and $\vec{\alpha}$ is the polarizability of the other. This induced moment is proportional to $R^{-(l+2)}$ where l is the order of the multipole ($l = 1$ for dipole, $l = 2$ for quadrupole, $l = 4$ for hexadecapole, etc.).

Electron exchange is a purely quantum mechanical effect. When two molecules are close together, their electron clouds will overlap. Since electrons are subject to the Pauli exclusion principle, some of the electrons will be excluded from the overlap region. This lowering of the electron density results in a charge transfer and an overlap induced moment. Electron exchange is possible only when the two molecules are very close together, and as such has a roughly exponential distance dependence, $exp(-\alpha R)$.

Dispersion interaction results from correlations between electron density fluctuations in the two molecules. At any instant, a molecule posseses an instantaneous electric dipole which fluctuates as electron density fluctuates. This electric dipole induces a dipole on the other molecule. The two dipoles (induced and inducing) interact to produce an attractive force. This force leads to a dipole moment function which can be expressed as an inverse odd power expansion in the intermolecular distance R,

$$D_7 R^{-7} + D_9 R^{-9} + \cdots \ . \tag{2.19}$$

We will begin by looking at the total dipole of a binary H_2-H_2 collision.

When two molecules are close enough to interact with each other the electric dipole moment of the system is given by

$$\vec{\mu}(\vec{r}_1 \vec{r}_2 \vec{R}) = \vec{\mu}_1(\vec{r}_1) + \vec{\mu}_2(\vec{r}_2) + \vec{\mu}^I(\vec{r}_1 \vec{r}_2 \vec{R}) \ . \tag{2.20}$$

where $\vec{\mu}_i(\vec{r}_i)$ is the permanent dipole moment of molecule i, $\vec{\mu}^I(\vec{r}_1\vec{r}_2\vec{R})$ is the induced dipole moment of the pair, the coordinates $\vec{r}_i$ are internuclear distances, and $\vec{R}$ is the intermolecular distance (see Figure 2.2). This dipole is defined in terms of the adiabatic approximation for electrons. (cf. Equation (2.12))

$$\vec{\mu}(\vec{r}_1\vec{r}_2\vec{R}) = \langle\Psi^{AD}|\vec{\mu}|\Psi^{AD}\rangle \ . \tag{2.21}$$

One can expand the spherical dipole components μ_q ($\mu_0 = \mu_z$, and $\mu_{\pm 1} = \mp(\mu_x \pm i\mu_y)/\sqrt{2}$) of the induced dipole moment in terms of a suitable basis, usually the spherical harmonics of ω_1, ω_2, and Ω, the angles giving the orientations of $\vec{r}_1$, $\vec{r}_2$, and $\vec{R}$ respectively. The function

$$\begin{aligned} Y^{\lambda_1\lambda_2 L\Lambda}_{J,q}(\omega_1,\omega_2,\Omega) &= \sum_{m_1,m_2,M} C(\lambda_1,\lambda_2,\Lambda; m_1,m_2,m_1+m_2) \\ &\times C(\Lambda,L,J; m_1+m_2,M,q) \\ &\times Y_{\lambda_1,m_1}(\omega_1)Y_{\lambda_2,m_2}(\omega_2)Y_{L,M}(\Omega) \ . \end{aligned} \tag{2.22}$$

is a tensor of rank J. The C's are Clebsch-Gordon coefficients, and the Y's are spherical harmonics. Since the dipole moment is a tensor of rank one, we can expand μ_q as

$$\mu_q(\vec{r}_1\vec{r}_2\vec{R}) = \frac{(4\pi)^{3/2}}{\sqrt{3}} \sum_{\lambda_1,\lambda_2,L,\Lambda} A_\Lambda(\lambda_1\lambda_2 L; r_1 r_2 R) Y^{\lambda_1\lambda_2 L\Lambda}_{1,q}(\omega_1,\omega_2,\Omega) \ . \tag{2.23}$$

for some $A_\Lambda(\lambda_1\lambda_2 L; r_1 r_2 R)$. These $A_\Lambda(\lambda_1\lambda_2 L; r_1 r_2 R)$ are the *dipole components*. They are a coordinate system independent classification of the dipole moment. The factor of $(4\pi)^{3/2}/\sqrt{3}$ has been introduced so the average of $\vec{\mu}^2$ over all angles is $\sum_{\lambda_1,\lambda_2,L,\Lambda} A_\Lambda(\lambda_1\lambda_2 L; r_1 r_2 R)^2$ [Poll and Van Kranendonk, 1961].

The total dipoles for molecule-molecule systems are given by:

$$\mu_q(\vec{r}_1\vec{r}_2\vec{R}) = \frac{(4\pi)^{3/2}}{\sqrt{3}} \sum_{\lambda_1,\lambda_2,L,\Lambda} A_\Lambda(\lambda_1\lambda_2 L; r_1 r_2 R)$$

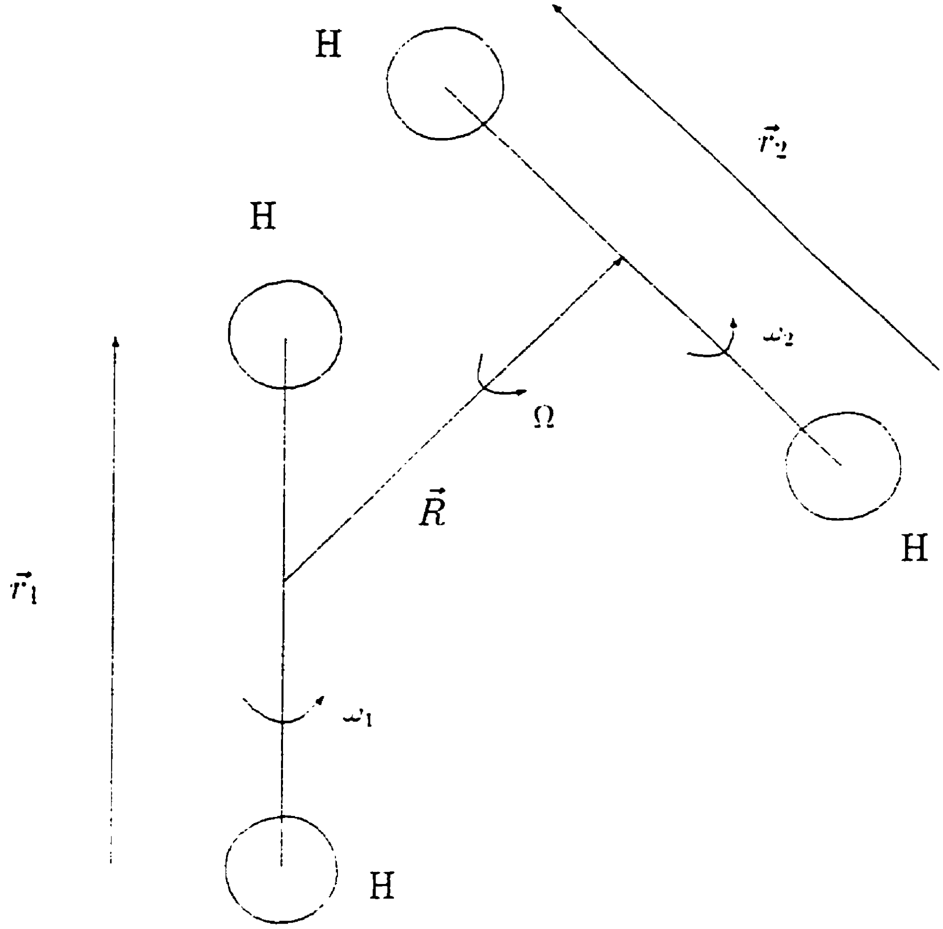

Figure 2.2:

H_2-H_2 collision coordinates

$$
\begin{aligned}
&\times \sum_{m_1, m_2, M} C(\Lambda, L, 1; m_1 + m_2, M, q) \\
&\times C(\lambda_1, \lambda_2, \Lambda; m_1, m_2, m_1 + m_2) \\
&\times Y_{\lambda_1, m_1}(\omega_1) Y_{\lambda_2, m_2}(\omega_2) Y_{L, M}(\Omega) \ . \qquad (2.24)
\end{aligned}
$$

or equivalently,

$$
\begin{aligned}
\mu_q(\vec{r}_1 \vec{r}_2 \vec{R}) &= \frac{(4\pi)^{3/2}}{\sqrt{3}} \sum_{\lambda_1, \lambda_2, L, \Lambda} A_\Lambda(\lambda_1 \lambda_2 L; r_1 r_2 R) \\
&\times \sum_{m_2, M} C(\Lambda, L, 1; q - M, M, q) \\
&\times C(\lambda_1, \lambda_2, \Lambda; q - M - m_2, m_2, q - M) \\
&\times Y_{\lambda_1, q-M-m_2}(\omega_1) Y_{\lambda_2, m_2}(\omega_2) Y_{L, M}(\Omega) \ . \qquad (2.25)
\end{aligned}
$$

Equation (2.25) is obtained by using the condition $m_1 + m_2 + M = q$ which is imposed by the Clebsch-Gordon coefficients. Triangle conditions $\Delta(\Lambda L 1)$ and $\Delta(\lambda_1 \lambda_2 \Lambda)$ are also imposed [Rose, 1957]. As well, parity considerations force $\lambda_1 + \lambda_2 + L$ to be odd, and for homonuclear diatomic molecules λ_1, λ_2, and Λ must be even.

In Equation (2.22) we coupled ω_1 to ω_2, and then coupled the result to Ω. Other couplings exist which would lead to different expansion coefficients. Specifically, coupling ω_1 to Ω and the result to ω_2 yields:

$$
\begin{aligned}
\mu_q(\vec{r}_1 \vec{r}_2 \vec{R}) &= \frac{(4\pi)^{3/2}}{\sqrt{3}} \sum_{\lambda_1, \lambda_2, L, \Lambda} A'_\Lambda(\lambda_1 \lambda_2 L; r_1 r_2 R) \times \\
&\sum_{m_1, m_2, M} C(\Lambda, \lambda_2, 1; m_1 + M, m_2, q) \\
&\times C(\lambda_1, L, \Lambda; m_1, M, m_1 + M) \\
&\times Y_{\lambda_1, q-M-m_2}(\omega_1) Y_{\lambda_2, m_2}(\omega_2) Y_{L, M}(\Omega) \ . \qquad (2.26)
\end{aligned}
$$

and coupling ω_2 to Ω and the result to ω_1 yields

$$
\mu_q(\vec{r}_1 \vec{r}_2 \vec{R}) = \frac{(4\pi)^{3/2}}{\sqrt{3}} \sum_{\lambda_1, \lambda_2, L, \Lambda} A''_\Lambda(\lambda_1 \lambda_2 L; r_1 r_2 R)
$$

$$
\begin{aligned}
&\times \sum_{m_1, m_2, M} C(\Lambda, \lambda_1, 1; m_2 + M, m_1, q) \\
&\times C(\lambda_2, L, \Lambda; m_2, M, m_2 + M) \\
&\times Y_{\lambda_1, q-M-m_2}(\omega_1) Y_{\lambda_2, m_2}(\omega_2) Y_{L, M}(\Omega) \; . \qquad (2.27)
\end{aligned}
$$

The different dipole components are related by [Tipping and Poll. 1985]:

$$
\begin{aligned}
A_\Lambda(\lambda_1\lambda_2L; r_1r_2R) &= \sum_{\Lambda'}[(2\Lambda+1)(2\Lambda'+1)]^{1/2} W(\lambda_1\lambda_2 1 L; \Lambda\Lambda') \\
&\quad \times A''_{\Lambda'}(\lambda_1\lambda_2L; r_1r_2R) \; . \qquad (2.28) \\
&= \sum_{\Lambda'}(-1)^{\lambda_1+\lambda_2-\Lambda}[(2\Lambda+1)(2\Lambda'+1)]^{1/2} W(L\lambda_1 1\lambda_2; \Lambda'\Lambda) \\
&\quad \times A'_{\Lambda'}(\lambda_1\lambda_2L; r_1r_2R) \; . \qquad (2.29)
\end{aligned}
$$

where W are *Racah coefficients* [Rose. 1957].

The importance of these other representations will become apparent later.

We now have an expansion for the total dipole moment, but it remains to calculate the coefficients $A_\Lambda(\lambda_1\lambda_2L; r_1r_2R)$. We will now discuss some nomenclature and multipolar induction in some detail.

The induced electric dipole is given in general by Equation (2.18). The second rank polarizability tensor $\vec{\alpha}$ can be split into isotropic and anisotropic parts. The anisotropic part can again be split into a symmetric and antisymmetric part. The electric potential at point $\vec{R}$ due to molecule 1 can be expressed as

$$
\vec{\Phi}^{(1)}(\vec{r}_1, \vec{R}) = \sum_{l,m} Q_l^{(1)}(r_1) R^{-(l+1)} \frac{4\pi}{2l+1} Y_{l,m}(\omega_1) Y^{*}_{l,m}(\Omega) \qquad (2.30)
$$

where $Q_l^{(1)}$ is the *multipole moment* of molecule 1. From this potential we can determine the electric field at $\vec{R}$ due to molecule 1 using $E_q^{(1)} = -\vec{\nabla}_q \cdot \vec{\Phi}^{(1)}$. Contracting this with the isotropic part of the polarizability of molecule 2, $\alpha^{(2)}(r_2)$, we obtain the contribution to the dipole moment:

$$\mu_q^{(1)} = 4\pi \left(\frac{l+1}{3}\right)^{1/2} (-1)^l Q_l^{(1)} R^{-(l+2)} \alpha^{(2)}(r_2) \times \sum_{m,M} C(l, l+1, 1; m, M, q) Y_{l,m_1}(\omega_1) Y_{l+1,M}(\Omega) . \quad (2.31)$$

Comparing Equation (2.31) with Equation (2.25) we find that this contribution comes from the dipole component

$$A_l(l, 0, l+1; r_1 r_2 R) = (l+1)^{1/2} (-1)^l \frac{Q_l^{(1)}(r_1) \alpha^{(2)}(r_2)}{R^{l+2}} . \quad (2.32)$$

This component results from isotropic multipolar induction of order l (isotropic since it came from the isotropic part of the polarizability; order l since it involves the multipole moment $Q_l^{(1)}$). Similarly, the isotropic part of the polarizability of molecule 1 interacts with the electric field from molecule 2 to give the dipole component:

$$A_l(0, l, l+1; r_1 r_2 R) = -(l+1)^{1/2} (-1)^l \frac{Q_l^{(2)}(r_2) \alpha^{(1)}(r_1)}{R^{l+2}} . \quad (2.33)$$

For $l = 0$ (*charge induction*), both these mechanisms contribute to $A_0(001; r_1 r_2 R)$. Since they have the same angular dependence the two mechanisms will interfere with each other. Charge induction would involve the interaction of two charged ions, and although it may be important to the spectrum of irradiated solid H_2, it would not arise in gaseous H_2.

An induction mechanism which would be significant to the spectrum for gaseous H_2 would be *isotropic quadrupolar induction*, given by the dipole component

$$A_2(2, 0, 3; r_1 r_2 R) = \sqrt{3}\, \frac{Q_2^{(1)}(r_1) \alpha^{(2)}(r_2)}{R^4} . \quad (2.34)$$

This dipole component is due to coupling of the isotropic part of the polarizability of molecule 2 with the quadrupole part of the electric field generated by molecule

1. A similar component, $A_2(0,2,3; r_1 r_2 R)$, is also present where the roles of the molecules are reversed from above.

Other dipole moments will arise from different mechanisms and hence have different names. Different A_Λ components will have different angular dependences and therefore will not interfere with each other.

We have already seen that HD has a nonzero allowed dipole moment. The allowed dipole moment of molecule 1 has angular dependence ω_1. There exists an induced component with this same angular dependence, the $A_1(100; r_1)$ component.

$$\mu_q(\vec{r}_1) = \sqrt{\frac{4\pi}{3}} A_1(100; r_1) Y_{1,q}(\omega_1) \ . \tag{2.35}$$

For homonuclear molecules this component is zero.

At this point it would be beneficial to elucidate the differences between HD and H_2. For H_2, the center of mass (c.m.) and center of charge (c.c.) coincide. However, the center of mass of HD is shifted away from the center of charge due to the presence of a neutron in the deuterium (the charge distribution remains the same). This fact allows one to obtain the HD-X induced dipole moment relative to the center of mass of the HD molecule from the H_2-X induced dipole moment via a shift in coordinates. (Figure 2.3).

$$\vec{S} = \vec{R} + \vec{d}_1 - \vec{d}_2 \ . \tag{2.36}$$

The HD induced dipole moment is given to first order in $\vec{d}_1 - \vec{d}_2$ as

$$\begin{aligned} \mu_q^{HD-X}(\vec{r}_1 \vec{r}_2 \vec{R}) &= \mu_q^{H_2-X}(\vec{r}_1 \vec{r}_2 \vec{S}) \\ &= (1 + (\vec{d}_1 - \vec{d}_2) \cdot \vec{\nabla}_R) \mu_q^{H_2-X}(\vec{r}_1 \vec{r}_2 \vec{R}) \ . \end{aligned} \tag{2.37}$$

The $(\vec{d}_1 - \vec{d}_2) \cdot \vec{\nabla}_R \mu_q^{H_2-X}(\vec{r}_1 \vec{r}_2 \vec{R})$ can be expanded in the $Y_{1,q}^{\lambda_1 \lambda_2 L \Lambda}$ basis with a shifted induced dipole component given by [Tipping and Poll, 1985]:

$$A_\lambda(l, \lambda_2, L + \gamma; r_1 r_2 R) = d_1 [O_\gamma^L A_\Lambda(\lambda_1 \lambda_2 L; r_1 r_2 R)] (-1)^{L+\lambda-1} \times$$

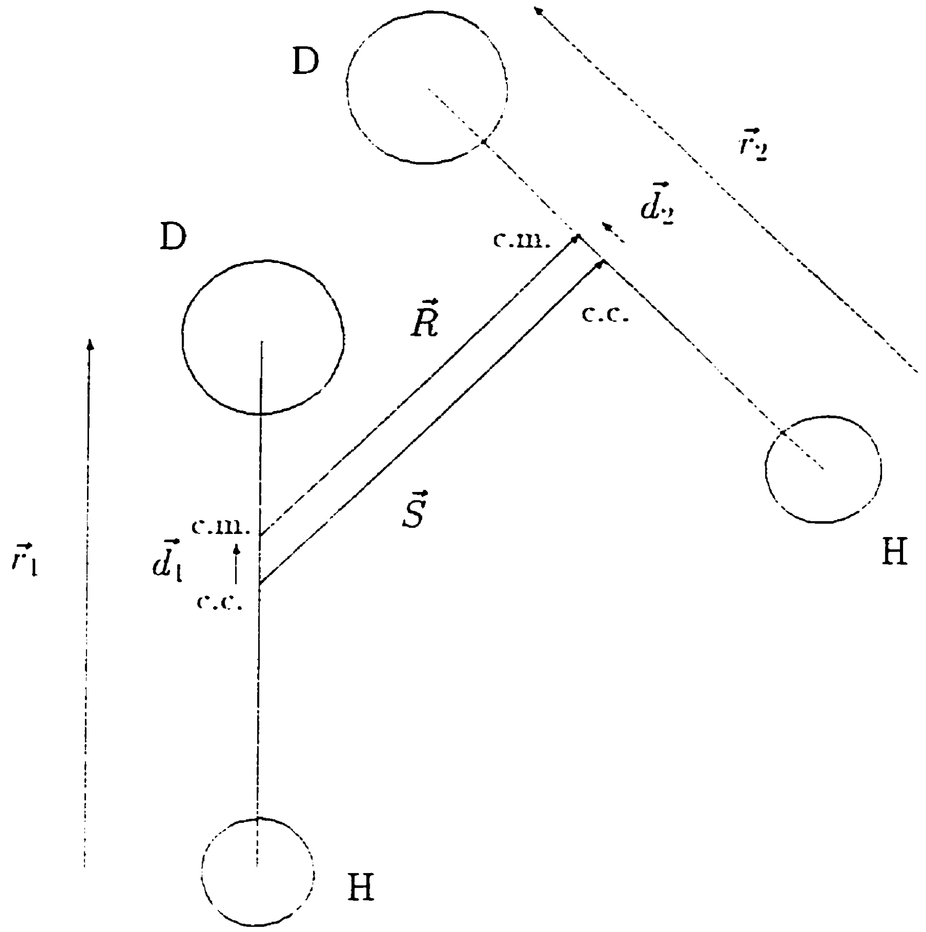

Figure 2.3:

HD-HD collision coordinates

$$
\begin{aligned}
& [(2\lambda_1+1)(2\Lambda+1)(2L+1)(2\lambda+1)]^{1/2} \\
& \times C(1,\lambda_1,l;0,0,0)C(1,L,L+\gamma;0,0,0) \\
& \times W(1l\Lambda\lambda_2;\lambda_1\lambda)W(L+\gamma L\lambda\Lambda;1,1)\ . \qquad (2.38)
\end{aligned}
$$

and

$$
\begin{aligned}
A_\lambda(\lambda_1,l,L+\gamma;r_1r_2R) &= d_2[O_\gamma^L A_\Lambda(\lambda_1\lambda_2L;r_1r_2R)](-1)^{\Lambda+L} \\
& \times [(2\lambda_2+1)(2\Lambda+1)(2L+1)(2\lambda+1)]^{1/2} \\
& \times C(1,\lambda_2,l;0,0,0)C(1,L,L+\gamma;0,0,0) \\
& \times W(1l\Lambda\lambda_1;\lambda_2\lambda)W(L+\gamma L\lambda\Lambda;1,1)\ . \qquad (2.39)
\end{aligned}
$$

The index $\gamma = \pm 1$, and the O_γ^L operators are given by

$$
\begin{aligned}
O_1^L &= \frac{d}{dr} - \frac{L}{R}\ , \qquad (2.40) \\
O_{-1}^L &= \frac{d}{dr} - \frac{L+1}{R}\ . \qquad (2.41)
\end{aligned}
$$

These shifted dipole components introduce odd powers of λ.

In this thesis we will be dealing only with HD-atom system (Figure 2.4). Equation (2.24) simplifies since $d_2 = 0$ and $d_1 = r_1/6$. We can approximate $r_1 \sim r_e$, where r_e is the equilibrium separation of the HD nuclei. The coupling simplifies since in this case $r_2 = 0$, $\lambda_2 = 0$, and $\lambda_1 = \Lambda$. Therefore Equation (2.25) reduces to:

$$
\begin{aligned}
\mu_q(\vec{r}_1\vec{R}) &= 4\pi \sum_{\Lambda,L} A_\Lambda(\Lambda L;r_1R)\sum_m(-1)^{1-q} \\
& \times \begin{bmatrix} 1 & \Lambda & L \\ -q & q-m & m \end{bmatrix} Y_{\Lambda,q-m}(\theta,\phi)Y_{L,M}(\Omega) \qquad (2.42)
\end{aligned}
$$

where $\omega_1 = \omega = (\theta,\phi)$, and the Clebsch-Gordon coefficient C has been replaced by a 3-j symbol [Rose, 1957]. The numerical estimates of the induced dipole components

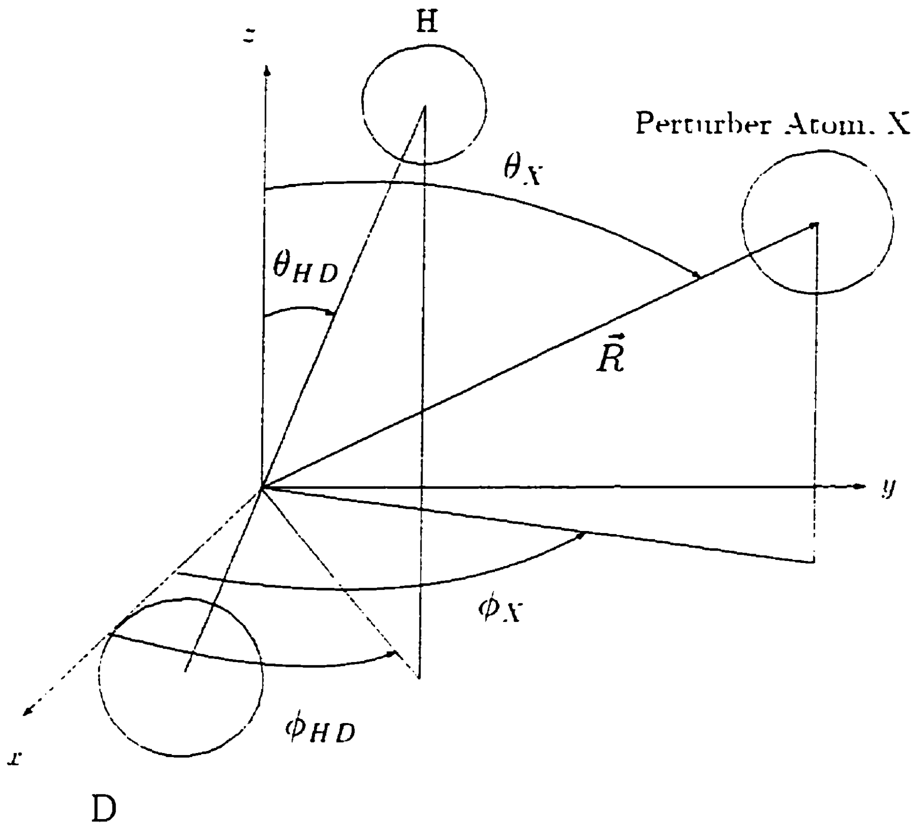

Figure 2.4:

HD-atom collision coordinates

for HD-X (X=He. Ar) are given by Borysow *et al.* (1988). They employed a sum over states technique. The A coefficients are replaced by analogous B coefficients which include a vibrational average:

$$B_{\Lambda}^{vv'}(\Lambda L; R) = \langle v' | A_{\Lambda}(\lambda_1 \lambda_2 L; r_1 r_2 R) | v \rangle \ . \qquad (2.43)$$

where v and v' denote initial and final vibrational states of the HD molecule.

2.3 Collisional Interference

For most gases. allowed lines usually have an intensity that is much larger than any collision-induced intensity. Thus. interference effects between the two transitions are negligible.

We have seen that the small permanent dipole moment of HD results in transitions which are comparable in magnitude to that of collision-induced transitions. Thus. interference between these two processes is possible and observable for HD [Poll *et al.*. 1976].

The most recent theory which models HD-X collisional interference [Gao *et al.*. 1991] incorporates the impact and the binary collision approximations.

The spectral profile looks in general like a broad background with a series of spikes corresponding to transitions between the molecular energy levels of the radiator (Figure 2.5: this Figure will be discussed in more detail in Chapter 3.1). The impact approximation assumes that we are only interested in a region near the line center of one of these spikes. Mathematically. this corresponds to assuming that for the frequency of absorption (or emission) the detuning is small compared to the inverse of the collision duration [Burnett. 1985]. That is.

$$\Delta\tau_c \ll 1.$$

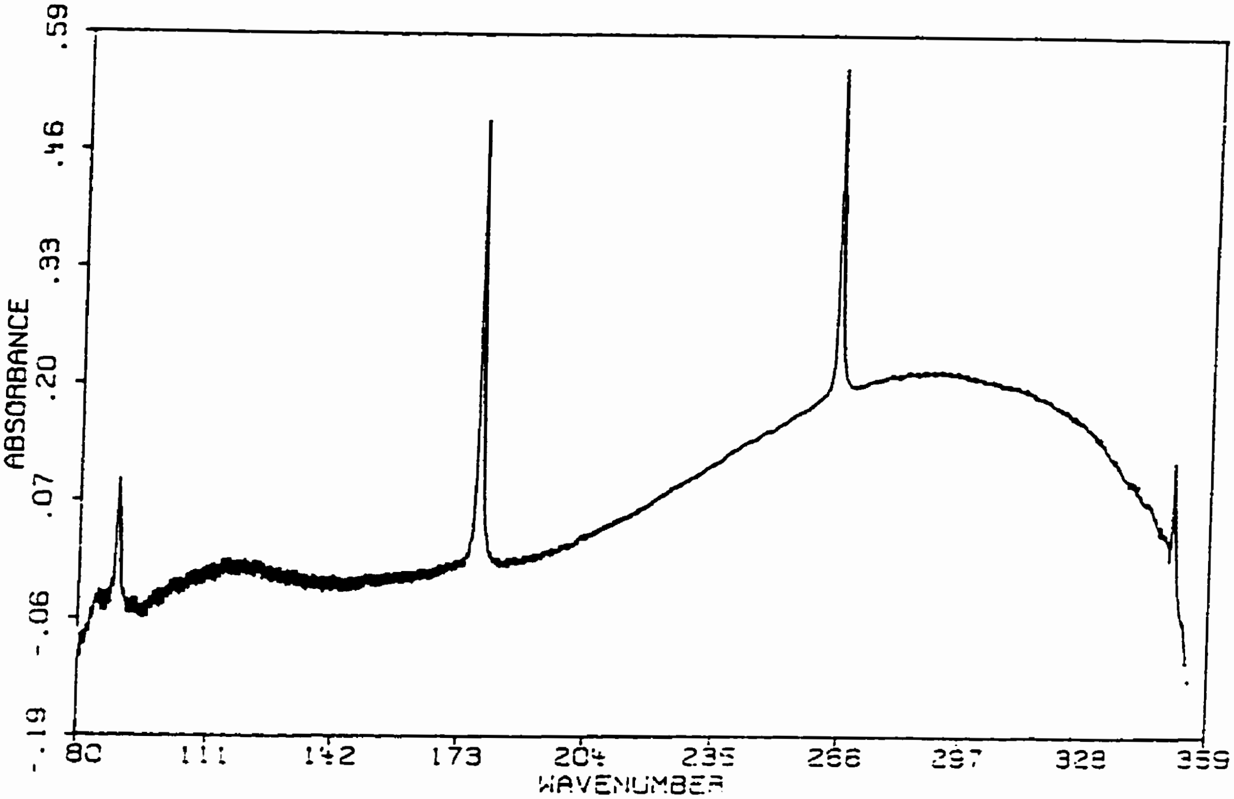

Figure 2.5:

Sample spectrum for the absorbance of HD at 50 amagat and 195 K. From Ph.D. thesis of Z. Lu, 1991.

where $\Delta = \omega - \omega_{eg}$ is the detuning and τ_c is the duration of the collision. For rotational HD in the pure band the detuning is of the order 10^{10} Hz and the duration of the collision is $10^{-12} - 10^{-14}$ seconds, so this condition is satisfied.

The binary collision approximation [Alber and Cooper, 1986] reduces the system under consideration from a gas of N perturbers around a single radiator to a collision between a single perturber and a single radiator.

The thermal motion of the particles of a gas will cause the particles to absorb at slightly different frequencies and give rise to *Doppler broadening* [London, 1983]. This results in a Gaussian line shape with a full width at half maximum given by

$$B_{Doppler} = 2\omega_0 \left(\frac{2k_bTln2}{mc^2}\right)^{\frac{1}{2}} \quad . \tag{2.44}$$

which is independent of gas density. For the pure rotational spectrum of HD, at a temperature of 295 K, the Doppler broadening of the $R_0(3)$ line will be $B_{Doppler} = 3.5 \times 10^{-3}$ cm^{-1}. Experimentally, the broadening coefficient of this line is found to be 1.8×10^{-2} cm^{-1}/amagat [Drakopoulos and Tabisz, 1987]. For densities above 10 amagat the Doppler broadening will be a factor of 100 smaller, and completely negligible. Doppler broadening is therefore not included in the theory of intracollisional interference.

The theory used to model the collisional interference is due to Gao, Tabisz, Trippenbach, and Cooper [Gao *et al.*, 1991]. It contains provisions for m and J mixing and collisional propagation, and reduces to the pioneering theory of Herman, Tipping, and Poll [Herman *et al.*, 1979].

The system considered is a single neutral radiator (HD) in a bath of N neutral foreign perturbers (X=He, Ar, Ne, ...) immersed in a radiation field. The radiation field consists of modes with wave vector $\mathbf{k}$ and polarization vector $\vec{\lambda}$. The radiator has closely spaced vibration-rotation energy levels, and the perturber has widespread electronic energy levels. The perturber thus remains in the same energy level for the duration of the collision, while the radiator can change energy levels, resulting in absorption or emission.

The system is solved via a master equation formulation [Alber and Cooper, 1986] in Liouville space [Burnett, 1985]. The density matrix of the gas is constructed, and the evolution of this density matrix is determined in the presence of the incident radiation. Solving the master equation then yields the absorption and stimulated emission spectra.

The absorption coefficient is given by:

$$\begin{aligned} \alpha(\omega) &= n_R \left(\frac{4\pi\omega}{3\hbar c}\right)(1 - e^{-\beta\hbar\omega})P(J_g) \\ &\quad \times Re\left[i(\Delta + i\gamma)^{-1}(\mu_{HD} + n_p\mu_1)(\mu_{HD} + n_p\mu_2)\right]. \end{aligned} \tag{2.45}$$

where $\beta = 1/k_BT$; ω is the frequency of the incident light; ω_{eg} is the molecular transition frequency; $\Delta = \omega - \omega_{eg}$ is the detuning; $P(J)$ is the normalized Boltzmann distribution; n_p and n_R are perturber and radiator number densities.

The complex line broadening coefficient γ is given by:

$$\begin{aligned} \gamma &= n_p \Bigg[1 - \sum_{m_e,q,m_g,m'_e,m'_g} (-1)^{m'_e+m_e} \begin{bmatrix} J_e & 1 & J_g \\ -m'_e & q & m'_g \end{bmatrix} \\ &\quad \times \begin{bmatrix} J_e & 1 & J_g \\ -m_e & q & m_e \end{bmatrix} \langle J_e m'_e|\hat{S}|J_e m_e\rangle\langle J_g m'_g|\hat{S}|J_g m_g\rangle^* \Bigg]_{coll} \end{aligned} \tag{2.46}$$

where $\hat{S}$ is the S matrix for the collision between the radiator and perturber, and $|Jm\rangle$ are spherical harmonic wavefunctions for HD. The subscript *coll* implies a collision average.

$$[F]_{coll} = \int_0^\infty dv\, 4\pi v^3 w(v) \int_0^\infty ds\, 2\pi s\, F. \tag{2.47}$$

where

$$w(v) = \frac{2}{\sqrt{2\pi}} \left(\frac{m}{k_B T} \right)^{\frac{1}{2}} exp \left(\frac{-mv^2}{2k_B T} \right) . \tag{2.48}$$

where s is impact parameter and v is velocity. In forming this collisional average the classical path approximation has been used. The classical path approximation [Allard and Kielkopf, 1982] assumes that the trajectories the particles follow during the collision are given by the classical solution to the Euler-Lagrange equations for the perturber-radiator system. For many systems this approximation is good, but for systems with a small reduced mass and small velocity (temperature) this approximation would not be valid (see Chapter 4).

The reduced matrix element for the allowed dipole moment of the radiator HD is given by:

$$\mu_{HD} = \langle J_e || \hat{\mu}_{HD} || J_g \rangle . \tag{2.49}$$

The dipole moments μ_1 and μ_2 are functions of the collision induced dipole operator $\hat{\mu}_e$:

$$\begin{aligned} \mu_1 \quad = \quad & \sum_{m_e, q, m_g} (-1)^{J_e - m_e} \begin{bmatrix} J_e & 1 & J_g \\ -m_e & q & m_g \end{bmatrix} \int_{-\infty}^{\infty} dt_0 e^{i\omega_{eg} t_0} \\ & \times \left[\langle J_e m_e | U^{I\dagger}(t_0, -\infty) \left[\hat{\mu}_e^I(t_0) \right]_q U^{I}(t_0, -\infty) | J_g m_g \rangle^* \right]_{coll} \end{aligned} \tag{2.50}$$

and

$$\mu_2 = \sum_{J_i} \mu_{2p}(J_i) e^{-\beta(E_i - E_g)} . \tag{2.51}$$

where

$$\begin{aligned} \mu_{2p}(J_i) \quad = \quad & \sum_{m_e, q, m_g, m_i} (-1)^{J_e - m_e} \begin{bmatrix} J_e & 1 & J_g \\ -m_e & q & m_g \end{bmatrix} \int_{-\infty}^{\infty} dt_0 e^{-i\omega_{eg} t_0} \\ & \times \left[\langle J_e m_e | U^{I}(\infty, t_0) \left[\hat{\mu}_e^I(t_0) \right]_q U^{I}(t_0, -\infty) | J_i m_i \rangle \langle J_g m_g | \hat{S} | J_i m_i \rangle^* \right]_{coll} . \end{aligned} \tag{2.52}$$

The superscript I on the collision induced dipole operator indicates that the interaction representation with respect to the radiator HD is being used:

$$\hat{\mu}_e^I = e^{iH_{HD}t}\hat{\mu}_e e^{-iH_{HD}t} \, . \tag{2.53}$$

The absorption coefficient may be written as a Fano profile - the sum of a Lorentzian and an asymmetric dispersion profile:

$$\begin{aligned} \alpha(\omega) &= n_R \left(\frac{4\pi\omega}{3\hbar c}\right)(1 - e^{-\beta\hbar\omega})P(J_g)|\mu_{HD}|^2 \\ &\quad \times \left[\frac{Bn_p/\pi}{(\Delta - Sn_p)^2 + (Bn_p)^2}(1 + an_p + bn_p^2)\right. \\ &\quad \left. - \frac{(\Delta - Sn_p)/\pi}{(\Delta - Sn_p)^2 + (Bn_p)^2}(cn_p + dn_p^2)\right] . \end{aligned} \tag{2.54}$$

where

$$\gamma = n_p(B + iS) \, . \tag{2.55}$$

$$\mu_1 = y_1' + iy_1'' \, . \tag{2.56}$$

$$\mu_2 = y_2' + iy_2'' \, . \tag{2.57}$$

are complex and the real parameters a, b, c, d are given by:

$$a = (y_1' + y_2')/\mu_{HD} \, . \tag{2.58}$$

$$b = (y_1'y_2' - y_1''y_2'')/\mu_{HD}^2 \, . \tag{2.59}$$

$$c = (y_1'' + y_2'')/\mu_{HD} \, . \tag{2.60}$$

$$d = (y_1'y_2'' + y_1''y_2')/\mu_{HD}^2 \, . \tag{2.61}$$

The line shape (Equation (2.54)) is seen to be a Lorentzian at low perturber density but can become more asymmetric as the perturber density increases. By determining the dipole moments μ_1 and μ_2 one is able to find the line shape parameters given in Equations (2.58) - (2.61). Details of how this is accomplished will be found in Chapters 3 and 4.

Chapter 3

Role of Induced Dipole: Pure Rotational Spectrum

The theory of Section 2.3 has been applied to the pure rotational spectrum of HD-X (X=He, Ar) systems [Gao *et al.*, 1992]. The inelastic effects due to mixing were shown to be essential to the final line shape. In the present chapter we will expand upon these results and determine the effect that each individual component of the induced dipole has upon the final line shape.

3.1 Theory

We begin with a short discussion on nomenclature. As we have seen, the spectral profile looks like a series of spikes (corresponding to transitions between the molecular energy levels of the radiator) on a broad collision-induced background (cf. Figure 2.5). The selection rule for absorption for pure rotational transitions of a molecule is $\Delta J = +1$, or $J_f = J_i + 1$. For the pure rotational spectrum these transitions are labelled $R_0(J_i) = R(J)$. The energy in wavenumbers is given approximately by $E_J = B_0 J(J+1)$, where B_0 is known as the rotational constant. Therefore the wavenumber of the $R_0(J)$ transition is given by $\omega_J = E_{J_f} - E_{J_i} = E_{J+1} - E_J = 2B_0(J+1)$. If the rotational constant is known, the location of the transitions for the spectrum is given roughly by $2B_0(J+1)$. For HD, $B_0 \sim 45$ cm^{-1}, and the transitions occur at $\omega_0 \sim 90$ cm^{-1} ($R_0(0)$); $\omega_1 \sim 180$ cm^{-1} ($R_0(1)$); $\omega_2 \sim 270$ cm^{-1} ($R_0(2)$); etc. (cf. Figure 2.5). Note that Figure 2.5 includes the shift, which increases as T increases and depends on gas density.

There are two main inputs to the calculation. They are the semiempirical adiabatic intermolecular potential and the pair induced dipole moments. We will discuss both in detail in the following sections.

3.1.1 Intermolecular Potential

For the case we are considering - a linear molecule treated as a rigid rotator interacting with an atom - the interaction potential depends only on the magnitude of the vector $\vec{R}$ connecting the center of mass of the molecule and atom and the angle Θ between $\vec{R}$ and the molecular axis. This potential can be expanded as:

$$V(R,\Theta) = \sum_{k=0}^{\infty} V^{(k)}(R) P_k(cos\Theta) \ . \tag{3.1}$$

This full potential should be used to calculate the trajectory and rotational transitions in the HD molecule. A semiclassical approximation is used and we split the potential into isotropic and anisotropic parts:

$$\begin{aligned} V^{(iso)}(R) &= V^{(0)}(R) \ , & (3.2) \\ V^{(ani)}(R,\Theta) &= \sum_{k=1}^{\infty} V^{(k)}(R) P_k(cos\Theta) \ . & (3.3) \end{aligned}$$

The isotropic part is used to determine the classical trajectory that the atom follows during collisions. The anisotropic part is used to form the time evolution operator for HD rotational transitions [Sakurai, 1985]:

$$i\hbar \frac{d}{dt} U^{I}(t,t') = V^{(ani)\,I}(\vec{R}(t))\, U^{I}(t,t') \,, \tag{3.4}$$

where we are working in the interaction representation

$$V^{(ani)\,I}(\vec{R}(t)) = e^{iH_{HD}t}\, V^{(ani)}(\vec{R}(t))\, e^{-iH_{HD}t} \,. \tag{3.5}$$

The classical trajectory determines $\vec{R}(t)$. For the HD molecule in its ground electronic state, the rotational wavefunctions are the spherical harmonics. The matrix elements of $V^{(ani)}$ are obtained using the spherical harmonic addition theorem [Rose,1957] (cf. Figure 2.4, $\Theta = \theta_{HD} - \theta_X$):

$$\begin{aligned} \langle J'm'|V^{(ani)}(t)|Jm\rangle &= (-1)^{m'}[(2J'+1)(2J+1)]^{1/2} \sum_{k} \left[\frac{4\pi}{2k+1}\right]^{1/2} \times \\ &\quad \begin{bmatrix} J' & k & J \\ -m' & m'-m & m \end{bmatrix} \begin{bmatrix} J' & k & J \\ 0 & 0 & 0 \end{bmatrix} \\ &\quad \times Y^{*}_{k,m'-m}(\theta(t),\phi(t))\, V^{(k)}(R(t)) \,, \end{aligned} \tag{3.6}$$

where $\theta(t) = \theta_X(t)$ and $\phi(t) = \phi_X(t)$.

Accurate, modern H_2-atom potentials are available. It is a simple matter to obtain the HD-atom potential from these potentials if nonadiabatic couplings are ignored. The HD-atom potentials are related to the H_2-atom potentials through a shift of the origin to the center of mass of HD. This results in [Kreek and Le Roy, 1975]:

$$V^{(k)}_{HD-X}(R) = \frac{2k+1}{2} \int_{-1}^{1} V_{H_2-X}(R',x')\, P_k(x)\, dx \,, \tag{3.7}$$

where

$$\begin{aligned} R' &= (R^2 + \delta^2 + 2R\delta x)^{1/2} \,, & (3.8) \\ x' &= (Rx + \delta)/R' \,. & (3.9) \end{aligned}$$

where $\delta = r_e/6$ with $r_e = 0.7666393$ Å being the average internuclear distance of the H_2 molecule.

The potentials used were from Mulder, Avoird and Wormer [Mulder *et al.* 1979] for helium as the perturber, and Le Roy and Hutson [Le Roy and Hutson, 1987] for argon.

3.1.2 Induced Dipole Moments

As we have seen (Equation (2.42), the induced dipole of a molecule-atom collision can be written as:

$$[\hat{\mu}_e(R)]_q = 4\pi \sum_{\Lambda,L} B_\Lambda^{vv'}(\Lambda L;R) \sum_m (-1)^{1-q} \times \begin{bmatrix} 1 & \Lambda & L \\ -q & q-m & m \end{bmatrix} Y_{\Lambda,q-m}(\theta,\phi) Y_{L,M}(\Omega) \qquad (3.10)$$

Nine important induced dipole components have been determined by Borysow, Frommhold and Meyer [Borysow *et al.*, 1988] in a parametric form as

$$B_\Lambda^{vv'}(\Lambda L;R) = Ae^{B(R-R_0)+C(R-R_0)^2} + C_n R^{-n} + C_{n+1} R^{-(n+1)} . \qquad (3.11)$$

The A, B, C, C_n, C_{n+1}, R_0, and n are the parameters given for a specific HD-X interaction. For the pure rotational spectrum treated in this chapter $v = v' = 0$ and the superscript will be dropped. Here, as in Chapter 2, Λ refers to the symmetry of the molecular charge distribution, and L refers to the rank of the field tensor for the charge distribution.

Each component in Equation (3.10) arises from a different mechanism. The $B_0(01)$ component comes from the short range isotropic overlap interaction. The $B_1(10)$ has the same symmetry as the allowed moment of the molecule and arises from a short range anisotropic overlap interaction. Five other components $B_1(12)$, $B_2(21)$, $B_3(32)$, $B_3(34)$, and $B_4(43)$ are also induced through anisotropic overlap interactions. The $B_2(23)$ component arises from long range quadrupole induction. The $B_4(45)$ component arises from long range hexadecapole induction. The largest of these components are $B_0(01)$, $B_2(23)$, $B_2(21)$ and $B_3(32)$. These components contribute the most to the purely induced absorption coefficient.

3.2 Results

Tables 3.1 - 3.6 present the results for the contribution to the line shape parameters (Equations (2.58) - (2.61)) from each induced dipole component for the following systems: HD-He, the $R_0(1)$ transition at 77, 195, and 295K, and the $R_0(0)$ transition at 295K; HD-Ar, the $R_0(0)$ and $R_0(1)$ transitions at 295K. The HD energy level constants for the rotational spectrum of HD were taken from Green [Green, 1974]. Terms to order $k = 3$ in Equation (3.1) were used. In Equation (2.51), the highest J state included was $J_{max} = 4$. The collisional average, Equation (2.47), was performed by a 4 point Gaussian quadrature in velocity, and 20 impact parameters.

We will discuss each parameter in turn.

3.2.1 Intensity Parameter a

The parameter a contributes to the Lorentzian part of the total line shape (Equation (2.54)), and hence to the total intensity of the line shape. It arises from single collision effects, and therefore has a linear dependence on the perturber density. The intensity parameter a for the total induced dipole is given by the sum of the contribution from each induced dipole component (Equation (2.58)).

In all cases the largest contribution results from $B_1(10)$. This is an expected result since this component of the induced dipole has the same symmetry as the permanent dipole of HD and as such can interfere with the allowed moment without the introduction of an anisotropic interaction potential.

Other components, however, do require an anisotropic interaction potential for interference to occur. The $B_2(21)$ component is in all cases the next most important, and acts to reduce the total a. The only transition where the $B_2(21)$ contribution is over 50% of the $B_1(10)$ contribution is $R_0(0)$ for HD-Ar at 295 K.

The $B_2(23)$ component arises from multipole induction, namely the coupling of the quadrupole moment of HD with the isotropic part of the polarizability of the perturber atom. Since the polarizability goes as a_0^3, where a_0 is the size of the atom, we would expect this component to be larger for HD-Ar than for HD-He, due to the fact that argon is larger than helium. In fact, we do see that the $B_2(23)$ component is more important to the intensity parameter a for HD-Ar than for HD-He.

3.2.2 Asymmetry Parameter c

The parameter c contributes to the dispersion part of the total line shape (Equation (2.54)), and hence to the asymmetry of the line shape. It arises from single collision effects, and therefore has a linear dependence on the perturber density. The asymmetry parameter c is also given by the sum of the contribution from each induced dipole component (Equation (2.60)).

The most important contributions to c come from $B_0(01)$, $B_2(21)$, or $B_2(23)$. These terms are the largest in the induced dipole, and thus have the greatest effect on purely induced absorption. However, there is a great deal of cancellation among the different components. In fact, this cancellation can act to change the sign of the total c relative to the largest single component. In all cases the $B_1(10)$ component is completely negligible. This result is expected, since for collisional broadening the linewidth is zero in the absence of an anisotropic interaction potential. It follows that the isotropic molecular interaction is unimportant to line asymmetry.

3.2.3 Intensity Parameter b

The contributions of the dipole moment components to b and d are more complex. These parameters describe terms in the absorption coefficient which arise from two separate collisions, and have quadratic dependence on the pertuber density. They depend on the product of μ_1 and μ_2, and therefore will in general have 81 contributions to the total, involving the various components of the induced dipole moment. As such, a simple sum of the contributions from the induced dipole components will not give the total as we saw for a and c. To assess the importance of each induced dipole component, the values reported in Tables 3.1 - 3.6 for b and d are derived from having the same induced dipole component act in both collisions.

The parameter b (Equation (2.59)) plays an analogous role to the intensity parameter a, but for successive collisions, and will be small for low densites. Typically this parameter becomes significant at densities of the order of 50 to 100 amagat.

The $B_1(10)$ component is the most important contribution to b, and the importance of the next most important component, the $B_2(21)$ component, is an order of magnitude smaller. The largest $B_2(21)$ relative to $B_1(10)$ is for $R_0(0)$ HD-Ar at 295 K, the same behaviour as we saw for the intensity parameter a. Comparing the $B_1(10)$ contribution with the total b contribution we find that the total is up to an order of magnitude smaller. The terms containing products of different components of the induced moment are therefore seen to be significant. The mixing process again acts to reduce the magnitude of the intensity interference that is obtained by a purely isotropic interaction.

3.2.4 Asymmetry Parameter d

The parameter d (Equation (2.61)) plays an analogous role to the asymmetry parameter c, but for successive collisions, and will also be small for low densities.

The $B_2(21)$ component is always the most dominant contribution to d. The second most important contribution is $B_2(23)$ for HD-Ar: $B_1(10)$ and $B_1(12)$ for HD-He.

3.3 Discussion

Highly quantitative statements about the importance of the induced dipole components cannot be made. The most important contribution to line intensity is $B_1(10)$, the overlap induced dipole with the same symmetry as the permanent moment. This component does not contribute significantly to the line asymmetry. The most important components to line asymmetry are $B_0(01)$ for single collisions contributions, and $B_2(21)$ for two collision contributions. These are the largest overlap components in the induced dipole moment. It had been speculated [Tipping, *et al.*, 1978] that the mixing process would allow contributions to the interference effect from $B_0(01)$, a large isotropic overlap induced component [Poll and Hunt, 1976]. We have seen, however, that other components can have a much greater effect on the interference parameters. In fact, for successive collisions the $B_0(01)$ component is completely negligible. The overall effect of inclusion of mixing is to allow line broadening and asymmetry to occur. We have seen that in most cases mix-

Induced dipole component	a (amagat^{-1})	c (amagat^{-1})	b (amagat^{-2})	d (amagat^{-2})
$B_0(01)$	1.168×10^{-4}	-6.081×10^{-4}	1.804×10^{-14}	-6.949×10^{-14}
$B_1(10)$	4.367×10^{-3}	3.188×10^{-5}	4.765×10^{-6}	6.716×10^{-8}
$B_1(12)$	3.072×10^{-5}	-1.102×10^{-4}	-3.331×10^{-9}	-1.898×10^{-9}
$B_2(21)$	-2.530×10^{-4}	8.610×10^{-4}	-6.972×10^{-8}	-9.229×10^{-8}
$B_2(23)$	-4.463×10^{-6}	-1.125×10^{-4}	-1.095×10^{-9}	3.208×10^{-10}
$B_3(32)$	1.054×10^{-5}	-4.658×10^{-6}	-7.905×10^{-11}	2.808×10^{-10}
$B_3(34)$	-8.903×10^{-6}	-2.261×10^{-6}	1.596×10^{-11}	8.979×10^{-12}
$B_4(43)$	-1.258×10^{-6}	-2.247×10^{-6}	-1.330×10^{-13}	1.339×10^{-12}
$B_4(45)$	-2.396×10^{-7}	1.167×10^{-6}	-3.631×10^{-13}	-5.153×10^{-14}
All	4.257×10^{-3}	5.409×10^{-5}	4.515×10^{-6}	1.200×10^{-7}

Table 3.1:

Values of interference parameters for $R_0(1)$ of HD-He at 77 K

Induced dipole component	a (amagat^{-1})	c (amagat^{-1})	b (amagat^{-2})	d (amagat^{-2})
$B_0(01)$	-1.422×10^{-5}	-1.647×10^{-3}	2.084×10^{-14}	-1.870×10^{-13}
$B_1(10)$	5.909×10^{-3}	1.874×10^{-6}	8.730×10^{-6}	6.187×10^{-9}
$B_1(12)$	-1.002×10^{-4}	-3.161×10^{-4}	-2.247×10^{-8}	1.590×10^{-8}
$B_2(21)$	-8.262×10^{-4}	7.084×10^{-4}	4.902×10^{-8}	-2.876×10^{-7}
$B_2(23)$	-8.039×10^{-5}	-1.064×10^{-4}	1.049×10^{-10}	3.235×10^{-9}
$B_3(32)$	-4.184×10^{-5}	1.572×10^{-5}	3.895×10^{-10}	-2.848×10^{-10}
$B_3(34)$	-1.489×10^{-5}	8.877×10^{-6}	3.698×10^{-11}	-6.609×10^{-11}
$B_4(43)$	-1.222×10^{-6}	-3.527×10^{-6}	-2.509×10^{-12}	3.021×10^{-12}
$B_4(45)$	1.903×10^{-6}	3.322×10^{-6}	-1.756×10^{-12}	3.487×10^{-12}
All	4.832×10^{-3}	-1.335×10^{-3}	5.988×10^{-6}	-3.350×10^{-6}

Table 3.2:

Values of interference parameters for $R_0(1)$ of HD-He at 195 K

Induced dipole component	a (amagat^{-1})	c (amagat^{-1})	b (amagat^{-2})	d (amagat^{-2})
$B_0(01)$	-1.138×10^{-3}	-1.672×10^{-3}	3.607×10^{-14}	7.671×10^{-15}
$B_1(10)$	6.701×10^{-3}	-5.036×10^{-5}	1.121×10^{-5}	-1.697×10^{-7}
$B_1(12)$	-6.309×10^{-4}	-5.465×10^{-4}	2.486×10^{-8}	1.724×10^{-7}
$B_2(21)$	-2.072×10^{-3}	1.886×10^{-4}	1.105×10^{-6}	-2.109×10^{-7}
$B_2(23)$	5.918×10^{-6}	5.729×10^{-4}	-8.555×10^{-8}	2.267×10^{-9}
$B_3(32)$	-6.740×10^{-5}	-1.320×10^{-5}	1.166×10^{-9}	4.275×10^{-10}
$B_3(34)$	1.798×10^{-5}	-4.245×10^{-7}	7.811×10^{-11}	-1.594×10^{-11}
$B_4(43)$	3.064×10^{-6}	9.109×10^{-7}	2.162×10^{-12}	1.944×10^{-12}
$B_4(45)$	1.460×10^{-6}	-1.783×10^{-6}	-2.722×10^{-13}	-1.296×10^{-12}
All	2.821×10^{-3}	-1.522×10^{-3}	1.819×10^{-6}	-3.799×10^{-6}

Table 3.3:

Values of interference parameters for $R_0(0)$ of HD-He at 295 K

Induced dipole component	a (amagat^{-1})	c (amagat^{-1})	b (amagat^{-2})	d (amagat^{-2})
$B_0(01)$	-2.297×10^{-4}	-2.153×10^{-3}	-7.805×10^{-15}	-3.412×10^{-14}
$B_1(10)$	6.911×10^{-3}	-2.619×10^{-6}	1.194×10^{-5}	-6.772×10^{-9}
$B_1(12)$	-2.120×10^{-4}	-4.705×10^{-4}	-4.436×10^{-8}	5.015×10^{-8}
$B_2(21)$	-1.323×10^{-3}	7.965×10^{-4}	2.769×10^{-7}	-5.266×10^{-7}
$B_2(23)$	-1.440×10^{-4}	-6.557×10^{-5}	4.828×10^{-9}	3.015×10^{-9}
$B_3(32)$	-7.109×10^{-5}	2.168×10^{-5}	1.159×10^{-9}	-7.616×10^{-10}
$B_3(34)$	-2.187×10^{-5}	2.079×10^{-5}	1.259×10^{-11}	-2.206×10^{-10}
$B_4(43)$	-9.570×10^{-7}	-4.657×10^{-6}	-5.653×10^{-12}	3.283×10^{-12}
$B_4(45)$	4.458×10^{-6}	4.042×10^{-6}	1.107×10^{-12}	9.321×10^{-12}
All	4.912×10^{-3}	-1.853×10^{-3}	6.279×10^{-6}	-5.139×10^{-6}

Table 3.4:

Values of interference parameters for $R_0(1)$ of HD-He at 295 K

Induced dipole component	a (amagat^{-1})	c (amagat^{-1})	b (amagat^{-2})	d (amagat^{-2})
$B_0(01)$	-9.608×10^{-4}	-1.410×10^{-3}	1.167×10^{-13}	-3.005×10^{-14}
$B_1(10)$	7.900×10^{-3}	-1.023×10^{-4}	1.553×10^{-5}	-4.014×10^{-7}
$B_1(12)$	-5.912×10^{-4}	-8.148×10^{-5}	8.756×10^{-8}	2.329×10^{-8}
$B_2(21)$	-5.673×10^{-3}	9.929×10^{-4}	8.092×10^{-6}	-2.863×10^{-6}
$B_2(23)$	1.662×10^{-3}	2.694×10^{-3}	-1.185×10^{-6}	2.164×10^{-6}
$B_3(32)$	4.557×10^{-5}	-1.166×10^{-4}	1.929×10^{-10}	-2.109×10^{-9}
$B_3(34)$	-3.466×10^{-5}	-1.015×10^{-4}	-2.872×10^{-9}	1.061×10^{-9}
$B_4(43)$	3.210×10^{-6}	7.460×10^{-6}	-1.029×10^{-11}	1.014×10^{-11}
$B_4(45)$	1.489×10^{-5}	9.918×10^{-6}	6.204×10^{-12}	3.927×10^{-11}
All	2.365×10^{-3}	1.892×10^{-3}	1.009×10^{-6}	-4.250×10^{-7}

Table 3.5:

Values of interference parameters for $R_0(0)$ of HD-Ar at 295 K

Induced dipole component	a (amagat^{-1})	c (amagat^{-1})	b (amagat^{-2})	d (amagat^{-2})
$B_0(01)$	-2.306×10^{-4}	-1.825×10^{-3}	-4.035×10^{-14}	-1.233×10^{-13}
$B_1(10)$	8.347×10^{-3}	-2.265×10^{-5}	1.741×10^{-5}	-8.457×10^{-8}
$B_1(12)$	-2.351×10^{-4}	-2.838×10^{-4}	-5.694×10^{-9}	3.433×10^{-8}
$B_2(21)$	-3.588×10^{-3}	2.443×10^{-3}	1.716×10^{-6}	-4.376×10^{-6}
$B_2(23)$	-9.531×10^{-4}	-3.855×10^{-4}	2.180×10^{-7}	1.078×10^{-7}
$B_3(32)$	-1.289×10^{-4}	-1.103×10^{-4}	1.067×10^{-9}	7.102×10^{-9}
$B_3(34)$	-9.652×10^{-5}	9.685×10^{-5}	1.563×10^{-10}	-4.672×10^{-9}
$B_4(43)$	3.790×10^{-7}	-7.486×10^{-6}	-1.520×10^{-11}	1.360×10^{-12}
$B_4(45)$	2.605×10^{-5}	3.468×10^{-6}	1.661×10^{-10}	4.779×10^{-11}
All	3.142×10^{-3}	-9.117×10^{-6}	3.262×10^{-6}	-1.200×10^{-6}

Table 3.6:

Values of interference parameters for $R_0(1)$ of HD-Ar at 295 K

Temperature	Transition	B ($cm^{-1}amagat^{-1}$)	S ($cm^{-1}amagat^{-1}$)
		HD-He	
77 K	$R_0(1)$	1.881×10^{-3}	6.241×10^{-4}
195 K	$R_0(1)$	7.131×10^{-3}	1.403×10^{-3}
295 K	$R_0(0)$	1.438×10^{-2}	1.186×10^{-3}
	$R_0(1)$	1.190×10^{-2}	1.772×10^{-3}
		HD-Ar	
295 K	$R_0(0)$	2.858×10^{-2}	1.063×10^{-3}
	$R_0(1)$	2.274×10^{-2}	4.055×10^{-3}

Table 3.7:

Broadening and shift coefficients of various transitions for HD-He and HD-Ar

ing reduces the line shape interference parameters from that obtained by a purely isotropic potential. A good measure of the mixing process is the pressure broadening coefficent B. The broader the line the more significant anisotropic effects should be. We see from Table 3.7 that the broadening is larger for HD-Ar than HD-He. Tables 3.1-3.6 show that contributions from terms other than $B_t(10)$ are indeed more important for HD-Ar than HD-He. The same should also be true as temperature increases. Both the broadening coefficient and the contribution from other components increase as temperature increases.

Chapter 4

Vibration Rotation Systems

The theory of Section 2.3 was developed to treat collisional interference in the purely rotational spectrum of HD-X. In this chapter we extend the theory to treat the vibration rotation spectrum.

4.1 Theory

The energy levels for the vibration rotation spectrum of an HD molecule are given by [Herzberg, 1950]

$$\begin{aligned} H_{HD}^{vJ} &= T_e + \omega_e(v+\frac{1}{2}) - \omega_e x_e(v+\frac{1}{2})^2 + \omega_e y_e(v+\frac{1}{2})^3 \\ &\quad + B_v J(J+1) - D_v J^2(J+1)^2 + H_v J^3(J+1)^3 \; . \qquad (4.1) \end{aligned}$$

The molecule never leaves its ground electronic state, and so $T_e = 0$. The values of the constants in Equation (4.1) which are used are from McKellar, Goetz and Ramsay [McKellar *et al.* 1976]. The selection rules for the fundamental absorption band are: $\Delta v = +1$, $\Delta J = +1$ ($R_1(J)$ lines) or $\Delta J = -1$ ($P_1(J)$ lines).

In principle collisional mixing can occur between levels in the ground vibrational state, between levels in the excited vibrational state, and also between levels in the ground and excited vibrational states. Mixing can occur in the system if $\Delta E \sim \hbar/\tau_c$, where τ_c is the duration of the collision. This relation results from the Heisenberg uncertainty principle, and if the collision duration is small, the energy levels of the two states will become more uncertain in nature and 'smear' out. If this smearing is large enough, the initial and final energies may come close together. If the energy level difference is not much larger than the thermal energy available to the system, $\Delta E \sim k_B T$, a transition can occur. For HD, collision durations are typically $\tau_c \sim 10^{-12} - 10^{-14}$ s, which translates into an uncertainty in the transition energy of $\sim 5 - 500$ cm^{-1}. At room temperature the thermal energy available to the system is approximately 200 cm^{-1}. We can see from Figure 4.1 that the energy difference between vibrational states is large enough to make contributions from mixing between ground and excited vibrational states insignificant. This mixing process is therefore not included in the calculation which follows. However, mixing between levels in the ground vibrational state, and between levels in the excited vibrational state is quite likely to occur.

The interaction potential is in general dependent on the vibrational state of the molecule. To include this fact in our calculations we have followed the method of Stefanov [Stefanov, 1992]. It involves introducing a new isotropic part of the potential to be used when the molecule is in its excited vibrational state. This new isotropic part is determined in the following manner. The rotational constant B_v is inversely proportional to the square of the internuclear distance r_v,

$$B_v = \frac{h}{8\pi^2 c\mu r_v^2} \; . \tag{4.2}$$

For two vibrational levels, with rotational energies given by B_0 and B_1 respectively,

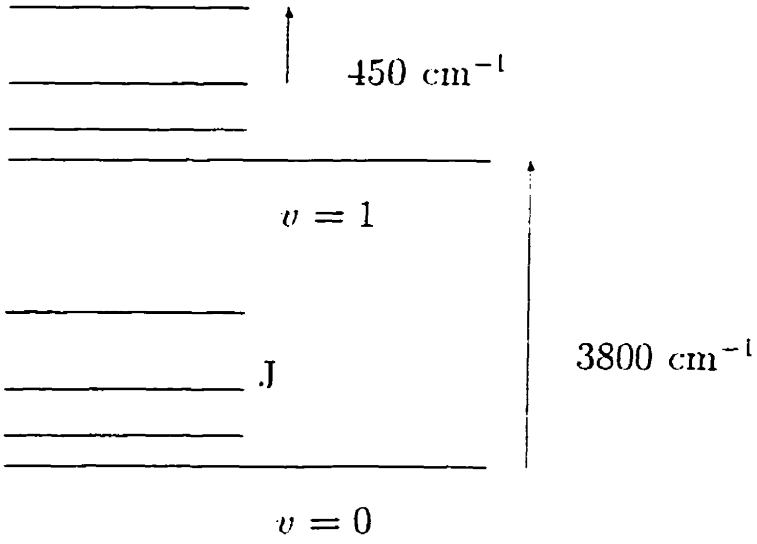

Figure 4.1:

Energy levels of vibration rotation band of HD.

we can define a parameter Δ relating the internuclear distances $r_1 = \Delta r_0$ where

$$\Delta = \sqrt{\frac{B_0}{B_1}} \,. \tag{4.3}$$

This information is incorporated into the interaction potential in the following manner. The molecule will have the same electronic configuration regardless of which vibrational state it is in (adiabatic approximation). Consider a head on collision. At closest approach, the molecule and atom are separated by an amount x. This corresponds to the zero of the interaction potential, or collisional diameter, σ. Since the intermolecular distance is measured from the center of the molecule to the center of the atom, we have a vibrationally dependent collision diameter,

$$\sigma_0 = x + \frac{r_0}{2} \,. \tag{4.4}$$

$$\sigma_1 = x + \frac{r_1}{2} = x + \frac{\Delta\, r_0}{2} \,. \tag{4.5}$$

for the molecule in vibrational state $v = 0, 1$, respectively. Subtracting Equations (4.4) and (4.5) yields the following relation for the collisional diameters of the two potentials:

$$\sigma_1 - \sigma_0 = \frac{r_0}{2}(\Delta - 1) \,. \tag{4.6}$$

A new potential V_1 that has a zero at σ_1 but remains unchanged at large distances is then defined. If the molecule is in vibrational state v then the potential V_v should be used to determine trajectories and the time evolution operators which control mixing. The trajectory for a particular collision should be modified when the HD molecule moves to its excited vibrational state. This change in the trajectory is negligibly small. In fact, in the calculation we use the isotropic H_2-He potential to calculate trajectories rather than the HD-He one, which introduces a small error. The vibrational state dependence of the trajectory is small compared to the change in the trajectory found via the H_2-He rather than HD-He isotropic potential.

Therefore, the trajectories have been calculated with the $v = 0$ H_2-He potential. Since the new isotropic part of the potential will also change the anisotropic part of the potential, the mixing process will also be affected. How these two potentials enter into the mixing process via the time evolution operators is more complex.

The modifications described above were applied to the isotropic part of the H_2-He intermolecular potential (see Figure 4.2) as given by Mulder, Avoird, and Wormer [Mulder *et al.*, 1979]. The governing parameter is $\Lambda = 1.022$. The short range part of the H_2-He potential was modified to give a zero at $\sigma_1 = 3.0466$. This change introduced small changes in the depth and position of the potential minimum (Table 4.1).

	$V_0^{H_2-He}(R)$	$V_1^{H_2-He}(R)$
σ (Å)	3.0382	3.0466
r_{min} (Å)	3.4200	3.4286
ϵ (K)	12.919	12.748

Table 4.1:

Vibrationally dependent potential parameters

It is possible to start with one H_2-He potential and introduce the vibrational state dependence at the level of the HD-He potential, but since we have an analytic form of the H_2-He potential it is easier to introduce the vibrational dependence immediately. The vibrationaly dependent potential introduced the following changes in the theory, where the subscript $v = 0, 1$ denotes the vibrational state of the HD molecule.

The HD-atom potentials which are defined from the H_2-atom potentials (Equa-

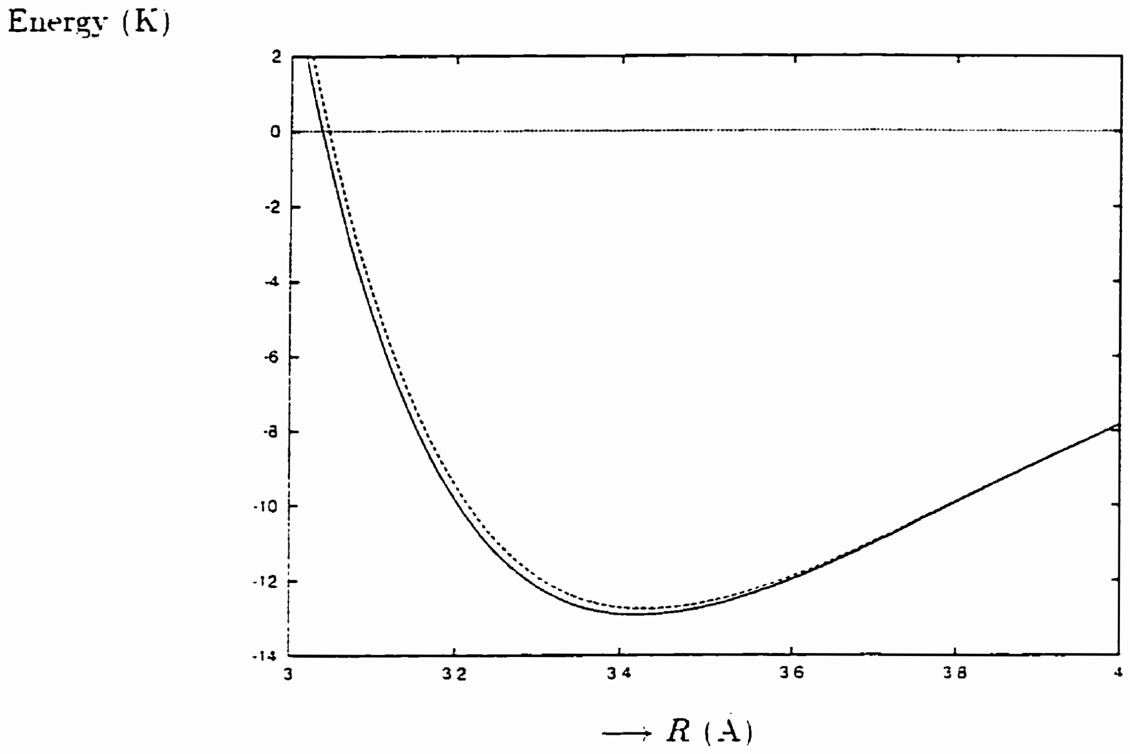

Figure 4.2:

Vibrationally dependent H_2-He potentials. The solid line represents the potential in the ground vibrational state, $V_0(R)$; the dotted line is the potential for the first excited vibrational state, $V_1(R)$.

tion (3.7)) become:

$$V^{(k)}_{HD,v}(R) = \frac{2k+1}{2}\int_{-1}^{1} V_{H_2,v}(R',x')P_k(x)\,dx\ . \tag{4.7}$$

The Heisenberg time evolution operators (Equation (3.4)) and S matrix become:

$$i\hbar\frac{d}{dt}\tilde{U}^I_v(t,t') = V^{aI}_v(\vec{R}(t))\tilde{U}^I_v(t,t')\ . \tag{4.8}$$

$$S_v = \tilde{U}^I_v(\infty,0)\tilde{U}^I_v(0,-\infty) \tag{4.9}$$

The collision induced dipole operator (Equation (2.53)) becomes:

$$\begin{aligned}\mu_{2p}(J_i) \quad = \quad & \sum_{m_e,q,m_g,m_i} (-1)^{J_e-m_e}\begin{bmatrix} J_e & 1 & J_g \\ -m_e & q & m_g \end{bmatrix}\int_{-\infty}^{\infty} dt_0 e^{-i\omega_{eg}t_0} \\ & \times\left[\langle J_e m_e|\tilde{U}^I_1(\infty,t_0)\left[\hat{\mu}^I_e(t_0)\right]_q \tilde{U}^I_0(t_0,-\infty)|J_i m_i\rangle\langle J_g m_g|\hat{S}_0|J_i m_i\rangle^*\right]_{coll}\ .\end{aligned} \tag{4.10}$$

Finally, the complex line broadening cooefficient (Equation (2.46)) becomes:

$$\begin{aligned}\gamma \quad = \quad n_p\Bigg[1 - & \sum_{m_e,q,m_g,m'_e,m'_g}(-1)^{m'_e+m_e}\begin{bmatrix} J_e & 1 & J_g \\ -m'_e & q & m'_g \end{bmatrix} \\ \times & \begin{bmatrix} J_e & 1 & J_g \\ -m_e & q & m_e \end{bmatrix}\langle J_e m'_e|\hat{S}_1|J_e m_e\rangle\langle J_g m'_g|\hat{S}_0|J_g m_g\rangle^*\Bigg]_{coll}\end{aligned} \tag{4.11}$$

Expanding one of the matrix elements which appears in Equation (4.10) will provide some insight into the collisional process:

$$\begin{aligned}\langle J_e m_e|\tilde{U}^I_1(\infty,t_0)\left[\hat{\mu}^I_e(t_0)\right]_q \tilde{U}^I_0(t_0,-\infty)|J_i m_i\rangle \quad = \quad & \sum_{J_k,m_k,J_l,m_l}\langle J_e m_e|\tilde{U}^I_1(\infty,t_0)|J_k m_k\rangle \\ & \times\langle J_k m_k|\left[\hat{\mu}^I_e(t_0)\right]_q|J_l m_l\rangle \\ & \times\langle J_l m_l|\tilde{U}^I_0(t_0,-\infty)|J_i m_i\rangle\end{aligned} \tag{4.12}$$

At the start of the collision the HD molecule is in state i, the initial rotational state in the ground vibrational state. Time progresses and the ground state time evolution operator U_0^I allows mixing to occur amongst the ground rotational states, leaving the molecule in state l. At time t_0 the induced dipoles act and move the molecule to an excited vibrational state k. Time evolves until the collision is over. During this final portion of the collision the excited state evolution operator U_1^I allows mixing to occur amongst the rotational states of the excited vibrational state, leaving the molecule in the final state e.

When going to the interaction picture we must be careful to use the appropriate energy level terms for the HD molecule. For the potential in the interaction picture we can simply write:

$$V_v^{\cdot aI}(\vec{R}(t)) = e^{iH_{HD}^v t} V_v^{\cdot a}(\vec{R}(t)) e^{-iH_{HD}^v t} . \tag{4.13}$$

since the HD molecule is in either the ground or the excited vibrational state. For the induced dipole, however, we must write:

$$\hat{\mu}_e^I(\vec{R}(t)) = e^{iH_{HD}^1 t} \hat{\mu}_e(\vec{R}(t)) e^{-iH_{HD}^0 t} . \tag{4.14}$$

since before the induced dipole acts the molecule is in its ground vibrational state, and after it is in the excited vibrational state.

4.2 Results

The interference parameters were calculated in two separate manners. The first used the same potential when the molecule was in the initial and final vibrational states (HD is a rigid rotator): the second incorporated the simply modelled vibrational state dependent potential (HD is a nonrigid rotator). Induced dipole moments were

Transition	a (amagat^{-1})	c (amagat^{-1})	b (amagat^{-2})	d (amagat^{-2})
		T = 295 K		
$P_1(1)$	-2.206×10^{-2}	-3.303×10^{-3}	1.140×10^{-4}	5.764×10^{-5}
$R_1(0)$	-1.859×10^{-2}	6.543×10^{-3}	8.233×10^{-5}	-8.725×10^{-5}
$R_1(1)$	-2.752×10^{-2}	5.554×10^{-3}	1.929×10^{-4}	-8.440×10^{-5}
		T = 195 K		
$P_1(1)$	-2.206×10^{-2}	-6.429×10^{-3}	1.224×10^{-4}	9.252×10^{-5}
$R_1(0)$	-1.889×10^{-2}	6.604×10^{-3}	8.885×10^{-5}	-7.951×10^{-5}
$R_1(1)$	-2.684×10^{-2}	3.708×10^{-3}	1.822×10^{-4}	-5.157×10^{-5}
		T = 77 K		
$P_1(1)$	-2.102×10^{-2}	-2.042×10^{-2}	1.205×10^{-4}	2.360×10^{-4}
$R_1(0)$	-1.838×10^{-2}	5.091×10^{-3}	8.526×10^{-5}	-5.102×10^{-5}
$R_1(1)$	-2.377×10^{-2}	-1.788×10^{-3}	1.405×10^{-4}	2.046×10^{-5}

Table 4.2:

Interference parameters: HD rigid rotator

taken from Borysow, Frommhold, and Meyer [Borysow *et al.*, 1988]. Terms to order $k = 3$ in Equation (3.1) were used. In Equation (2.51), the highest J state included was $J_{max} = 4$. The collisional average, Equation (2.47), was performed by a 4 point Gaussian quadrature in velocity, and 20 impact parameters.

Transition	B	S
	($\mathrm{cm^{-1}}$ $\mathrm{amagat^{-1}}$)	($\mathrm{cm^{-1}}$ $\mathrm{amagat^{-1}}$)
	T = 295 K	
$P_1(1)$	1.451×10^{-2}	-1.172×10^{-3}
$R_1(0)$	1.452×10^{-2}	1.119×10^{-3}
$R_1(1)$	1.209×10^{-2}	1.636×10^{-3}
	T = 195 K	
$P_1(1)$	9.349×10^{-3}	-9.779×10^{-4}
$R_1(0)$	9.369×10^{-3}	9.395×10^{-4}
$R_1(1)$	7.277×10^{-3}	1.307×10^{-3}
	T = 77 K	
$P_1(1)$	3.136×10^{-3}	-6.718×10^{-4}
$R_1(0)$	3.142×10^{-3}	6.508×10^{-4}
$R_1(1)$	1.940×10^{-3}	3.896×10^{-4}

Table 4.3:

Broadening and shift coefficients: HD rigid rotator

Transition	a (amagat^{-1})	c (amagat^{-1})	b (amagat^{-2})	d (amagat^{-2})
		T = 295 K		
$P_1(1)$	-2.197×10^{-2}	-2.486×10^{-3}	1.135×10^{-4}	4.911×10^{-5}
$R_1(0)$	-1.845×10^{-2}	7.174×10^{-3}	7.815×10^{-5}	-9.274×10^{-5}
$R_1(1)$	-2.743×10^{-2}	6.283×10^{-3}	1.891×10^{-4}	-9.430×10^{-5}
		T = 195 K		
$P_1(1)$	-2.193×10^{-2}	-5.802×10^{-3}	1.225×10^{-4}	8.580×10^{-5}
$R_1(0)$	-1.877×10^{-2}	7.066×10^{-3}	8.567×10^{-5}	-8.362×10^{-5}
$R_1(1)$	-2.682×10^{-2}	4.224×10^{-3}	1.808×10^{-4}	-5.854×10^{-5}
		T = 77 K		
$P_1(1)$	-2.088×10^{-2}	-2.002×10^{-2}	1.221×10^{-4}	2.312×10^{-4}
$R_1(0)$	-1.832×10^{-2}	5.333×10^{-3}	8.400×10^{-5}	-5.318×10^{-5}
$R_1(1)$	-2.386×10^{-2}	-1.575×10^{-3}	1.417×10^{-4}	1.800×10^{-5}

Table 4.4:

Interference parameters: HD non-rigid rotator

Transition	B	S
	(cm^{-1} amagat^{-1})	(cm^{-1} amagat^{-1})
	T = 295 K	
$P_1(1)$	1.470×10^{-2}	-1.460×10^{-3}
$R_1(0)$	1.469×10^{-2}	8.772×10^{-4}
$R_1(1)$	1.222×10^{-2}	1.484×10^{-3}
	T = 195 K	
$P_1(1)$	9.495×10^{-3}	-1.180×10^{-3}
$R_1(0)$	9.495×10^{-3}	7.830×10^{-4}
$R_1(1)$	7.360×10^{-3}	1.222×10^{-3}
	T = 77 K	
$P_1(1)$	3.204×10^{-3}	-7.605×10^{-4}
$R_1(0)$	3.192×10^{-3}	6.003×10^{-4}
$R_1(1)$	1.959×10^{-3}	5.791×10^{-4}

Table 4.5:

Broadening and shift coefficients: HD non-rigid rotator

4.3 Discussion

Vibration-rotation transitions typically have larger interference effects than the purely rotational transitions, since the allowed dipole moment is smaller (Table 2.1, and Equations (2.58) - (2.61)).

As shown in Equations (2.58)-(2.61), the parameters a and c depend on μ_{HD}^{-1} and b and d on μ_{HD}^{-2}. Recall that μ_{HD} is about -8.3×10^{-4} for the pure rotational transitions and $+5.5 \times 10^{-5}$ for the lines of the fundamental band (cf. Table 2.1). By this reckoning, a and c should differ by about a factor of -15 between the two types of transitions; similarly, b and d should differ by a factor of 230 between these cases. In fact, we see that a and c are always of opposite sign and have larger magnitude for the vibrational lines; b and d usually have the same sign and are again larger for vibrational lines. Their ratios for corresponding $R(J)$ transitions can, however, be considerably different from 15 and 230. This shows that collisional propagation in the excited vibrational state is important.

Comparison with experiment is only possible for $R_1(0)$ and $R_1(1)$ at 77 K [Mckellar and Rich, 1984; Lu, Tabisz, and Ulivi, 1993]. This is unfortunate as the calculated values are least reliable at lowest temperature. Table 4.6 contains the experimental and calculated results. Agreement with a is quite good, and reasonable for b. Although the values predicted for the asymmetry parameters c and d are large, they are smaller than the experimental results. For the $R_1(1)$ transition the calculated line asymmetry values are opposite in sign to the experimental values. The broadening and shift as reported from the paper of Schaefer and Monchick were calculated in a fully quantal manner, and as such are the most reliable results.

All the parameters are affected by the use of a potential which is dependent of vibrational state (Table 4.7). The intensity parameter a decreases in all but one

Line Shape Parameter	Calculation	Experiment†	Experiment‡	Calulation*
		$R_1(0)$		
a	-1.832	-1.44		
b	8.400	1.7		
c	5.333	11.8		
d	-5.318	-8.5		
B	3.192	2.8	1.5	1.7
S	6.003	36.	5.8	7.3
		$R_1(1)$		
a	-2.236	-2.46		
b	14.17	12.		
c	-1.575	1.1		
d	1.800	-1.4		
B	1.959	3.1	2.0	2.2
S	5.791	43.	6.5	10.3

Table 4.6:

Comparison of calculated line shape parameters (non rigid rotator) with experimentally determined results for HD-He at $T = 77$ K. † McKellar and Rich, 1984; ‡ Lu, Tabisz, and Ulivi, 1993; * Schaefer and Monchick, 1987.

Units: a: 10^{-2} amagat^{-1}; c: 10^{-3} amagat^{-1}; b: 10^{-5} amagat^{-1}; d: 10^{-5} amagat^{-2}; B: 10^{-3} cm^{-1} amagat^{-1}; S: 10^{-4} cm^{-1} amagat^{-1}.

($R_1(1)$ at T = 77 K) case, and the change is always less than 1%. The intensity parameter b either increases or decreases, by an amount up to 5%. The line asymmetry is more greatly affected. The asymmetry parameter c decreases by as much as 25%. The asymmetry parameter d increases by up to 13%. The broadening coefficient B is only minimally affected, decreasing in all cases by at most 2%. The shift, however, is greatly affected, typically by 7 to 25%. These results are not surprising in light of the findings of Chapter 3. The line asymmetry is governed by the anisotropic part of the interaction potential, and is more dependent on the mixing process than line intensity. The vibrationally dependent potential enters into the time evolution operators and as such will affect the mixing process more than any other part of the calculation. The largest effect on the parameters occurs at 295 K, where the rigid rotator model of the HD molecule is least valid, and where mixing is most important.

A theoretical model of HD-X interactions has been developed which includes the important effects due to m and J mixing to treat the pure rotational spectrum of HD. In Chapter 3 the importance of mixing and each component of the collision-induced dipole was investigated. In the present Chapter the theory was extended to include the vibration-rotation band of HD for HD-He interactions.

4.4 Failure of the Classical Path Approximation for HD-X collisions

The theory of collisional interference of Gao *et al.* which was used in Chapters 3 and 4 has proved very effective in reproducing trends that appear in the experimental HD-X collisionally induced line shape. Results agree with experiment to the order of

Transition	a	b	c	d	B	S
			T = 295 K			
$P_1(1)$	0.41	0.44	24.74	14.80	1.31	24.57
$R_1(0)$	0.75	5.08	9.64	6.29	1.17	21.61
$R_1(1)$	0.33	1.97	13.13	11.73	1.07	9.29
			T = 195 K			
$P_1(1)$	0.59	0.08	9.75	7.26	1.56	20.67
$R_1(0)$	0.64	3.58	7.00	5.17	1.34	16.66
$R_1(1)$	0.07	0.77	13.92	13.51	1.14	6.50
			T = 77 K			
$P_1(1)$	0.67	1.33	1.86	2.03	2.17	13.20
$R_1(0)$	0.33	1.48	4.75	4.23	1.59	7.76
$R_1(1)$	0.38	0.85	11.91	12.02	0.98	48.64

Table 4.7:

Percent changes in interference parameters for HD-He system upon inclusion of vibrationally dependent potential, i.e.: 100 × $|a_{nonrigid} - a_{rigid}|/a_{rigid}$.

Units: a, c: amagat^{-1}; b, d: amagat^{-2}; B, S: cm^{-1} amagat^{-1}.

magnitude, and terms of the induced dipole which are mixed in via the anisotropic potential are seen to be important.

The question now is how to proceed to seek to improve the agreement with experiment. The induced dipoles are obviously very important to the calculation, and they are largest when the HD molecule and perturber atom are close together. Thus the collisional average which is performed is critical to the final results. This collisional average employs the classical path approximation (CPA). This approximation is considered to be good if the de Broglie wavelength is very small compared to the collision diameter for the interaction potential [Allard and Kielkopf, 1982]. Using $\lambda_{\rm deBroglie} = h/mv$ and $T = mv_p^2/2k$ to relate temperature to the most probable velocity of the Maxwell Boltzmann velocity distribution, the de Broglie wavelength can be expressed as a function of temperature as $\lambda_{\rm deBroglie} = h/\sqrt{2kTm}$.

The following table shows that in fact the classical path approximation for HD-He and HD-Ar is not a good approximation, and the collisional average which is performed should be treated quantum mechanically.

	$\lambda_{\rm deBroglie}(T)$ (Å)			σ (Å)
	77 K	195 K	295 K	
HD-He	2.69	1.69	1.38	3.04
HD-Ar	2.11	1.33	1.08	3.20

This motivates the development of Moyal quantum mechanics to treat collisions. This is a desirable approach since the Moyal formalism can then be used to extend any calculation which uses the CPA. The CPA result can be recovered in a simple $\hbar \to 0$ limit, and quantum effects can be examined in a semiclassical manner.

Chapter 5

Moyal Quantum Mechanics

5.1 Introduction

Moyal quantum mechanics is an alternative to Schrödinger or Heisenberg mechanics that presents quantum mechanics as a form of a general statistical dynamics. It develops a complete description of quantum mechanics that is set in classical phase space, where expectation values are found via an asymptotic expansion in Planck's constant. The quantum nature of the system is evident in corrections to the classical result, and these corrections are built from classical quantities. Although the formalism used in Moyal quantum mechanics is well developed [Voros, 1977; Estrada, *et al.*, 1989; Carruthers and Zachariasen, 1983], the mathematical complexity involved in the formalism had given it limited ability to solve real physical systems [Braunss and Rompf, 1993].

Part of the problem was that to obtain the $O(\hbar^2)$ correction to the quantum trajectories, it was necessary to calculate the quantity $\nabla_{\alpha_1}\nabla_{\alpha_2}\nabla_{\alpha_3}g_\beta$. In three dimensions, this quantity has $6^4 = 1296$ elements! Computer limitations in speed and memory would have made accurate solution for this quantity nearly impossible for real physical systems.

The situation changed with the paper of Osborn and Molzahn in 1995. They were able to present a formulation of Moyal quantum mechanics based on a cluster-graph expansion that was computationally easier to implement than the traditional Poisson bracket formulation [Osborn and Molzahn, 1995]. To obtain the $O(\hbar^2)$ correction, it is now only necessary to calculate to the quantity $\nabla_{\alpha_1}\nabla_{\alpha_2}g_3$, which in three dimensions has 216 elements.

In this Chapter we will develop a computational form of Moyal quantum mechanics that can be used to treat three dimensional scattering. We begin with a summary of the results we need from Obsorn and Molzahn's paper. This is contained in Sections 5.2 to 5.2.3. The remainder of the Chapter contains results which were derived during the course of the research to solve to $O(\hbar^2)$ the average values of a three dimensional Gaussian wave packet scattered from a central potential. Section 5.2.3 deals with rotations and tensor representations of quantum trajectories; Section 5.3.1 the quantum trajectory; Section 5.3.2 planar motion of quantum trajectory; and finally, in Section 5.3.3 we put it all together to obtain expressions for expectation values.

5.2 Formalism

The Moyal formalism is based on the Wigner-Weyl isomorphism that maps operators to symbols on classical phase space. The action of the operators on the system is then studied via their corresponding symbols. Notationally, this is defined on an operator $\hat{A}$, which exists in a Hilbert space $\mathcal{H} = L^2(\mathbb{R}^3)$, by the map σ, $A_W = \sigma\hat{A}$. This map σ, which takes an operator from the Hilbert space $\mathcal{H}$ into a function on phase space $T^*(\mathbb{R}^3) \simeq \mathbb{R}^3_q \times \mathbb{R}^3_p$, is defined by the partial Fourier transform (known as the *Wigner transform* [Wigner, 1932]),

$$A_W(q,p) = \int dx\, e^{-ip\cdot x/\hbar}\langle q + \frac{x}{2}|\hat{A}|q - \frac{x}{2}\rangle \ . \tag{5.1}$$

where the $\langle x|\hat{A}|y\rangle$ denotes the Dirac matrix element of the operator $\hat{A}$ in the coordinate space.

The inverse map σ^{-1} (known as *Weyl quantization* [Weyl, 1927]) takes symbols to operators and is given by the inverse Fourier transform of Equation (5.1). The quantum position $\hat{q}_j$ and momentum $\hat{p}_j w = -i\hbar\partial w/\partial q_j$ have as symbols the phase space functions $(q_j)_W = q_j$ and $(p_j)_W = p_j$ respectively. Also, functions of $\hat{q} = (\hat{q}_1, \hat{q}_2, \hat{q}_3)$ alone, $f(\hat{q})$, or $\hat{p} = (\hat{p}_1, \hat{p}_2, \hat{p}_3)$ alone, $g(\hat{p})$, will have as symbols $f(q)$ and $g(p)$ respectively. This is true because the $\hat{q}_j$'s commute with one another, as do the $\hat{p}_j$'s. A function of both $\hat{q}$ and $\hat{p}$ will in general have a more complicated symbol due to noncommutivity.

A system defined by a Hamiltonian operator $\hat{H}$ has Schrödinger time evolution operator $U(t) = exp(-\frac{i}{\hbar}\hat{H}t)$. The Heisenberg time evolution operator for an observable $\hat{A}$ is given by

$$\Gamma(t)\hat{A} = \hat{A}(t) = U^{\dagger}(t)\hat{A}U(t) \ . \tag{5.2}$$

The Heisenberg-Weyl evolution operator acts on the Wigner transform of the observable, A_W, and is given by

$$\Gamma_t = \sigma\Gamma(t)\sigma^{-1} \ . \tag{5.3}$$

A Hamiltonian is said to be semiclassically admissible if its symbol $H_W(\hbar, z)$ has a regular asymptotic expansion about $\hbar = 0$,

$$H_W(\hbar, z) = H_c(z) + \sum_{r=1}^{\infty}\frac{\hbar^r}{r!}h_r(z) \ . \tag{5.4}$$

In this notation $z = (q,p) = (q_1, q_2, q_3, p_1, p_2, p_3)$ denotes a generic point in phase space. The $\hbar$ independent part of the symbol, $H_c(z)$, is the classical counterpart of $\hat{H}$ in the Moyal description. A Hamiltonian that has representation given simply by

$$H_W(\hbar, z) = H_c(z) , \tag{5.5}$$

is said to be Weyl quantized.

If both $\hat{H}$ and $\hat{A}$ are semiclassically admissible, then the Heisenberg-Weyl evolution operator admits a small $\hbar$ expansion [Osborn and Molzahn, 1995]

$$\Gamma_t A_W = \sum_{n=0}^{\infty} \frac{\hbar^n}{n!} \gamma_t^{(n)}(A_W) . \tag{5.6}$$

The $\gamma_t^{(n)}$ are operators in the space of Weyl symbols. The leading term $\gamma_t^{(0)}$ is determined from the classical flow generated by the classical part of the Hamiltonian $H_c(z)$.

Expectation values in the Moyal formalism are evaluated in the following manner. If $\hat{\rho} = |\psi\rangle\langle\psi|$ is the density matrix for a unit normalized initial state ψ, then the Wigner function is the σ image of $\hat{\rho}$, namely

$$\begin{aligned} w_\psi(z) &= h^{-3}\sigma\hat{\rho} , \\ &= \int dx\, e^{-ip\cdot x/\hbar}\langle q + \frac{x}{2}|\psi\rangle\langle\psi|q - \frac{x}{2}\rangle . \end{aligned} \tag{5.7}$$

The expectation value for an operator $\hat{A}(t)$ is determined via the trace,

$$\begin{aligned} \langle\hat{A}(t)\rangle_\psi &= Tr\hat{A}(t)\hat{\rho} = \int dz\, w_\psi(z)\Gamma_t A_W(z) , \\ &= \sum_{n=0}^{\infty} \frac{\hbar^n}{n!} \int dz\, w_\psi(z)\gamma_t^{(n)}(A_W(z)) , \end{aligned} \tag{5.8}$$

where the integral over z is over all of phase space.

We will be considering Weyl quantized Hamiltonians of the form

$$H(\hbar, z) = H_c(z) = \frac{p^2}{2m} + v(r) \; . \tag{5.9}$$

where $p = \sqrt{p_1^2 + p_2^2 + p_3^2}$ and $r = \sqrt{q_1^2 + q_2^2 + q_3^2}$. The potential $v(r)$ will be the spherically symmetric potential for either helium or argon. As well, since the Hamiltonian is invariant under $\hbar \rightarrow -\hbar$, all odd powers of $\hbar$ will vanish in any semiclassical expansions. Thus the leading quantum correction is due to $\gamma_t^{(2)}$. It is to this order that we will calculate expectation values in Equation (5.8).

5.2.1 Weyl Symbol Calculus

To be able to calculate the Heisenberg-Weyl evolution operator we will require some details of the Weyl symbol calculus [Hörmander, 1979].

The linear operators on the Hilbert space form a Lie algebra whose bracket is the commutator. The Wigner transform (Equation (5.1)) from operators to symbols preserves the commutator operation. In order that the multiplication of operators correspond to a product of symbols, the commutator scalar product must be extended. Let $\hat{X}, \hat{Y}$ be operators with symbols $X_W = X, Y_W = Y$ (from now on the subscript W will be dropped when referring to symbols). The star product (or *twisted product* [Estrada *et al.*, 1989]) is defined as

$$X * Y \equiv \sigma(\hat{X}\hat{Y}) \; , \tag{5.10}$$

which can be evaluated via the integral formula [Estrada et al., 1989]

$$X * Y(z) = (\pi\hbar)^{-6} \int\int d\zeta \, d\zeta' X(z+\zeta) Y(z+\zeta') exp\left\{\frac{2i}{\hbar}\zeta \cdot J\zeta'\right\} \; . \tag{5.11}$$

where J is the Poisson matrix which carries the symplectic structure

$$J = \begin{bmatrix} 0 & \delta \\ -\delta & 0 \end{bmatrix} \; . \tag{5.12}$$

where δ is the 3×3 matrix identity and the $\cdot$ represents the six dimensional scalar product.

The Moyal bracket is the σ image of the quantum commutator.

$$\{X, Y\}_M = \sigma\left(\frac{1}{i\hbar}[\hat{X}, \hat{Y}]\right) = \frac{1}{i\hbar}(X * Y - Y * X) . \tag{5.13}$$

If the symbols of operators are smooth differentiable functions on phase space the star product and Moyal bracket will have derivative based representations. Define the extended Poisson bracket operator $B_{12} = \nabla_1 \cdot J\nabla_2$ which acts on the tuple $\prec X, Y \succ$ as

$$B_{12}^n \prec X, Y \succ (z) = X_{;\mu_1\cdots\mu_n}(z) J_{\mu_1\nu_1} \cdots J_{\mu_n\nu_n} Y_{;\nu_1\cdots\nu_n}(z) . \tag{5.14}$$

where the $;\mu$ indicates differentiation with respect to μ, ie. $X_{;\mu} = \nabla_\mu X = \frac{\partial}{\partial z_\mu} X$. The Poisson bracket can be represented as

$$\{X, Y\}(z) \equiv \nabla X(z) \cdot J\nabla Y(z) = B_{12} \prec X, Y \succ (z) . \tag{5.15}$$

The star product (Equation (5.10)) can be represented in terms of the B_{12} by the Groenewold representation [Groenewold, 1946]

$$X * Y(z) = exp\left\{\frac{i\hbar}{2}B_{12}\right\} \prec X, Y \succ (z) . \tag{5.16}$$

We will require small $\hbar$ asymptotic expansions of the Moyal bracket. Using the Groenewold formula (Equation (5.16)), the definition of the Moyal bracket (Equation (5.13)) and the relation

$$B_{12}^n \prec X, Y \succ (z) = (-1)^n B_{12}^n \prec Y, X \succ (z) . \tag{5.17}$$

it is a simple matter to show

$$\begin{aligned} \{X, Y\}_M(z) &= \frac{2}{\hbar}\sin\frac{\hbar}{2}B_{12} \prec X, Y \succ (z) . && (5.18) \\ &= \{X, Y\}(z) - \left(\frac{\hbar}{2}\right)^2 \frac{1}{3!}B_{12}^3 \prec X, Y \succ (z) + \cdots . && (5.19) \end{aligned}$$

5.2.2 The Heisenberg-Weyl Evolution Operator

We now turn our attention to the task of building the $\gamma_t^{(0)}$ and $\gamma_t^{(2)}$. For a Hamiltonian $\hat{H}$ and observable $\hat{A}$ the familiar Heisenberg equation of motion is [Sakurai, 1985 p. 83]

$$\frac{\partial}{\partial t}\Gamma(t)\hat{A} = \frac{1}{i\hbar}\left[\Gamma(t)\hat{A}, \hat{H}\right] . \tag{5.20}$$

The Weyl symbol image of this equation of motion yields the Moyal equation of motion

$$\frac{\partial}{\partial t}\Gamma_t A = \{\Gamma_t A, H\}_M . \tag{5.21}$$

with initial condition $\Gamma_0 A = A$.

We will only be dealing with Weyl quantized Hamiltonians (Equation (5.9)), and so will drop the subscript c on the symbol for the Hamiltonian, writing $H_W(\hbar, z) = H(z)$. The $O(\hbar^0)$ part of Equation (5.21) is

$$\frac{\partial}{\partial t}\gamma_t^{(0)}(A) = \left\{\gamma_t^{(0)}(A), H\right\} . \tag{5.22}$$

which is a Poisson bracket equation of motion for the unknown phase space function $\gamma_t^{(0)}(A)$. We define $g(t|z)$ to be the solution to Hamilton's equation for classical flow

$$\frac{d}{dt}g(t|z) = J\nabla H\left(g(t|z)\right) . \tag{5.23}$$

where $\nabla H = (\nabla_q H, \nabla_p H)$ is the phase space gradient of the Hamiltonian and J introduces the symplectic structure. The initial condition on the classical flow is $g(0|z) = z$. With the classical phase space flow defined for all t, the solution of Equation (5.22) can be written as

$$\gamma_t^{(0)}(A(z)) = A\left(g(t|z)\right) = \left(A \circ g(t)\right)(z) . \tag{5.24}$$

The flow operator $\gamma_t^{(0)}$ is seen to be trivial to calculate, as it mirrors directly the classical motion.

The flow operator $\gamma_t^{(2)}$ will, however, be nontrivial. It requires a number of auxiliary functions and will introduce nontrivial aspects of the Weyl calculus formalism. The Jacobi field along the trajectory must be calculated and the concept of a quantum trajectory introduced. We will begin by looking at the required Jacobi fields.

Simply differentiating Equation (5.23) with respect to z will give us an equation for the Jacobi fields

$$\mathcal{J}(t)\nabla g(t|z) \equiv \left[\frac{d}{dt} - J\nabla\nabla H\left(g(t|z)\right)\right]\nabla g(t|z) = 0\ . \tag{5.25}$$

The 6 × 6 matrix $\nabla g(t|z)$ is made up of the Jacobi fields, and obeys the initial condition $\nabla g(0|z) = \delta_{6\times 6}$. At all times the Jacobi fields form a symplectic matrix and as such must satisfy $det\,\nabla g(t|z) = 1$ (which is a statement of the incompressability of phase space under classical flow). Jacobi fields describe the stability of the trajectory under small changes in the initial conditions.

Differentiating again will yield equations for $\nabla\nabla g(t|z)$. The Jacobi fields will be discussed in greater detail in the next section.

The concept of a quantum trajectory arises from calculating the Heisenberg-Weyl flow of the coordinate function $z = (q, p) = (z_1, \cdots, z_6)$.

$$Z_\mu(t, \hbar; z) \equiv \Gamma_t z_\mu\ . \tag{5.26}$$

Since the coordinate functions are semiclassically admissable they have an asymptotic expansion in $\hbar$

$$Z_\mu(t, \hbar; z) = g_\mu(t|z) + \frac{\hbar^2}{2} z_\mu^{(2)}(t|z) + O(\hbar^4)\ . \tag{5.27}$$

The equation of motion for $z_\mu^{(2)}(t|z)$ is given by Osborn and Molzahn [Osborn and Molzahn, 1995] as

$$\mathcal{J}_{\mu\nu}(t) z_\nu^{(2)}(t|z) \quad = \quad -\frac{1}{8} B_{12}^2 \prec g_\alpha(t), g_\beta(t) \succ (z) J_{\mu\gamma} H_{;\alpha\beta\gamma}\left(g(t|z)\right) + \tag{5.28}$$

$$\frac{1}{12}B_{12}B_{23} \prec g_\alpha(t), g_\beta(t), g_\gamma(t) \succ (z) J_{\mu\rho} H_{;\alpha\beta\gamma\rho}(g(t|z)) \ .$$

where repeated indices are summed, the indices run from 1 ~ 6. $\mathcal{J}_{\mu\nu}(t)$ is defined in Equation (5.25) and

$$\begin{aligned} B_{12}^2 \prec a, b \succ (z) &= -tr\nabla\nabla a(z) J \nabla\nabla b(z) J \ , & (5.29) \\ B_{12}B_{23} \prec a, b, c \succ (z) &= -J\nabla a(z) \cdot \nabla\nabla b(z) J \nabla c(z) \ . & (5.30) \end{aligned}$$

The flow operator $\gamma_t^{(2)}$ is then given by

$$\begin{aligned} \gamma_t^{(2)}(A(z)) &= z_\alpha^{(2)}(t|z) A_{;\alpha}(g(t|z)) - \frac{1}{8}B_{12}^2 \prec g_\alpha(t), g_\beta(t) \succ A_{;\alpha\beta}(g(t|z)) \\ &\quad + \frac{1}{12}B_{12}B_{23} \prec g_\alpha(t), g_\beta(t), g_\gamma(t) \succ A_{;\alpha\beta\gamma}(g(t|z)) \ . \qquad (5.31) \end{aligned}$$

5.2.3 Rotations and Tensor Representation

Before we begin to look at the scattering of a wave packet in detail, it will be beneficial to examine phase space rotations and the tensor structure of the quantum corrections.

Consider a rotation about the unit vector $\hat{e}$ by an amount θ, $R = R(\hat{e}, \theta)$. For example, if we rotate about the $\hat{e}_2$ axis the rotation matrix would be

$$R(\hat{e}_2, \theta) = \begin{pmatrix} \cos\theta & 0 & \sin\theta \\ 0 & 1 & 0 \\ -\sin\theta & 0 & \cos\theta \end{pmatrix} \ . \qquad (5.32)$$

The transformation $z' = \mathcal{R}z$ is then a rotation in phase space, given by

$$\begin{pmatrix} q' \\ p' \end{pmatrix} = \mathcal{R} \begin{pmatrix} q \\ p \end{pmatrix} \ . \qquad (5.33)$$

where

$$\mathcal{R}(\theta) = \begin{pmatrix} R(\hat{e}_2, \theta) & 0 \\ 0 & R(\hat{e}_2, \theta) \end{pmatrix} . \tag{5.34}$$

The transformation $\mathcal{R}$ is a real orthogonal six dimensional matrix.

Quantum rotations are generated by $\hat{L} = \hat{q} \times \hat{p}$ in the familiar manner

$$U^{\dagger}(R)\hat{z}_{\mu}U(R) = \mathcal{R}_{\mu\nu}\hat{z}_{\nu} . \tag{5.35}$$

where $U(R) = exp\left\{-\frac{i}{\hbar}\theta\hat{e}\cdot\hat{L}\right\}$. This, of course, is the definition of a rank one tensor. A rank n tensor operator $\hat{X}_{\mu_1\cdots\mu_n}$ transforms as

$$\begin{aligned} \hat{X}'_{\mu_1\cdots\mu_n} &\equiv U^{\dagger}(R)\hat{X}_{\mu_1\cdots\mu_n}U(R) . & (5.36) \\ &= \mathcal{R}_{\mu_1\nu_1}\cdots\mathcal{R}_{\mu_n\nu_n}\hat{X}_{\nu_1\cdots\nu_n} . & (5.37) \end{aligned}$$

The Wigner transform of Equation (5.37) yields the tensor transformation in symbol space

$$X'_{\mu_1\cdots\mu_n} = \mathcal{R}_{\mu_1\nu_1}\cdots\mathcal{R}_{\mu_n\nu_n}X_{\nu_1\cdots\nu_n} . \tag{5.38}$$

The quantum trajectories $Z_{\mu}(t, \hbar; z)$ transform as rank one tensors under the rotation $\mathcal{R}$.

$$Z_{\mu}(t, \hbar; \mathcal{R}z) = \mathcal{R}_{\mu\nu}Z_{\nu}(t, \hbar; z) . \tag{5.39}$$

If we write this tensor relation as a semiclassical expansion and collect powers of $\hbar$ we find that the classical trajectory and quantum corrections are rank one tensors.

$$\begin{aligned} g_{\mu}(t|\mathcal{R}z) &= \mathcal{R}_{\mu\nu}g_{\nu}(t|z) . & (5.40) \\ z^{(n)}_{\mu}(t|\mathcal{R}z) &= \mathcal{R}_{\mu\nu}z^{(n)}_{\nu}(t|z) . & (5.41) \end{aligned}$$

At the classical level, the main symmetry of a Hamiltonian which is spherically symmetric is that of angular momentum conservation. We now show that this classical symmetry results in a quantum symmetry that can be exploited to simplify the calculation.

Let $\hat{L}_j = \epsilon_{jkm}\hat{q}_k\hat{p}_m$ denote the j^{th} component of the angular momentum operator. The Weyl symbol of this operator is simply $L_j = \epsilon_{jkm}q_k p_m$, since q_k and p_m commute if $k \neq m$. At the classical level rotational invariance implies

$$\left[\hat{H},\hat{L}_j\right] = 0 \; , \tag{5.42}$$

and by taking the Weyl symbol one obtains the related symbol expression

$$\{H, L_j\}_M = \{H, L_j\} = 0 \; . \tag{5.43}$$

The Moyal and the Poisson bracket are equal. Equations (5.14) and (5.19) show that the Moyal and Poisson brackets differ in general by terms involving third and higher order derivatives of L_j; since L_j is only quadratic in z, these terms are zero in this case.

Since the angular momentum is a constant of motion, $\hat{L}_j(t) = \hat{L}_j(0) = \hat{L}_j$. The quantum planar motion restriction is

$$\hat{q}(t)\cdot\hat{L} \;=\; 0 \; , \tag{5.44}$$

$$\hat{p}(t)\cdot\hat{L} \;=\; 0 \; . \tag{5.45}$$

Before we proceed to derive the Moyal equivalent property, it would be useful to determine the star product of a function and the angular momentum.

Proposition 5.1 *The star product of an arbitrary smooth function f with the angular momentum symbol L_j is*

$$f * L_j(z) = f(z)L_j(z) + \frac{i\hbar}{2}\{f, L_j\}(z) + \frac{\hbar^2}{4}\epsilon_{jkm}\frac{\partial^2 f(z)}{\partial p_k \partial q_m} \; . \tag{5.46}$$

Proof. The star product can be expanded using Groenewold's formula. Equation (5.16)

$$\begin{aligned} f * L_j(z) &= exp\left\{\frac{i\hbar}{2}B_{12}\right\} \prec f, L_j \succ (z) . \\ &= \prec f, L_j \succ (z) + \frac{i\hbar}{2}B_{12} \prec f, L_j \succ (z) - \frac{\hbar^2}{8}B_{12}^2 \prec f, L_j \succ (z) . \end{aligned} \tag{5.47}$$

This series terminates since $L_j(z)$ is only quadratic in z. We have for the first term $\prec f, L_j \succ (z) = f(z)L_j(z)$, and the second term can be expressed in terms of the Poisson bracket, $\{f, L_j\}(z)$ (Equation (5.15)). The third term can be simplified as follows

$$\begin{aligned} B_{12}^2 \prec f, L_j \succ (z) &= f_{;\mu_1\mu_2}(z)J_{\mu_1\nu_1}J_{\mu_2\nu_2}(L_j(z))_{;\nu_1\nu_2} . \\ &= f_{;\mu_1\mu_2}(z)J_{\mu_1\nu_1}J_{\mu_2\nu_2}\nabla_{\nu_1}\nabla_{\nu_2}\epsilon_{jkm}z_k z_{m+3} . \\ &= f_{;\mu_1\mu_2}(z)J_{\mu_1\nu_1}J_{\mu_2\nu_2}\epsilon_{jkm}(\delta_{\nu_1,m+3}\delta_{\nu_2,k} + \delta_{\nu_1,k}\delta_{\nu_2,m+3}) . \\ &= f_{;\mu_1\mu_2}(z)\epsilon_{jkm}(J_{\mu_1,m+3}J_{\mu_2,k} + J_{\mu_1,k}J_{\mu_2,m+3}) . \\ &= -\epsilon_{jkm}f_{;m,k+3}(z) - \epsilon_{jkm}f_{;k+3,m}(z) . \\ &= -2\epsilon_{jkm}\frac{\partial^2 f(z)}{\partial q_m \partial p_k} . \end{aligned}$$

Substituting back recovers Equation (5.46). ☐

To obtain the Moyal equivalent conditions for planar motion, we need to take the Wigner transform of Equation (5.44). This results in a star product, and applying Equation (5.46) we find

$$q_j(t,\hbar;z) * L_j(z) = q_j(t,\hbar;z)L_j(z) + \frac{i\hbar}{2}\{q_j(t,\hbar), L_j\}(z) + \frac{\hbar^2}{4}\epsilon_{jkm}\frac{\partial^2 q_j(t,\hbar;z)}{\partial p_k \partial q_m} . \tag{5.48}$$

It should be emphasized that $q_j(t,\hbar;z)$ is the coordinate part of the quantum trajectory $Z_j(t,\hbar;z)$ (Equation (5.26)), and as such contains all terms in the semiclassical expansion. Substituting this semiclassical expansion and collecting powers of $\hbar$ will yield the following results. For $O(\hbar^0)$, we obtain

$$q_j(t|z)L_j(z) = 0 \; . \tag{5.49}$$

which is a statement of the classical planar motion result. For $O(\hbar^1)$, we have the Poisson bracket of $q_j(t|z)$ and L_j, which is zero. There is no $O(\hbar^1)$ contribution. The first and third terms in Equation (5.48) will contribute to the $O(\hbar^2)$ part, and this yields the important result

$$q_j^{(2)}(t|z)L_j(z) = -\frac{1}{2}\epsilon_{jkm}\frac{\partial^2 q_j(t|z)}{\partial p_k \partial q_m} \; . \tag{5.50}$$

A similar analysis on the Equation (5.45) yields the Moyal equivalent equations

$$p_j(t|z)L_j(z) = 0 \; . \tag{5.51}$$

$$p_j^{(2)}(t|z)L_j(z) = -\frac{1}{2}\epsilon_{jkm}\frac{\partial^2 p_j(t|z)}{\partial p_k \partial q_m} \; . \tag{5.52}$$

In the following section it will be shown that if the classical trajectory remains in the $e_1 - e_2$ plane, the quantum corrections $z^{(2)}(t|z) = (q^{(2)}(t|z), p^{(2)}(t|z))$ will also remain in that plane.

5.3 Scattering of a Wave Packet

We wish to develop the Moyal formalism to a level that is capable of calculating expectation values for physically interesting observables $\hat{A}$ and suitable initial wave functions ψ. Suitable wave functions at this time should be simple, well defined functions for which the Wigner function is easily obtainable, but which retain some physical relevance.

As a first application of the Moyal formalism, we will look at the dynamical evolution of a Gaussian wave packet under the influence of a central potential in three dimensions. The Hamiltonian for this situation is

$$H(z) = \frac{p^2}{2m} + v(q)\,. \tag{5.53}$$

The dynamically evolving Hamiltonian is

$$\gamma_t^{(0)}(H)(z) = H \circ g(t)(z) = H(g(t|z))\,. \tag{5.54}$$

where

$$\begin{aligned} p^2(t) &= g_4^2(t|z) + g_5^2(t|z) + g_6^2(t|z)\,. && (5.55)\\ q(t) &= \sqrt{g_1^2(t|z) + g_2^2(t|z) + g_3^2(t|z)}\,. && (5.56)\\ &= r(t) = r\,. \end{aligned}$$

The potential, $V(r) = v(q(t))$, will eventually be chosen to be the Lennard-Jones (12-6) potential for helium, neon, or argon gases.

We begin by examining quantities which are needed at the level of a single trajectory, and then specialize our Gaussian to simplify the phase space integral needed to determine expectation values.

Appendix A contains an overview of the process used to determine the spread in coordinate space of a three dimensional free Gaussian.

5.3.1 The Quantum Trajectory

As shown in the previous section, the classical trajectory is found from Hamilton's equations, Equation (5.23). The notation of the previous section is very compact.

the equations written in a more expanded form are:

$$
\begin{aligned}
\frac{d}{dt}g_1(t|z) &= \frac{g_4(t|z)}{m} ,\\
\frac{d}{dt}g_2(t|z) &= \frac{g_5(t|z)}{m} ,\\
\frac{d}{dt}g_3(t|z) &= \frac{g_6(t|z)}{m} ,\\
\frac{d}{dt}g_4(t|z) &= -\frac{\partial V(r)}{\partial g_1} ,\\
\frac{d}{dt}g_5(t|z) &= -\frac{\partial V(r)}{\partial g_2} ,\\
\frac{d}{dt}g_6(t|z) &= -\frac{\partial V(r)}{\partial g_3} .
\end{aligned}
\tag{5.57}
$$

To solve this set of differential equations we need to specify the initial conditions, $z = g(0|z)$, for the trajectory. It is to our benefit to solve the most reduced form of these and Jacobi field equations, and to do so we will introduce rotational invariance.

We have already seen that the classical trajectory $z(t|z)$ transforms as a tensor under rotations. A standard fixed axis Euler angle representation of $\mathbb{R}^3$ is given by $R(\alpha,\beta,\gamma) = R_{e_1}(\alpha)R_{e_2}(\beta)R_{e_3}(\gamma)$ [Goldstein, 1980]. The $\mathcal{R}$ rotation of a phase space point is then given by

$$q = R(\alpha,\beta,\gamma)q_0 , \tag{5.58}$$

$$p = R(\alpha,\beta,\gamma)p_0 . \tag{5.59}$$

The three $\mathcal{R}$ rotation invariant scalars are

$$|q| = |q_0| \equiv r , \tag{5.60}$$

$$|p| = |p_0| \equiv p_r , \tag{5.61}$$

$$q\cdot p = q_0\cdot p_0 = rp_r\cos\theta . \tag{5.62}$$

The three vectors $q_0, p_0, q_0 \times p_0$ define a rigid body that is rotated into all possible orientations by $\mathcal{R}$. The scalar variables r, p_r, θ characterize the internal degrees of freedom of this rigid body.

For our purposes, the scalar variables are defined as follows

$$\begin{aligned} q_0 &= r\sin\theta e_1 + r\cos\theta e_2 = q_1 e_1 + q_2 e_2 \; , & (5.63)\\ p_0 &= p_r e_2 \; , & (5.64)\\ \theta &\in [0, \pi) \; , & (5.65) \end{aligned}$$

resulting in trajectories that are contained in the $e_1 - e_2$ plane (labelled the z_0 plane) and which have an initial momentum in the e_2 direction (Figure 5.1). As θ sweeps from 0 to π all initial coordinate points in the $e_1 - e_2$ plane will be recovered. The rotation $\mathcal{R}$ completes the map of phase space. We thus have an Euler angle, scalar invariant coordinatization of phase space given by $z = z(\alpha, \beta, \gamma; r, p_r, \theta)$. Thus, Equations (5.57) are solved with the initial conditions

$$\begin{aligned} z_0 = g(0|z_0) &= (g_1(0|z_0), g_2(0|z_0), g_3(0|z_0), g_4(0|z_0), g_5(0|z_0), g_6(0|z_0)) \; , \\ &= (q_1, q_2, 0, 0, p_r, 0) \; . & (5.66) \end{aligned}$$

This means that we will have for all time:

$$g_3(t|z_0) = g_6(t|z_0) = 0 \; . \qquad (5.67)$$

and must solve the reduced set of equations

$$\begin{aligned} \frac{d^2}{dt^2} g_1(t|z_0) &= -\frac{1}{m}\frac{\partial}{\partial g_1} V(r) \; , & (5.68)\\ \frac{d^2}{dt^2} g_2(t|z_0) &= -\frac{1}{m}\frac{\partial}{\partial g_2} V(r) \; , & (5.69) \end{aligned}$$

where $g_{i+3}(t|z_0) = m\dot{g}_i(t|z_0)$, $i = 1, 2$.

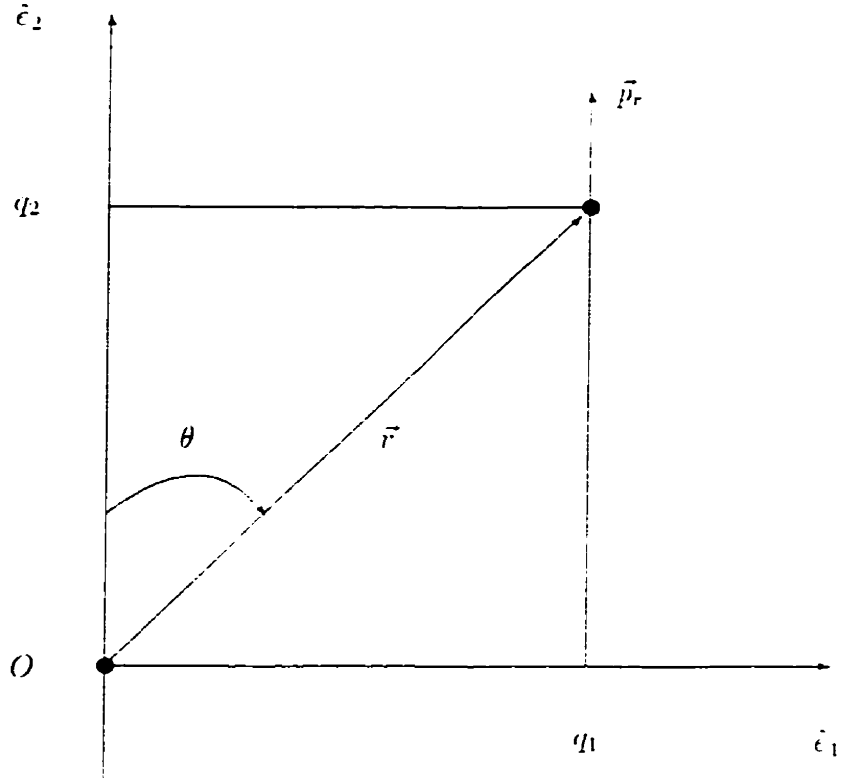

Figure 5.1:

Collision Geometry

The use of rotational invariance will produce simplifications in the calculation of ∇g and $\nabla\nabla g$ when we restrict ourselves to the z_0 plane. Before we examine these structures, it would be beneficial to specify the derivatives of the potential which will be needed in the future. If we use the notation $V^{(n)} = d^nV(r)/dr^n$, and restrict the indices to the range $1 \sim 3$, then simple application of the chain rule yields

$$\frac{\partial V(r)}{\partial g_i} = V^{(1)}\frac{g_i(t|z)}{r} , \tag{5.70}$$

$$\frac{\partial^2 V(r)}{\partial g_i \partial g_j} = g_i(t|z)g_j(t|z)\left(\frac{V^{(2)}}{r^2} - \frac{V^{(1)}}{r^3}\right) + \delta_{ij}\frac{V^{(1)}}{r} . \tag{5.71}$$

$$\begin{aligned} \frac{\partial^3 V(r)}{\partial g_i \partial g_j \partial g_k} &= g_i(t|z)g_j(t|z)g_k(t|z)\left(\frac{V^{(3)}}{r^3} - 3\frac{V^{(2)}}{r^4} + 3\frac{V^{(1)}}{r^5}\right) \\ &\quad + (g_i(t|z)\delta_{jk} + g_j(t|z)\delta_{ik} + g_k(t|z)\delta_{ij})\left(\frac{V^{(2)}}{r^2} - \frac{V^{(1)}}{r^3}\right) . \end{aligned} \tag{5.72}$$

$$\begin{aligned} \frac{\partial^4 V(r)}{\partial g_i \partial g_j \partial g_k \partial g_l} &= g_i(t|z)g_j(t|z)g_k(t|z)g_l(t|z)\left(\frac{V^{(4)}}{r^4} - 6\frac{V^{(3)}}{r^5} + 15\frac{V^{(2)}}{r^6} - 15\frac{V^{(1)}}{r^7}\right) \\ &\quad + (g_j(t|z)g_k(t|z)\delta_{il} + g_i(t|z)g_k(t|z)\delta_{jl} + g_i(t|z)g_j(t|z)\delta_{kl} \\ &\quad + g_i(t|z)g_l(t|z)\delta_{jk} + g_j(t|z)g_l(t|z)\delta_{ik} + g_k(t|z)g_l(t|z)\delta_{ij}) \\ &\quad \times \left(\frac{V^{(3)}}{r^3} - 3\frac{V^{(2)}}{r^4} + 3\frac{V^{(1)}}{r^5}\right) \\ &\quad + (\delta_{il}\delta_{jk} + \delta_{jl}\delta_{ik} + \delta_{kl}\delta_{ij})\left(\frac{V^{(2)}}{r^2} - \frac{V^{(1)}}{r^3}\right) . \end{aligned} \tag{5.73}$$

Equation (5.25) gives the Jacobi field ∇g for an arbitrary Hamiltonian. For our Hamiltonian, the Hessian $\nabla\nabla H$ simplifies and we have

$$\left[\frac{d}{dt} + \begin{pmatrix} 0 & -m^{-1}\delta \\ \nabla\nabla V & 0 \end{pmatrix}\right]\begin{pmatrix} Y_\lambda(t|z) \\ W_\lambda(t|z) \end{pmatrix} = 0 \ , \ \lambda = 1 \sim 6 \ . \tag{5.74}$$

The Jacobi fields have been split into an upper and lower part, $Y(t|z)$ and $W(t|z)$ respectively. Rewriting as before in terms of a second order differential equation one has

$$\left[m\frac{d^2}{dt^2} + \nabla\nabla V(q(t|z))\right] Y_{\cdot\lambda}(t|z) = 0 \; . \tag{5.75}$$

where $W(t|z) = m\,\dot{Y}(t|z)$.

Now consider how the symmetry of being in the z_0 plane simplifies the Jacobi field equation. The initial conditions under which Equation (5.75) is solved are $Y_{i\lambda}(0|z_0) = \delta_{i\lambda}$ and $\dot{Y}_{i\lambda}(0|z_0) = m^{-1}\delta_{i\lambda}$. Since the classical trajectory remains in the z_0 plane, $\nabla\nabla V$ which is determined from Equation (5.71) is given by

$$\nabla\nabla V(q(t|z_0) = \begin{pmatrix} V_{11} & V_{12} & 0 \\ V_{21} & V_{22} & 0 \\ 0 & 0 & V_{33} \end{pmatrix} \; . \tag{5.76}$$

where $V_{ij} = \partial^2 V(r)/\partial q_i \partial q_j$. This block diagonalization of the Hessian causes Equation (5.75) to decouple into two parts

$$\left[m\frac{d^2}{dt^2} + \begin{pmatrix} V_{11} & V_{12} \\ V_{21} & V_{22} \end{pmatrix}\right] \begin{pmatrix} Y_{1\lambda}(t|z_0) \\ Y_{2\lambda}(t|z_0) \end{pmatrix} \;=\; 0 \; . \tag{5.77}$$

$$\left[m\frac{d^2}{dt^2} + V_{33}\right] Y_{3\lambda}(t|z_0) \;=\; 0 \; . \tag{5.78}$$

Due to the initial conditions, if $\lambda = 3, 6$ while $i = 1, 2$, then $Y_{i\lambda}(t|z_0) = 0$. This also occurs if $\lambda = 1, 2, 4, 5$ and $i = 3$. Therefore, the Jacobi fields are

$$\nabla g(t|z_0) = \begin{pmatrix} Y_{1\lambda} \\ Y_{2\lambda} \\ Y_{3\lambda} \\ W_{1\lambda} \\ W_{2\lambda} \\ W_{3\lambda} \end{pmatrix} = \begin{pmatrix} g_{1:1} & g_{1:2} & 0 & g_{1:4} & g_{1:5} & 0 \\ g_{2:1} & g_{2:2} & 0 & g_{2:4} & g_{2:5} & 0 \\ 0 & 0 & g_{3:3} & 0 & 0 & g_{3:6} \\ g_{4:1} & g_{4:2} & 0 & g_{4:4} & g_{4:5} & 0 \\ g_{5:1} & g_{5:2} & 0 & g_{5:4} & g_{5:5} & 0 \\ 0 & 0 & g_{6:3} & 0 & 0 & g_{6:6} \end{pmatrix} \; . \tag{5.79}$$

We see that sixteen are identically zero, and we have gone from solving six sets of six equations to solving four sets of four equations and two sets of two equations. Equations (5.77) and (5.78) are written in explicit form as

$$\begin{aligned} m\frac{d^2}{dt^2}\nabla_i g_1(t|z_0) &= -\frac{\partial^2\tilde{V}(r)}{\partial g_1^2}\nabla_i g_1(t|z_0) - \frac{\partial^2\tilde{V}(r)}{\partial g_2\partial g_1}\nabla_i g_2(t|z_0)\ , \\ m\frac{d^2}{dt^2}\nabla_i g_2(t|z_0) &= -\frac{\partial^2\tilde{V}(r)}{\partial g_1\partial g_2}\nabla_i g_1(t|z_0) - \frac{\partial^2\tilde{V}(r)}{\partial g_2^2}\nabla_i g_2(t|z_0)\ , \\ &\quad for\ i = 1,2,4,5 \end{aligned} \tag{5.80}$$

and

$$\begin{aligned} m\frac{d^2}{dt^2}\nabla_i g_3(t|z_0) &= -\frac{\partial^2\tilde{V}(r)}{\partial g_3^2}\nabla_i g_3(t|z_0)\ , \\ &\quad for\ i = 3,6 \end{aligned} \tag{5.81}$$

where $\nabla_i g_{l+3}(t|z_0) = m\frac{d}{dt}\nabla_i g_l(t|z_0)$.

To determine decoupled equations for $\nabla\nabla g$ we begin by taking the z derivative of Equation (5.75). Proceeding in a manner similar to before, one obtains the inhomogeneous equations

$$\left[m\frac{d^2}{dt^2} + \begin{pmatrix} \tilde{V}_{11} & \tilde{V}_{12} \\ \tilde{V}_{21} & \tilde{V}_{22} \end{pmatrix}\right]\begin{pmatrix} \tilde{Y}_{1\lambda\rho}(t|z_0) \\ \tilde{Y}_{2\lambda\rho}(t|z_0) \end{pmatrix} = -\begin{pmatrix} \tilde{V}_{1jk}\tilde{Y}_{j\lambda}\tilde{Y}_{k\rho} \\ \tilde{V}_{2jk}\tilde{Y}_{j\lambda}\tilde{Y}_{k\rho} \end{pmatrix}\ . \tag{5.82}$$

$$\left[m\frac{d^2}{dt^2} + \tilde{V}_{33}\right]\tilde{Y}_{3\lambda\rho}(t|z_0) = -\tilde{V}_{3jk}\tilde{Y}_{j\lambda}\tilde{Y}_{k\rho}\ . \tag{5.83}$$

In these equations the j and k are summed over. The $\tilde{Y}_{i\lambda\rho} = g_{i:\lambda\rho}$, and the inhomogeneous term is seen to depend on the Jacobi fields $\tilde{Y}_{i\lambda} = g_{i:\lambda}$. The $g_{i+3:\lambda\rho}$ terms are calculated from $g_{i+3:\lambda\rho} = m\dot{\tilde{Y}}_{i\lambda\rho}$.

It is beneficial to determine which $g_{i:\lambda\rho}$ are zero because of the planar motion. Since the initial conditions are zero, if $\tilde{V}_{ijk}\tilde{Y}_{j\lambda}\tilde{Y}_{k\rho} = 0$ then $\tilde{Y}_{i\lambda\rho}(t|z_0) = 0$. We see from Equation (5.72) that $\tilde{V}_{ijk}$ is zero if one of i, j, or k is 3 while the other two are in (1,2). As well, $V_{333} = 0$ (basically, an odd number of derivatives with respect to g_3). Equation (5.79) identifies the zero values of $Y_{i\lambda}$. We define two sets, $A = (1,2,4,5)$ and $B = (3,6)$. There are two situations which yield $V_{ijk}Y_{j\lambda}Y_{k\rho} = 0$. Case 1 involves $i \in (1,2)$ where the $\lambda\rho$ are disjointly assigned to A and B. Case 2 involves $i = 3$ and $\lambda\rho$ both in A or both in B.

Equations (5.82) and (5.83) are written in explicit form as

$$
\begin{aligned}
m\frac{d^2}{dt^2}\nabla_j\nabla_i g_1(t|z_0) \;=\;& -\left(\frac{\partial^3 V(r)}{\partial g_1^3}\nabla_j g_1(t|z) + \frac{\partial^3 V(r)}{\partial g_2\partial g_1^2}\nabla_j g_2(t|z)\right)\nabla_i g_1(t|z) \\
& -\left(\frac{\partial^3 V(r)}{\partial g_1^2\partial g_2}\nabla_j g_1(t|z) + \frac{\partial^3 V(r)}{\partial g_2^2\partial g_1}\nabla_j g_2(t|z)\right)\nabla_i g_2(t|z) \\
& -\left(\frac{\partial^3 V(r)}{\partial g_1\partial g_3^2}\nabla_j g_3(t|z)\right)\nabla_i g_3(t|z) \\
& -\frac{\partial^2 V(r)}{\partial g_1^2}\nabla_j\nabla_i g_1(t|z) - \frac{\partial^2 V(r)}{\partial g_1\partial g_2}\nabla_j\nabla_i g_2(t|z) \\
m\frac{d^2}{dt^2}\nabla_j\nabla_i g_2(t|z_0) \;=\;& -\left(\frac{\partial^3 V(r)}{\partial g_1^2\partial g_2}\nabla_j g_1(t|z) + \frac{\partial^3 V(r)}{\partial g_1\partial g_2^2}\nabla_j g_2(t|z)\right)\nabla_i g_1(t|z) \\
& -\left(\frac{\partial^3 V(r)}{\partial g_1\partial g_2^2}\nabla_j g_1(t|z) + \frac{\partial^3 V(r)}{\partial g_2^3}\nabla_j g_2(t|z)\right)\nabla_i g_2(t|z) \\
& -\left(\frac{\partial^3 V(r)}{\partial g_2\partial g_3^2}\nabla_j g_3(t|z)\right)\nabla_i g_3(t|z) \\
& -\frac{\partial^2 V(r)}{\partial g_1\partial g_2}\nabla_j\nabla_i g_1(t|z) - \frac{\partial^2 V(r)}{\partial g_2^2}\nabla_j\nabla_i g_2(t|z) \\
m\frac{d^2}{dt^2}\nabla_j\nabla_i g_3(t|z_0) \;=\;& -\left(\frac{\partial^3 V(r)}{\partial g_1\partial g_3^2}\nabla_j g_3(t|z)\right)\nabla_i g_1(t|z) \\
& -\left(\frac{\partial^3 V(r)}{\partial g_2\partial g_3^2}\nabla_j g_3(t|z)\right)\nabla_i g_2(t|z) \\
& -\left(\frac{\partial^3 V(r)}{\partial g_1\partial g_3^2}\nabla_j g_1(t|z) + \frac{\partial^3 V(r)}{\partial g_2\partial g_3^2}\nabla_j g_2(t|z)\right)\nabla_i g_3(t|z) \\
& -\frac{\partial^2 V(r)}{\partial g_1\partial g_3}\nabla_j\nabla_i g_1(t|z) - \frac{\partial^2 V(r)}{\partial g_2\partial g_3}\nabla_j\nabla_i g_2(t|z) \qquad (5.84)
\end{aligned}
$$

We are now able to calculate in the most efficient manner the classical trajectories as well as ∇g and $\nabla\nabla g$. With these solutions in hand we are now able to proceed to calculate the quantum correction $z^{(2)}(t|z_0) = (q^{(2)}(t|z_0), p^{(2)}(t|z_0))$.

5.3.2 Planar Motion and the Quantum Correction

We begin by showing that planar motion implies that the quantum corrections to $O(\hbar^2)$ will remain in the plane. From Equation (5.50) we have the expression

$$q_3^{(2)}(t|z_0)L_3(z_0) = (Y'_{1;53} - Y'_{1;62}) + (Y'_{2;61} - Y'_{2;43}) + (Y'_{3;42} - Y'_{3;51}) \,. \tag{5.85}$$

The first four Y' terms are zero from Case 1 above, and the last two are zero from Case 2. Therefore, we have for all time that the quantum correction in $\hbar^2$ remains in the z_0 plane, $q_3^{(2)}(t|z_0) = 0$. Similar reasoning from Equation (5.52) yields the result $p_3^{(2)}(t|z_0) = 0$.

The quantum correction is given by Equation (5.28). The form of this equation is a 6 component column vector. The top three components of the right hand side of this equation are zero since they are built from either q, p mixed derivatives of H or third and fourth order derivatives in p of H, both of which are zero (cf. Equation (5.9)). The top three components therefore reduce to

$$\mathcal{J}_{i\nu}(t)z_\nu^{(2)}(t|z_0) = 0 \,, \; i = 1 \sim 3 \,. \tag{5.86}$$

This is similar to Equation (5.74), and implies that

$$\frac{d}{dt}q^{(2)}(t|z_0) = \frac{1}{m}p^{(2)}(t|z_0) \,. \tag{5.87}$$

Inserting this result into the bottom portion of Equation (5.28) yields a result similar to Equation (5.75), only inhomogeneous

$$m\frac{d^2}{dt^2}q_i^{(2)}(t|z_0) + V_{ij}(q(t|z_0))q_j^{(2)}(t|z_0) = -\frac{1}{8}B_{12}^2 \prec q_j(t), q_k(t) \succ (z_0)V_{ijk}(q(t|z_0)) +$$

$$\frac{1}{12} B_{12} B_{23} \prec q_j(t), q_k(t), q_m(t) \succ (z_0) V_{ijkm}(q(t|z_0)) \ . \tag{5.88}$$

Since $q_3^{(2)}(t|z_0) = 0$, the i, j indices are restricted to 1,2. Equation (5.88) is a set of two equations for the two unknowns $(q_1^{(2)}(t|z_0), q_2^{(2)}(t|z_0))$.

5.3.3 Expectation Values

Now that we have all the tools required to calculate the relevant quantities for individual trajectories in the Moyal formalism, we turn our attention to the expectation values.

The quantum expectation values in Moyal quantum mechanics are given by:

$$\langle \hat{A}(t) \rangle_{\psi} = \int_{R^6} dz\, w_{\psi}(z) \Gamma_t A_W \ . \tag{5.89}$$

The observable is usually a tensor,

$$\hat{A} = \hat{T}_{\mu_1 \cdots \mu_n} \ , \tag{5.90}$$

here represented as a general tensor of rank n.

For a three dimensional system, the integration is over:

$$\begin{aligned} \int dz &= \int_{-\infty}^{\infty} dg_1 \int_{-\infty}^{\infty} dg_2 \int_{-\infty}^{\infty} dg_3 \int_{-\infty}^{\infty} dg_4 \int_{-\infty}^{\infty} dg_5 \int_{-\infty}^{\infty} dg_6 \ . & (5.91) \\ &= m^3 \int_0^{2\pi} d\alpha \int_0^{\pi} d\beta \int_0^{2\pi} d\gamma \int_0^{\infty} dv \int_0^{\infty} db \int_{-\infty}^{\infty} dq_2\, bv^2 \sin\beta \ . & (5.92) \end{aligned}$$

where we are working with the familiar Euler angles in the y-convention [Goldstein, 1981]. The mass is m, the impact parameter is b, the displacement along the $\hat{e}_2$ axis is q_2, and the velocity is v. In general this would be a difficult integral to evaluate. To simplify the phase space integral we will work with a Gaussian which is 'squeezed' in the momentum direction, allowing an expansion and subsequent momentum integration to be done analytically. This leaves us with a three dimensional integral in the coordinates, which we will reduce to a two dimensional integral.

Consider the Gaussian wave packet centered at the origin with spread Δ:

$$\psi(\Delta,x) = \left(\frac{1}{\pi\Delta^2}\right)^{3/4} exp\left\{-\frac{1}{2\Delta^2}(x_1^2+x_2^2+x_3^2)\right\} , \tag{5.93}$$

which has been normalized so that

$$\int_{\mathbf{R}^3} |\psi(\Delta,x)|^2 d^3x = 1 . \tag{5.94}$$

We wish to construct the Wigner function of this Gaussian (Equation (5.7))

$$\begin{aligned} w_{\psi(\Delta)}(z) &= \frac{1}{h^3}(|\psi(\Delta,x)\rangle\langle\psi(|\Delta,x)|)_W(z) , \\ &= \frac{1}{h^3}\int_{\mathbf{R}^3} dv'\, exp\left(\frac{-ip\cdot v'}{\hbar}\right)\langle q+\frac{v'}{2}|\psi(\Delta,x)\rangle\langle\psi(\Delta,x)|q-\frac{v'}{2}\rangle , \\ &= \left(\frac{1}{\pi\hbar}\right)^3 exp\left\{-\frac{1}{\Delta^2}(q_1^2+q_2^2+q_3^2)-\frac{\Delta^2}{\hbar^2}(p_1^2+p_2^2+p_3^2)\right\} . \end{aligned} \tag{5.95}$$

This Wigner function is centered at the origin and has a mean momentum of zero. We would like to construct a more general Gaussian and obtain a Wigner function which has been translated by $\bar{z} = (\bar{q},\bar{p})$ from $\bar{z} = 0$. This is accomplished via the Heisenberg phase space translation operator [Molzahn and Osborn, 1994]:

$$T(\bar{z}) = exp\left\{\frac{i}{\hbar}\bar{z}\cdot J\hat{z}\right\} = exp\left\{\frac{i}{\hbar}(\bar{p}\cdot\hat{q}-\bar{q}\cdot\hat{p})\right\} . \tag{5.96}$$

The effect of the translation operator on a function is [Molzahn and Osborn, 1994]

$$[T(\bar{z})\psi](x) = exp\left\{-\frac{i}{\hbar}(\bar{p}\cdot\bar{q}+\bar{p}\cdot x)\right\}\psi(x-\bar{q}) , \tag{5.97}$$

and so we have the new translated Gaussian

$$\begin{aligned} \psi(\Delta,\bar{z},x) &= [T(\bar{z})\psi(\Delta)](x) = exp\left\{-\frac{i}{\hbar}(\bar{p}\cdot\bar{q}+\bar{p}\cdot x)\right\}\psi(\Delta,x-\bar{q}) , \\ &= \left(\frac{1}{\pi\Delta^2}\right)^{3/4} exp\left\{-\frac{i}{\hbar}(\bar{p}\cdot\bar{q}+\bar{p}\cdot x)\right\} \\ &\quad\times exp\left\{-\frac{1}{2\Delta^2}\left((x_1-\bar{q}_1)^2+(x_2-\bar{q}_2)^2+(x_3-\bar{q}_3)^2\right)\right\} . \end{aligned} \tag{5.98}$$

The effect of the translation operator on an operator $\hat{A}$ can be expressed as [Molzahn and Osborn, 1994]

$$\left[T(\bar{z})\hat{A}T^{\dagger}(\bar{z})\right]_W(z) = A_W(z-\bar{z}) \ . \tag{5.99}$$

Therefore, the translated Wigner function is

$$\begin{aligned} w_{\psi(\Delta,\bar{z})}(z) &= \frac{1}{h^3}\left(|\psi(\Delta,\bar{z},x)\rangle\langle\psi(\Delta,\bar{z},x)|\right)_W(z) \ , \\ &= \frac{1}{h^3}\left(T(\bar{z})\,|\psi(\Delta,x)\rangle\langle\psi(\Delta,x)|\,T^{\dagger}(\bar{z})\right)_W(z) \ , \\ &= \left(\frac{1}{\pi\hbar}\right)^3 exp\left\{-\frac{1}{\Delta^2}\left((q_1-\bar{q}_1)^2+(q_2-\bar{q}_2)^2+(q_3-\bar{q}_3)^2\right)\right. \\ &\quad \left.-\frac{\Delta^2}{\hbar^2}\left((p_1-\bar{p}_1)^2+(p_2-\bar{p}_2)^2+(p_3-\bar{p}_3)^2\right)\right\} \ . \end{aligned} \tag{5.100}$$

For our purposes, imposing Equation (5.66), we set $\bar{q}_3 = \bar{p}_1 = \bar{p}_2 = 0$, since nonzero $\bar{q}_3, \bar{p}_1, \bar{p}_2$ only introduces a constant multiplier. The translated Wigner function is then given by:

$$w_{\psi}(z) = \left(\frac{1}{\pi\hbar}\right)^3 exp\left\{-\frac{(q_1-\bar{q}_1)^2+(q_2-\bar{q}_2)^2}{\Delta^2} - \frac{\Delta^2(p_2-\bar{p}_2)^2}{\hbar^2}\right\} \ . \tag{5.101}$$

For a tensor of rank n observable, the expectation value is

$$\begin{aligned} \langle T_{\alpha_1\cdots\alpha_n}(t)\rangle_{\psi} &= \int dz\ w_{\psi}(z)\Gamma_t(T_{\alpha_1\cdots\alpha_n}) \ , \\ &= \left(\frac{1}{\pi\hbar}\right)^3\int dz\ \Gamma_t(T_{\alpha_1\cdots\alpha_n}) \\ &\quad \times exp\left\{-\frac{(q_1-\bar{q}_1)^2+(q_2-\bar{q}_2)^2}{\Delta^2} - \frac{\Delta^2(p_2-\bar{p}_2)^2}{\hbar^2}\right\} \end{aligned} \tag{5.102}$$

The Wigner function remains fixed at its value at $t = 0$ and the observable is evolved. It is interesting to note that the expectation value could also be obtained by evolving the Wigner function and leaving the obervable fixed at its $t = 0$ value

$$\langle T_{\alpha_1\cdots\alpha_n}(t)\rangle_{\psi} = \int dz\ T_{\alpha_1\cdots\alpha_n}\Gamma_{-t}(w_{\psi}(z)) \ . \tag{5.103}$$

We will only evaluate expectation values by Equation (5.102) in this thesis.

To simplify the integration over phase space, we can expand the function in an asymptotic series about the maximum momentum of our Gaussian, $\bar{p}_2$. The momentum integration can then be performed analytically. The validity of this procedure is dependent on the function being expanded, and is affected by the size of $\hbar/\Delta$.

Consider a general smooth function of p, $F(p)$, for which we require

$$I(F;\bar{p},\Delta) = \int_{\Re} d^3p \; F(p) \left(\frac{1}{\pi\hbar}\right)^3 \; exp\left\{-\frac{\Delta^2(p-\bar{p})^2}{\hbar^2}\right\} . \tag{5.104}$$

By introducing a change of variables $p'_j = p_j - \bar{p}_j$, this integral becomes

$$I(F;\bar{p},\Delta) = \int_{\Re} d^3p' \; F(\bar{p}+p') \left(\frac{1}{\pi\hbar}\right)^3 \; exp\left\{-\frac{\Delta^2(p')^2}{\hbar^2}\right\} . \tag{5.105}$$

By performing a Taylor series expansion of $F(\bar{p}-p')$ about $\bar{p}$, the integral is found to be

$$\begin{aligned} I(F;\bar{p},\Delta) \;\; \sim \;\; & \left(\frac{1}{\pi^{1/2}\Delta}\right)^3 \left\{ F(\bar{p}) + \frac{1}{4}\left(\frac{\hbar}{\Delta}\right)^2 \left[\frac{\partial^2 F(\bar{p})}{\partial p_1^2} + \frac{\partial^2 F(\bar{p})}{\partial p_2^2} + \frac{\partial^2 F(\bar{p})}{\partial p_3^2}\right] \right. \\ & \left. + \, O\left(\left|\frac{\hbar}{\Delta}\right|^4\right) \right\} . \end{aligned} \tag{5.106}$$

Since we are only taking the expansion of Γ_t to $O(\hbar^2)$, this is an appropriate method of performing the d^3p part of the phase space integral. The momentum expansion is correct to $O\left(|\hbar/\Delta|^4\right)$, so by increasing Δ this approximation will be improved. Increasing Δ causes the Wigner function of the original Gaussian (Equation (5.95)) to be sharply peaked in the momentum direction, and spread out in the position. Thus we refer to this as a *squeezed Gaussian*. Although this method allows us to perform the momentum integration analytically, there is a price to pay. Since our Wigner function is now spread out in position, performing the coordinate integration accurately will require a larger range of values in the coordinate variables.

Applying Equation (5.106) to Equation (5.102), we obtain for the expectation value

$$\begin{aligned}\langle T_{\alpha_1\cdots\alpha_n}\rangle_v &= \left(\frac{1}{\pi^{1/2}\Delta}\right)^3 \int_{R^3} d^3q\; exp\left\{-\frac{(q_1-\bar{q}_1)^2+(q_2-\bar{q}_2)^2}{\Delta^2}\right\} \\ &\quad\times \Gamma_t\left\{T_{\alpha_1\cdots\alpha_n}(q,\bar{p}) + \left(\frac{\hbar}{2\Delta}\right)^2\left[\frac{\partial^2}{\partial p_1^2}T_{\alpha_1\cdots\alpha_n}(q,\bar{p}) + \right.\right. \\ &\quad\left.\left. + \frac{\partial^2}{\partial p_2^2}T_{\alpha_1\cdots\alpha_n}(q,\bar{p}) + \frac{\partial^2}{\partial p_3^2}T_{\alpha_1\cdots\alpha_n}(q,\bar{p})\right] + O\left(\left|\frac{\hbar}{\Delta}\right|^4\right)\right\} \end{aligned} \tag{5.107}$$

To simplify the notation slightly we can write

$$\begin{aligned}\langle T_{\alpha_1\cdots\alpha_n}\rangle_v &= \left(\frac{1}{\pi^{1/2}\Delta}\right)^3 \int_{R^3} d^3q\; exp\left\{-\frac{(q_1-\bar{q}_1)^2+(q_2-\bar{q}_2)^2}{\Delta^2}\right\} \\ &\quad\times S_{\alpha_1\cdots\alpha_n}(t,q,\bar{p}) \;, \end{aligned} \tag{5.108}$$

where

$$\begin{aligned} S_{\alpha_1\cdots\alpha_n}(t,q,\bar{p}) &= \gamma_t^{(0)}(T_{\alpha_1\cdots\alpha_n}(q,\bar{p})) + \frac{\hbar^2}{2}\gamma_t^{(2)}(T_{\alpha_1\cdots\alpha_n}(q,\bar{p})) \\ &\quad + \left(\frac{\hbar}{2\Delta}\right)^2 \partial_p^2\gamma_t^{(0)}(T_{\alpha_1\cdots\alpha_n}(q,\bar{p})) \;, \end{aligned} \tag{5.109}$$

where

$$\gamma_t^{(0)}(T_{\alpha_1\cdots\alpha_n}(q,\bar{p})) = T_{\alpha_1\cdots\alpha_n}(g(t|z),\bar{p}) \;, \tag{5.110}$$

$$\begin{aligned}\partial_p^2\gamma_t^{(0)}(T_{\alpha_1\cdots\alpha_n}(q,\bar{p})) &= \frac{\partial^2}{\partial p_1^2}T_{\alpha_1\cdots\alpha_n}(g(t|z),\bar{p}) + \frac{\partial^2}{\partial p_2^2}T_{\alpha_1\cdots\alpha_n}(g(t|z),\bar{p}) \\ &\quad + \frac{\partial^2}{\partial p_3^2}T_{\alpha_1\cdots\alpha_n}(g(t|z),\bar{p}) \;. \end{aligned} \tag{5.111}$$

Equation (5.110) is the classical $O(\hbar^0)$ contribution to the expectation value. Equation (5.111) arose from the asymptotic expansion used to perform the momentum integration, and is $O(|\hbar/\Delta|^2)$. The other term in Equation (5.109) is the first quantum correction to the expectation value, and is $O(\hbar^2)$. The term

$$\left(\frac{\hbar}{2\Delta}\right)^2\frac{\hbar^2}{2}\partial_p^2\gamma_t^{(2)}(T_{\alpha_1\cdots\alpha_n}(q,\bar{p})) \tag{5.112}$$

is $O(\hbar^4)$ and is therefore neglected.

It now simply remains to perform the coordinate part of the phase space integral which remains in Equation (5.108). To do this will will switch to cylindrical coordinates and end up with an integration over $y \in (-\infty, \infty)$ and impact parameter $b \in (0, \infty)$. The angular integral can be done analytically and will introduce Bessel functions.

The cylindrical coordinates are defined as:

$$x = r\cos\theta , \tag{5.113}$$

$$y = y , \tag{5.114}$$

$$z = r\sin\theta , \tag{5.115}$$

with Jacobian $J = r$. It is a simple matter to show that Equation (5.108) becomes

$$\begin{aligned} \langle T_{\alpha_1\cdots\alpha_n}\rangle_c = & \frac{\epsilon^{-\Delta^{-2}\bar{R}^2}}{\pi^{3/2}\Delta^3}\int_0^{\infty} dr \int_{-\infty}^{\infty} dy\, r\, exp\left\{-\Delta^{-2}(R^2 - 2y\bar{q}_2)\right\} \\ & \times \int_0^{2\pi} d\theta\, exp\left\{2\Delta^{-2} r\bar{q}_1\cos\theta\right\} S_{\alpha_1\cdots\alpha_n}(t, r\cos\theta, y, r\sin\theta) . \end{aligned} \tag{5.116}$$

where $R = \sqrt{r^2 + y^2}$ and $\bar{R} = \sqrt{\bar{q}_1^2 + \bar{q}_2^2}$. The angle θ is a rotation about the y-axis, and a rotation of zero denotes the z_0 plane, $q_0 = (q_1, q_2, 0) = (b, y, 0)$, and so we can write:

$$S_{\alpha_1\cdots\alpha_2}(t, r\cos\theta, y, r\sin\theta) = \mathcal{R}_{\alpha_1\nu_1}(\theta)\cdots\mathcal{R}_{\alpha_n\nu_n}(\theta)S_{\nu_1\cdots\nu_n}(t, r, y, 0) . \tag{5.117}$$

where

$$\mathcal{R}(\theta) = \begin{pmatrix} \tilde{R}(\hat{e}_2, \theta) & 0 \\ 0 & \tilde{R}(\hat{e}_2, \theta) \end{pmatrix} . \tag{5.118}$$

$$\tilde{R}(\hat{e}_2, \theta) = \begin{pmatrix} \cos\theta & 0 & \sin\theta \\ 0 & 1 & 0 \\ -\sin\theta & 0 & \cos\theta \end{pmatrix} . \tag{5.119}$$

Thus we can write for the expectation value

$$\begin{aligned} \langle T_{\alpha_1 \cdots \alpha_n} \rangle_c &= \frac{e^{-\Delta^{-2} \bar{R}^2}}{\pi^{3/2} \Delta^3} \int_0^\infty db \int_{-\infty}^{\infty} dy \, b \, exp \left\{ -\Delta^{-2} (R^2 - 2 y \bar{q}_2) \right\} \\ &\quad \times \Omega_{\alpha_1 \nu_1 \alpha_2 \nu_2 \cdots \alpha_n \nu_n} (2 \Delta^{-2} b \bar{q}_1) S_{\nu_1 \cdots \nu_n} (t, b, y, 0) \, . \end{aligned} \tag{5.120}$$

where

$$\Omega_{\alpha_1 \nu_1 \alpha_2 \nu_2 \cdots \alpha_n \nu_n} (2 \Delta^{-2} b \bar{q}_1) = \int_0^{2\pi} d\theta \, exp \left\{ 2 \Delta^{-2} b \bar{q}_1 \cos \theta \right\} \mathcal{R}_{\alpha_1 \nu_1} (\theta) \cdots \mathcal{R}_{\alpha_n \nu_n} (\theta) \tag{5.121}$$

is a combination of Bessel functions and is known analytically (cf. Appendix B).

It should be emphasized that the contribution of order $(\hbar/\Delta)^2$ is due solely to the momentum expansion that was employed and is *not* a contribution to the quantum deviation from the classical found via Moyal quantum mechanics. The Moyal contributions to the expectation value are found in the $\gamma_t^{(0)}$ parts (the classical result, which includes the $(\hbar/\Delta)^2$ term as well), and the $\gamma_t^{(2)}$ part (the quantum deviation).

Chapter 6

Application to Helium, Neon and Argon

The formalism developed in the previous section is now used to treat the evolution of a Gaussian wave packet under the influence of a central potential. Before the wave packet is introduced, however, the Jacobi fields and the quantum trajectory will be examined in detail for a single trajectory.

The three systems considered are helium-helium, neon-neon, and argon-argon. These systems were chosen since they exhibit a factor of 10 change in the mass, and will produce elastic scattering at the energies chosen. The potential in all cases is taken to be the Lennard-Jones (12-6) potential which is modified at small r to be finite at $r = 0$

$$V(r) = \begin{cases} 4\epsilon\left(\left(\frac{\sigma}{r}\right)^{12} - \left(\frac{\sigma}{r}\right)^{6}\right) & r > r_0 \\ \\ \frac{Ar^5}{120} + \frac{Br^4}{24} + \frac{Cr^3}{6} + \frac{Dr^2}{2} + Er + F & r \leq r_0 \end{cases} . \tag{6.1}$$

The A, B, C, D, E, F are defined so that the potential is smooth up to the fifth derivative at the point r_0. This smoothness is necessary since we are using the fourth derivative of the potential (Equation (5.73)). We require the wall of our potential to be modelled by the Lennard Jones structure, and hence choose r_0 to be smaller than σ. We impose that $V(r_0) > 3 \times$ energy of collision. The values of the constants in the potential are given in Table 6.1.

For the work in this thesis, units are chosen so that energy is always expressed in cm^{-1}. This choice leads to the units as described in Table 6.2. Conversion to other units is accomplished by use of the multiplicative factors included in Table 6.2. Atomic masses are based on ^{12}C having a mass of exactly 12 amu, and the masses used are the mass of the most stable isotope.

6.1 The Quantum Trajectory

In this section we will look at the Jacobi fields (Equations (5.80), (5.81), and (5.84)) and the quantum trajectory (Equation (5.88)) in detail. Appendix C examines the error propagation that occurs in the numerical solution.

We begin with the classical trajectory. Figure 6.1 shows the classical trajectory that results for a given impact parameter b and y.

The Jacobi fields $\nabla g(t|z_0)$ are the first functions which must be calculated in order to obtain the quantum trajectory. Figure 6.2 shows how two representative elements of $\nabla g(t|z_0)$ develop with time. In regions where the potential is essentially zero, the Jacobi fields are linear in time. It is also evident that after the collision the Jacobi fields can develop a linear time dependence with a slope which is quite steep, resulting in very large values for the Jacobi fields at large times. Since the Jacobi fields indicate the dependence of trajectories on initial conditions, this is not

	He	Ne	Ar
ϵ (cm^{-1})	7.103 296[†]	24.812 881[‡]	87.018 840[*]
r_{min} (Å)	2.556[†]	3.131[‡]	3.822[*]
σ (Å)	2.277[†]	2.789[‡]	3.405[*]
r_0 (Å)	1.8	2.1	3.1
A (cm^{-1}/Å^5)	$-1.305\,767 \times 10^7$	$-3.787\,479 \times 10^7$	$-1.900\,680 \times 10^6$
B (cm^{-1}/Å^4)	$+2.496\,021 \times 10^7$	$+8.447\,639 \times 10^7$	$+6.252\,860 \times 10^6$
C (cm^{-1}/Å^3)	$-2.394\,704 \times 10^7$	$-9.457\,013 \times 10^7$	$-1.032\,289 \times 10^7$
D (cm^{-1}/Å^2)	$+1.538\,266 \times 10^7$	$+7.088\,689 \times 10^7$	$+1.140\,793 \times 10^7$
E (cm^{-1}/Å)	$-7.447\,284 \times 10^6$	$-4.004\,876 \times 10^7$	$-9.498\,711 \times 10^6$
F (cm^{-1})	$+2.900\,597 \times 10^6$	$+1.820\,423 \times 10^7$	$+6.359\,796 \times 10^6$
mass (amu)	4.0026	20.179	39.948

Table 6.1:

Constants used in helium, neon, and argon modified Lennard-Jones (12-6) potential. References: [†]: de Boer, 1938; [‡]: Hirschfelder *et al.*, 1954; [*]: Fender and Halsey, 1962.

Energy	cm^{-1}
Temperature	K
Distance	Å
Time	10^{-10} s = 0.1 ns
Velocity	m/s = Å/(10^{-10} s)
Mass	cm^{-1} s^2 / m^2
Momentum	cm^{-1} 0.1 ns/Å
$\hbar$	5.3088374×10^{-2} cm^{-1} 0.1 ns
	$1.0545727 \times 10^{-34}$ J s
c	$2.99792458 \times 10^{10}$ cm/s
k_B	1.380658×10^{-23} J/K
1 K	0.6950387 cm^{-1}
1 J	5.0341125×10^{22} cm^{-1}
1 amu	$1.6605402 \times 10^{-27}$ kg

Table 6.2: Units

surprising.

An interesting note is that if the Jacobi fields are linear when the potential is zero, then they have nonlinear structure only when the potential is acting. Therefore, when the Jacobi fields are nonlinear the collision is actively occuring. For example, in Figure 6.2 we see that for the given trajectory the collision occurs during $t \in (0.01, 0.0175)10^{-10}$ s. This circumstance can provide a rough estimate for the duration of a collision, and we see that the duration of a He-He collision with velocity 600 m/s is $\sim 10^{-12}$ seconds (of course, this result can be recovered in a similar manner from a graph of the momentum).

Figure 6.3 shows two representative elements of $\nabla\nabla g(t|z_0)$. These functions as well are linear in time when the potential is essentially zero, and show the possibility for growth to large size for large time.

Figure 6.4 shows the classical trajectory as well as the quantum trajectory (Equation (5.26)). The quantum trajectory begins at the same value as the classical trajectory, and does not differ appreciably from the classical trajectory until the trajectory enters the region where the potential is significantly nonzero. For trajectories which have a large impact parameter the quantum and classical trajectories are essentially the same. This result occurs since the potential is nearly zero over the entire trajectory.

Figures 6.5 and 6.6 shows the contributions to the classical and quantum trajectories for $g_1(t|z_0)$ and $g_4(t|z_0)$ as a function of time. It can be seen that the first quantum correction to the trajectory $\frac{\hbar^2}{2} z_i^{(2)}(t|z_0)$ has a stronger oscillatory structure than the classical trajectory when the collision is occuring. This behaviour impacts the integration over y, as we shall see in section 6.3.1.

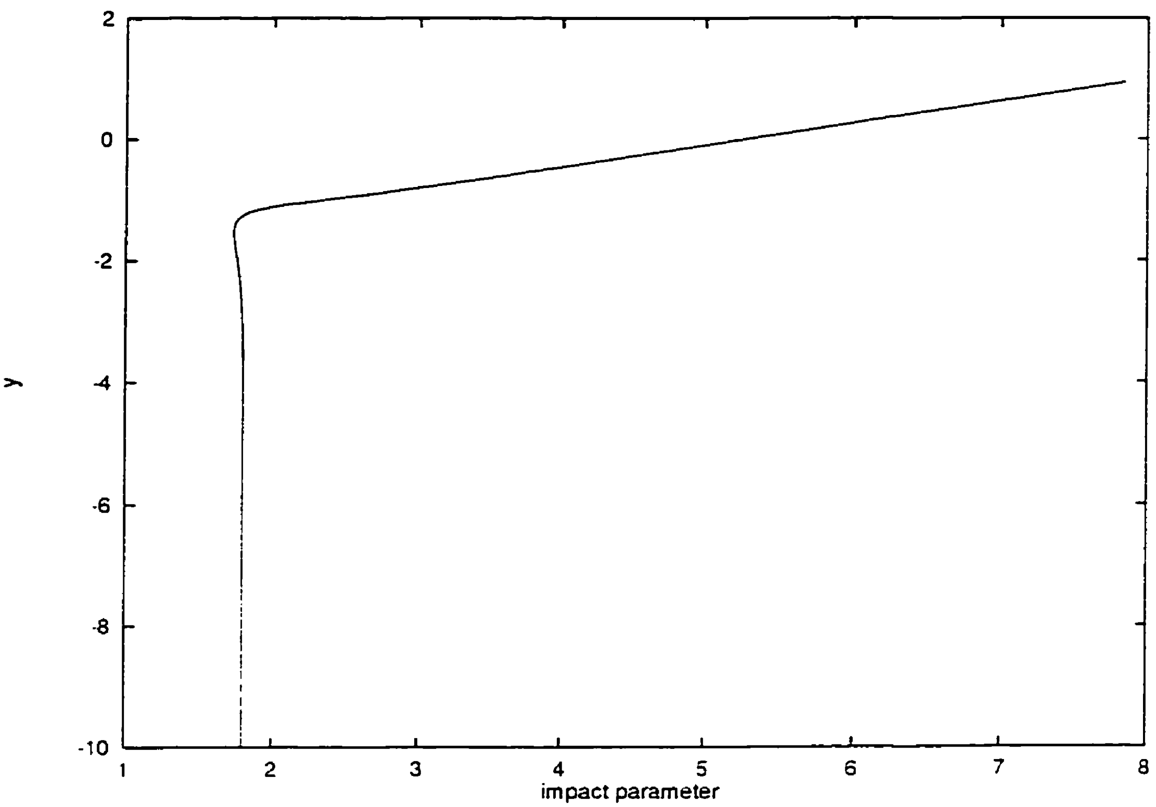

Figure 6.1:

Classical trajectory $(z_1^{(0)}(t|z_0), z_2^{(0)}(t|z_0))$

The potential is helium, and the initial conditions are velocity = 600 m/s, $b = 1.8$A, $y = -10$A.

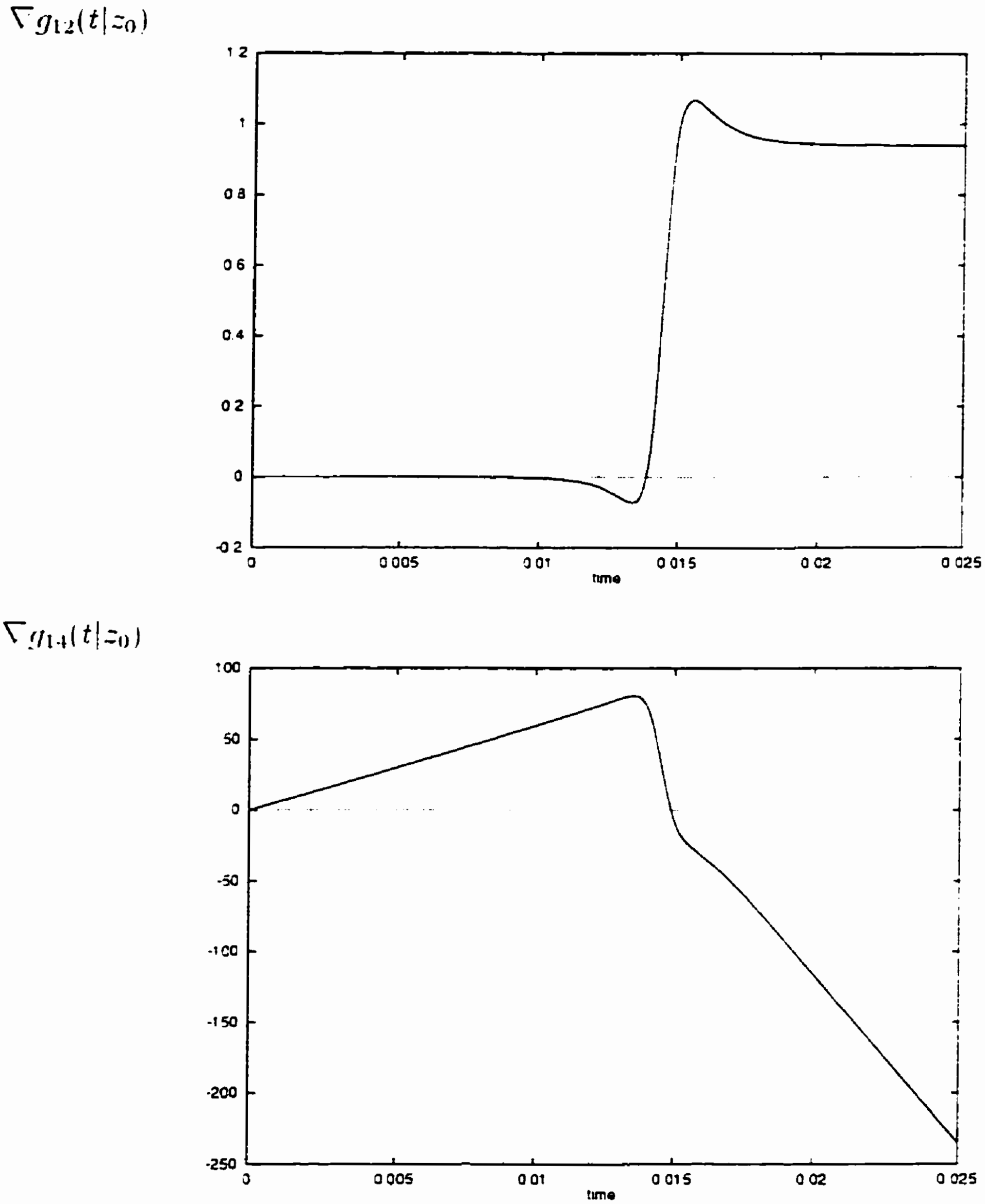

Figure 6.2:

Sample Jacobi fields as a function of time. The potential is helium, and the initial conditions are velocity = 600 m/s, $b = 1.8$A, $y = -10$A. The x-axis is time in units of 10^{-10} seconds.

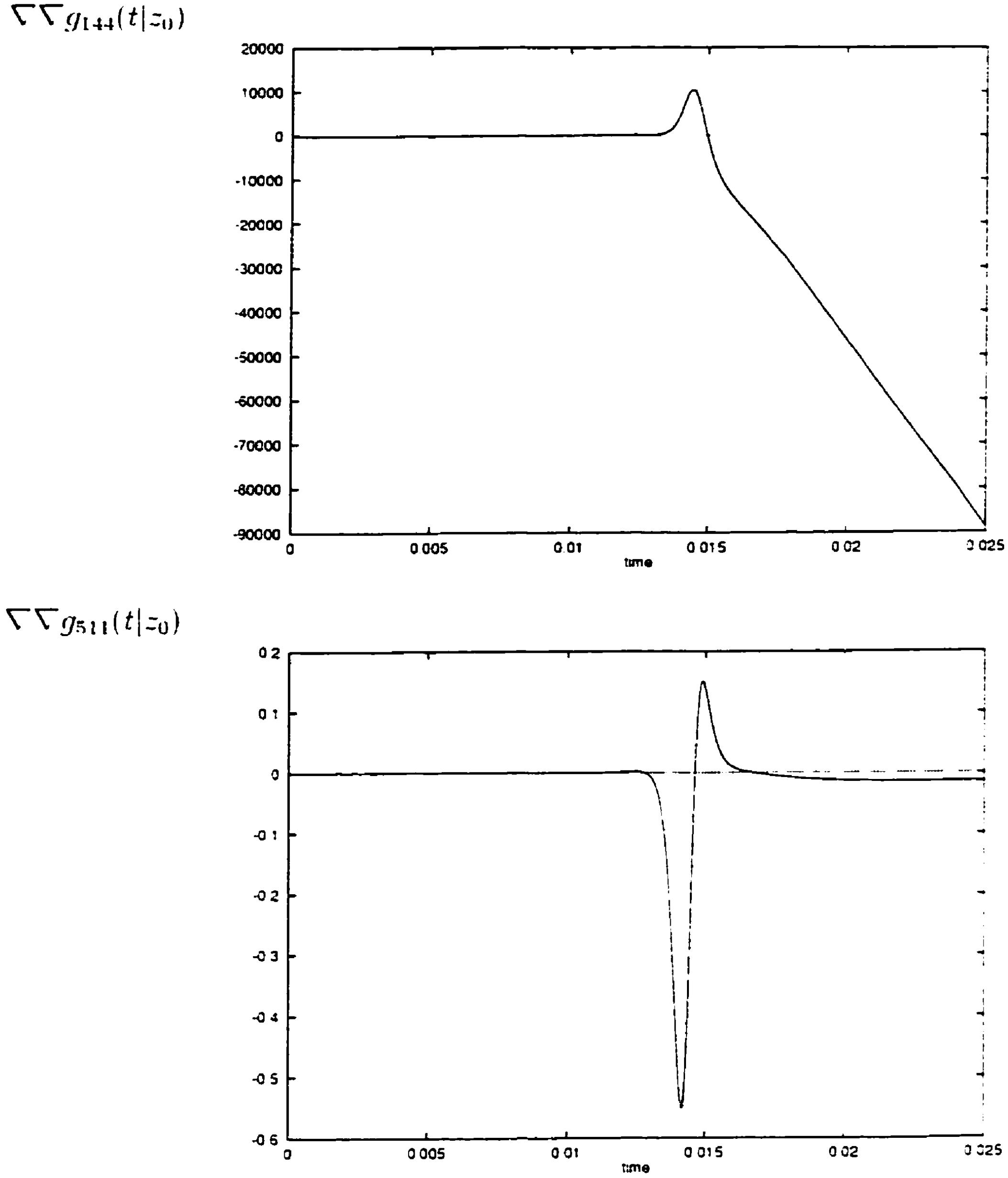

Figure 6.3:

Sample $\nabla\nabla g(t|z_0)$ as a function of time. The potential is helium, and the initial conditions are velocity = 600 m/s, $b = 1.8$Å, $y = -10$Å. The x-axis is time in units of 10^{-10} seconds.

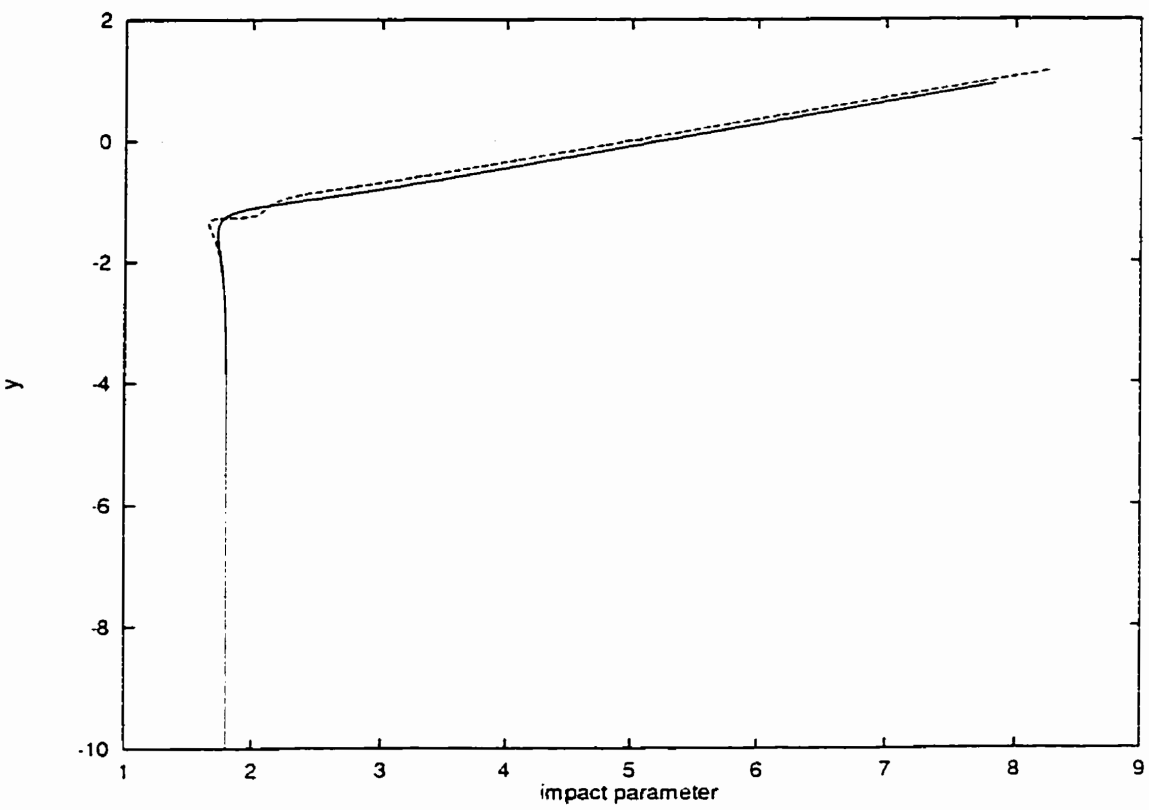

Figure 6.4:

Classical and quantum trajectory

Plots: solid line: $(z_1^{(0)}(t|z_0), z_2^{(0)}(t|z_0))$

dotted line: $(z_1^{(0)}(t|z_0) + \frac{\hbar^2}{2} z_1^{(2)}(t|z_0), z_2^{(0)}(t|z_0) + \frac{\hbar^2}{2} z_2^{(2)}(t|z_0))$

The potential is helium, and the initial conditions are velocity = 600 m/s, $b = 1.8$A, $y = -10$A.

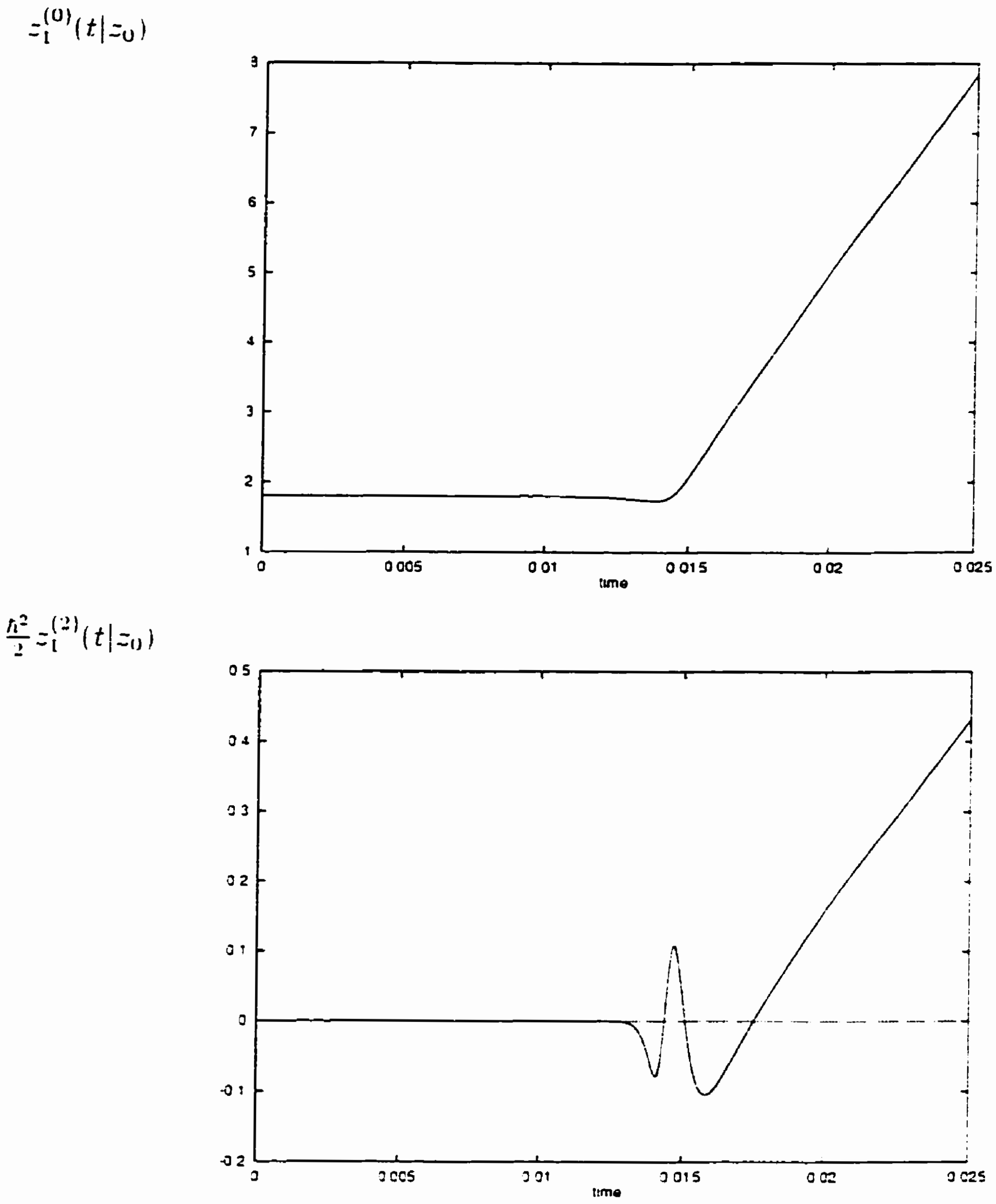

Figure 6.5:

Plots of $z_1^{(0)}(t|z_0)$ and $\frac{\hbar^2}{2} z_1^{(2)}(t|z_0)$. The potential is helium, and the initial conditions are velocity = 600 m/s, $b = 1.8$Å, $y = -10$Å. The x-axis is time in units of 10^{-10} seconds.

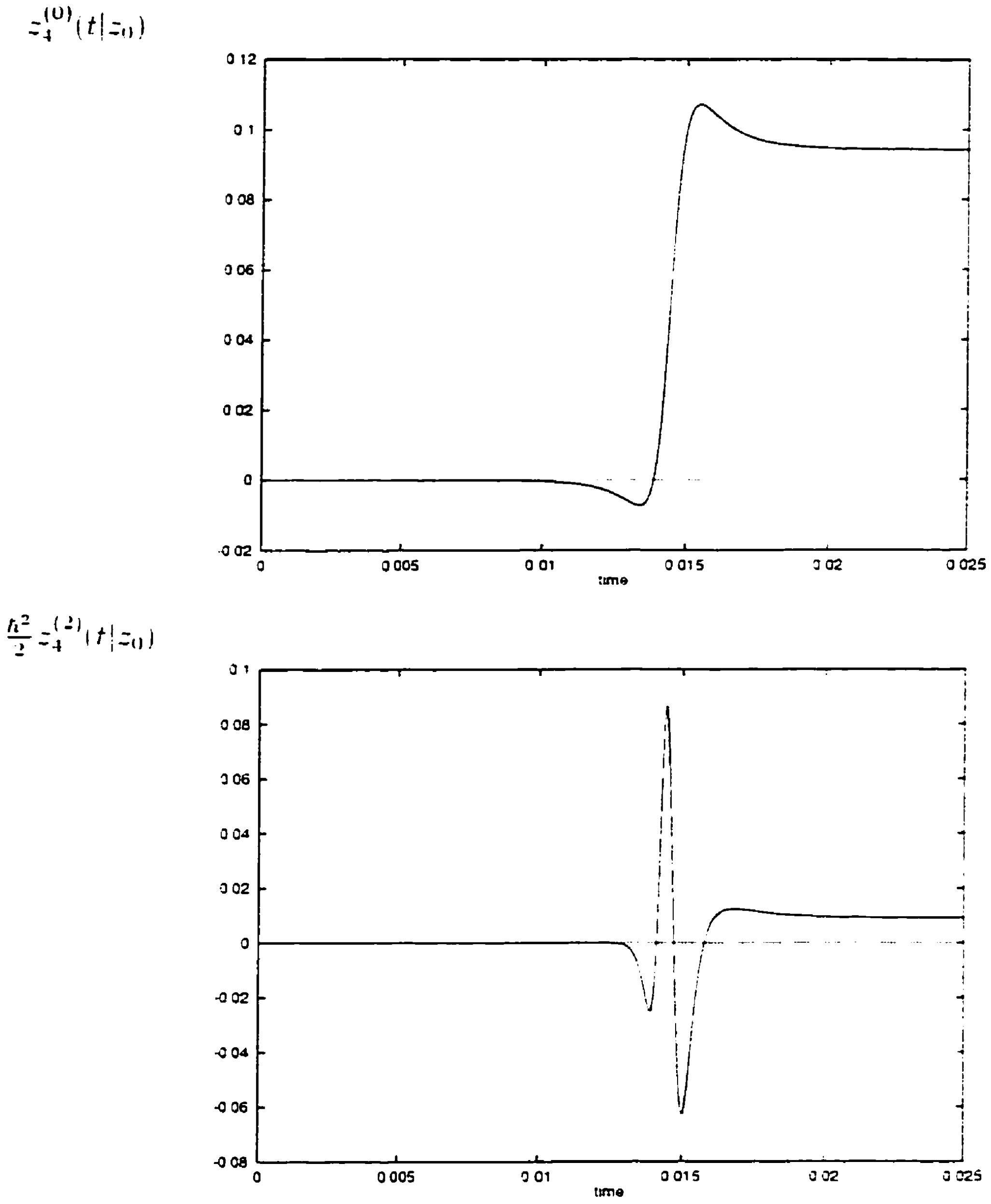

Figure 6.6:

Plots of $z_4^{(0)}(t|z_0)$ and $\frac{\hbar^2}{2} z_4^{(2)}(t|z_0)$. The potential is helium, and the initial conditions are velocity = 600 m/s, $b = 1.8$Å, $y = -10$Å. The x-axis is time in units of 10^{-10} seconds.

6.2 Orbiting in a Lennard Jones Potential

In this section we will examine forward glory and rainbow scattering, and derive conditions for which orbiting occurs in the Lennard Jones (12-6) potential.

Two cases which make the differential cross section singular are *forward glory scattering* and *rainbow scattering* [Child, 1974; Zare, 1988]. Forward glory scattering occurs at an impact parameter b_{glory} when the angle of deflection (χ) is equal to zero. Rainbow scattering occurs at an impact parameter b_{rainbow} when the rate of change of the angle of deflection with impact parameter ($\partial\chi/\partial b$) is zero. For an example of the effects of rainbow and glory contributions to the JWKB semiclassical approximation see Ford and Wheeler, 1959.

The angle of deflection as a function of impact parameter is shown in Figure 6.7, along with an estimate of the size of the quantum corrections after the collision. It is seen that the quantum corrections to the coordinates are largest for trajectories which have an impact parameter slighlty less than b_{rainbow}; the quantum corrections to the momentum are largest here as well.

Forward glory scattering is shown in Figure 6.8. The quantum trajectory does not differ from the classical trajectory to the degree that is seen in rainbow scattering at large times (see below). However, the quantum trajectory is seen to oscillate about the classical trajectory near closest approach. This oscillation is evident in all trajectories near closest approach (c.f. Figure 6.4), and is not a property of forward glory scattering.

The classical and quantum trajectories for rainbow scattering are shown in Figure 6.9. It is seen that the quantum trajectory near the classical rainbow trajectory can deviate markedly from the classical. For low velocities this deviation can be very significant, and the expansion to $O(\hbar^2)$ may not be valid. However, as long as the expansion is valid over all but a small region of phase space, the average values of dynamical quantities should still be correct. This result is not surprising since the particle spends the most time engaged in a close collision for rainbow scattering, and this is precisely the region where quantum effects will be largest. Rainbow scattering is also very sensitive to initial conditions, a property which the Jacobi fields measure.

Orbiting can be thought of as a special case of rainbow scattering where the angle of deflection is $-\infty$, that is, there exists a vertical asymptote at b_{orbit} rather than a minimum at b_{rainbow}. For the Lennard Jones potential, the existence and position of b_{orbit} can be derived analytically [Stogryn and Hirschfelder, 1959].

Figure 6.10 illustrates the situation which results in orbiting. The effective potential, $V_{\text{eff}}(b,r,E)$, contains the centrifugal potential and is given by [Goldstein, 1981]

$$V_{\text{eff}}(b,r,E) = 4\epsilon\left(\left(\frac{\sigma}{r}\right)^{12} - \left(\frac{\sigma}{r}\right)^{6}\right) + \frac{b^2E}{r^2}\,. \qquad (6.2)$$

In Figure 6.10, the top curve is $V_{\text{eff}}(b_c,r,E_c)$, and has a point of inflection at $\tilde{r}_c$ for $b=b_c$ and $E=E_c$. The middle curve is $V_{\text{eff}}(b_0,r,E)$, and it has a maximum at $\tilde{r}$ for $b=b_0$ and energy E. The bottom curve is $V_{\text{eff}}(0,r,E)$, which is simply the Lennard Jones (12-6) potential since the centrifugal potential is zero for trajectories with zero angular momentum.

Analytically, the conditions for orbiting are

$$V_{\text{eff}}(b_0,\tilde{r},E_0) = E_0\,, \qquad (6.3)$$

$$V'_{\text{eff}}(b_0,\tilde{r},E_0) = 0\,, \qquad (6.4)$$

where b_0 is the initial impact parameter at infinity, $\tilde{r}$ is the radius of the orbit, and

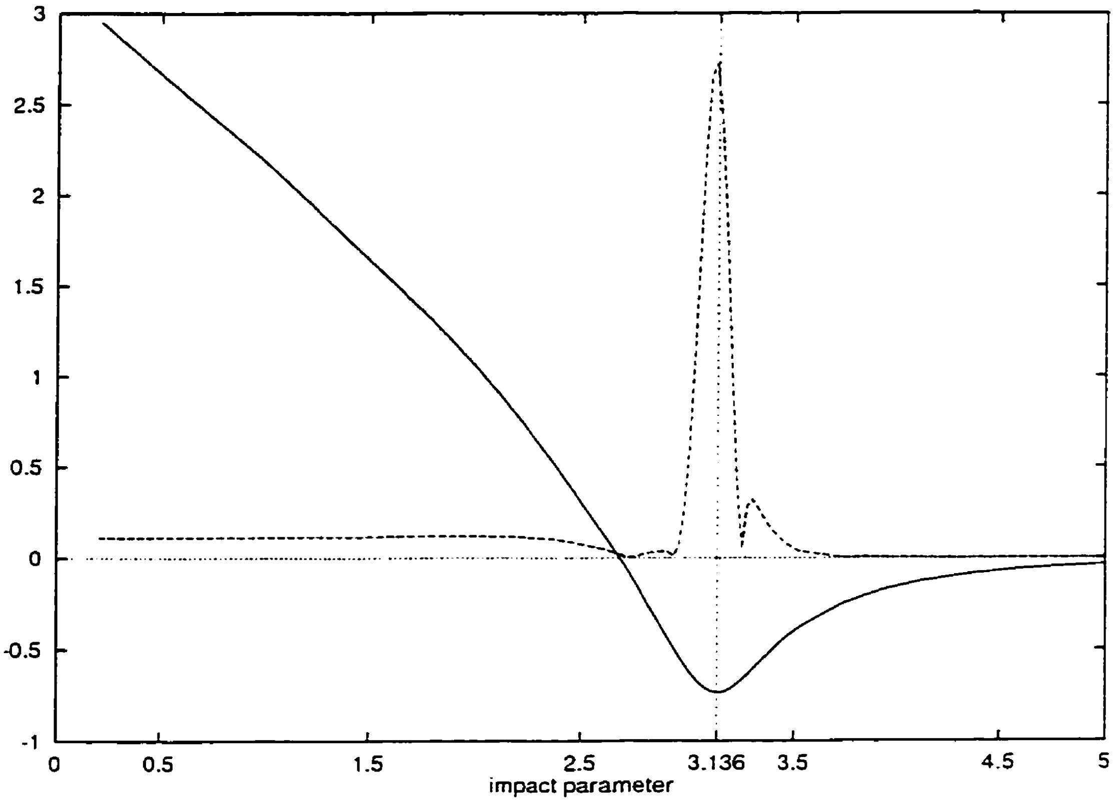

Figure 6.7:

Solid line: classical angle of deflection (radians).

Dotted line: $|R_c - R_q|/R_c$. (size of quantum correction)

where $R_c = \sqrt{(z_1^{(0)}(t|z_0)^2 + z_2^{(0)}(t|z_0))^2}$.

and $R_q = \sqrt{\left(z_1^{(0)}(t|z_0) + \frac{\hbar^2}{2} z_1^{(2)}(t|z_0)\right)^2 + \left(z_2^{(0)}(t|z_0) + \frac{\hbar^2}{2} z_2^{(2)}(t|z_0)\right)^2}$.

The potential is helium, and the initial conditions are velocity = 500 m/s, $q = -20$A. The time is taken to be 0.1×10^{-10} s. Rainbow scattering is seen to occur at $b = 3.136$A. Forward glory scattering occurs at $b = 2.675$A. The vertical scale applies to both functions

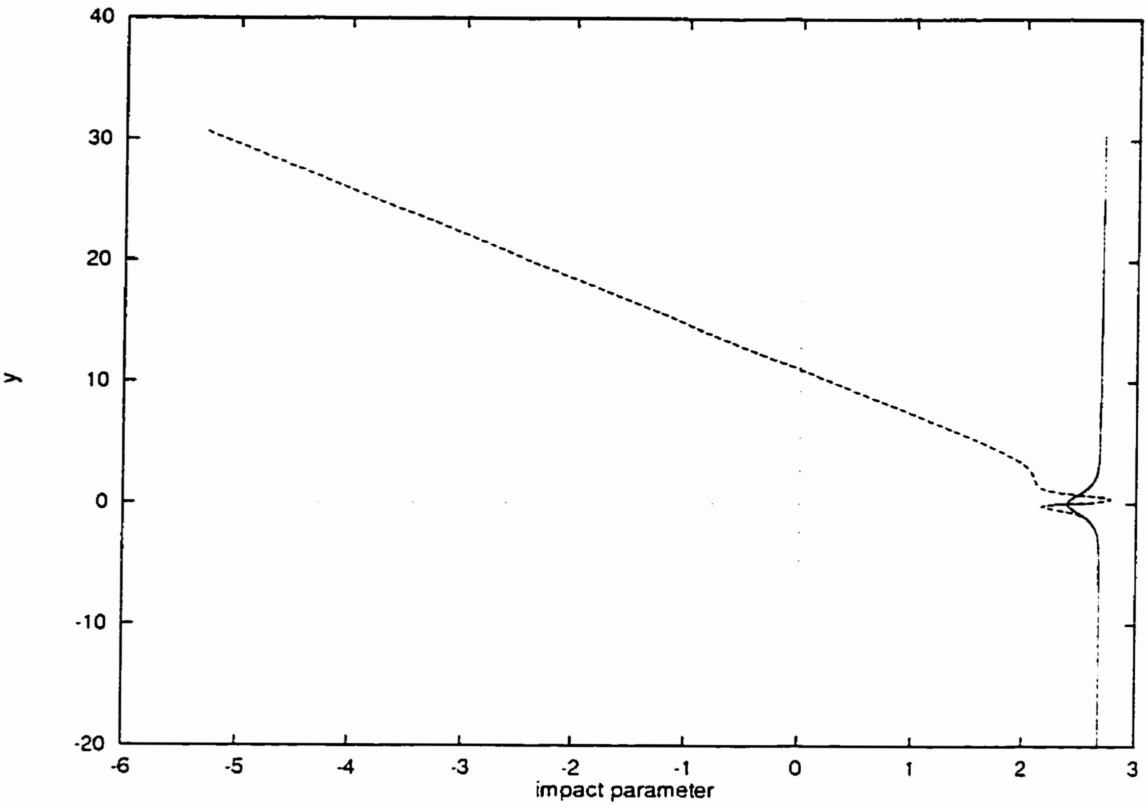

Figure 6.8:

Classical and quantum trajectory for forward glory scattering

Plots: solid line: $(z_1^{(0)}(t|z_0), z_2^{(0)}(t|z_0))$

dotted line: $(z_1^{(0)}(t|z_0) + \frac{\hbar^2}{2} z_1^{(2)}(t|z_0), z_2^{(0)}(t|z_0) + \frac{\hbar^2}{2} z_2^{(2)}(t|z_0))$

The potential is He-He, and the initial conditions are velocity = 500 m/s, $y = -20$Å, $b = 2.675$Å.

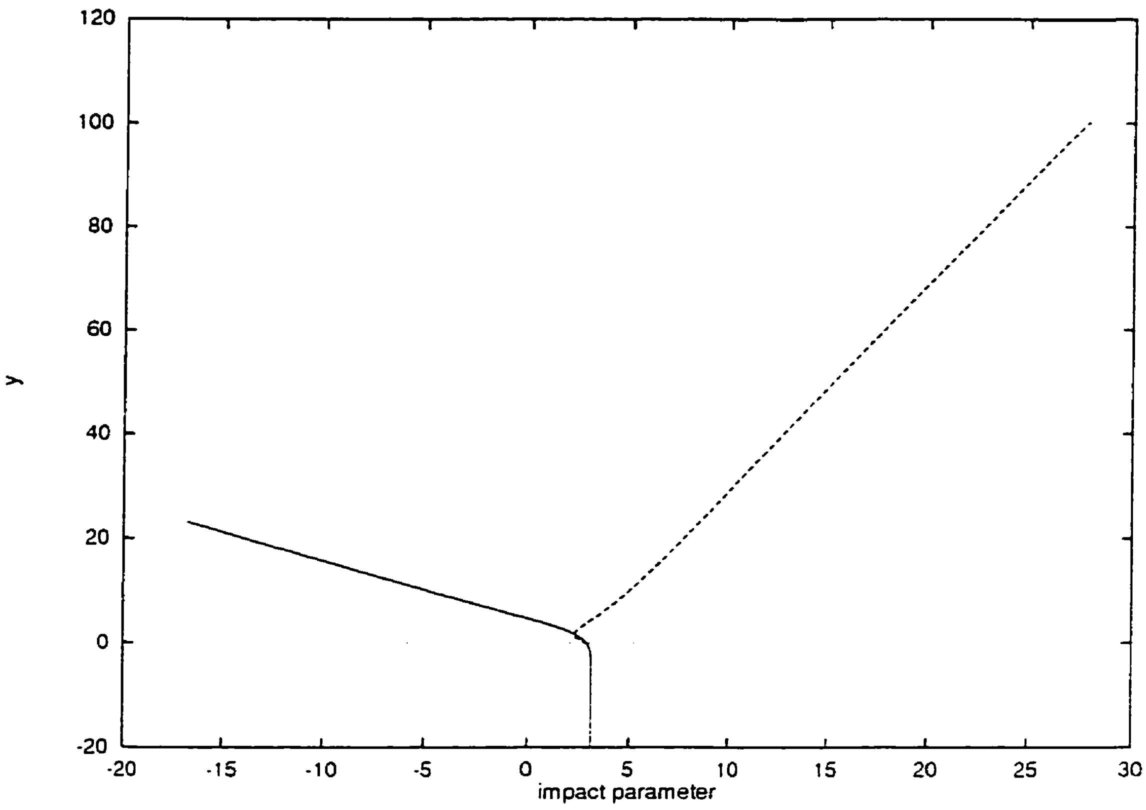

Figure 6.9:

Classical and quantum trajectory for rainbow scattering

Plots: solid line: $(z_1^{(0)}(t|z_0), z_2^{(0)}(t|z_0))$

dotted line: $(z_1^{(0)}(t|z_0) + \frac{\hbar^2}{2} z_1^{(2)}(t|z_0), z_2^{(0)}(t|z_0) + \frac{\hbar^2}{2} z_2^{(2)}(t|z_0))$

The potential is He-He, and the initial conditions are velocity = 500 m/s, $y = -20$A, $b = 3.136$A.

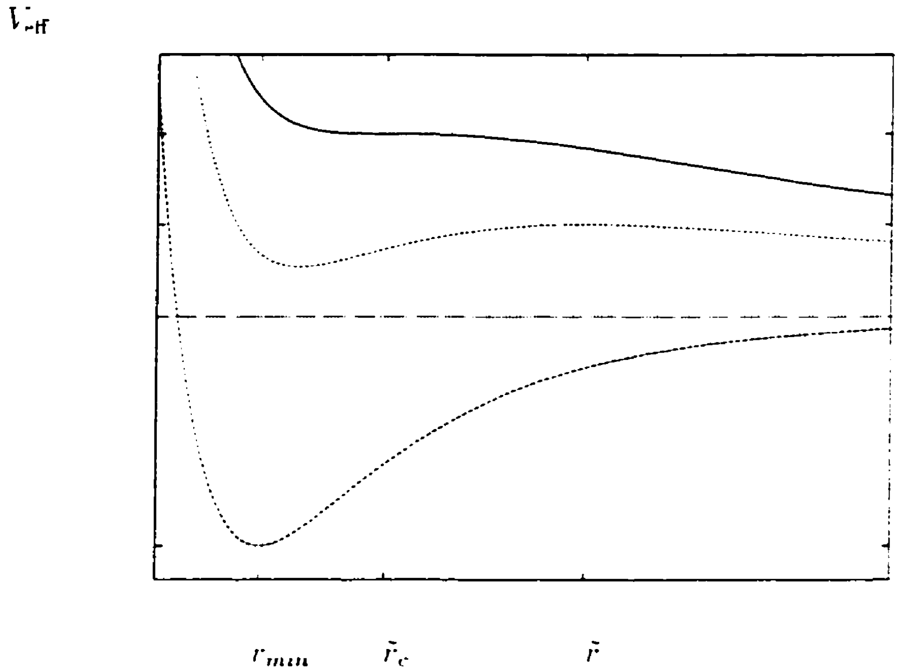

Figure 6.10:

Effective potential energy curves

E_0 is the kinetic energy at infinity. Solving this set of equations for b_0 and $\tilde{r}$ yields

$$\tilde{r} = \left[\frac{4\sigma^6\epsilon}{E_0}\left(1+\sqrt{1-\frac{E_0}{E_c}}\right)\right]^{\frac{1}{6}} . \tag{6.5}$$

$$b_0 = \left[\frac{2\epsilon\tilde{r}^3}{E_0}\left(\frac{-12\sigma^{12}}{\tilde{r}^{13}}+\frac{6\sigma^6}{\tilde{r}^6}\right)\right]^{\frac{1}{2}} . \tag{6.6}$$

where we have identified the critical energy $E_c = \frac{4}{5}\epsilon$. For $E > E_c$ no orbiting will occur (as $\tilde{r}$ is no longer real). For $E = E_c$ we have the condition for classical orbiting. The critical values of the parameters become

$$\tilde{r}_c = 5^{\frac{1}{6}}\sigma\ ,\ b_c = \frac{3\sigma}{5^{\frac{1}{3}}}\ ,\ L_c = b_c^2 E_c = \frac{36\epsilon\sigma^2}{5^{\frac{5}{3}}}\ . \tag{6.7}$$

The critical values in Equation (6.7) can also be obtained by solving the triple of equations which must be satisfied at the onset of orbiting, $V_{\text{eff}}(b_c, \tilde{r}_c, E_c) = E_c$, $V'_{\text{eff}}(b_c, \tilde{r}_c, E_c) = 0$, $V''_{\text{eff}}(b_c, \tilde{r}_c, E_c) = 0$ for E_c, b_c, and $\tilde{r}_c$.

Metastable states exist for a region around b_{orbit} for which the angle of deflection is $\geq -2\pi$. The quantum correction is largest for these metastable states, and the expansion to $O(\hbar^2)$ may not be valid for large times for these trajectories. Figure 6.11 shows a typical metastable state. Numerical instabilities for these trajectories do not allow us to calculate with accuracy the quantum trajectory. It has been noted for the problem of line shapes [Meinander, 1995] that bound and free states have to be computed with different methods since the trajectories have such different character.

Bound states, which correspond to negative energy solutions, are not possible for two body scattering systems.

In this section we have seen that the quantum corrections are most dominant for trajectories which exhibit rainbow scattering, or, if the energy is low enough,

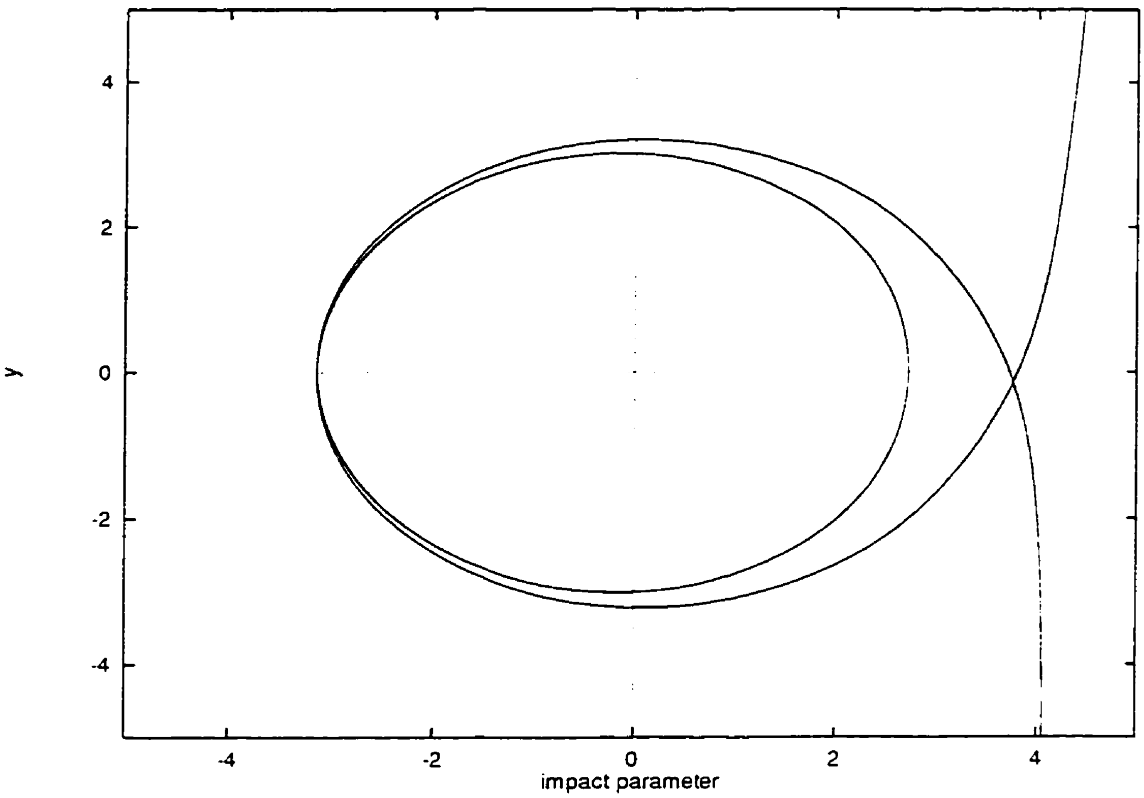

Figure 6.11:

Classical trajectory for metastable scattering

The potential is He-He, and the initial conditions are velocity = 250 m/s, $y = -70$A, $b = 4.064$A.

	He-He	Ne-Ne	Ar-Ar
E_c (cm^{-1})	5.6826	19.850	69.615
velocity$_c$ (m/s)	260.64	216.95	288.76

Table 6.3: Critical values for orbiting

orbiting. The present numerical package is unable to correctly determine the quantum corrections in the case of metastable states. Any future attempts to extend the theory to higher orders of $\hbar$ should concentrate on these regions of phase space. Table 6.3 contains the critical values for He, Ne, Ar.

6.3 Expectation Values

We now are able to calculate expectation values using the formalism of Moyal quantum mechanics. In this section, typical functions will be examined in detail with respect to their behaviour with changing b and y for various times.

The parameters for the Wigner function of the Gaussian, Equation (5.100), are given in Table 6.4. We can see that the Gaussian is indeed squeezed, with a large dispersion in the coordinates and a small dispersion in the momentum (recall that the dispersion in the momentum is $\hbar^2/2\Delta^2$). The Taylor series expansion in the momentum that was performed means that we are working with only one momentum, and so the Gaussian is centered at that momentum. The Gaussian is roughly forty times as large as the potential ($\Delta^2/2 = 200 \sim 40 \times (2r_{min})$).

Figure 6.12 shows how classical and quantum trajectories evolve for a typical initial y and changing impact parameter for a helium potential and initial velocity $v = 450$ m/s. Both sets of trajectories stay outside of the smooth core region

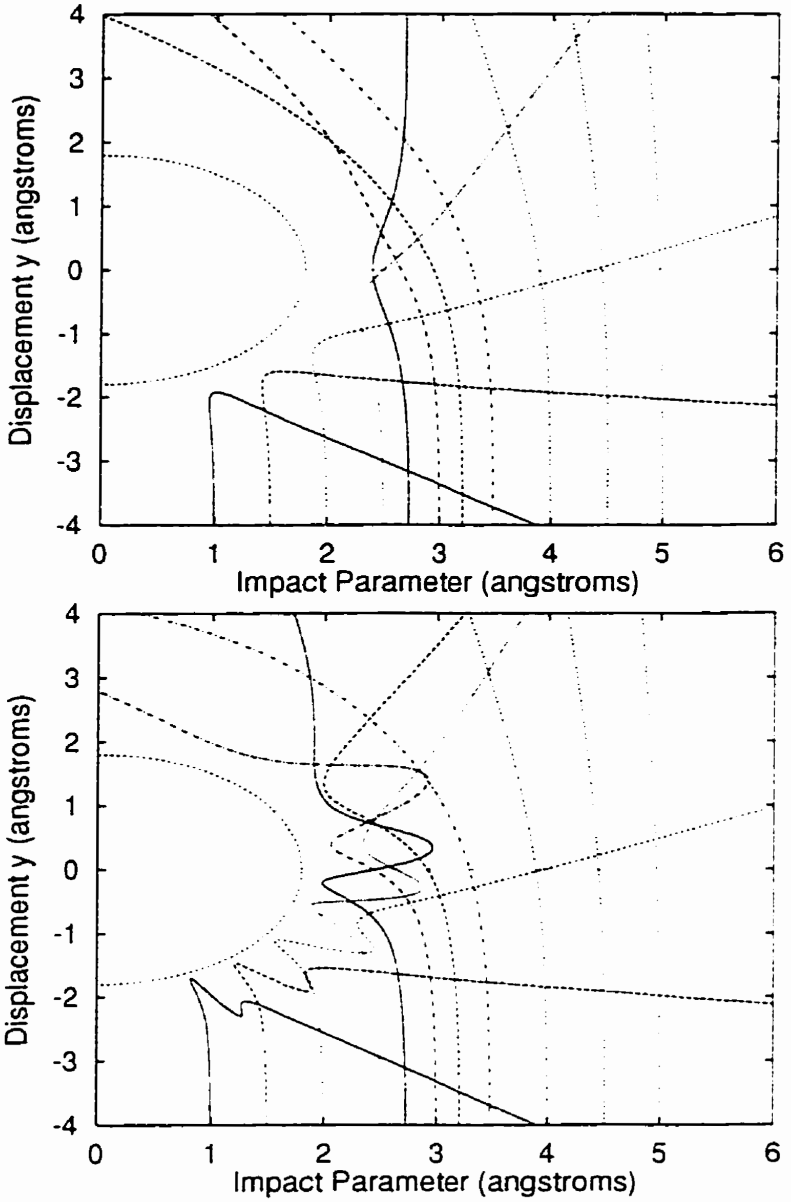

Figure 6.12:

Classical (top) and quantum (bottom) trajectories for He-He near closest approach for a velocity of 450 m/s.

Δ	20 Å
$\bar{q}_1$	2 Å
$\bar{q}_2$	-140 Å
$\bar{p}$	v m cm^{-1} 0.1 ns/Å

Table 6.4: Gaussian parameters

$r < r_0 = 1.8$ Å. It is seen that trajectories are significantly scattered only for small impact parameters, usually $b \sim b_{rainbow} + (b_{rainbow} - b_{glory})$. This region must be treated accurately in the phase space average to obtain meaningful results. As well, it can be seen that for the b's in this region the y integral can involve functions that are changing rapidly (if the time at which the average is needed puts the particle near closest approach). These considerations are discussed in detail along with associated errors with the numerical integration in Appendix C. The next sections examine the structure of typical functions which are to be integrated.

6.3.1 y Dependence

In this section we will examine typical functions that are to be averaged for structure in y. The range of the y integration was taken to be [-240,-70]. This Gaussian is isolated from the potential at $t = 0$ and we are treating a true scattering situation. This isolation of the Gaussian at $t = 0$ allows us to exploit composition rules which greatly simplifies the calculation.

The classical $g(t|z)$ satisfies the composition formula

$$g_\alpha(t_2|z) = g_\alpha(t_2 - t_1|g(t_1|z)) \,. \tag{6.8}$$

Taking derivatives yields composition formulas for ∇g and $\nabla\nabla g$.

$$\begin{aligned} \nabla g_{\alpha\beta}(t_2|z) &= \nabla g_{\alpha\gamma}(t_2 - t_1|g(t_1|z))\nabla g_{\gamma\beta}(t_1|z) \; . & (6.9) \\ \nabla\nabla g_{\alpha\beta\rho}(t_2|z) &= \nabla\nabla g_{\alpha\gamma\xi}(t_2 - t_1)|g(t_1|z))\nabla g_{\xi\rho}(t_1|z)\nabla g_{\gamma\beta}(t_1|z) \\ &\quad +\nabla g_{\alpha\gamma}(t_2 - t_1|g(t_1|z))\nabla\nabla g_{\gamma\beta\rho}(t_1|z) \; . & (6.10) \end{aligned}$$

Consider a trajectory with fixed impact trajectory b and momentum $\bar{p}$. For this impact parameter, there is a y_n for which at all $y < y_n$ the potential is essentially zero. The initial y for the trajectory will be one of the $y < y_n$. Let t_n be the time it takes to reach y_n from y.

$$t_n(y) = t_n = (y_n - y)m/\bar{p} \; . \tag{6.11}$$

For $t < t_n$ the trajectory is in a region where the potential is essentially zero, and we can use the free particle results to define g, ∇g, and $\nabla\nabla g$. For $t \geq t_n$, Equations (6.8)-(6.10) can be used by identifying $t_1 = t_n$, $t_2 = t$, and $z_n = g(t_n|z)$ and we have

$$\begin{aligned} g_\alpha(t|z) &= g_\alpha^{(y_n)}(t - t_n|z_n) \; , \\ \nabla g_{\alpha\beta}(t|z) &= \nabla g_{\alpha\gamma}^{(y_n)}(t - t_n)|z_n)\nabla g_{\gamma\beta}^{\text{free}}(t_n|z) \; , \\ \nabla\nabla g_{\alpha\beta\rho}^{(y_n)}(t|z) &= \nabla\nabla g_{\alpha\gamma\xi}(t - t_n|z_n)\nabla g_{\xi\rho}^{\text{free}}(t_n|z)\nabla g_{\gamma\rho}^{\text{free}}(t_n|z) \; . & (6.12) \end{aligned}$$

The function $z_\alpha^{(2)}$ has the same form of the composition rules as g_α in the zeroth order approximation.

$$\begin{aligned} z_\alpha^{(2)}(t|z) &= 0 \; , \; t \leq t_n \\ &= z_\alpha^{(2)(y_n)}(t - t_n|z_n) & (6.13) \end{aligned}$$

This structure is useful to us since for a wave packet which is isolated from the potential at $t = 0$ the z_n which appear in Equations (6.12) are the same for a fixed

Percentage Error		
$\langle \gamma^{(0)}_{0.373}(g_5) \rangle$	$\langle \gamma^{(2)}_{0.373}(g_5) \rangle$	$\langle \gamma^{(0)}_{0.373}(\partial^2_p g_5) \rangle$
5.0×10^{-8}	1.1×10^{-6}	4.4×10^{-7}

Table 6.5:

Accuracy of zeroth order perturbation scheme

impact parameter. For a given impact parameter b_i, the dynamics of g, ∇g, and $\nabla\nabla g$ need only be solved from differential equations for the trajectory with the largest g. All other trajectories that begin with impact parameter b_i can be defined via the time shift composition rules (Equation (6.12)).

Of course, the potential is never truly zero, even at large distances - decaying as $1/r^6$ for the Lennard Jones potential. The z_n are not identical for different g's with the same impact parameter. Table 6.5 examines this *zeroth order perturbation* approximation for a typical function, g_5. The potential used was helium, with an initial velocity of 600 m/s. The columns represent the quantity $100 \times (A_1 - A_2)/A_1$, where A_1 is the result from solving ordinary differential equations for each trajectory, and A_2 is the result from using the zeroth order perturbation approximation. We can see that the wavepacket treated in this thesis is far enough removed from the potential at $t = 0$ that this approximation is valid. This zeroth order approximation reduces the time of the calculation by a factor of 17, which was the motivation for its inclusion.

Figures 6.13 and 6.14 show the structure of typical functions that have to be integrated at five times during the collision. These graphs show the functions (cf.

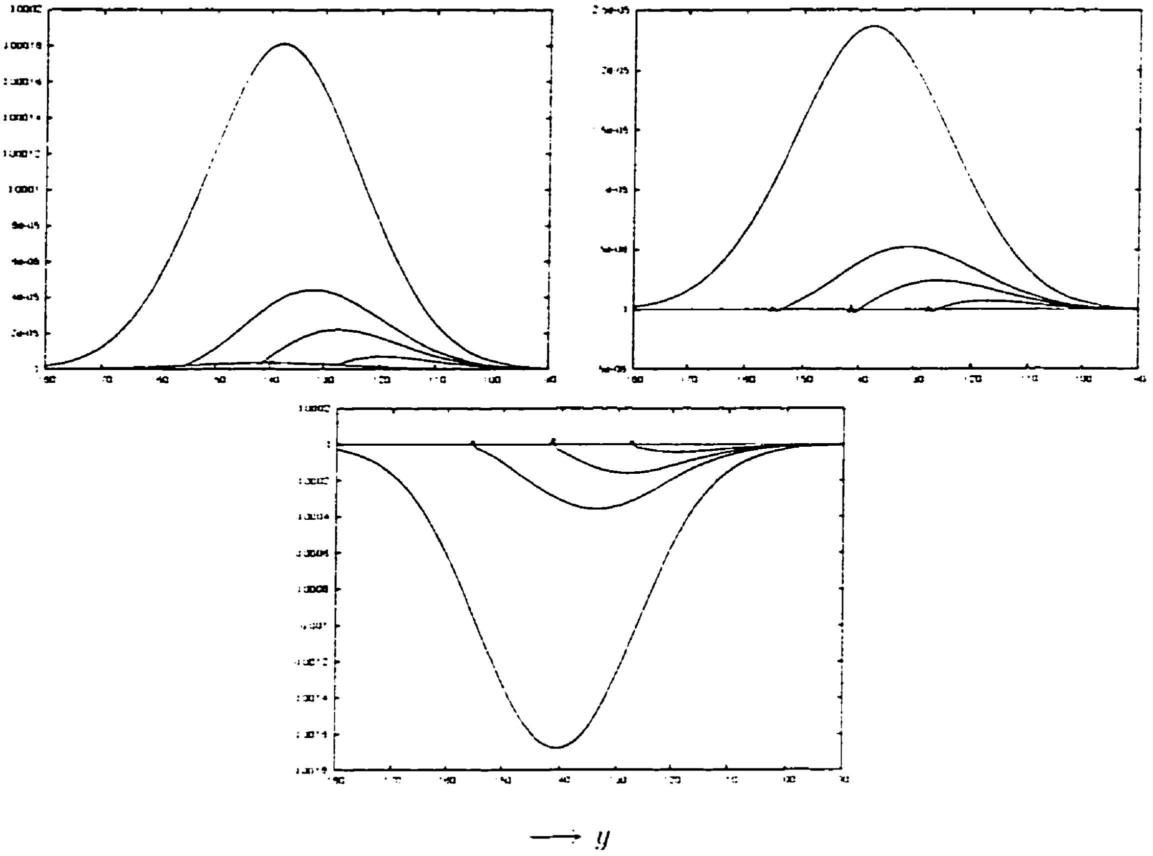

Figure 6.13:

F_{y_1} (cf. Equation (6.14)) as a function of y, for $b = 1.7362$Å. Left-right-top-bottom: Classical part, first Moyal correction, momentum expansion correction. The system is helium at velocity = 500 m/s. All plots are given for the function at the five times 0.0, 0.252, 0.280, 0.308 and 0.448 $\times 10^{-10}$ s. See text for discussion.

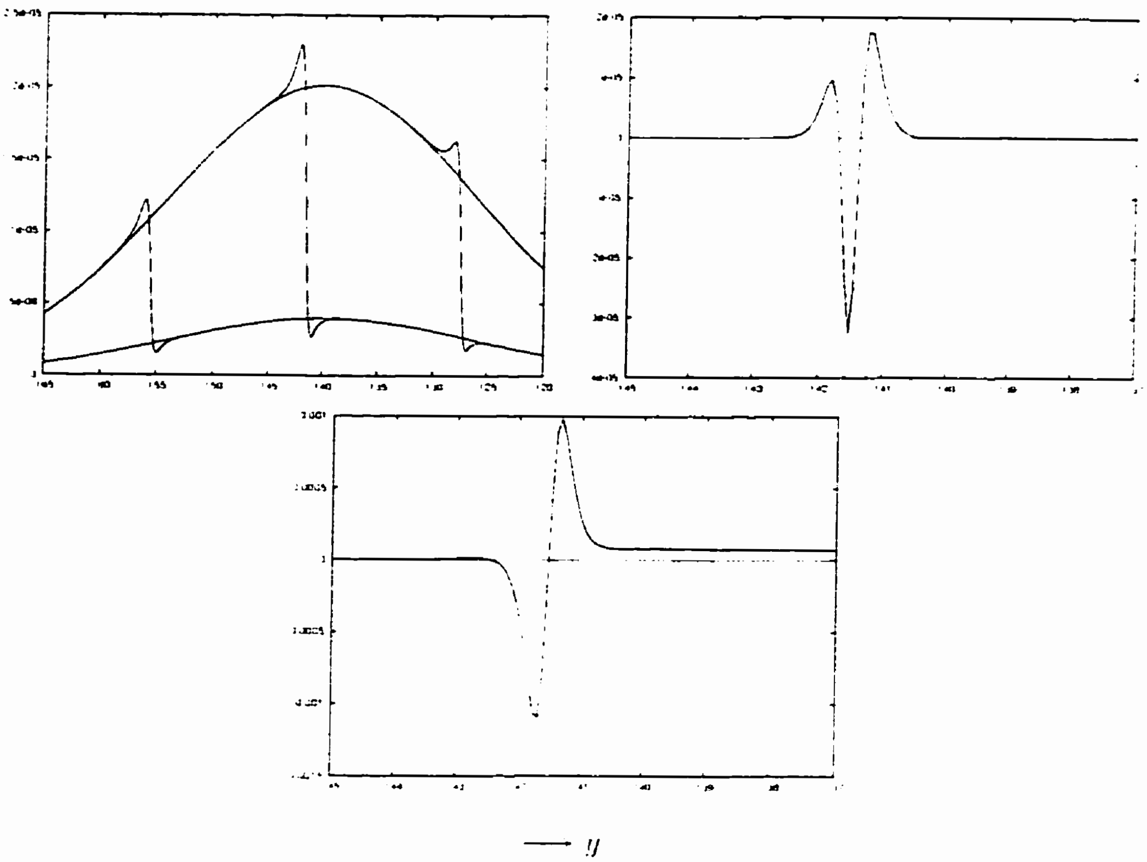

Figure 6.14:

F_{gs} (cf. Equation (6.14)) as a function of y, for $b = 1.7362$Å. Left-right-top-bottom: Classical part, first Moyal correction, momentum expansion correction. The system is helium at velocity = 500 m/s. The classical part is given for the function at the five times 0.0, 0.252, 0.280,0.308 and 0.448 $\times 10^{-10}$ s. The Moyal and momentum correction are given at 0.280 $\times 10^{-10}$ s. See text for discussion.

Equation (5.120))

$$F_{g_\alpha} = \frac{\epsilon^{-\Delta^{-2}\bar{R}^2}}{\pi^{3/2}\Delta^3} b\, exp\left\{-\Delta^{-2}(R^2 - 2y\bar{q}_2)\right\} \Omega_{\alpha\nu}(2\Delta^{-2}b\bar{q}_1) S'_\nu(t,b,y,0) \,. \tag{6.14}$$

where $S'_\nu(t,b,y,0)$ is one of (cf. Equation (5.109)) $\gamma_t^{(0)}(g_\alpha(t|z_0))$ (classical part), $\frac{\hbar^2}{2}\gamma_t^{(2)}(g_\alpha(t|z_0))$ (first Moyal correction), or $\left(\frac{\hbar}{2\Delta}\right)^2 \partial_p^2\gamma_t^{(0)}(g_\alpha(t|z_0))$ (momentum expansion correction).

Figure 6.13 shows all three contributions to the average value for the coordinate $g_1(t|z_0)$. The first graph in Figure 6.13 is the classical contribution. The large Gaussian curve is the function at $t = 0.448 \times 10^{-10}$ s; the next largest curve is the function at time $t = 0.308 \times 10^{-10}$ s; etc. At $t = 0$ this function is simply a scaled version of the Gaussian being scattered. For $t > 0.448 \times 10^{-10}$ s, $\gamma_t^{(0)}(g_1(t|z_0))$ will be linear in time. This results in a function which grows so that the area under the curve grows linearly with time. The shape of the function for these large times is simply a scaled version of the original Gaussian shape.

The second graph in Figure 6.13 is the first Moyal correction to the average value for the coordinate $g_1(t|z_0)$. The five curves represent the function at the five times in a manner analogous to the classical part. For this function, however, we see the appearance of a 'spike' structure for times during which the significantly nonzero portion of the Gaussian is located near the potential. This is directly due to the spike structure which occurs in the functions $z_1^{(2)}(t|z_0)$ (cf. Figure 6.5). The function $z_1^{(0)}(t|z_0)$ has a much smoother profile near closest approach and this translates into a smooth classical part. For large times we see that the spike structure is given a small weight by the Gaussian and this function is a scaled version of the original Gaussian which will grow in a manner that ensures the area under the curve grows linearly with time. At $t = 0$ this function is strictly zero, as the quantum corrections are zero at $t = 0$.

The final graph in Figure 6.13 is the momentum expansion correction to the average value for the coordinate $g_1(t|z_0)$. The five curves represent the function at the five times. The spike structure in this function does not oscillate as much as in the Moyal correction, and is due to the structure exhibited at closest approach by the functons $\nabla\nabla g_{1\alpha\alpha}(t|z_0)$ for $\alpha = 4, 5, 6$ (cf. Figure 6.3). The same large time growth that was present in the classical and Moyal parts is seen in the momentum correction. At $t = 0$ this function is zero, however this is not true for all functions - most notably, the rank two tensors g_α^2 with $\alpha = 4, 5, 6$ have a momentum correction part which is equal to $\frac{1}{2}(\frac{\hbar}{\Delta})^2$ at $t = 0$.

Figure 6.14 contains the classical part of the average for $g_5(t|z_0)$. The structure which is present here at times when the Gaussian is near the potential center is due to a rapidly changing momentum along the trajectories at those times (cf. Figure 6.6). The smooth upper and lower curves denote the integrand at the pre-collision time $t = 0$ and the post-collision time $t = 0.448$, respectively. The upper curve is determined solely by the Wigner function. Its slow variation is a result of the large value of Δ. The $\gamma_t^{(0)}$ plot is read as follows: for the intermediate time 0.280×10^{-10} s, the y function begins on the top branch ($y < -145$ Å). In a region around $y = -141$ Å the trajectories are undergoing active interaction with the potential and here the curve shifts to the smooth lower branch. In this manner the orginal $t = 0$ function which must be integrated is changed to a new function at later times by the movement of the Gaussian over the potential. After a large elapsed time the function becomes constant.

The behaviour of the Moyal correction to the average value for $g_5(t|z_0)$ for the single time 0.280×10^{-10} s is also shown in Figure 6.14, and is similar in structure to that for the classical part of the average. Here, however, the structure near closest approach is determined by the action of $z_5^{(2)}(t|z_0)$, which is much more oscillatory (cf. Figure 6.6 for an example of the differences in structure for the $z^{(0)}$ and $z^{(2)}$ parts of the quantum trajectory for momentum).

The momentum expansion correction for $t = 0.280 \times 10^{-10}$ s is shown in Figure 6.14 and is similar to the Moyal correction in structure.

6.3.2 b Dependence

Once all the y integrations have been performed, a b integration must be performed. The functions which are described in this section are obtained after the y integration discussed in the previous section is done, and thus are not for a fixed y value. The functions are of the form

$$F_{g_\alpha} = \frac{e^{-\Delta^{-2}\bar{R}^2}}{\pi^{3/2}\Delta^3} \int_{-\infty}^{\infty} dy\, b\, exp\left\{-\Delta^{-2}(R^2 - 2y\bar{q}_2)\right\} \Omega_{\alpha\nu}(2\Delta^{-2}b\bar{q}_1) S'_\nu(t, b, y, 0) . \tag{6.15}$$

where $S'_\nu(t, b, y, 0)$ is one of (cf. Equation (5.109)) $\gamma_t^{(0)}(g_\alpha(t|z_0))$ (classical part), or $\frac{\hbar^2}{2}\gamma_t^{(2)}(g_\alpha(t|z_0))$ (first Moyal correction), or $\left(\frac{\hbar}{2\Delta}\right)^2 \partial_p^2 \gamma_t^{(0)}(g_\alpha(t|z_0))$ (momentum expansion correction).

Figures 6.15 and 6.16 show the types of functions which must be integrated. For both $g_1(t|z_0)$ and $g_5(t|z_0)$ the classical part of the average has a large Gaussian shape for large impact parameters. This is of course expected due to the large size of our Gaussian. Any modification to the functions for $t > 0$ occur near $b_{rainbow}$, for which trajectories (classical and quantum alike) are significantly scattered. From the graph of the classical part of the average for $g_1(t|z_0)$ we can identify $b_{glory} \sim 2.65$ Å, and $b_{rainbow} \sim 3.15$ Å. Forward glory impact parameter will result in $g_1(t|z_0)$ being essentially constant for all time, and rainbow impact parameter will result in a minimum of $g_1(t|z_0)$.

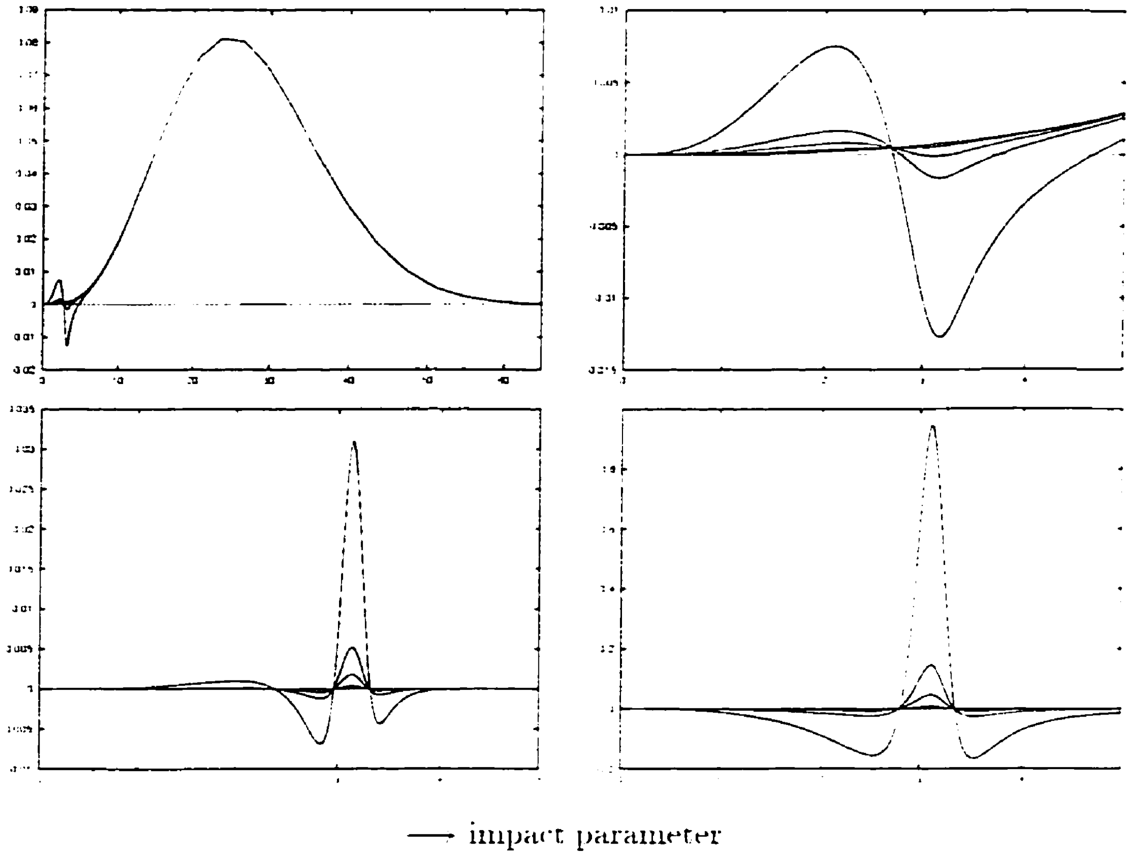

Figure 6.15:

F_{g_1} (Equation (6.15)) as a function of b. Left-right-top-bottom: Classical part, zoom of classical part, first Moyal correction, momentum expansion correction. The system is helium at velocity = 500 m/s. All plots are given for the function at the five times 0.0, 0.252, 0.280, 0.308 and 0.448 $\times 10^{-10}$ s. See text for discussion.

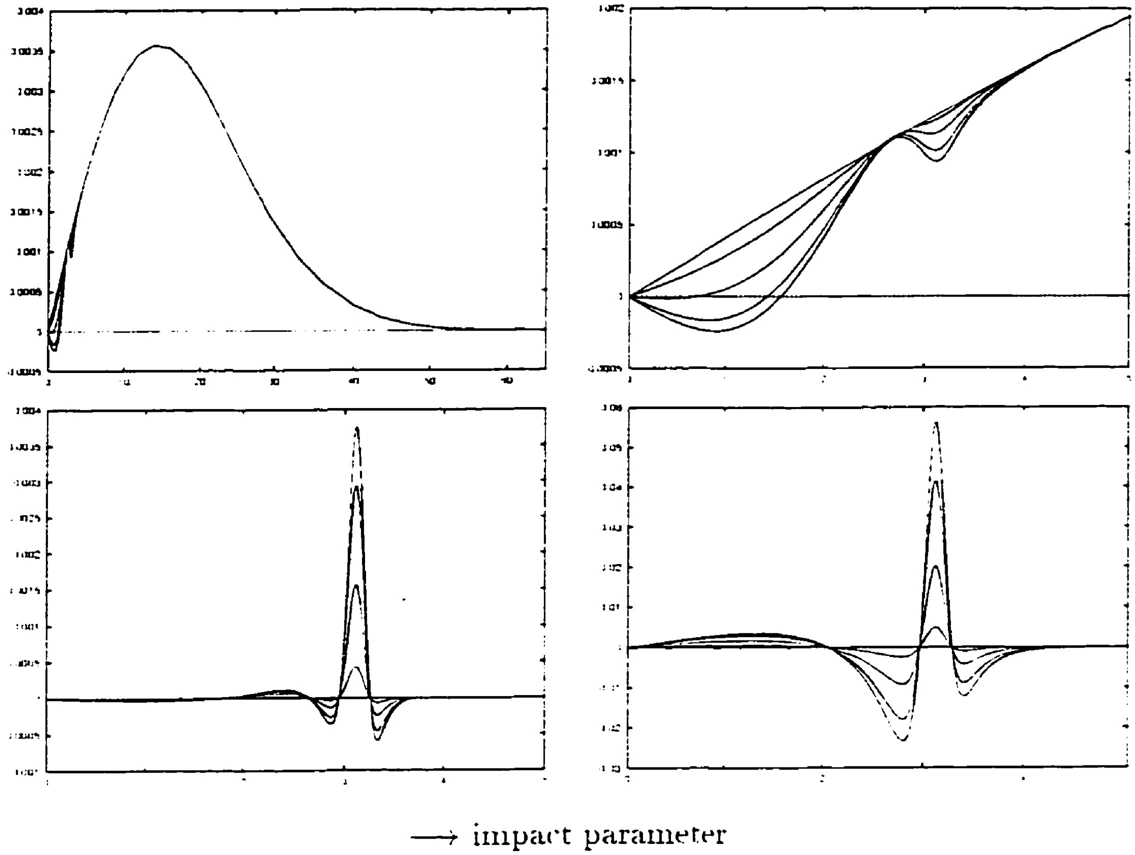

Figure 6.16:

F_{gs} (Equation (6.15)) as a function of b. Left-right-top-bottom: Classical part, zoom of classical part, first Moyal correction, momentum expansion correction. Initial conditions given by velocity = 500 m/s. All plots are given for the function at the five times 0.0, 0.252, 0.280, 0.308 and 0.448 $\times 10^{-10}$ s. See text for discussion.

The Moyal and momentum corrections both show similar behaviour. They begin to have significant structure near b_{glory}, and they have a maximum near $b_{rainbow}$ (in fact, always for a b slightly smaller). The Moyal correction is seen to be significantly nonzero only for impact parameters which are less than $2b_{rainbow} - b_{glory}$. In fact, for helium at a velocity of 450 m/s, $\sim 90\%$ of the total value of $\langle\gamma_t^{(2)}(g_i)\rangle$ is contained in $b \in [0, 2b_{\mathrm{rainbow}} - b_{glory}]$. However, the momentum correction in general can have support at larger impact parameters and the large degree of cancellation which occurs for momentum correction integrals makes these contributions important.

6.4 Results

In this section we will examine the data that were obtained in a number of different ways.

The average value for a function is separated into contributions from three sources, the classical part, the Moyal correction, and the momentum expansion correction (cf. Equation (5.108)-(5.111))

$$\langle\gamma_t^{(0)}(A)\rangle , \quad \frac{\hbar^2}{2}\langle\gamma_t^{(2)}(A)\rangle , \quad \left(\frac{\hbar}{2\Delta}\right)^2 \langle\partial_p^2\gamma_t^{(0)}(A)\rangle .$$

The spread in g_i, $i = 1,6$ is given by

$$\mathrm{spread}_i = \langle\hat{g}_i{}^2(t)\rangle - \langle\hat{g}_i(t)\rangle^2 . \qquad (6.16)$$

which is expanded to $O(\hbar^4)$ as

$$\mathrm{spread} = \mathrm{Classical} + \mathrm{Moyal} + \mathrm{Momentum} + O(\hbar^4)$$

where

$$\mathrm{Classical} \;=\; \langle\gamma_t^{(0)}(g_i^2)\rangle - \left(\langle\gamma_t^{(0)}(g_i)\rangle\right)^2 .$$

$$\begin{aligned} \text{Moyal} &= \frac{\hbar^2}{2}\left[\langle\gamma_t^{(2)}(g_i^2)\rangle - 2\langle\gamma_t^{(2)}(g_i)\rangle\,\langle\gamma_t^{(0)}(g_i)\rangle\right] , \\ \text{Momentum} &= \left(\frac{\hbar}{2\Delta}\right)^2\left[\langle\partial_p^2\gamma_t^{(0)}(g_i^2)\rangle - 2\langle\partial_p^2\gamma_t^{(0)}(g_i)\rangle\,\langle\gamma_t^{(0)}(g_i)\rangle\right] . \end{aligned} \qquad (6.17)$$

Error estimates are provided using the notation 12.3456(7) which means that the calculation was done using two different b grids and the result from the first calculation was 12.3456 and the result from the second was 12.3457.

6.4.1 Correction Dependence on Time

At $t = 0$ the Moyal $\gamma_t^{(2)}$ corrections are always strictly zero. The momentum correction, however, can be nonzero at time zero. How these corrections vary with time will be examined for helium with a velocity of 300 m/s. The state of this system was found at a total of twenty-six times. This required five runs of the program with different times for each run.

The collision occurs from $t = 0$ to $t = \infty$, however, there is a time interval during which the Gaussian is near the potential and the collision is actively occuring. This time interval was arbitrarily decided to be when the classical average momentum in the $\hat{e}_2$ direction ($\langle\gamma_t^{(0)}(g_5)\rangle$) is not constant to a part in 10^{-5}. This gives an interval from 0.288 to 0.637 $\times 10^{-10}$ s as the collision time. For $t < 0.288 \times 10^{-10}$ s the Gaussian has yet to have significant interaction with the potential, and we are in a *pre-collision time interval*. For $t > 0.637 \times 10^{-10}$ s the Gaussian has effectively completed its interaction with the potential, and we are in an *asymptotic time region*. The time of closest approach for the Gaussian is taken as the time when the classical average R^2, $\langle\gamma_t^{(0)}(g_1^2 + g_2^2)\rangle$, is a minimum. This results in a classical time of closest approach of $t_{cca} = 0.467 \times 10^{-10}$ s.

Times reported include three pre-collision times. fourteen collisional times. and nine asymptotic times. Tables 6.6-6.12 contain the data.

Note that the spread $\sim \langle g_i^2 \rangle$. and that the labeling we have employed in Equation (6.17) is appropriate since the classical part of the spread corresponds to the $\gamma^{(0)}$ part. the Moyal with $\gamma^{(2)}$. and the momentum with $\partial_p^2\gamma^{(0)}$. Table 6.11 can be compared with Table A.1 to illustrate how this wave packet spreads relative to a free wave packet. It is seen that at $t = 0.420 \times 10^{-10}$s the wave packet is still behaving essentially as a free wave packet. By $t = 0.530 \times 10^{-10}$s. however. the wave packet has interacted sufficiently with the potential to deviate markedly from the free case.

The product of the spread in the coordinate g_i and the associated momentum g_{i+3} yields the Heiseinberg uncertainty principle (HUP). which must be obeyed by quantum systems. Table 6.12 contains the HUP as a function of time for $i = 1$. At $t = 0$ the HUP is satisfied by the minimum relation. as expected since we have a Gaussian wave packet. As time progresses. the HUP product is always greater than $\hbar^2/4$. These results demonstrate the quantum nature of our system. It is interesting to note that at $t = 0$ the contribution to the spread in coordinate is entirely contained in the classical part of the average. and the spread in the momentum is entirely from the momentum correction. This result highlights the fact that the momentum correction is fundamentally different from the Moyal correction. The classical part and momentum correction are both determined by $\gamma_t^{(0)}$ evolution (which can be nonzero at $t = 0$). whereas the Moyal correction is determined by $\gamma_t^{(2)}$ evolution (which is always zero at $t = 0$). The momentum correction could. in fact. have been grouped with the classical part to decrease the time of calculation.

Figures 6.17 and 6.19 are graphs of the average values with respect to time. Graphs of the spread are not included as they are similar to the graphs for $\langle g_i^2 \rangle$.

The contribution to the total average value from the momentum correction is seen to be small, and the use of the Taylor expansion for our squeezed Gaussian is seen to be valid.

From Tables 6.9 and 6.10 it is obvious that the asymptotic behaviour with respect to time for all three contributions to the average value of a strictly momentum based operator are constant. Since the data points for the asymptotic region occur at equally spaced points, the asymptotic time behaviour of coordinate observables is best presented in terms of *forward difference tables*. The forward differences of a function c_j defined at equally spaced j are defined by the recursion relations

$$\begin{aligned} \Delta^{(1)}c_j &= \Delta_j^{(1)} = c_{j+1} - c_j \, , \\ \Delta^{(i)}c_j &= \Delta_j^{(i)} = \Delta^{(i-1)}(c_{j+1} - c_j) \, . \end{aligned} \tag{6.18}$$

If $c_j \to j^k$ as $j \to \infty$, the forward differences exhibit the behaviour

$$\Delta^{(k)}c_j \to \text{constant}, \ j \to \infty \tag{6.19}$$

$$\Delta^{(k+1)}c_j \to 0, \ j \to \infty \, . \tag{6.20}$$

Table 6.13 shows that the average values of g_1 have the asymptotic time dependence

$$\langle \gamma_t^{(0)}(g_1)\rangle \sim \langle \gamma_t^{(2)}(g_1)\rangle \sim \langle \partial_p^2 \gamma_t^{(0)}(g_1)\rangle \sim t, \ t \to \infty \, . \tag{6.21}$$

Table 6.14 shows that the average values of g_1^2 have the asymptotic time dependence

$$\langle \gamma_t^{(0)}(g_1^2)\rangle \sim \langle \gamma_t^{(2)}(g_1^2)\rangle \sim \langle \partial_p^2 \gamma_t^{(0)}(g_1^2)\rangle \sim t^2, \ t \to \infty \, . \tag{6.22}$$

The relative size of the corrections is of course important, and Figure 6.20 shows how the relative size of the corrections for typical observables grow.

In the case of g_2^2 both the Moyal and momentum correction do not grow to large size after the collision. The Moyal correction only begins to become significantly

Time (10^{-10} s)	$\langle\gamma_t^{(0)}(g_1)\rangle$	$\frac{\hbar^2}{2}\langle\gamma_t^{(2)}(g_1)\rangle$ (Å)	$\left(\frac{\hbar}{2\Delta}\right)^2\langle\partial_p^2\gamma_t^{(0)}(g_1)\rangle$	Total
0	1.99999999	10^{-48}	10^{-41}	2.000000
0.240	1.99999997	10^{-11}	10^{-11}	1.999999
0.288	1.99999994	-7.95×10^{-8}	-1.4×10^{-8}	1.999999
0.335	1.99999664	-4.98×10^{-6}	-1.9×10^{-7}	1.999990
0.383	1.99993770	-1.20800×10^{-4}	5.2477×10^{-6}	1.999822
0.393	1.99989721	-2.11708×10^{-4}	1.1896×10^{-5}	1.999697
0.403	1.99983567	-3.58311×10^{-4}	2.4146×10^{-5}	1.999501
0.420	1.99966589	$-7.98522(17) \times 10^{-4}$	$6.610(08) \times 10^{-5}$	1.998933
0.467	1.99842729	$-4.70509(10) \times 10^{-3}$	$4.9944(37) \times 10^{-4}$	1.994221
0.513	1.99572925	$-1.526557(5) \times 10^{-2}$	$1.6782(79) \times 10^{-3}$	1.982142
0.530	1.99448274	-2.07157×10^{-2}	2.2570×10^{-3}	1.976024
0.540	1.99369158	-2.43041×10^{-2}	2.6279×10^{-3}	1.972015
0.550	1.99287781	-2.80775×10^{-2}	3.0106×10^{-3}	1.967811
0.572	1.99106629	-3.66938×10^{-2}	3.8624×10^{-3}	1.958238
0.593	1.98922311	-4.56498×10^{-2}	4.7267×10^{-3}	1.948300
0.615	1.98736920	-5.47450×10^{-2}	5.5936×10^{-3}	1.938222
0.637	1.98551236	-6.38871×10^{-2}	6.4606×10^{-3}	1.928082
0.658	1.98365489	-7.30419×10^{-2}	7.3275×10^{-3}	1.917942
0.680	1.98179774	-8.21994×10^{-2}	8.1948×10^{-3}	1.907793
0.693	1.98065459	-8.78353×10^{-2}	8.7282×10^{-3}	1.901547
0.707	1.97951089	-9.34714×10^{-2}	9.2611×10^{-3}	1.895301
0.720	1.97836774	-9.91073×10^{-2}	9.7946×10^{-3}	1.889055
0.733	1.9772250(2)	$-1.047432(1) \times 10^{-1}$	$1.0328(7) \times 10^{-2}$	1.882810
0.747	1.9760819(20)	$-1.103790(1) \times 10^{-1}$	$1.0861(0) \times 10^{-2}$	1.876564
0.760	1.97494842	-1.16015×10^{-1}	1.1395×10^{-2}	1.870338
0.773	1.97379527	-1.21651×10^{-1}	1.1928×10^{-2}	1.864125

Table 6.6:

Averages values for g_1 as a function of time.

The potential is helium, and the velocity is 300 m/s.

Time	$\langle\gamma_t^{(0)}(g_1^2)\rangle$	$\frac{\hbar^2}{2}\langle\gamma_t^{(2)}(g_1^2)\rangle$	$\left(\frac{\hbar}{2\Delta}\right)^2 \partial_p^2\langle\gamma_t^{(0)}(g_1^2)\rangle$	Total
(10^{-10} s)		(Å^2)		
0	203.999999	10^{-47}	10^{-20}	204.000
0.240	203.999999	10^{-8}	7.2252	211.225
0.288	204.000010	1.6×10^{-5}	10.4044	214.404
0.335	204.000820	0.0014375	14.1618	218.164
0.383	204.021979	0.0490329	18.5020	222.573
0.393	204.039325	0.0919187	19.4828	223.614
0.403	204.067939	0.166286	20.4900	224.724
0.420	204.157052	0.4137729(33)	22.22728(9)	226.797
0.467	205.054005	3.3304768(1)	27.45390(86)	235.838
0.513	208.121465	14.920349(52)	33.0245(3)	256.044
0.530	210.050856	22.7397	35.0358	267.826
0.540	211.457676	28.5872	36.2400	276.284
0.550	213.060448	35.3607	37.4408	285.808
0.572	217.228143	53.3699	40.0291	310.624
0.593	222.236977	76.1053	42.5986	340.940
0.615	228.498018	103.6643	45.1506	377.313
0.637	235.617078	136.0808	47.6866	419.385
0.658	243.728097	173.3645	50.2074	467.299
0.680	252.831361	215.5167	52.7111	521.059
0.693	258.926546	243.8776	54.2455	557.048
0.707	265.397474	274.0837	55.7767	596.014
0.720	272.244205	306.1331	57.3000	635.677
0.733	279.466707(42)	340.026(5)	58.818(21)	678.311
0.747	287.06498(501)	375.764(3)	60.330(3)	723.744
0.760	295.039032	413.346	61.836	770.221
0.773	303.388852	452.772	63.337	819.498

Table 6.7:

Averages values for g_1^2 as a function of time.

The potential is helium, and the velocity is 300 m/s.

Time (10^{-10} s)	$\langle \gamma_t^{(0)}(g_2^2) \rangle$	$\frac{\hbar^2}{2} \langle \gamma_t^{(2)}(g_2^2) \rangle$ (Å^2)	$\left(\frac{\hbar}{2\Delta}\right)^2 \langle \partial_p^2 \gamma_t^{(0)}(g_2^2) \rangle$	Total
0	19800.005	10^{-39}	10^{-19}	19800.005
0.240	4841.0157	10^{-9}	7.2252	4848.241
0.288	3089.0625	-5×10^{-5}	10.4044	3099.467
0.335	1750.3895	-0.003739	14.1610	1764.546
0.383	824.96414	-0.113305	18.4870	843.338
0.393	683.93542	-0.208330	19.4585	703.186
0.403	560.88665	-0.370421	20.4525	580.969
0.420	395.73034	-0.8992821(4)	22.15855(6)	416.989
0.467	198.03333	-6.909003(8)	27.31525(17)	218.439
0.513	387.96675	-30.251148(64)	33.4272(69)	391.143
0.530	549.10311	-45.8999	35.9706	539.174
0.540	669.27291	-57.5863	37.6041	649.291
0.550	807.05971	-71.1146	39.3204	775.265
0.572	1165.9323	-107.0648	43.3262	1102.194
0.593	1607.3463	-152.4425	47.7238	1502.628
0.615	2131.2829	-207.4542	52.5099	1976.339
0.637	2737.7367	-272.1746	57.6816	2523.244
0.658	3426.7062	-346.6257	63.2380	3143.318
0.680	4198.1911	-430.8110	69.1827	3836.563
0.693	4713.9649	-487.4581	73.0300	4299.537
0.707	5260.9884	-547.7948	77.0181	4790.212
0.720	5839.2593	-611.8169	81.1561	5308.598
0.733	6448.7751(76)	-679.526(4)	85.439(3)	5854.688
0.747	7089.5430(55)	-750.923(1)	89.869(1)	6428.489
0.760	7761.5622	-826.008	94.443	7029.997
0.773	8464.8272	-904.780	99.163	7659.210

Table 6.8:

Averages values for g_2^2 as a function of time.

The potential is helium, and the velocity is 300 m/s.

Time (10^{-10} s)	$\langle\gamma_t^{(0)}(g_4)\rangle$	$\frac{\hbar^2}{2}\langle\gamma_t^{(2)}(g_4)\rangle$	$\left(\frac{\hbar}{2\Delta}\right)^2\langle\partial_p^2\gamma_t^{(0)}(g_4)\rangle$	Total
	(10^{-5}(cm^{-1} 0.1 ns/Å))			
0	10^{-31}	10^{-46}	10^{-36}	10^{-31}
0.240	-0.000001670	10^{-7}	-2.8×10^{-6}	10^{-5}
0.288	-0.000117796	-1.4×10^{-4}	-1.6×10^{-5}	-0.0013
0.335	-0.003880639	-0.0062	-7.4×10^{-5}	-0.0485
0.383	-0.053800422	-0.1169	0.00782	-0.1629
0.393	-0.083411010	-0.1925	0.01506	-0.2608
0.403	-0.124592386	-0.3051	0.02682	-0.4029
0.420	-0.224270167(76)	-0.605312(4)	0.061155(60)	-0.7684
0.467	-0.70335908(13)	-2.4491268(3)	0.27991(87)	-2.8725
0.513	-1.19465186(94)	-5.085327(8)	0.55017(1)	-5.7300
0.530	-1.300399204	-5.8239	0.6082	-6.5161
0.540	-1.344534509	-6.1702	0.6316	-6.8831
0.550	-1.376437191	-6.4433	0.6477	-7.1720
0.572	-1.414840203	-6.8191	0.6645	-7.5694
0.593	-1.428932991	-6.9865	0.6689	-7.7465
0.615	-1.433101735	-7.0478	0.6695	-7.8114
0.637	-1.434097440	-7.0660	0.6694	-7.8307
0.658	-1.434289748	-7.0704	0.6693	-7.8354
0.680	-1.434318924	-7.0713	0.6693	-7.8363
0.693	-1.434324435	-7.0714	0.6693	-7.8363
0.707	-1.434324723	-7.0715	0.6693	-7.8363
0.720	-1.434325056	-7.0715	0.6693	-7.8363
0.733	-1.43432548(61)	-7.071484(0)	0.6693(2)	-7.8363
0.747	-1.43432555(67)	-7.071484(0)	0.6693(2)	-7.8363
0.760	-1.434325396	-7.0715	0.6693	-7.8363
0.773	-1.434325424	-7.0715	0.6693	-7.8363

Table 6.9:

Averages values for g_4 as a function of time.

The potential is helium, and the velocity is 300 m/s.

Time (10^{-10} s)	$\langle \gamma_t^{(0)}(g_4^2) \rangle$	$\frac{\hbar^2}{2} \langle \gamma_t^{(2)}(g_4^2) \rangle$ (10^{-5}(cm^{-1} 0.1 ns/Å)^2)	$\left(\frac{\hbar}{2\Delta}\right)^2 \partial_p^2 \langle \gamma_t^{(0)}(g_4^2) \rangle$	Total
0	10^{-43}	10^{-45}	0.352296884(0)	0.3523
0.240	0.000004952	1.8×10^{-7}	0.3523	0.3523
0.288	0.000342318	2.4×10^{-4}	0.3524	0.3537
0.335	0.011434595	0.0117	0.3551	0.3616
0.383	0.148427565	0.2238	0.3671	0.7393
0.393	0.225950579	0.3701	0.3679	0.9640
0.403	0.331088229	0.5891	0.3657	1.2860
0.420	0.5763920(1)	1.17707(8)	0.34783(5)	2.1013
0.467	1.6445565(6)	4.8558315(2)	0.1787(91)	6.6790
0.513	2.58799625(44)	10.26257(5)	-0.0165(55)	12.8340
0.530	2.765539736	11.8141	-0.04356	14.5360
0.540	2.835091136	12.5497	-0.05107	15.3337
0.550	2.882906075	13.1351	-0.05376	15.9642
0.572	2.935987916	13.9492	-0.05206	16.8268
0.593	2.952916441	14.3227	-0.04741	17.2282
0.615	2.957073206	14.4617	-0.04523	17.3742
0.637	2.957829172	14.5040	-0.04453	17.4176
0.658	2.957918961	14.5145	-0.04423	17.4282
0.680	2.957923423	14.5165	-0.04434	17.4301
0.693	2.957922154	14.5169	-0.04454	17.4303
0.707	2.957919861	14.5170	-0.04437	17.4305
0.720	2.957919767	14.5170	-0.04440	17.4305
0.733	2.95792026(51)	14.51701(699)	-0.04440(17)	17.4305
0.746	2.95792023(46)	14.51701(699)	-0.04440(17)	17.4305
0.760	2.957919816	14.5170	-0.04440	17.4305
0.773	2.957919814	14.5170	-0.04440	17.4305

Table 6.10:

Averages values for g_4^2 as a function of time.

The potential is helium, and the velocity is 300 m/s.

Time	Spread in g_1			
	Classical	Moyal	Momentum	Total
(10^{-10} s)	(Å^2)			
0	199.99996	10^{-47}	10^{-19}	199.99996
0.383	200.02223	0.04952	18.5020	218.5737
0.393	200.03974	0.09276	19.4828	219.6153
0.403	200.06860	0.1677	20.4900	220.7262
0.420	200.15839	0.4170	22.2270	222.8024
0.467	201.06029	3.3493	27.4519	231.8614
0.513	204.13853	14.9813	33.0176	252.1374
0.530	206.07289	22.8223	35.0268	263.9220
0.540	207.48287	28.6842	36.2294	272.2396
0.550	209.08889	35.4727	37.4288	281.9903
0.680	248.90384	215.8426	52.6786	517.4250
0.693	255.00355	244.2255	54.2110	553.4401
0.707	261.47901	274.4538	55.7400	591.6728
0.720	268.33027	306.5253	57.2613	632.1168
0.733	275.55729	340.0441	58.7769	674.7749
0.747	283.16008	376.2006	60.2869	719.6475

Table 6.11:

Spread for g_1 as a function of time.

The potential is helium, and the velocity is 300 m/s.

	Spread in g_4				Spread in g_1	HUP
Time	Classical	Moyal	Momentum	Total	Total	
(10^{-10} s)		(10^{-5}(cm^{-1} 0.1 ns/Å)^2)			(Å^2)	($\hbar^2/4$)
0	10^{-38}	10^{-40}	0.35229679	0.35229679	200.0000	1.000
0.383	0.14842754	0.2238	0.3671	0.7393	218.5737	2.293
0.393	0.22595051	0.3701	0.3679	0.9640	219.6153	3.005
0.403	0.33108807	0.5891	0.3657	1.2859	220.7262	4.028
0.420	0.57639148	1.1771	0.3478	2.1013	222.8024	6.644
0.467	1.6445516	4.8558	0.1787	6.6790	231.8614	21.978
0.513	2.5879820	10.2624	-0.01649	12.8339	252.1374	45.926
0.530	2.7655228	11.8140	-0.04355	14.5360	263.9220	54.448
0.540	2.8350731	12.5496	-0.05106	15.3336	272.2396	59.246
0.550	2.8828871	13.1349	-0.05375	15.9640	281.9903	63.891
0.680	2.9579029	14.5164	-0.04432	17.4300	517.4250	127.999
0.693	2.9579016	14.5167	-0.04452	17.4300	553.4401	136.908
0.707	2.9578993	14.5168	-0.04435	17.4303	591.6728	146.366
0.720	2.9578992	14.5168	-0.04438	17.4303	632.1168	156.371
0.733	2.9578997	14.5168	-0.04438	17.4303	674.7749	166.923
0.746	2.9578997	14.5168	-0.04438	17.4303	719.6475	178.024

Table 6.12:

Spread for g_4 as a function of time.

The potential is helium, and the velocity is 300 m/s.

Special unit: $\hbar^2/4 = 7.045938 \times 10^{-4}$ (cm^{-1} 0.1 ns)^2.

$F = g_1$

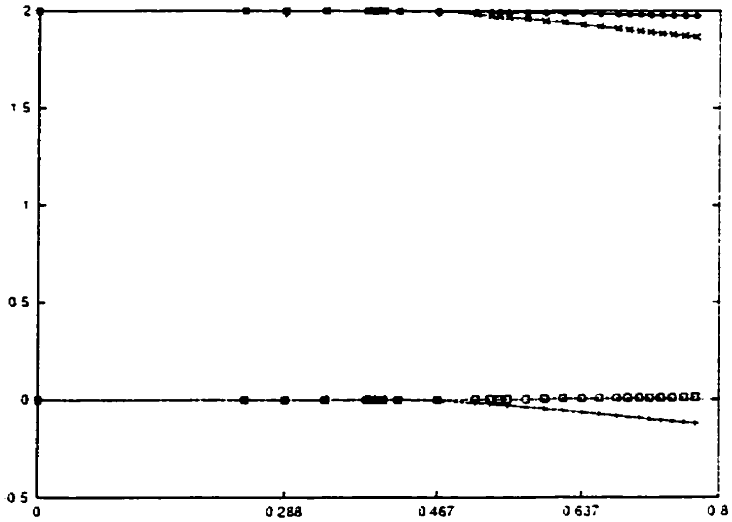

$F = g_1^2$

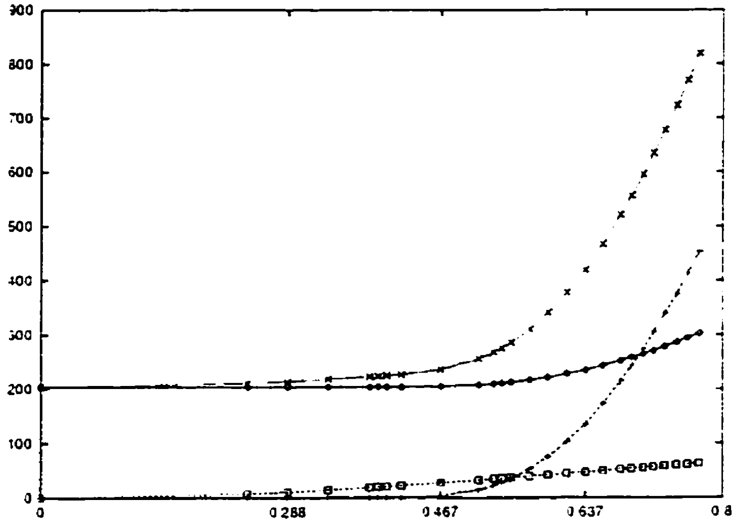

⟶ Time (10^{-10} s)

Figure 6.17:

The potential is helium, the velocity is 300 m/s.
◇: $\langle\gamma_t^{(0)}(F)\rangle$; +: $\frac{\hbar^2}{2}\langle\gamma_t^{(2)}(F)\rangle$; □: $\left(\frac{\hbar}{2\Delta}\right)^2\langle\partial_p^2\gamma_t^{(0)}(F)\rangle$; ×: total.

$F = g_4$

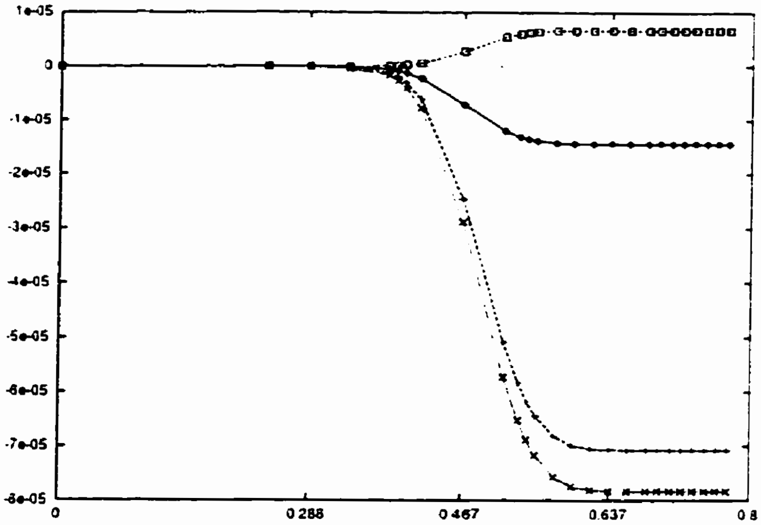

$F = g_4^2$

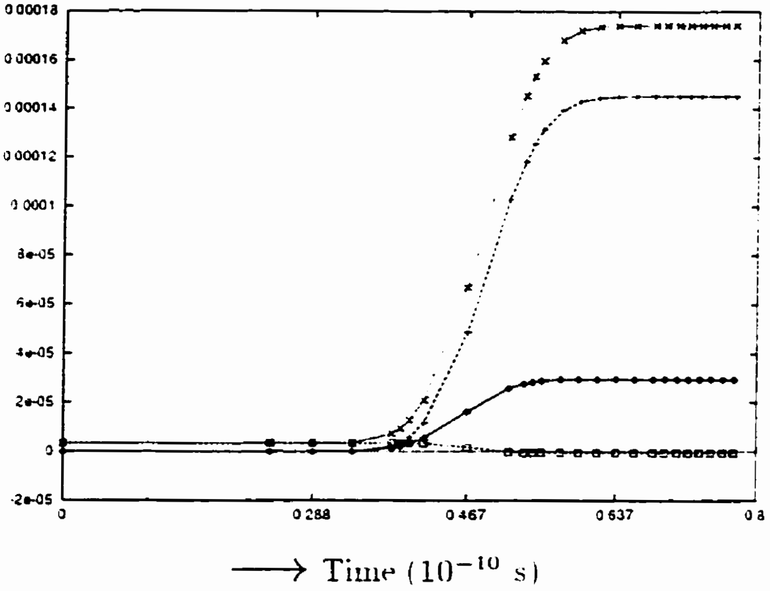

Figure 6.18:

The potential is helium, the velocity is 300 m/s.

◇: $\langle \gamma_t^{(0)}(F) \rangle$; +: $\frac{\hbar^2}{2} \langle \gamma_t^{(2)}(F) \rangle$; □: $\left(\frac{\hbar}{2\Delta}\right)^2 \langle \partial_p^2 \gamma_t^{(0)}(F) \rangle$; ×: total.

$F = q_2^2$

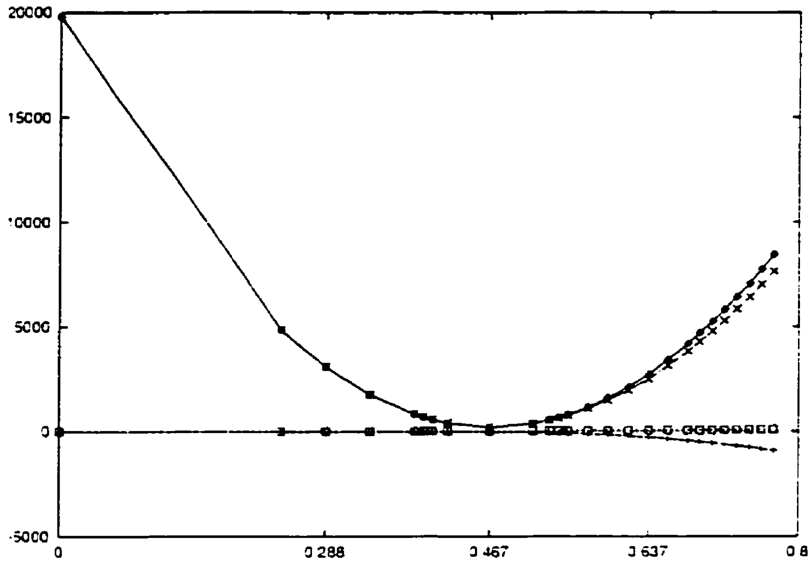

$\longrightarrow$ Time (10^{-10} s)

Figure 6.19:

The potential is helium, the velocity is 300 m/s.

◇: $\langle\gamma_t^{(0)}(F)\rangle$; +: $\frac{\hbar^2}{2}\langle\gamma_t^{(2)}(F)\rangle$, : □: $\left(\frac{\hbar}{2\Delta}\right)^2\langle\partial_p^2\gamma_t^{(0)}(F)\rangle$.

Time	$\langle \gamma_t^{(0)}(g_1) \rangle$	$\Delta_j^{(1)}$	$\frac{\hbar^2}{2}\langle \gamma_t^{(2)}(g_1) \rangle$	$\Delta_j^{(1)}$	$\left(\frac{\hbar}{2\Delta}\right)^2 \langle \partial_p^2 \gamma_t^{(0)}(g_1) \rangle$	$\Delta_j^{(1)}$
$(10^{-10}$ s)	A	10^{-3}A	10^{-2}A		10^{-3}A	
0.680	1.9817977	-1.1431	-8.220	-0.00563	8.195	0.0533
0.693	1.9806546	-1.1437	-8.783	-0.00564	8.728	0.0533
0.707	1.9795109	-1.1432	-9.347	-0.00564	9.261	0.0533
0.720	1.9783677	-1.1427	-9.911	-0.00563	9.794	0.0536
0.733	1.9772250	-1.1438	-10.474	-0.00564	10.329	0.0532
0.747	1.9760818	-1.1334	-11.038	-0.00563	10.861	0.0534
0.760	1.9749484	-1.1531	-11.601	-0.00564	11.395	0.0533
0.773	1.9737953		-12.165		11.928	

Table 6.13:

Forward difference tables. The potential is helium, and the velocity is 300 m/s.

nonzero once times are reached for which significant portions of the Gaussian have been scattered. During the time when the Gaussian is near closest approach the Moyal correction grows most rapidly. Although this collisional time appears to be the period of most rapid growth, the Moyal correction can aquire an asymptotic dependence which grows more rapidly than the classical part, causing the Moyal correction to dominate the average value at large times. This effect is seen for the observable g_1^2 (Figure 6.17), where the Moyal correction is seen to grow to exceed the classical part. Since g_1 at $t = 0$ corresponds to the impact parameter, this is not an unexpected result, as the classical part of the average for g_1 will remain near its initial value for our system. We see that the size of the momentum correction remains well bounded for all times.

Time	$\langle\gamma_t^{(0)}(g_1^2)\rangle$	$\Delta_j^{(1)}$	$\Delta_j^{(2)}$	$\frac{\hbar^2}{2}\langle\gamma_t^{(2)}(g_1^2)\rangle$	$\Delta_j^{(1)}$	$\Delta_j^{(2)}$
$(10^{-10}$ s)		Å			Å	
0.680	252.8314	6.0951	0.3759	215.517	28.360	1.847
0.693	258.9265	6.4710	0.3757	243.877	30.207	1.842
0.707	265.3975	6.8467	0.3758	274.084	32.049	1.844
0.720	272.2442	7.2225	0.3758	306.133	33.893	1.845
0.733	279.4667	7.5983	0.3757	340.026	35.738	1.844
0.747	287.0650	7.9740	0.3760	375.764	37.582	1.844
0.760	295.0390	8.3500		413.346	39.426	
0.773	303.3890			452.772		

Time	$\left(\frac{\hbar}{2\Delta}\right)^2\langle\partial_p^2\gamma_t^{(0)}(g_1^2)\rangle$	$\Delta_j^{(1)}$	$\Delta_j^{(2)}$
$(10^{-10}$ s)		Å	
0.680	52.7111	1.5344	-0.0032
0.693	54.2455	1.5312	-0.0790
0.707	55.7767	1.5233	-0.0056
0.720	57.3000	1.5177	-0.0056
0.733	58.8177	1.5121	-0.0057
0.747	60.3298	1.5064	-0.0057
0.760	61.8362	1.5007	
0.773	63.3369		

Table 6.14:

Forward difference tables. The potential is helium, and the velocity is 300 m/s.

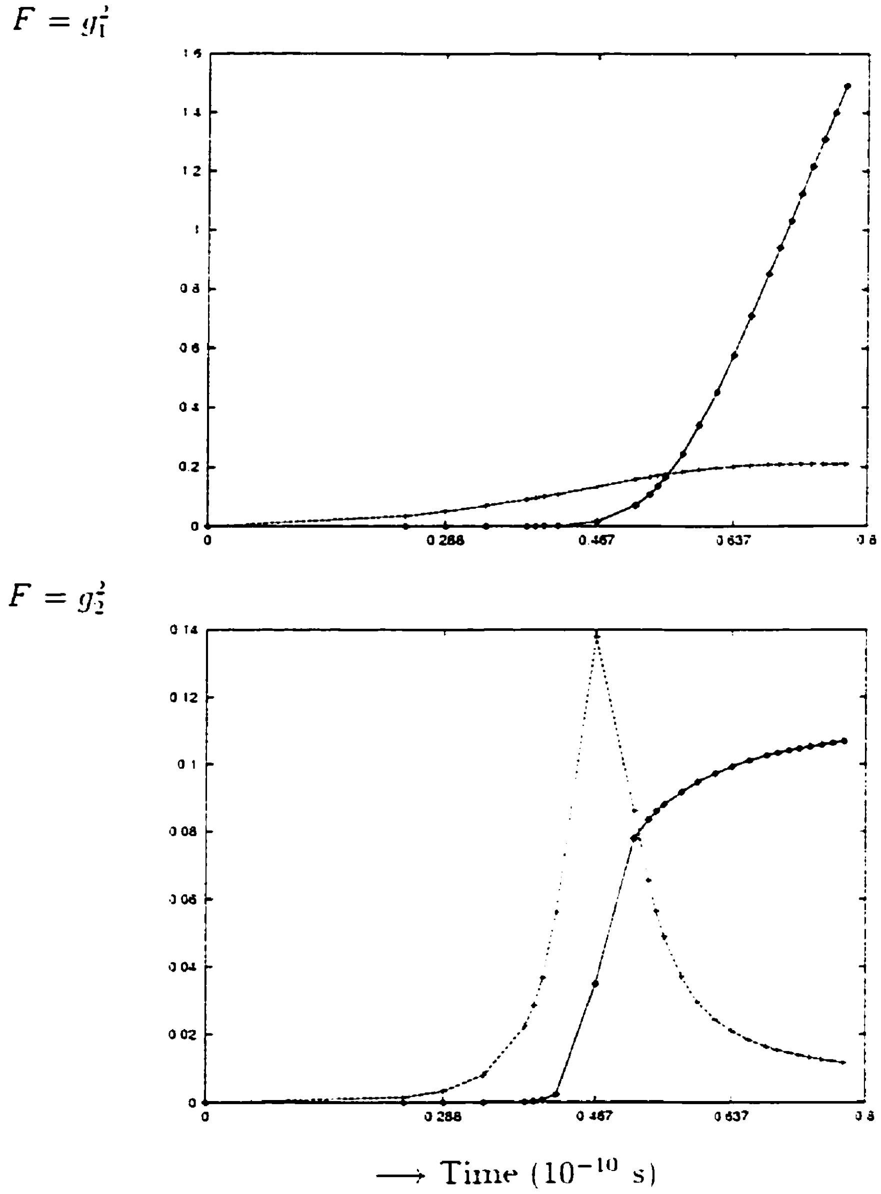

Figure 6.20:

Relative size of Moyal and momentum corrections:

$$\diamond : \left| \frac{\hbar^2}{2} \langle \gamma_t^{(2)}(F) \rangle / \langle \gamma_t^{(0)}(F) \rangle \right| \quad + : \left| \left(\frac{\hbar}{2\Delta} \right)^2 \langle \partial_p^2 \gamma_t^{(0)}(F) \rangle / \langle \gamma_t^{(0)}(F) \rangle \right|$$

6.4.2 Correction Dependence on Mass

The mass enters the Moyal and momentum expansion corrections in a complex manner, and its effect is not easy to predict without numerical analysis. In this section we will examine the effect of changing the mass on a system with fixed potential and velocity. We examine the corrections at the same final time after the collision is over. Changing the mass affects the kinetic energy, and so the average position of the Gaussian wave packet at this time will be different for different masses.

Increasing the Mass

In this section we examine the asymptotic behaviour of the corrections as mass approaches infinity. The six systems analyzed are helium at a velocity of 300 m/s for the following multiples of the mass of helium, $m = 2, 4, 6, 8, 10, 12, 14$. Two observables were chosen,

$$F_1 = g_1^2(t|z) + g_2^2(t|z) + g_3^2(t|z) , \tag{6.23}$$

$$F_2 = g_4^2(t|z) + g_5^2(t|z) + g_6^2(t|z) , \tag{6.24}$$

and the effect of increasing the mass was determined by examining the quantities in Table 6.15, which are at the time $t_f = 0.747 \times 10^{-10}$ s.

Figure 6.21 show that the momentum correction for both functions has the asymptotic value

$$F_i \sim m^{-2}, \; m \to \infty. \tag{6.25}$$

This is not at all surprising since the momentum correction involves two derivatives with respect to momentum. If the observable has a dependence of m^a on mass, then

Mass (m_{He})	$\frac{\frac{\hbar^2}{2}\langle\gamma_{t_f}^{(2)}(F_1)\rangle}{\langle\gamma_{t_f}^{(0)}(F_1)\rangle}$	$\frac{\left(\frac{\hbar}{2\Delta}\right)^2\langle\partial_p^2\gamma_{t_f}^{(0)}(F_1)\rangle}{\langle\gamma_{t_f}^{(0)}(F_1)\rangle}$	$\frac{\frac{\hbar^2}{2}\langle\gamma_{t_f}^{(2)}(F_2)\rangle}{\langle\gamma_{t_f}^{(0)}(F_2)\rangle}$	$\frac{\left(\frac{\hbar}{2\Delta}\right)^2\langle\partial_p^2\gamma_{t_f}^{(0)}(F_2)\rangle}{\langle\gamma_{t_f}^{(0)}(F_2)\rangle}$
2	3.6433×10^{-5}	6.8579×10^{-3}	2.0711×10^{-7}	1.0489×10^{-3}
4	1.0496×10^{-5}	1.7129×10^{-3}	9.2128×10^{-9}	2.6224×10^{-4}
6	4.8327×10^{-6}	7.6112×10^{-4}	1.8778×10^{-9}	1.1655×10^{-4}
8	2.7537×10^{-6}	4.2810×10^{-4}	6.6416×10^{-10}	6.5560×10^{-5}
10	1.7708×10^{-6}	2.7398×10^{-4}	3.0960×10^{-10}	4.1958×10^{-5}
12	1.2311×10^{-6}	1.9026×10^{-4}	1.7168×10^{-10}	2.9138×10^{-5}
14	9.0378×10^{-7}	1.3979×10^{-4}	1.0514×10^{-10}	2.1407×10^{-5}
16	6.9075×10^{-7}	1.0703×10^{-4}	6.9910×10^{-11}	1.6390×10^{-5}
18	5.4452×10^{-7}	8.4571×10^{-5}	4.9356×10^{-11}	1.2950×10^{-5}

Table 6.15:

Effect of increasing the mass on averages values. The potential is helium. the results are at $t = 0.747 \times 10^{-10}$ s for $v = 300$ m/s. Mass unit is $m_{\mathrm{He}} = 4.0026$ amu.

we have

$$\frac{\partial_p^2\gamma_t^{(0)}(O)}{\gamma_t^{(0)}(O)} \sim \frac{m^{a-2}}{m^a} \sim m^{-2}\ .$$

This is not an asymptotic result. it applies for any value of the mass.

Figure 6.22 shows that the Moyal correction for the function F_1 is asymptotic to m^{-2}. The Moyal correction for F_2. however. seems to be asymptotic to m^{-4}.

Decreasing the Mass

To examine the effect of decreasing the mass. we determined the corrections for eight systems - helium at a velocity of 600 m/s for the masses taken to be the following fractions of the mass of helium. $m = 24/16. 16/16. 12/16. 8/16. 7/16. 6/16. 5/16. 4/16$. Table 6.16 contains the data. and Figures 6.23-6.24 are plots for F_1 and

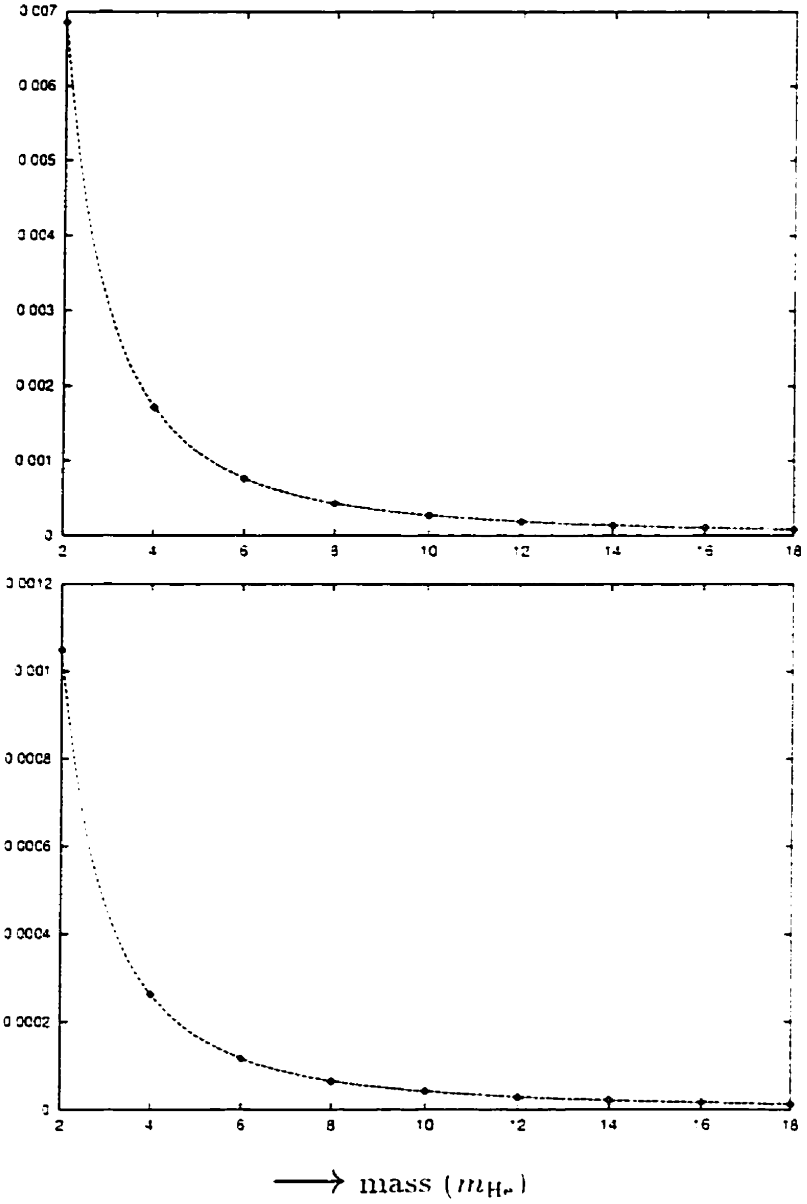

Figure 6.21:

Plots of data in Table 6.15 for momentum correction. The top graph is for the function F_1, the bottom is for the function F_2. The lines are m^{-2} fits.

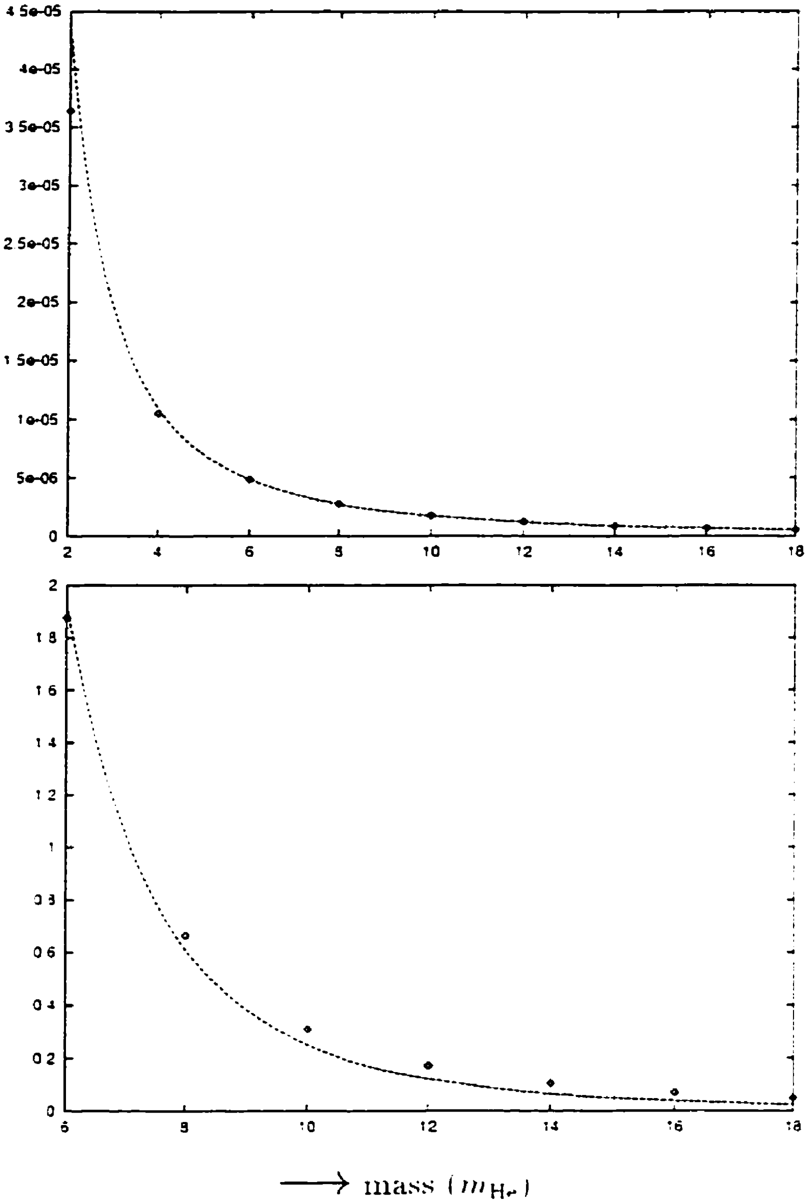

Figure 6.22:

Plots of data in Table 6.15 for Moyal correction. The top graph is for the function F_1, the line a m^{-2} fit.The bottom graph is for the function F_2 with an m^{-4} fit.

$\hat{\epsilon}_2$ values of the Moyal correction. The momentum correction is not examined since it has been shown that it will possess an m^{-2} dependence.

The Moyal correction is seen to have a strong dependence on mass when the mass becomes small. For all observables examined the Moyal correction changes sign relative to the classical part at low mass. Decreasing the mass increases the angle of deflection for rainbow scattering, and thus increases the importance of the corrections for reasons already discussed (cf. Chapter 6.2). At sufficiently small mass orbiting will occur and the approximation breaks down.

6.4.3 Correction Dependence on Velocity

We have seen how the corrections vary with mass, now we wish to examine the dependence of the corrections on initial velocity. How the Moyal corrections vary with velocity will be important for future work when no momentum expansion is made and an integral over all momentums will be required. Neglecting the Moyal correction in appropriate regions will greatly improve the speed of such calculations.

Tables 6.17-6.18 contain the data for a helium system which has initial velocities of $v = 1200, 1000, 800, 700, 600, 500, 450, 400, 350, 300$ m/s.

For a high velocity, the corrections will decay in an asymptotic manner. It must be noted that how the corrections will decay is a function of the observable being considered. It can be seen in Figure 6.25 that the momentum correction enters its asymptotic region before the Moyal correction does. As well, the Moyal correction for g_1^2 exhibits an asymptotic decay towards v^{-4}, while the momentum correction decays as v^{-2}.

It is seen that it is possible for the classical part of the average to become zero for some velocity, thus increasing the importance of the corrections even though we

Mass (m_{He})	$\frac{\frac{\hbar^2}{2}\langle\gamma^{(2)}_{0\ 373}(g_1)\rangle}{\langle\gamma^{(0)}_{0\ 373}(g_1)\rangle}$	$\frac{\frac{\hbar^2}{2}\langle\gamma^{(2)}_{0\ 373}(g_1^2)\rangle}{\langle\gamma^{(0)}_{0\ 373}(g_1^2)\rangle}$	$\frac{\frac{\hbar^2}{2}\langle\gamma^{(2)}_{0\ 373}(g_4)\rangle}{\langle\gamma^{(0)}_{0\ 373}(g_4)\rangle}$	$\frac{\frac{\hbar^2}{2}\langle\gamma^{(2)}_{0\ 373}(g_4^2)\rangle}{\langle\gamma^{(0)}_{0\ 373}(g_4^2)\rangle}$
24/16	7.21×10^{-4}	-2.17×10^{-2}	-1.79	-1.54×10^{-1}
16/16	1.59×10^{-3}	-7.52×10^{-2}	-7.88×10^{-1}	-4.63×10^{-1}
12/16	2.45×10^{-3}	-1.67×10^{-1}	-6.78×10^{-1}	-9.03×10^{-1}
8/16	1.17×10^{-3}	-3.55×10^{-1}	-1.86×10^{-1}	-1.53
7/16	-2.71×10^{-3}	-3.15×10^{-1}	3.34×10^{-1}	-1.24
6/16	-1.45×10^{-2}	8.29×10^{-2}	1.57	4.34×10^{-1}
5/16	-5.43×10^{-2}	1.89	5.12	7.26
4/16	-2.24×10^{-1}	5.22	19.73	19.60

Mass (m_{He})	$\frac{\frac{\hbar^2}{2}\langle\gamma^{(2)}_{0\ 373}(g_2)\rangle}{\langle\gamma^{(0)}_{0\ 373}(g_2)\rangle}$	$\frac{\frac{\hbar^2}{2}\langle\gamma^{(2)}_{0\ 373}(g_2^2)\rangle}{\langle\gamma^{(0)}_{0\ 373}(g_2^2)\rangle}$	$\frac{\frac{\hbar^2}{2}\langle\gamma^{(2)}_{0\ 373}(g_5)\rangle}{\langle\gamma^{(0)}_{0\ 373}(g_5)\rangle}$	$\frac{\frac{\hbar^2}{2}\langle\gamma^{(2)}_{0\ 373}(g_5^2)\rangle}{\langle\gamma^{(0)}_{0\ 373}(g_5^2)\rangle}$
24/16	8.37×10^{-4}	1.47×10^{-3}	8.47×10^{-4}	1.51×10^{-3}
16/16	2.75×10^{-3}	5.19×10^{-3}	2.80×10^{-3}	5.31×10^{-3}
12/16	6.44×10^{-3}	1.18×10^{-2}	6.57×10^{-3}	1.21×10^{-2}
8/16	2.10×10^{-2}	2.66×10^{-2}	3.38×10^{-2}	2.70×10^{-2}
7/16	3.05×10^{-2}	2.41×10^{-2}	3.15×10^{-2}	2.41×10^{-2}
6/16	4.52×10^{-2}	-6.24×10^{-3}	4.73×10^{-2}	-9.29×10^{-3}
5/16	6.28×10^{-2}	-1.51×10^{-1}	6.69×10^{-2}	-1.69×10^{-1}
4/16	-2.12×10^{-2}	-4.23×10^{-1}	-1.77×10^{-1}	-4.71×10^{-1}

Table 6.16:

Effect of decreasing the mass on average values for ϵ_1 and ϵ_2. The potential is helium, the velocity is 600 m/s. The results are at $t = 0.373 \times 10^{-10}$ s. Special unit is $m_{\text{He}} = 4.0026$ amu.

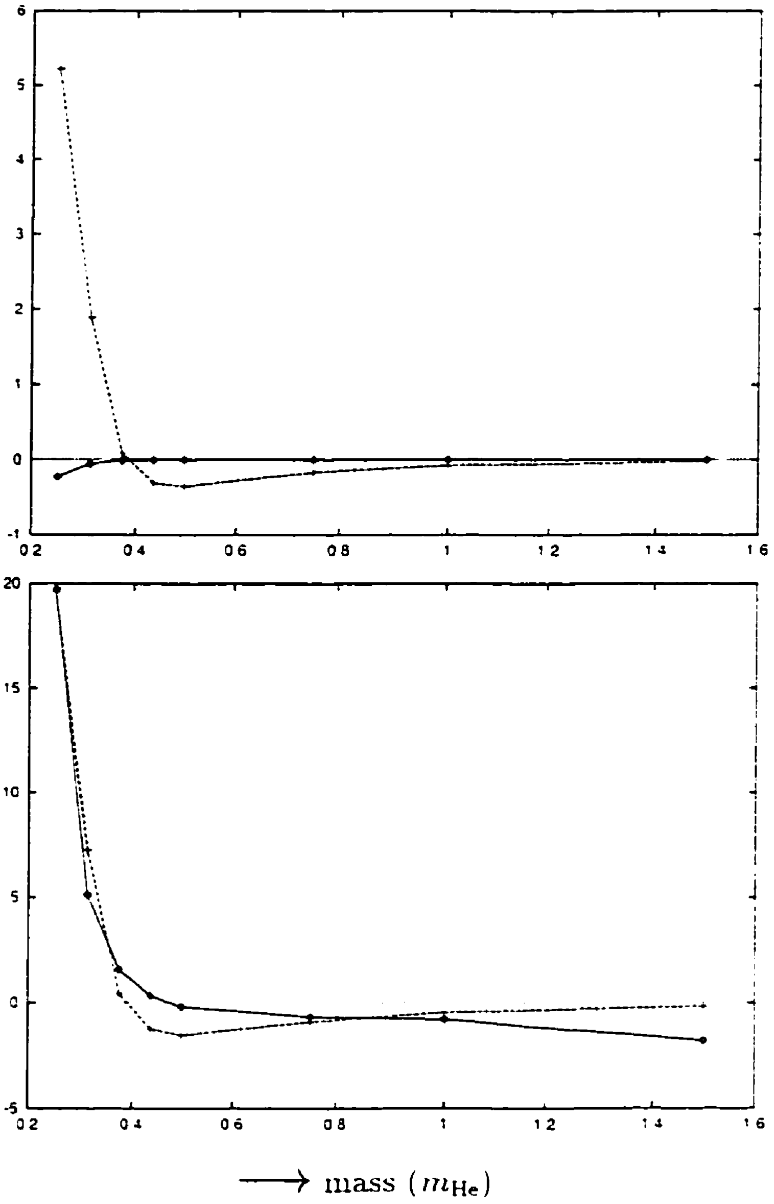

Figure 6.23:

Moyal corrections for $\hat{\epsilon}_1$ as a function of mass, $\frac{\hbar^2}{2}\langle\gamma^{(2)}_{0.373}(F)\rangle/\langle\gamma^{(0)}_{0.373}(F)\rangle$. The solid lines are $F = g_i$ and the dotted lines are $F = g_i^2$. The top graph is for $i = 1$, the bottom graph is $i = 4$.

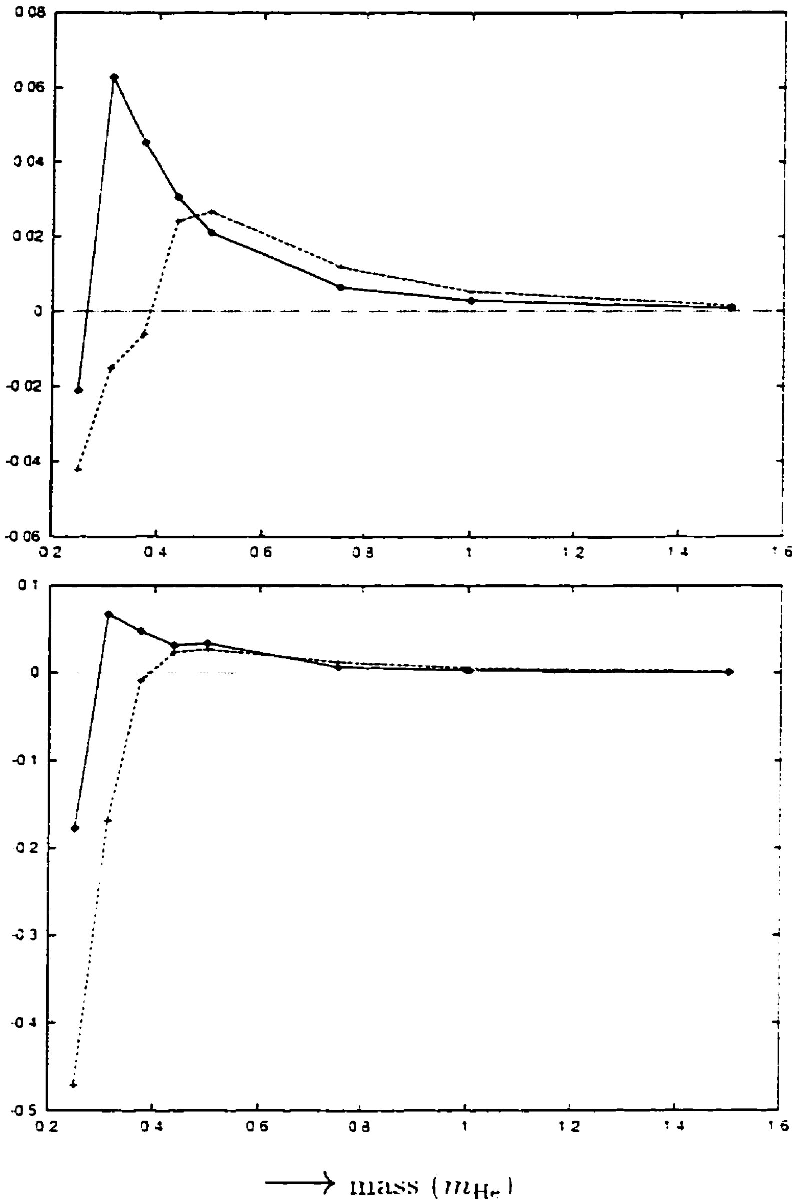

Figure 6.24:

Moyal corrections for $\hat{\epsilon}_2$ as a function of mass. $\frac{\hbar^2}{2}\langle\gamma^{(2)}_{0.373}(F)\rangle/\langle\gamma^{(0)}_{0.373}(F)\rangle$. The solid lines are $F = g_i$ and the dotted lines are $F = g_i^2$. The top graph is for $i = 2$, the bottom graph is $i = 5$.

are in a region where the corrections themselves are becoming small (Table 6.18 for g_4 near $v = 800$ m/s).

The question of kinetic energy dependence arises, and Figure 6.26 addresses this issue. At the time t_f the collision is essentially over, and the average position for the Gaussian is approximately the same for all systems shown in the graph, yet a quit different dependence is shown from changing the velocity and changing the mass. This shows that there is a mass and velocity dependence, and not a kinetic energy dependence. This is since the individual trajectories have a mass and velocity dependence, not a kinetic energy dependence.

6.4.4 Correction Dependence on Perturber

Finally, we examine the how the corrections differ between helium, neon, and argon for a fixed velocity. In Table 6.20 we compare ratios of the corrections to the classical part for the average value of g_5 at a velocity of 450 m/s.

As expected, the corrections are largest for helium, the lightest system. What might be surprising is that the corrections are comparable for argon and neon, even though argon has a larger mass than neon. The reason for this is that the potential depth as well as mass affect the size of the corrections. Comparing helium and neon we see that the mass and potential depth change by factors of (cf. Table 6.1)

$$\frac{m_{\mathrm{Ne}}}{m_{\mathrm{He}}} \sim \frac{20}{4} \sim 5 \, , \quad \frac{\epsilon_{\mathrm{Ne}}}{\epsilon_{\mathrm{He}}} \sim \frac{25}{7} \sim 3.5 \, ,$$

while for neon and argon we have

$$\frac{m_{\mathrm{Ar}}}{m_{\mathrm{Ne}}} \sim \frac{40}{20} \sim 2 \, , \quad \frac{\epsilon_{\mathrm{Ar}}}{\epsilon_{\mathrm{Ne}}} \sim \frac{87}{25} \sim 3.5 \, .$$

The depth of the argon potential is much greater than that for neon and this

v	t_f	$\langle\gamma_{t_f}^{(0)}(g_1)\rangle$	$\frac{\hbar^2}{2}\langle\gamma_{t_f}^{(2)}(g_1)\rangle$	$\left(\frac{\hbar}{2\Delta}\right)^2\langle\partial_p^2\gamma_{t_f}^{(0)}(g_1)\rangle$	Total
(m/s)	(10^{-10} s)		(Å)		
1200	0.187	2.0030680	7.0516×10^{-4}	5.0581×10^{-5}	2.0038237
1000	0.224	2.0021555	1.0798×10^{-3}	1.0400×10^{-4}	2.0033393
800	0.280	2.0003009	1.7981×10^{-3}	2.5249×10^{-4}	2.0023515
700	0.320	1.9986480	2.3930×10^{-3}	4.3101×10^{-4}	2.0013511
600	0.373	1.9960584	3.1722×10^{-3}	8.0017×10^{-4}	2.0000308
500	0.448	1.9918044	3.6353×10^{-3}	1.6654×10^{-3}	1.9971051
450	0.498	1.9846424	2.7126×10^{-3}	2.5339×10^{-3}	1.9898889
400	0.560	1.9846424	-1.8003×10^{-3}	4.0184×10^{-3}	1.9868605
350	0.640	1.9798413	-2.0409×10^{-2}	6.6218×10^{-3}	1.9660541
300	0.747	1.9760829	-1.1047×10^{-1}	1.0814×10^{-2}	1.8764269
v	t_f	$\langle\gamma_{t_f}^{(0)}(g_1^2)\rangle$	$\frac{\hbar^2}{2}\langle\gamma_{t_f}^{(2)}(g_1^2)\rangle$	$\left(\frac{\hbar}{2\Delta}\right)^2\langle\partial_p^2\gamma_{t_f}^{(0)}(g_1^2)\rangle$	Total
(m/s)	(10^{-10} s)		(Å^2)		
1200	0.187	233.65897	-0.7216	4.1609	237.0983
1000	0.224	235.46522	-1.8692	5.9706	239.5666
800	0.280	238.47436	-5.3538	9.2713	242.3918
700	0.320	241.09326	-9.6815	12.0413	243.4530
600	0.373	245.50004	-18.4586	16.2368	243.2782
500	0.448	253.85618	-35.6909	22.9495	241.1148
450	0.498	260.84906	-45.8073	27.9002	242.9420
400	0.560	270.55028	-39.5060	34.5686	265.6129
350	0.640	281.78404	74.5227	44.0980	400.4047
300	0.747	287.06501	375.1015	60.2485	722.4150

Table 6.17:

Averages values for g_1 and g_1^2 at time after collision as a function of velocity

v	t_f	$\langle\gamma_{t_f}^{(0)}(g_4)\rangle$	$\frac{\hbar^2}{2}\langle\gamma_{t_f}^{(2)}(g_4)\rangle$	$\left(\frac{\hbar}{2\Delta}\right)^2\langle\partial_p^2\gamma_{t_f}^{(0)}(g_4)\rangle$	Total
(m/s)	(10^{-10} s)		(10^{-5}(cm^{-1} 0.1 ns/Å))		
1200	0.187	0.7150111	0.16915	0.01209	0.89625
1000	0.224	0.4117744	0.21622	0.02073	0.64872
800	0.280	0.0308340	0.28892	0.04050	0.36025
700	0.320	-0.2056469	0.33734	0.06067	0.19236
600	0.373	-0.4885755	0.38495	0.09683	-0.00679
500	0.448	-0.8347512	0.37100	0.16854	-0.29521
450	0.498	-1.0344293	0.25267	0.23130	-0.55046
400	0.560	-1.2433154	-0.14014	0.32699	-1.05646
350	0.640	-1.4234017	-1.46672	0.47345	-2.41667
300	0.747	-1.4343256	-7.07778	0.66598	-7.84612

v	t_f	$\langle\gamma_{t_f}^{(0)}(g_4^2)\rangle$	$\frac{\hbar^2}{2}\langle\gamma_{t_f}^{(2)}(g_4^2)\rangle$	$\left(\frac{\hbar}{2\Delta}\right)^2\langle\partial_p^2\gamma_{t_f}^{(0)}(g_4^2)\rangle$	Total
(m/s)	(10^{-10} s)		(10^{-5}(cm^{-1} 0.1 ns/A)^2		
1200	0.187	15.687944	-0.45296	0.21836	15.4534
1000	0.224	11.629129	-0.77631	0.20905	11.0618
800	0.280	8.247720	-1.38336	0.19273	7.0571
700	0.320	6.857019	-1.89796	0.17807	5.1371
600	0.373	5.707976	-2.64270	0.15415	3.2194
500	0.448	4.840317	-3.53773	0.10755	1.4101
450	0.498	4.510374	-3.67082	0.06944	0.9090
400	0.560	4.205878	-2.45638	0.01635	1.7658
350	0.640	3.782359	3.98200	-0.04660	7.7178
300	0.747	2.957920	14.48862	-0.04828	17.3982

Table 6.18:

Averages values for g_4 and g_4^2 at time after collision as a function of velocity

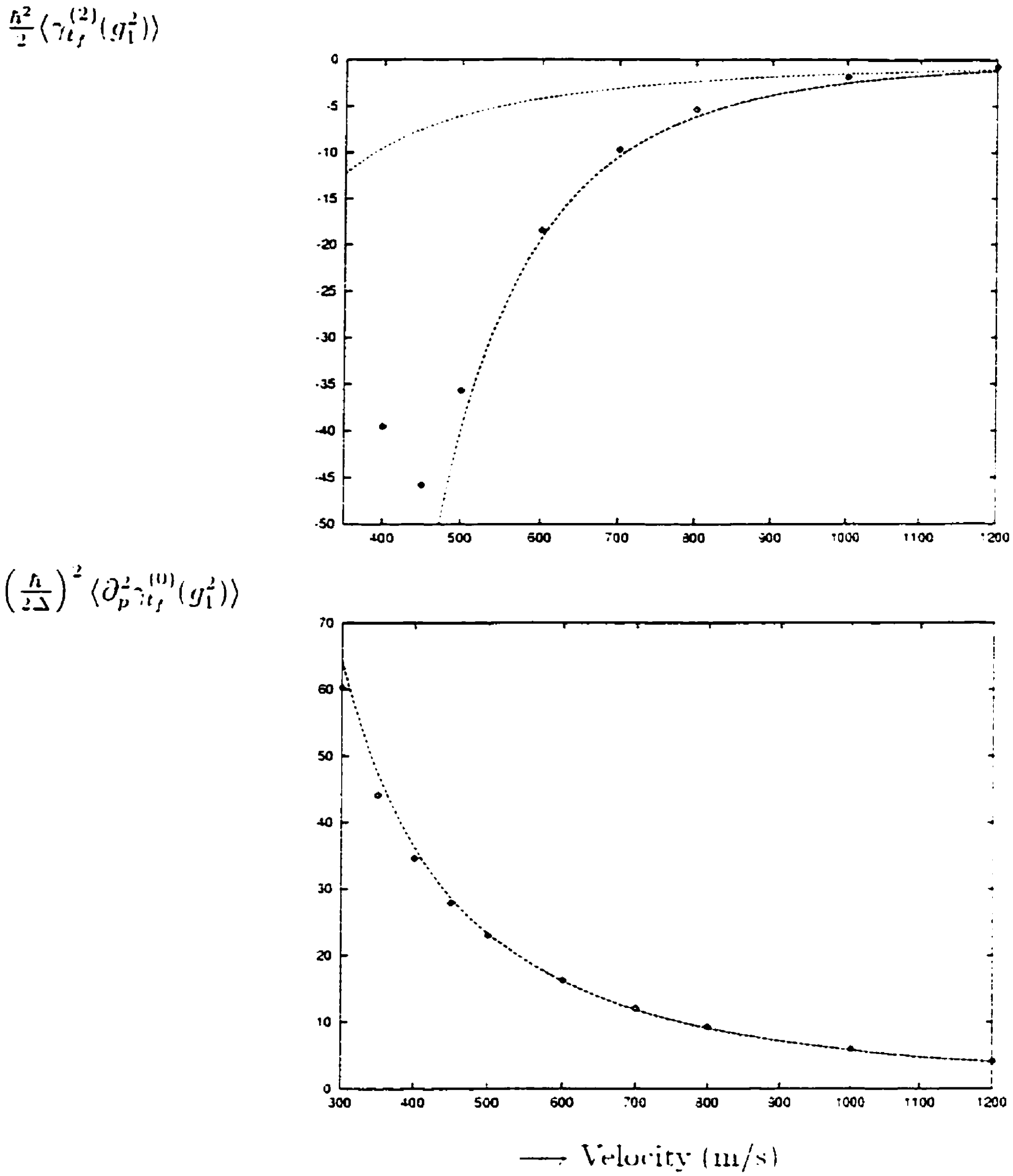

Figure 6.25:

Moyal and momentum corrections as a function of velocity.

Top graph: dashed line: v^{-4} fit, dotted line: v^{-2} fit.

Bottom graph: dashed line: v^{-2} fit.

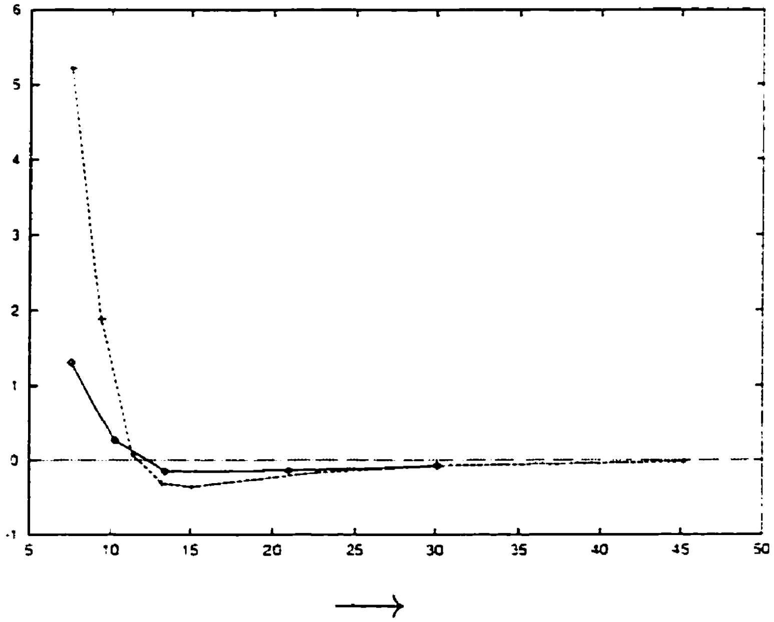

Kinetic Energy (cm^{-1})

Figure 6.26:

Moyal correction $\frac{\hbar^2}{2}\langle \gamma_{t_f}^{(2)}(y_1^2)\rangle / \langle \gamma_{t_f}^{(0)}(y_1^2)\rangle$ as a function of kinetic energy. The solid line is kinetic energy being varied by varying the velocity: t_f for this curve can be found in Table 6.17. The dotted line is from varying the mass: $t_f = 0.747 \times 10^{-10}$s.

v (m/s)	$\frac{\frac{\hbar^2}{2}\langle\gamma^{(2)}_{t_f}(g_1)\rangle}{\langle\gamma^{(0)}_{t_f}(g_1)\rangle}$	$\frac{\left(\frac{\hbar}{2\Delta}\right)^2\langle\partial_p^2\gamma^{(0)}_{t_f}(g_1)\rangle}{\langle\gamma^{(0)}_{t_f}(g_1)\rangle}$	$\frac{\frac{\hbar^2}{2}\langle\gamma^{(2)}_{t_f}(g_1^2)\rangle}{\langle\gamma^{(0)}_{t_f}(g_1^2)\rangle}$	$\frac{\left(\frac{\hbar}{2\Delta}\right)^2\langle\partial_p^2\gamma^{(0)}_{t_f}(g_1^2)\rangle}{\langle\gamma^{(0)}_{t_f}(g_1^2)\rangle}$
1200	3.5204×10^{-4}	2.5387×10^{-5}	3.0881×10^{-3}	1.7808×10^{-2}
1000	5.3932×10^{-4}	5.1945×10^{-5}	7.9383×10^{-3}	2.5357×10^{-2}
800	8.9889×10^{-4}	1.2622×10^{-4}	2.2451×10^{-2}	3.8878×10^{-2}
700	1.1973×10^{-3}	2.1565×10^{-4}	4.0157×10^{-2}	4.9945×10^{-2}
600	1.5893×10^{-3}	4.0087×10^{-4}	7.5187×10^{-2}	6.6138×10^{-2}
500	1.8251×10^{-3}	8.3612×10^{-4}	1.4059×10^{-1}	9.0403×10^{-2}
450	1.3640×10^{-3}	1.2742×10^{-3}	1.7561×10^{-1}	1.0696×10^{-1}
400	9.0714×10^{-4}	2.0247×10^{-3}	1.4602×10^{-1}	1.2777×10^{-1}
350	1.0308×10^{-2}	3.3446×10^{-3}	2.6447×10^{-1}	1.5649×10^{-1}
300	5.5904×10^{-2}	5.4723×10^{-3}	1.3067	2.0988×10^{-1}

Table 6.19: Average values as a function of velocity.

stronger interaction overcomes the fact that the mass is increased to produce comparable corrections.

t $(10^{-10}$ s)	$\frac{\hbar^2}{2}\langle\gamma_{t_f}^{(2)}(g_5)\rangle/\langle\gamma_{t_f}^{(0)}(g_5)\rangle$ Helium	 Neon	 Argon
0	0	0	0
0.280	1.0930×10^{-3}	3.1054×10^{-5}	1.0325×10^{-5}
0.311	3.7748×10^{-3}	1.0563×10^{-4}	3.9127×10^{-5}
0.342	6.8811×10^{-3}	1.9077×10^{-4}	7.7220×10^{-5}
0.498	8.6448×10^{-3}	2.3837×10^{-4}	1.0272×10^{-4}
t $(10^{-10}$ s)	$\left(\frac{\hbar}{2\Delta}\right)^2 \langle\partial_p^2\gamma_{t_f}^{(0)}(g_5)\rangle/\langle\gamma_{t_f}^{(0)}(g_5)\rangle$ Helium	 Neon	 Argon
0	0	0	0
0.280	1.8057×10^{-5}	1.0238×10^{-6}	5.1141×10^{-7}
0.311	4.4036×10^{-4}	2.2627×10^{-5}	1.0980×10^{-5}
0.342	9.7128×10^{-4}	4.8762×10^{-5}	2.4404×10^{-5}
0.498	1.0382×10^{-3}	5.1978×10^{-5}	2.6279×10^{-5}

Table 6.20: The size of the corrections for He, Ne, and Ar at $v = 450$ m/s.

	$b_{rainbow}$ (Å)	$\chi_{rainbow}$ (radians)
Helium	3.22	-0.93
Neon	3.77	-0.62
Argon	4.98	-1.18

Table 6.21: Rainbow scattering particulars ($v = 450$ m/s).

Chapter 7

Conclusion

The research contained in this thesis has resulted in a number of advances in collisional dynamics.

The role of the components of the induced dipole moment in collisional interference in the pure rotational spectrum was determined for HD-He and HD-Ar. Line intensity was found to be largely determined by the component with the same symmetry as the allowed dipole moment. The mixing of other components acts to reduce the line intensity. Line asymmetry, however, was found to depend to a great extent on the mixing process due to cancellation among contributions from various components. Thus, line intensity and asymmetry are sensitive to different details of the HD-X interaction.

The line shape due to collision-induced interference for the vibration-rotation spectrum of HD-He was calculated, using both a rigid rotator model of HD and a model that included HD vibrations via a vibrationally dependent potential. The results indicate that line intensity is not very sensitive to the vibrational state dependence of the intermolecular potential but that the line asymmetry is. Collisional propagation effects were shown to be important among rotational levels in the ground and excited vibrational state. The collisional interference phenomenon seems to consist of two distinct effects which may be complementary sources of information on intermolecular interactions.

The first computational version of Moyal quantum mechanics to treat three dimensional systems with physically relevant parameters was developed. The system treated was the scattering of a Gaussian wave packet by the helium, neon, and argon interaction potentials.

A large number of checks from a variety of sources were derived and used to test the consistancy and accuracy of the results.

Sensitive areas of the phase space average were identified. Integrals over impact parameter and y were examined in detail. It was found that the classical part of the average in general has smoother functions in b and y than the corrections. Also, coordinate dependent functions are smoother than momentum dependent functions.

The region of phase space which produces rainbow scattering was determined to result in the largest quantum effects. The Moyal correction was found to be small for impact parameters greater than $2b_{rainbow} - b_{glory}$.

The corrections to average values was examined in detail for helium at a velocity of 300 m/s. It was shown that the corrections have an asymptotic time behaviour which is the same as that of the classical part of the average, but that they may grow as $t \to \infty$ to dominate the total average.

The corrections to the average value was examined as a function of mass and velocity. The Moyal corrections were seen to change sign relative to the classical part of the average in both cases. The momentum correction was shown to have an m^{-2} dependence. More complex asymptotic behaviour of the Moyal correction was examined for both the mass and the velocity.

Comparison between the size of the correction for the systems helium, neon, and argon was performed. Helium was found to exhibit the largest corrections. Although argon has a mass twice that of neon, and thus might be expected to have relatively small corrections, the corrections for argon and neon were found to be comparable. This is due to the stronger interaction in the argon potential.

Possibilities for future research in Moyal quantum mechanics are many and varied:

1 Include the integral over momentum in the phase space average and thus remove the momentum expansion correction, allowing one to treat scattering for Gaussians which are not squeezed.

2 Develop a version of the theory which can calculate accurately the quantum correction for metastable and orbiting trajectories.

3 Develop a first order perturbation theory which would allow the wave packet to be located closer to the potential center at $t = 0$.

4 The theory as presented is Cartesian based. A spherical version can be developed which would more naturally treat the symmetries of a central force collision problem.

5 Rather than treat a pure state as we have with the scattered Gaussian ($\hat{\rho} = |\psi><\psi|$), treat a statistical ensemble ($\hat{\rho} = e^{-\hat{H}/T}/\mathrm{Tr}\, e^{-\hat{H}/T}$).

6 Apply Moyal quantum mechanics to line shape problems in general, or to other theories which use the classical path approximation.

7 Apply Moyal quantum mechanics to the collisional interference in the spectrum of HD-X problem.

Work has already begun on 3 and 4. Before problem 6 can be addressed. 1-5 should be investigated and well understood.

Appendix A

Spread of Wave Packet

The calculation of the spread of a three dimensional Gaussian wave packet for a free particle, although simple, will provide a useful overview of the structures Moyal quantum mechanics uses to calculate expectation values.

The three dimensional Gaussian wave packet at time $t = 0$ is given by

$$\begin{aligned}\psi_0(\Delta, \Xi, x) &= \left(\frac{1}{\pi\Delta^2}\right)^{3/4} exp\Big\{+\frac{i}{\hbar}(\bar{p}_1 x_1 + \bar{p}_2 x_2 + \bar{p}_3 x_3) \\ &\qquad -\frac{1}{2\Delta^2}\left((x_1 - \bar{q}_1)^2 + (x_2 - \bar{q}_2)^2 + (x_3 - \bar{q}_3)^2\right)\Big\} . \qquad (A.1)\end{aligned}$$

This wave packet is centered about $\bar{q}$, has mean momentum $\bar{p}$, and spread Δ. It is unit normalized,

$$\int_{\mathbf{R}^3} \psi_0^*(\Delta, \Xi, x)\psi_0(\Delta, \Xi, x)\, dx = 1 . \qquad (A.2)$$

The Wigner function of the wave packet is given by

$$\begin{aligned}w_{\psi_0(\Delta,\Xi)} &= \frac{1}{h^3}\left(|\psi_0(\Delta, \Xi, x)\rangle\langle\psi_0(\Delta, \Xi, x)|\right)_W(z) . \\ &= \frac{1}{h^3}\int_{\mathbf{R}^3} dv\, e^{-ip\cdot v/\hbar}\langle q + \frac{v}{2}|\psi_0(\Delta, \Xi, x)\rangle\langle\psi_0(\Delta, \Xi, x)|q - \frac{v}{2}\rangle. \qquad (A.3)\end{aligned}$$

In the position representation we have [Sakuri, 1985]

$$\begin{aligned}\langle q+\frac{v}{2}|\psi_0(\Delta,\bar{z},x)\rangle\langle\psi_0(\Delta,\bar{z},x)|q-\frac{v}{2}\rangle &= \psi_0(\Delta,\bar{z},q+\frac{v}{2})\psi_0^*(\Delta,\bar{z},q-\frac{v}{2})\ .\\ &= \left(\frac{1}{\pi\Delta^2}\right)^{3/2} exp\left\{-\frac{1}{4\Delta^2}\left(v_1^2+v_2^2+v_3^2\right)+\frac{i}{\hbar}\left(\bar{p}_1v_1+\bar{p}_2v_2+\bar{p}_3v_3\right)\right.\\ &\qquad\left.-\frac{1}{\Delta^2}\left((q_1-\bar{q}_1)^2+(q_2-\bar{q}_2)^2+(q_3-\bar{q}_3)^2\right)\right\}\ . \qquad (A.4)\end{aligned}$$

and performing the integral in Equation (A.3) we find that the Wigner function of the Gaussian is

$$\begin{aligned}w_{\psi_0(\Delta,\bar{z})} &= \left(\frac{1}{\pi\hbar}\right)^3 exp\left\{-\frac{\Delta^2}{\hbar^2}\left((p_1-\bar{p}_1)^2+(p_2-\bar{p}_2)^2+(p_3-\bar{p}_3)^2\right)\right.\\ &\qquad\left.-\frac{1}{\Delta^2}\left((q_1-\bar{q}_1)^2+(q_2-\bar{q}_2)^2+(q_3-\bar{q}_3)^2\right)\right\}\ . \qquad (A.5)\end{aligned}$$

Equation (A.5) is the same as Equation (5.100) which was derived in a different manner.

Expectation values are found from

$$\langle\hat{A}(t)\rangle_{\psi_0(\Delta,\bar{z})} = \int_{R^6} dp\,dq\,\Gamma_t(A_W)w_{\psi_0(\Delta,\bar{z})}(z)\ . \qquad (A.6)$$

For a free particle the trajectory is of course known, and is given simply by:

$$\begin{aligned}q_i(t) &= q_i+\frac{p_i}{m}t\ . &(A.7)\\ p_i(t) &= p_i = constant\ . &(A.8)\end{aligned}$$

Since the free particle Hamiltonian $H = p^2/2m$ is quadratic in z, the Weyl symbol evolution operator is given strictly by the classical part.

$$\Gamma_t(A_W) = \gamma_t^{(0)}(A_W) = A_W(g(t|z))\ . \qquad (A.9)$$

To evaluate the spread of the wave packet we will require $(\hat{q}_i)_W$ and $(\hat{q}_i^2)_W$. Since these are functions only of $\hat{q}_i$ and not $\hat{p}_i$, the symbols are simply q_i and q_i^2.

It is a simple matter to show that

$$\begin{aligned}
\langle \hat{q}_i(t)\rangle_{\psi_0(\Delta,z)} &= \int_{\mathbf{R}^3} dp \int_{\mathbf{R}^3} dq \left(q_i + \frac{p_i}{m}t\right) w_{\psi_0(\Delta,z)} \\
&= \bar{q}_i + \frac{\bar{p}_i}{m}t\ . \qquad (A.10) \\
\langle \hat{q}_i^{\,2}(t)\rangle_{\psi_0(\Delta,z)} &= \int_{\mathbf{R}^3} dp \int_{\mathbf{R}^3} dq \left(q_i + \frac{p_i}{m}t\right)^2 w_{\psi_0(\Delta,z)} \\
&= \frac{\Delta^2}{2} + \frac{\hbar^2 t^2}{2m^2\Delta^2} + (\bar{q}_i + \frac{\bar{p}_i}{m}t)^2\ . \qquad (A.11)
\end{aligned}$$

and the spread of the Gaussian is given by the familiar [Merzbacher, 1970 pg. 164]

$$\begin{aligned}
\textit{spread in } q_i &= \langle \hat{q}_i^{\,2}(t)\rangle_{\psi_0(\Delta,z)} - \langle \hat{q}_i(t)\rangle^2_{\psi_0(\Delta,z)}\ . \qquad (A.12) \\
&= \frac{\Delta^2}{2}\left(1 + \frac{\hbar^2 t^2}{m^2\Delta^4}\right)\ . \qquad (A.13)
\end{aligned}$$

In a similar manner one can determine the spread in the momentum to be

$$\begin{aligned}
\textit{spread in } p_i &= \langle \hat{p}_i^{\,2}(t)\rangle_{\psi_0(\Delta,z)} - \langle \hat{p}_i(t)\rangle^2_{\psi_0(\Delta,z)}\ . \qquad (A.14) \\
&= \left(\frac{\hbar^2}{2\Delta^2} + \bar{p}_i^2\right) - (\bar{p}_i)^2\ . \qquad (A.15) \\
&= \frac{\hbar^2}{2\Delta^2}\ . \qquad (A.16)
\end{aligned}$$

In this thesis, we use a wave packet that has $\Delta = 20$ Å. The spreading in p is the same for all atoms at all times for a free wave packet, and is 1.3902×10^{-51} (kg m/s)^2 = 3.522967×10^{-6} (cm^{-1} 0.1 ns/Å)^2. The spreading in the position of a free wave packet for different atoms is given in Table A.1.

The spread can also be calculated using the alternate method of obtaining expectation values, namely evolving the Wigner function and leaving the symbol for the operator fixed at its $t = 0$ value.

$$\langle \hat{A}(t)\rangle_{\psi_0(\Delta,z)} = \int_{\mathbf{R}^6} dq\,dp\,A_W \Gamma_{-t}\left(w_{\psi_0(\Delta,z)}(z)\right)\ .$$

$$= \frac{1}{\pi\hbar}\int_{\mathbf{R}^6} dq\, dp\, A_W \prod_{i=1}^{3} exp\left\{-\frac{\Delta^2}{\hbar^2}(p_i(-t)-\bar{p})^2 - \frac{1}{\hbar^2}(q_i(-t)-\bar{q})^2\right\}.$$

$$= \frac{1}{\pi\hbar}\int_{\mathbf{R}^6} dq\, dp\, A_W \prod_{i=1}^{3} exp\left\{-\frac{\Delta^2}{\hbar^2}(p_i-\bar{p})^2 - \frac{1}{\hbar^2}(q_i - p_i t/m - \bar{q})^2\right\}.$$

Setting A_W equal to q_i, q_i^2, p_i, p_i^2 will recover Equations (A.13) and (A.16).

	Reduced Mass (amu)	Spread in q (A^2) $t = 0.42$	$t = 0.53$	$t = 0.68$
		(10^{-10} s)		
He-He	2.0013	222.233	235.358	258.205
Ne-Ne	10.0895	200.872	201.391	202.290
Ar-Ar	19.974	200.222	200.355	200.584

Table A.1:

Spread in position of a free Gaussian with a $t = 0$ spread of 200 A^2.

Appendix B

Bessel Function Reduction of Equation (5.121)

In this appendix we wish to explicitly determine the Bessel function form of Equation (5.121)

$$\Omega_{\mu_1\nu_1\mu_2\nu_2\cdots\mu_n\nu_n}(\xi) = \int_0^{2\pi} d\theta \, exp\{-\xi\cos\theta\} \, \mathcal{R}_{\alpha_1\nu_1}(\theta)\cdots\mathcal{R}_{\alpha_n\nu_n}(\theta) \tag{B.1}$$

that is used for scalar, vector, and rank two tensor observables. We have introduced $\xi = -2\Delta^{-2}b\bar{q}_1$.

To begin we will rewrite Equation (B.1) in a form that exposes the sine and cosine dependence explicitly. The rotation matrix $\mathcal{R}$ is given as

$$\mathcal{R}(\theta) = \begin{pmatrix} \cos\theta & 0 & \sin\theta & 0 & 0 & 0 \\ 0 & 1 & 0 & 0 & 0 & 0 \\ -\sin\theta & 0 & \cos\theta & 0 & 0 & 0 \\ 0 & 0 & 0 & \cos\theta & 0 & \sin\theta \\ 0 & 0 & 0 & 0 & 1 & 0 \\ 0 & 0 & 0 & -\sin\theta & 0 & \cos\theta \end{pmatrix} . \tag{B.2}$$

The rotation matrix can be expressed by using matrices which define its structure.

$$A = \begin{pmatrix} 1 & 0 & 0 & 0 & 0 & 0 \\ 0 & 0 & 0 & 0 & 0 & 0 \\ 0 & 0 & 1 & 0 & 0 & 0 \\ 0 & 0 & 0 & 1 & 0 & 0 \\ 0 & 0 & 0 & 0 & 0 & 0 \\ 0 & 0 & 0 & 0 & 0 & 1 \end{pmatrix} \qquad B = \begin{pmatrix} 0 & 0 & 1 & 0 & 0 & 0 \\ 0 & 0 & 0 & 0 & 0 & 0 \\ 1 & 0 & 0 & 0 & 0 & 0 \\ 0 & 0 & 0 & 0 & 0 & 1 \\ 0 & 0 & 0 & 0 & 0 & 0 \\ 0 & 0 & 0 & 1 & 0 & 0 \end{pmatrix}$$

$$C = \begin{pmatrix} 0 & 0 & 0 & 0 & 0 & 0 \\ 0 & 1 & 0 & 0 & 0 & 0 \\ 0 & 0 & 0 & 0 & 0 & 0 \\ 0 & 0 & 0 & 0 & 0 & 0 \\ 0 & 0 & 0 & 0 & 1 & 0 \\ 0 & 0 & 0 & 0 & 0 & 0 \end{pmatrix} \qquad D = \begin{pmatrix} 0 & 1 & 0 & 1 & 1 & 1 \\ 1 & 0 & 1 & 1 & 1 & 1 \\ 0 & 1 & 0 & 1 & 1 & 1 \\ 1 & 1 & 1 & 0 & 1 & 0 \\ 1 & 1 & 1 & 1 & 0 & 1 \\ 1 & 1 & 1 & 0 & 1 & 0 \end{pmatrix}$$

$$E = \begin{pmatrix} 0 & 0 & 0 & 0 & 0 & 0 \\ 0 & 0 & 0 & 0 & 0 & 0 \\ 1 & 0 & 0 & 0 & 0 & 0 \\ 0 & 0 & 0 & 0 & 0 & 0 \\ 0 & 0 & 0 & 0 & 0 & 0 \\ 0 & 0 & 0 & 1 & 0 & 0 \end{pmatrix}$$

These matrices are such that A locates the $\cos\theta$'s; B locates the $\sin\theta$'s; C locates the ones; D locates the zeros; E locates the $-\sin\theta$'s. The entries of $\mathcal{R}$ are then given by

$$\mathcal{R}_{\mu\nu}(\theta) = (A_{\mu\nu} + B_{\mu\nu} + C_{\mu\nu})(-1)^{E_{\mu\nu}}(\cos\theta)^{A_{\mu\nu}}(\sin\theta)^{B_{\mu\nu}} \,. \tag{B.3}$$

Thus, Equation (B.1) can be expressed in general as

$$\Omega_{\mu_1\nu_1\cdots\mu_n\nu_n}(\xi) \;=\; \left(\prod_{j=1}^{n}\left(1 - D_{\mu_j\nu_j}\right)\right)(-1)^{\sum_{j=1}^{n} E_{\mu_j\nu_j}} \times$$

$$\int_0^{2\pi} d\theta \, exp\{-\xi \cos\theta\} (\cos\theta)^{\sum_{j=1}^{n} A_{\mu_j\nu_j}} (\sin\theta)^{\sum_{j=1}^{n} B_{\mu_j\nu_j}} \quad (B.4)$$

where we have used the fact that $1 - D_{\mu\nu} = A_{\mu\nu} + B_{\mu\nu} + C_{\mu\nu}$. These integrals will have $\cos^j\theta \sin^k\theta$ in the integrand, and can be converted to multiple angle form using trigonometric identities.

The Bessel function is defined as [Bowman, 1958 p. 90]:

$$J_n(z) = \frac{1}{2\pi}\int_{-\pi}^{\pi} e^{-in\theta + iz\sin\theta} d\theta \,. \quad (B.5)$$

where n is an integer, and z is a complex number. Using Euler's relation, ($e^{-ix} = \cos x + i \sin x$), the modified Bessel function $I_n(\xi)$ ($J_n(i\xi) = i^n I_n(\xi)$), and $z = i\xi$ we can cast Equation (B.5) into the form:

$$\begin{aligned} i^n I_n(\xi) &= \frac{1}{2\pi}\int_{-\pi}^{\pi} (\cos n\theta - i \sin n\theta) e^{-\xi\sin\theta} d\theta \,, \\ &= \frac{1}{2\pi}\int_{-\pi}^{\pi} \cos n\theta e^{-\xi\sin\theta} d\theta - i\frac{1}{2\pi}\int_{-\pi}^{\pi} \sin n\theta e^{-\xi\sin\theta} d\theta \,. \end{aligned} \quad (B.6)$$

Equating real and imaginary parts for n odd or even yields the important relations *for n odd, $n = 2n' + 1$:*

$$\int_{-\pi}^{\pi} [\sin(2n'+1)\theta] e^{-\xi\sin\theta} d\theta = 2\pi(-1)^{n'+1} I_{2n'+1}(\xi) \,. \quad (B.7)$$

$$\int_{-\pi}^{\pi} [\cos(2n'+1)\theta] e^{-\xi\sin\theta} d\theta = 0 \,. \quad (B.8)$$

for n even, $n = 2n'$:

$$\int_{-\pi}^{\pi} [\sin(2n')\theta] e^{-\xi\sin\theta} d\theta = 0 \,. \quad (B.9)$$

$$\int_{-\pi}^{\pi} [\cos(2n'+1)\theta] e^{-\xi\sin\theta} d\theta = 2\pi(-1)^{n'} I_{2n'}(\xi) \,. \quad (B.10)$$

For a scalar observable, we need to evaluate the function

$$\Omega(\xi) = \int_0^{2\pi} e^{-\xi\cos\theta} d\theta \,. \quad (B.11)$$

The integrand is a periodic function, and the range is a complete period. Therefore, we may safely replace the range of integration with $(-\pi, \pi)$. If $\theta = \theta' - \pi/2$, then $\cos\theta = \sin\theta'$, and Equation (B.11) becomes

$$\begin{aligned}\Omega(\xi) &= \int_{-\pi}^{\pi} \epsilon^{-\xi\sin\theta'} d\theta' , \\ &= 2\pi I_0(\xi) . \qquad \text{(B.12)}\end{aligned}$$

which follows from Equation (B.10) with $n' = 0$.

For a vector observable, consider the element $\Omega_{11}(y)$. Using a method similar to the scalar observable analysis, we have

$$\begin{aligned}\Omega_{11}(\xi) &= \int_0^{2\pi} \epsilon^{-\xi\cos\theta} \cos\theta \, d\theta , \\ &= \int_{-\pi}^{\pi} \epsilon^{-\xi\sin\theta'} \sin\theta' d\theta' , \\ &= -2\pi I_1(\xi) . \qquad \text{(B.13)}\end{aligned}$$

where the last step employed Equation (B.7) with $n' = 0$. In a similar manner, we can show that the only nonzero components of $\Omega_{\alpha\nu}(\xi)$ are

$$\begin{aligned}\Omega_{11}(\xi) &= -2\pi I_1(\xi) , \\ &= \Omega_{33} = \Omega_{44} = \Omega_{66} . \qquad \text{(B.14)} \\ \Omega_{22}(\xi) &= 2\pi I_0(\xi) , \\ &= \Omega_{55} . \qquad \text{(B.15)}\end{aligned}$$

For a rank two tensor observable, consider the element

$$\begin{aligned}\Omega_{1111}(\xi) &= \int_0^{2\pi} \epsilon^{-\xi\cos\theta} \cos^2\theta \, d\theta , \\ &= \int_{-\pi}^{\pi} \epsilon^{-\xi\sin\theta'} \sin^2\theta' d\theta' , \\ &= \int_{-\pi}^{\pi} \epsilon^{-\xi\sin\theta'} \left(\frac{1-\cos 2\theta'}{2}\right) d\theta' .\end{aligned}$$

$$\begin{aligned}
&= \frac{1}{2}\left[\int_{-\pi}^{\pi} \epsilon^{-\xi\sin\theta'} d\theta' - \int_{-\pi}^{\pi} \epsilon^{-\xi\sin\theta'} \cos 2\theta' d\theta'\right] . \\
&= \pi\left[I_0(\xi) + I_2(\xi)\right] . \qquad \text{(B.16)}
\end{aligned}$$

where the first integral is from Equation (B.10) with $n' = 0$: the second is from Equation (B.10) with $n' = 1$. The nonzero components of $\Omega_{\alpha_1\nu_1\alpha_2\nu_2}(\xi)$ are determined to be

$$\begin{aligned}
\Omega_{1111}(\xi) &= \pi\left[I_0(\xi) + I_2(\xi)\right] \\
&= \Omega_{1133} = \Omega_{1144} = \Omega_{1166} = \Omega_{3311} = \Omega_{3333} \\
&= \Omega_{3344} = \Omega_{3366} = \Omega_{4411} = \Omega_{4433} = \Omega_{4444} \\
&= \Omega_{4466} = \Omega_{6611} = \Omega_{6633} = \Omega_{6644} = \Omega_{6666} . \\
\Omega_{1313}(\xi) &= \pi\left[I_0(\xi) - I_2(\xi)\right] \\
&= \Omega_{1346} = \Omega_{3131} = \Omega_{3164} = \Omega_{4613} = \Omega_{4646} \\
&= \Omega_{6431} = \Omega_{6464} = -\Omega_{1331} = -\Omega_{1364} = -\Omega_{4631} \\
&= -\Omega_{4664} = -\Omega_{3113} = -\Omega_{3146} = -\Omega_{6413} = -\Omega_{6446} . \\
\Omega_{1122}(\xi) &= -2\pi I_1(\xi) \\
&= \Omega_{1155} = \Omega_{2211} = \Omega_{2233} = \Omega_{2244} = \Omega_{2266} \\
&= \Omega_{3322} = \Omega_{3355} = \Omega_{4422} = \Omega_{4455} = \Omega_{5511} \\
&= \Omega_{5533} = \Omega_{5544} = \Omega_{5566} = \Omega_{6622} = \Omega_{6655} . \\
\Omega_{2222}(\xi) &= 2\pi I_0(\xi) \\
&= \Omega_{2255} = \Omega_{5522} = \Omega_{5555} . \qquad \text{(B.17)}
\end{aligned}$$

Appendix C

Error Estimation

Equation sets (5.80), (5.81), and (5.84) show the complexity involved in calculating the necessary Jacobi fields. To obtain the next higher Jacobi field it is necessary to know all the lower order Jacobi fields. Since these equations are solved numerically rather than analytically, we would expect the $\nabla g(t|z)$ to be less accurate than the $g(t|z)$ purely on the grounds that the error in the $g(t|z)$ will be propagated into the solution for the $\nabla g(t|z)$. This consequence will be especially true of the $\nabla\nabla g(t|z)$, which will have the numerical error of both the $g(t|z)$ and the $\nabla g(t|z)$ built into its solution. Numerical solution of these equations for trajectories which are significantly scattered can be difficult. As this is the first time that Moyal quantum mechanics has been cast into a computational form, it would be beneficial to discuss in some detail the checks that can be used to determine the accuracy of the calculation. We will begin with checks that exist at the level of the individual trajectory for the Jacobi fields.

C.1 Quantum Trajectories

To help reduce the propogation of error through the calculation, we calculated g and ∇g at twice the number of time steps as $\nabla\nabla g$. We would like to calculate the $\nabla\nabla g$ at the same time steps as the g's, but since there are $6^3 = 216$ elements of $\nabla\nabla g$ enough memory was not available to do this.

A simple but necessary condition that must be satisfied comes from the fact that phase space is incompressible:

$$det \nabla g(t|z) = 1 \; . \tag{C.1}$$

A more rigorous test that the Jacobi fields must satisfy is the symplectic condition for a canonical transformation [Goldstein, 1981]:

$$\nabla_\alpha g_\gamma(t|z) J^{\alpha\beta} \nabla_\beta g_\mu(t|z) - J^{\gamma\mu} = \Delta_{\gamma\mu} = 0 \; . \tag{C.2}$$

$$\sum_{\gamma,\mu} |\Delta_{\gamma\mu}| = 0 \; . \tag{C.3}$$

Taking derivatives of the above equation gives checks on higher order Jacobi fields.

$$\nabla_i \nabla_k g_\alpha(t|z) J^{ij} \nabla_j g_\beta(t|z) + \nabla_i g_\alpha(t|z) J^{ij} \nabla_j \nabla_k g_\beta(t|z) = \Delta_{k\alpha\beta} = 0 \; . \tag{C.4}$$

$$\sum_{k,\alpha,\beta} |\Delta_{k\alpha\beta}| = 0 \; . \tag{C.5}$$

Figure C.1 shows a typical result for Equation (C.5). At first glance it may appear that the check is not very good, but in the region where it appears to be growing quadratically the terms in Equation (C.5) which cancel are extremely large and growing quadratically. The cancellation is between terms of order $\sim 10^8$ at the final time.

Equations (C.3) and (C.5) are necessary but not sufficient conditions for the correct Jacobi fields. Since they were derived from the symplectic condition, they only guarantee that the Jacobi fields have the correct symplectic structure. If the Jacobi fields have been solved for in a manner which imposes the symplectic nature, it is quite possible to obtain results which satisfy the symplectic checks but in fact vary greatly from the actual solutions. Due to this problem, a variety of other checks were used, and an attempt was made to use checks that came from a wide variety of backgrounds.

The Jacobi fields also form a Lie algebra, and as such will be subject to the constraints of that Lie algebra. An example is the relation

$$\frac{1}{i\hbar}\left[\hat{L}_3(t), \hat{q}_2(t)\right] = -\hat{q}_1(t) . \tag{C.6}$$

Taking the Weyl symbol of the above equation yields

$$\begin{aligned} \{L_3(t), q_2(t)\}_M (z) &= \{L_3(t), q_2(t)\}_{Poisson} (z) , && \text{(C.7)} \\ &= -q_1(t) . && \text{(C.8)} \end{aligned}$$

where Equation (C.7) results from L_3 being quadratic in z. The q's in the above are the full $\hbar$ dependent quantities. Inserting their $\hbar$ expansion and collecting powers of $\hbar$ will yield equations which the Jacobi fields must satisfy. The type of checks the Lie algebra generates are (where $g_3(t|z) = g_6(t|z) = 0$ has been employed):

$$\begin{aligned} 0 &= g_1(t|z) + g_5(0|z)\nabla_4 g_2(t|z) - g_1(0|z)\nabla_2 g_2(t|z) \\ &\quad -g_4(0|z)\nabla_5 g_2(t|z) + g_2(0|z)\nabla_1 g_2(t|z) . \end{aligned} \tag{C.9}$$

$$\begin{aligned} 0 &= -g_2(t|z) + g_5(0|z)\nabla_4 g_1(t|z) - g_1(0|z)\nabla_2 g_1(t|z) \\ &\quad -g_4(0|z)\nabla_5 g_1(t|z) + g_2(0|z)\nabla_1 g_1(t|z) . \end{aligned} \tag{C.10}$$

$$\begin{aligned} 0 &= g_4(t|z) + g_5(0|z)\nabla_4 g_5(t|z) - g_1(0|z)\nabla_2 g_5(t|z) \\ &\quad -g_4(0|z)\nabla_5 g_5(t|z) + g_2(0|z)\nabla_1 g_5(t|z) . \end{aligned} \tag{C.11}$$

$$
\begin{aligned}
0 &= -g_5(t|z) + g_5(0|z)\nabla_4 g_4(t|z) - g_1(0|z)\nabla_2 g_4(t|z) \\
&\quad -g_4(0|z)\nabla_5 g_4(t|z) + g_2(0|z)\nabla_1 g_4(t|z)\ . \qquad (C.12)
\end{aligned}
$$

As with the symplectic checks, we can differentiate Equations (C.9)-(C.12) to obtain another 24 checks which contain higher order Jacobi fields. For example, taking ∇_k of Equation (C.10) yields the 6 checks ($k = 1 \sim 6$):

$$
\begin{aligned}
\Delta_k &= -\nabla_k g_2(t|z) + g_5(0|z)\nabla_k\nabla_4 g_1(t|z) - g_1(0|z)\nabla_k\nabla_2 g_1(t|z) \\
&\quad - g_4(0|z)\nabla_k\nabla_5 g_1(t|z) + g_2(0|z)\nabla_k\nabla_1 g_1(t|z) \qquad (C.13) \\
&\quad + \nabla_4 g_1(t|z)\delta_{k5} - \nabla_2 g_1(t|z)\delta_{k1} - \nabla_5 g_1(t|z)\delta_{k4} + \nabla_1 g_1(t|z)\delta_{k2} \\
&= 0\ .
\end{aligned}
$$

Figure C.1 shows the results for Equation (C.13) when $k = 2$. The Lie algebra check is seen to be linear at large time rather than quadratic as seen in the symplectic check. This is true since $\nabla g(t|z)$ and $\nabla\nabla g(t|z)$ are linear in t when the potential is zero. Cancellation in the Lie algebra case is between terms with a maximum of $\sim 10^2$.

Constants of motion can also be used to check the $\gamma^{(0)}(\cdot)$, $\gamma^{(2)}(\cdot)$, and $z^{(2)}$ structures. For example, the Hamiltonian H, the total angular momentum L^2, or the angular momentum component L_k should satisfy the relations:

$$\gamma_t^{(0)}(O) = \text{constant}\ . \qquad (C.14)$$

$$\gamma_t^{(2)}(O) = 0\ . \qquad (C.15)$$

where O is the symbol of the constant of motion under consideration. These provide useful checks on all the structures which are in the equations for $\gamma^{(0)}(\cdot)$ and $\gamma^{(2)}(\cdot)$.

Figure C.2 contains plots of $\gamma_t^{(2)}(H)$. A great deal of structure is seen in the terms which make up this quantity and the cancellation is excellent.

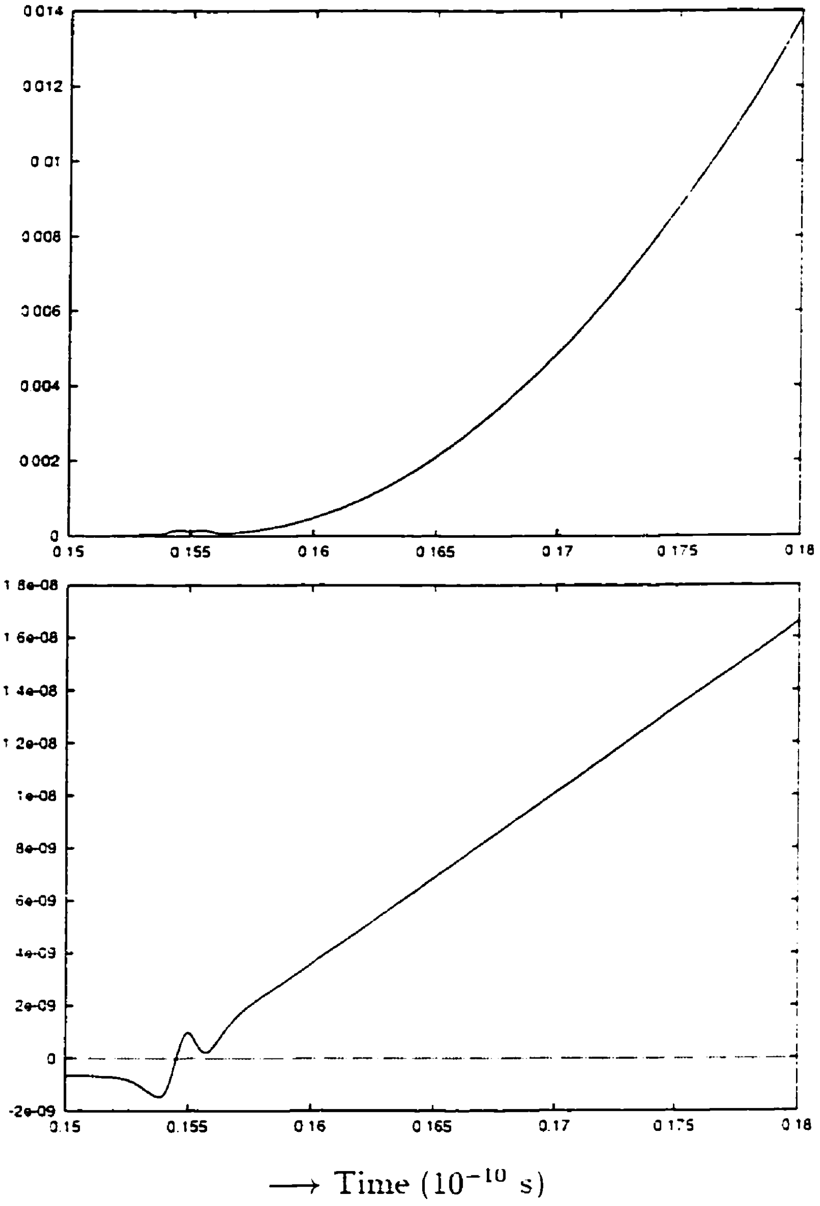

Figure C.1:

The potential is helium, the velocity is 450 m/s, $b = 2.722$Å, $y = -70$Å.

Top: Symplectic condition check (Equation (C.5))

Bottom: Lie algebra check (Equation (C.13), $k = 2$)

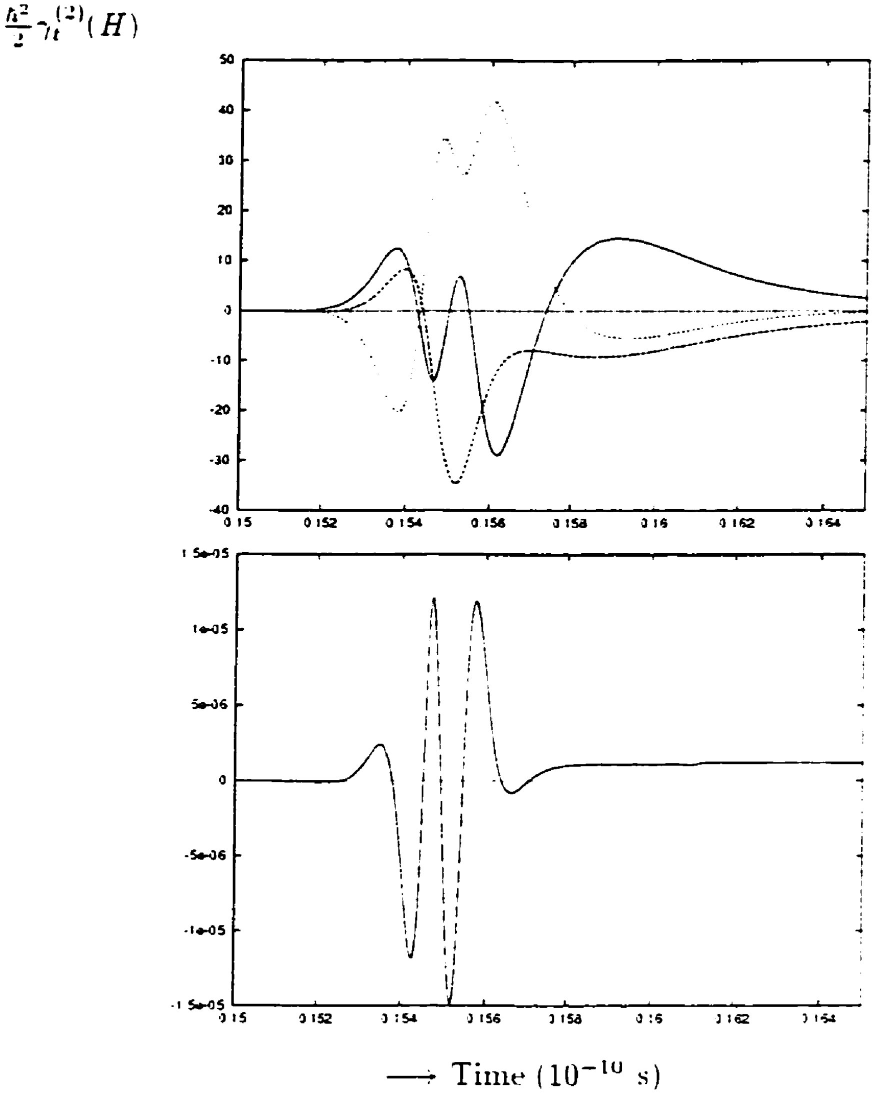

Figure C.2:

The potential is helium. the velocity is 450 m/s. $b = 2.722$A. $y = -70$A.

The plots are:

solid : $\frac{\hbar^2}{2} z_\alpha^{(2)}(t|z) H_{:\alpha}$
Top: large dash : $-\frac{\hbar^2}{2}\frac{1}{8} B_{12}^2 \prec g_\alpha(t).g_\beta(t) \succ H_{:\alpha\beta}$
small dash : $+\frac{\hbar^2}{2}\frac{1}{12} B_{12}B_{23} \prec g_\alpha(t).g_\beta(t).g_\gamma(t) \succ H_{:\alpha\beta\gamma}$
Bottom: total

A more sophisticated type of check involves compound constants of motion. A more complex Weyl symbol that is a constant of motion under the Γ_t flow is formed by combining two or more of the simple constants of motion described above.

Proposition C.1 *Let $\hat{A}, \hat{B}$ be constants of motion with symbols a, b, respectively. The compound constant of motion $(\hat{A}\hat{B})$ will satisfy the relation*

$$B_{12}^{2}\langle a, b\rangle(z) - B_{12}^{2}\langle a, b\rangle(g(t|z)) + 4\tilde{\gamma}_t^{(2)}(ab)(z) = 0 \,. \tag{C.16}$$

where

$$\begin{aligned}\tilde{\gamma}_t^{(2)}(ab)(z) &= -\frac{1}{8}B_{12}^{2}\langle g_\alpha(t), g_\beta(t)\rangle \left[(\nabla_\alpha a\nabla_\beta b)_s\right](g(t|z)) \\ &\quad +\frac{1}{12}B_{12}B_{23}\langle g_\alpha(t), g_\beta(t), g_\gamma(t)\rangle \\ &\quad \times \left[(\nabla_\alpha a\nabla_\beta\nabla_\gamma b)_s + (\nabla_\alpha b\nabla_\beta\nabla_\gamma a)_s\right](g(t|z)) \,. \end{aligned} \tag{C.17}$$

where

$$(\nabla_\alpha a\nabla_\beta b)_s = \nabla_\alpha a\nabla_\beta b + \nabla_\beta a\nabla_\alpha b \,. \tag{C.18}$$

$$(\nabla_\alpha a\nabla_\beta\nabla_\gamma b)_s = \nabla_\alpha a\nabla_\beta\nabla_\gamma b + \nabla_\beta a\nabla_\gamma\nabla_\alpha b + \nabla_\gamma a\nabla_\alpha\nabla_\beta b \,. \tag{C.19}$$

Proof. The Weyl symbol of the product of the operators $\hat{A}$ and $\hat{B}$ is given by the star product (Equation (5.16)) as

$$\begin{aligned}\left(\hat{A}\hat{B}\right)_W(z) &= a * b(z) \,. \\ &= a(z)b(z) + \frac{i\hbar}{2}\{a, b\}(z) + \frac{1}{2}\left(\frac{i\hbar}{2}\right)^2 B_{12}^{2} \prec a, b \succ (z) + O(\hbar^3) \,. \end{aligned} \tag{C.20}$$

The statement of constant of motion in the Moyal formalism is

$$\Gamma_t(a * b)(z) = a * b(z) \,. \tag{C.21}$$

or

$$\gamma_t^{(0)}(ab)(z) + \frac{\hbar^2}{2}\gamma_t^{(2)}(ab)(z) + \frac{i\hbar}{2}\gamma_t^{(0)}(\{a,b\})(z) + \frac{1}{2}\left(\frac{i\hbar}{2}\right)^2 B_{12}^2\gamma_t^{(0)}(\prec a,b \succ)(z)$$

$$= a(z)b(z) + \frac{i\hbar}{2}\{a,b\}(z) + \frac{1}{2}\left(\frac{i\hbar}{2}\right)^2 B_{12}^2 \prec a,b \succ (z) + O(\hbar^3)\,. \tag{C.22}$$

We then collect powers of $\hbar$. The $O(\hbar^0)$ part yields the equation

$$\gamma_t^{(0)}(ab)(z) = a(g(t|z))b(g(t|z)) = a(z)b(z)\,. \tag{C.23}$$

This result is trivial since a and b are separately constants of motion. The $O(\hbar^1)$ part yields

$$\{a,b\}(g(t|z)) = \{a,b\}(z)\,. \tag{C.24}$$

This is again a classical result for two constants of motion. The $O(\hbar^2)$ part yields

$$-\frac{1}{8}B_{12}^2 \prec a,b \succ (z) = -\frac{1}{8}B_{12}^2 \prec a,b \succ (g(t|z)) + \frac{1}{2}\gamma_t^{(2)}(ab)(z)\,. \tag{C.25}$$

Expand $\gamma_t^{(2)}(ab)(z)$ using the Leibniz rule, $(ab)_{:\alpha} = a_{:\alpha}b + b_{:\alpha}a$, and employ Equation (C.15) to obtain

$$\begin{aligned}\gamma_t^{(2)}(ab)(z) &= a(z)\gamma_t^{(2)}(b)(z) + b(z)\gamma_t^{(2)}(a)(z) + \tilde\gamma_t^{(2)}(ab)(z)\,. && \text{(C.26)}\\ &= \tilde\gamma_t^{(2)}(ab)(z)\,. && \text{(C.27)}\end{aligned}$$

Equations (C.25) and (C.27) recover Equation (C.16). □

Figure C.3 displays the results from one of these compound constant of motion checks, the HL^2 case. The fact that there is a great deal of structure in the terms ($\sim 10^3$ at maximum) which cancel to near zero ($\sim 10^{-3}$) is an excellent check of the computational accuracy of the program at the level of the individual trajectories. It also provides an excellent check on the internal consistency of the formal theory underlying the calculation.

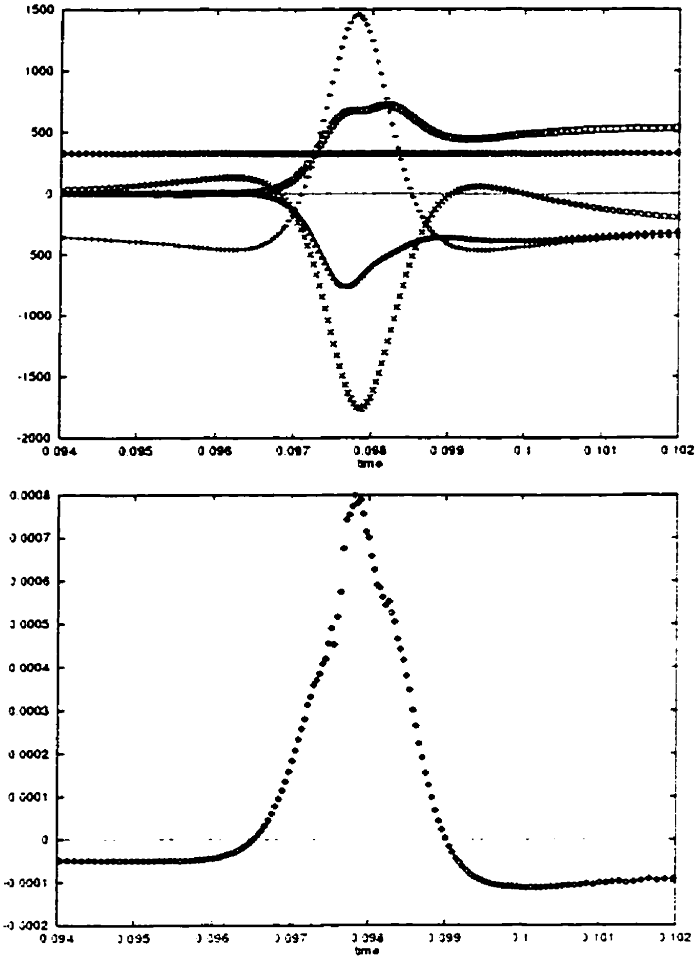

Figure C.3:

Compound constant of motion HL^2. The system is helium for a trajectory which has initial conditions $b = 2$, $y = -70$.

Bottom: total. Top: The curves are the terms which make up Equation (C.16), given by:

◇ : $B_{12}^2\langle H, L^2\rangle(z)$

+ : $-B_{12}^2\langle H, L^2\rangle(g(t|z))$

□ : $-\frac{1}{8}B_{12}^2\langle g_\alpha(t), g_\beta(t)\rangle\,[(\nabla_\alpha H\nabla_\beta L^2)_s]\,(g(t|z))$

× : $\frac{1}{12}B_{12}B_{23}\langle g_\alpha(t), g_\beta(t), g_\gamma(t)\rangle(\nabla_\alpha H\nabla_\beta\nabla_\gamma L_2)_s(g(t|z))$

△ : $\frac{1}{12}B_{12}B_{23}\langle g_\alpha(t), g_\beta(t), g_\gamma(t)\rangle(\nabla_\alpha L^2\nabla_\beta\nabla_\gamma H)_s(g(t|z))$

C.2 Average Values

Obtaining estimates of the error associated with the integration procedures used in the program is essential. As we have seen, the functions that must be integrated can have extremely sharp peaks that sit on a broad Gaussian background. In general, it appears that the classical part of the average are functions which are smoother (and therefore easier to integrate) than the Moyal correction or the momentum correction. As well, functions which depend on the coordinates are smoother than functions which depend on momentum.

It should be emphasized again that the important structure to these functions occurs for $b \in [0, 2b_{rainbow} - b_{glory}]$. Although contributions to the average values from $b \in [2b_{rainbow} - b_{glory}, \infty]$ can be large, the functions are smooth and slowly varying in this region. The computer program in fact spends $\sim 88\%$ of its time calculating the contribution from $b \in [0, 2b_{rainbow} - b_{glory}]$.

The integration will never be any better than the results at time zero. To start, a grid in y and b must be chosen that can reproduce accurately the time zero results (basically a reasonable sampling of phase space for which the initial Gaussian is nonzero). For results at times other than zero the grid must be modified, but retain the basic characteristics which produce good $t = 0$ results. This will involve adding extra points in the y and b integrations where functions are changing rapidly. Computing time is an issue with the calculation, and so it is not sufficient to simply impose a fine grid over all of phase space - extra points must be added with care. Extra points in the y integration are added in a manner which is determined by the time average values are required at, the potential used, and the initial momentum of the packet. The b integration points are dependent on the forward glory and rainbow impact parameters (which in turn are dependent on the potential and momentum).

For all functions the time zero results are known either analytically or numerically through a sympolic language like Maple or Mathematica, and Tables C.1 and C.2 compares these results with program values. The results are seen to be excellent, on the order of seven digits.

It is evident from the graphs in Chapter 6 (Figures 6.13-6.14) that a higher density of points in the y region is required for times during which the collision is actively occurring, and that this region of high density is a function of the time.

The scale of the region of interaction is given by the scale of the potential, and as time progresses the region of interaction sweeps out a function that is a scaled version of the Wigner function of the Gaussian. It should be noted that if one is only interested in the state of the system at time t sufficiently long that the collision is over then the integration in y is much simpler to perform. The functions (which have evolved into scaled versions of the Gaussian) are simple to integrate accurately.

The y integration is the most subject to error. As we shall see, the b integration does not suffer from a moving region that requires a high density of points, and so can be done accurately with relative ease.

For the impact parameter held fixed, we have functions of y which must be integrated. At a given time, only trajectories that began in the small region of the coordinate space $[y_-, y_+]$ will be in a region near the potential. All trajectories that had initial $y < y_+$ will have moved beyond the potential (this of course assumes that no orbiting has occured), and all trajectories with initial $y > y_-$ have yet to reach the region of strong interaction. To be able to do the integration in y accurately, it is obvious that the functions must be defined well in the y regions that have

	Analytical	Program
$<\gamma_0^{(0)}(g_1)>$	$\bar{b}=2$	1.999 999 73
$<\gamma_0^{(0)}(g_2)>$	$\bar{y}=-140$	$-140.000\ 014$
$<\gamma_0^{(0)}(g_4)>$	0	10^{-36}
$<\gamma_0^{(0)}(g_5)>$	$\bar{p}=0.050\ 188\ 678\ 5$	0.050 188 671 7
$<\gamma_0^{(0)}(g_1^2)>$	$\frac{\Delta^2}{2}+\bar{b}=204$	203.999 973
$<\gamma_0^{(0)}(g_2^2)>$	$\frac{\Delta^2}{2}+\bar{y}=19800$	19800.004 9
$<\gamma_0^{(0)}(g_3^2)>$	$\frac{\Delta^2}{2}=200$	199.999 973
$<\gamma_0^{(0)}(g_5^2)>$	$\bar{p}^2=2.518\ 903\ 41\times 10^{-3}$	$2.518\ 903\ 11\times 10^{-6}$
$<\left(\frac{\hbar}{2\Delta}\right)^2\partial_p^2\gamma_0^{(0)}(g_4^2)>$	$\frac{1}{2}\left(\frac{\hbar}{\Delta}\right)^2=3.522\ 969\ 3\times 10^{-6}$	$3.522\ 968\ 8\times 10^{-6}$
$<\left(\frac{\hbar}{2\Delta}\right)^2\partial_p^2\gamma_0^{(0)}(g_5^2)>$	$\frac{1}{2}\left(\frac{\hbar}{\Delta}\right)^2=3.522\ 969\ 3\times 10^{-6}$	$3.522\ 968\ 8\times 10^{-6}$
$<\left(\frac{\hbar}{2\Delta}\right)^2\partial_p^2\gamma_0^{(0)}(g_6^2)>$	$\frac{1}{2}\left(\frac{\hbar}{\Delta}\right)^2=3.522\ 969\ 3\times 10^{-6}$	$3.522\ 968\ 8\times 10^{-6}$
$<\nabla_5 H>$	$\bar{v}=300$	299.999 959
$<\nabla_5\nabla_5 H>$	$\frac{1}{m}=5977.442\ 3$	5977.443 7

Table C.1:

Accuracy of $t=0$ values. The potential is helium, the velocity is 300 m/s.

	Mathematica	Program
$<\gamma_0^{(0)}(\mathrm{KE})>$	7.528 30	7.528 301
$<\gamma_0^{(0)}(V)>$	-6.1988×10^{-10}	-6.19867×10^{-10}
$<\gamma_0^{(0)}(L_3)>$	0.100 377	0.100 377 357
$<\gamma_0^{(0)}(L^2)>$	1.017 64	1.017 637
$<\gamma_0^{(0)}(HL_3)>$	0.755 671	0.755 670 9
$<\gamma_0^{(0)}(HL^2)>$	7.661 08	7.661 077

Table C.2:

Accuracy of $t = 0$ values. The potential is helium, the velocity is 300 m/s.

arrived at the region of strong interaction at the times you are interested in. At sufficiently large times the region $[y_-, y_+]$ will be located far from the center of the Gaussian, and the weighting factor of the Gaussian will make their contribution to the average negligible.

Figure C.4 shows the points that were used to map a typical function in both the y and b directions. One of the best methods for checking the integration routines is to do the calculation twice, the second time using a different set of points in phase space. If the functions are well defined a shuffling of the integration points will have only a small effect on the results. How well the two sets of data agree will give at least a lower bound on the accuracy of the results. Table C.3 contains estimates of the error in integration using this idea for helium at a velocity of 450 m/s. All the functions are seen to be well defined.

Yet another check results from the rotational invariance that exists between the

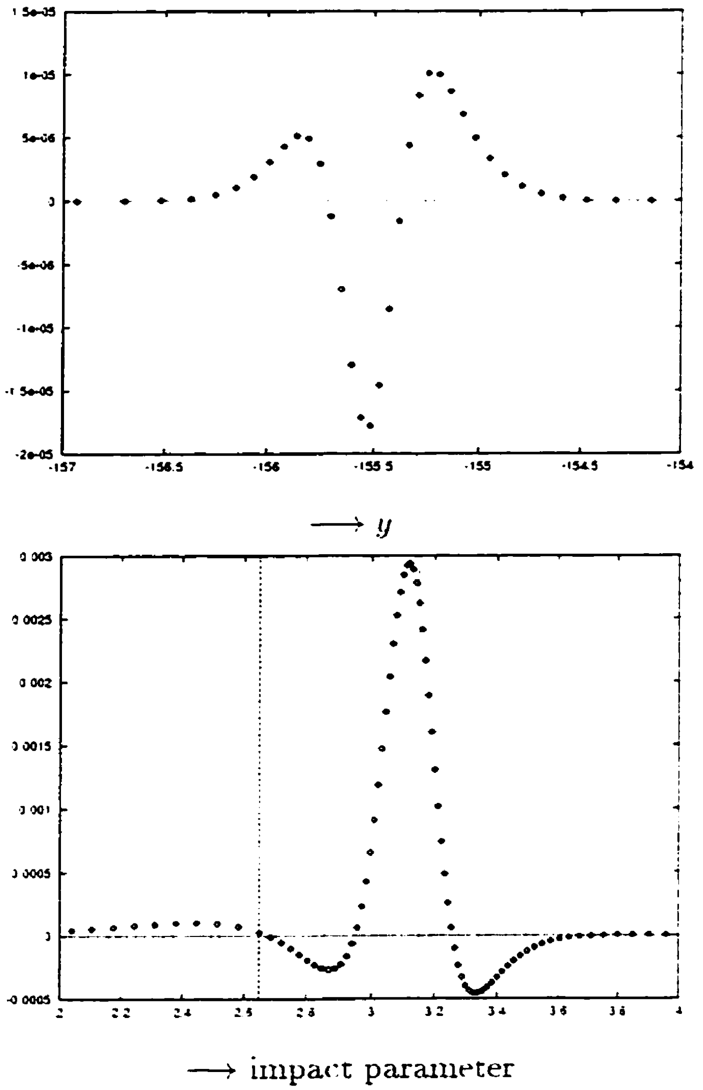

Figure C.4:

Moyal correction to average value for $g_5(t|z_0)$ as a function of y (top) and as a function of impact parameter (bottom). Initial conditions are velocity = 500 m/s and $b = 1.7362$ Å for the y graph. Plots are given for the function at the time 0.308 (10^{-10} seconds). The impact parameter graph includes $b_{\text{glory}} = 2.65$ Å and $b_{\text{rainbow}} = 3.15$ Å.

time (10^{-10} s)	$\langle \gamma_t^{(0)}(g_4) \rangle$	$\frac{\hbar^2}{2} \langle \gamma_t^{(2)}(g_4) \rangle$	$\left(\frac{\hbar}{2\Delta}\right)^2 \langle \partial_p^2 \gamma_t^{(0)}(g_4) \rangle$
Percentage Change from using different $y - b$ Grid			
0.280	3×10^{-5}	7×10^{-4}	4×10^{-3}
0.311	1×10^{-6}	7×10^{-4}	7×10^{-3}
0.342	6×10^{-6}	7×10^{-4}	9×10^{-3}
0.498	2×10^{-4}	6×10^{-4}	1×10^{-2}

Table C.3: Effect of changing integration grids

directions $\hat{e}_1$ and $\hat{e}_3$. This invariance causes the spreads in these two directions to be equal. Any deviation from equality will be due to numerical error. The fact that the spreads should be equal while the average values that are included in the spread are not make this an excellent check on the integration procedures. Table C.4 examines this check at four times for helium at a velocity of 450 m/s. The results are again excellent.

Another method of checking the integration is to examine the average value of any constants of motion. These should remain constant at all times, since they are constant at the level of the individual trajectories. The $\gamma_t^{(0)}$ and $\partial_p^2 \gamma_t^{(0)}$ parts of the average should remain constant. The $\gamma_t^{(2)}$ part of a constant of motion is strictly zero, and how close these functions stay to zero are excellent indicators of the accuracy of the code at the level of an individual trajectory (cf. Figures C.2 and C.3). Unfortunately, average values for the constants of motion do not provide a very good check on the integration accuracy. Since the constant of motion is constant at the level of individual trajectories, it does not provide a reliable means of testing the integration. However, if the $\gamma_t^{(2)}$ part of a constant of motion is not zero to sufficient accuracy, it usually indicates the presence of metastable states

time (10^{-10} s)	(spread$_1$ - spread$_3$)/spread$_1$
0.280	2×10^{-4}
0.311	7×10^{-4}
0.342	2×10^{-3}
0.462	7×10^{-3}
time (10^{-10} s)	(spread$_4$ - spread$_6$)/spread$_4$
0.280	2×10^{-3}
0.311	7×10^{-4}
0.342	7×10^{-3}
0.462	1×10^{-1}

Table C.4: Rotational invariance of spreads in $\hat{e}_1$ and $\hat{e}_3$

Tables C.5 shows results for a case without metastable states. and Table C.6 shows results for a case where orbiting is possible. The classical part of the average can be obtained accurately when orbiting occurs. but the Moyal correction cannot with the present program.

Using different methods of integration is also possible. employing a cubic spline rather than a finite difference or Gaussian quadrature. Other methods of integration were examined during the early developement of the code. but average values were not calculated using other than the finite difference and Gaussian techniques.

Time	$\langle \gamma_t^{(0)}(H) \rangle$	$\frac{\hbar^2}{2}\langle \gamma_t^{(2)}(H) \rangle$	$\langle \gamma_t^{(0)}(H * L^2) \rangle$	$\frac{\hbar^2}{2}\langle \gamma_t^{(2)}(H * L^2) \rangle$
(10^{-10} s)	(cm^{-1})		(cm^{-3} 0.1 ns/Å)	
0.000	16.9386795	10^{-44}	38.784210	10^{-32}
0.156	16.9386795	1.183×10^{-13}	38.784210	1.889×10^{-9}
0.189	16.9386794	1.877×10^{-11}	38.784210	5.967×10^{-8}
0.280	16.9386767	3.973×10^{-8}	38.784204	5.622×10^{-5}
0.311	16.9386767	1.139×10^{-7}	38.784204	9.754×10^{-5}
0.342	16.9386767	1.814×10^{-7}	38.784204	6.591×10^{-5}
0.489	16.9386767	2.114×10^{-7}	38.784201	2.116×10^{-7}
0.498	16.9386767	2.114×10^{-7}	38.784201	2.115×10^{-7}

Table C.5: Average values of constants of motion: no orbiting. (He $v = 450$ m/s)

Time	$\langle \gamma_t^{(0)}(H) \rangle$	$\frac{\hbar^2}{2}\langle \gamma_t^{(2)}(H) \rangle$	$\langle \gamma_t^{(0)}(H * L^2) \rangle$	$\frac{\hbar^2}{2}\langle \gamma_t^{(2)}(H * L^2) \rangle$
(10^{-10} s)	(cm^{-1})		(cm^{-3} 0.1 ns/Å)	
0.000	5.22798655	10^{-40}	3.69457815	10^{-34}
0.504	5.22798653	8.21×10^{-2}	3.69457813	8.19×10^{-2}
0.560	5.22798653	7.66×10^{-1}	3.69457813	7.63×10^{-1}
0.616	5.22798653	3.59	3.69457813	3.57
0.880	5.22798653	16.18	3.69457813	16.11
0.896	5.22978653	16.20	3.69457813	16.10

Table C.6: Average values of constants of motion: orbiting. (He $v = 250$ m/s)

Appendix D

Flow Chart of Program

This appendix contains flow charts for the more important sections of the computer program. Subroutine and/or NAG libraries used are quoted, as well as the mathematical method used, if appropriate. Times quoted are approximate CPU time spent on that portion of the calculation. The calculation used to determine these times was helium at a velocity of 700 m/s (total time for this system was 6 hours). Other systems will have different times. The computer used was a VAX AlphaStation 400 4/233 with 96 MB RAM running VMS V6.2.

D.1 Trajectories

For a given e, b, g, determine $g(t)$, $\nabla g(t)$, $\nabla\nabla g(t)$, $z^{(0)}(t)$, $z^{(2)}(t)$.

$\boxed{\text{START}}$

↓

Is this the first trajectory calculation at this impact parameter? $\xrightarrow{F} \boxed{1}$

Routine: DYNAMICS

↓ T

Calculate $g(t)$ and determine time steps t_k

Routines: PATH, NAG D02LAF Time: 0.28 s

Method: Second order ordinary differential equation

↓

Spline $g_1(t)$ and $g_2(t)$

Routines: PATH, NAG E01BAF Time: 0.01 s

↓

Calculate $\nabla g(t)$

Routine: PATH, NAG D02LAF Time: 3.50 s

Method: Second order ordinary differential equation

↓

Define $t_k, g(t), \nabla g(t)$ at half the points used to originally define them

Routine: PATH

↓

Calculate $\nabla\nabla g(t)$ (Each inhomogeneous term is splined separately)

Routines: PATH, NAG D02LAF, NAG E01BAF Time: 21.00 s

Method: Second order ordinary differential equation

↓

Calculate $-\frac{1}{8}B_{12}^2 \prec g_\alpha(t), g_\beta(t) \succ (z)$ and $\frac{1}{12}B_{12}B_{23} \prec g_\alpha(t), g_\beta(t), g_\gamma(t) \succ (z)$

Routine: BTUPLES Time: 0.07 s

↓

Calculate $z^{(2)}(t)$ and assign $z^{(0)}(t)$

Routines: Z0Z2, NAG D02LAF Time: 1.60 s

Method: Second order ordinary differential equation

↓

Assign: $t^{(y_n)} = t,\ g^{(y_n)} = g,\ \nabla g^{(y_n)} = \nabla g,\ \nabla\nabla g^{(y_n)} = \nabla\nabla g,\ z^{(2)(y_n)} = z^{(2)}$.

Routine: DYNAMICS

↓

$\boxed{\text{RETURN}}$

↓

$\boxed{1}$

↓

Define y_n, t_n

Routine: DYNAMICS

↓

Define time steps t_k for this trajectory

Routine: DYNAMICS

↓

For $t_i \leq t_n$ define $g, \nabla g, \nabla\nabla g, z^{(0)}, z^{(2)}$ via free evolution formulas

Routine: DYNAMICS Time: 0.08 s

↓

For $t_i > t_n$ define $g, \nabla g, \nabla\nabla g, z^{(0)}, z^{(2)}$ via composition formulas

Routine: DYNAMICS Time: 0.08 s

↓

Calculate $-\frac{1}{8}B_{12}^2 \prec g_\alpha(t), g_\beta(t) \succ (z)$ and $\frac{1}{12}B_{12}B_{23} \prec g_\alpha(t), g_\beta(t), g_\gamma(t) \succ (z)$

Routine: BTUPLES Time: 0.07 s

↓

$\boxed{\text{RETURN}}$

D.2 Functions

Define the functions at the times $\bar{t}_l$ along the trajectories. The time taken by a call to this routine is approximately 0.71 seconds. A list of the functions that are defined is found in Table D.1.

$\boxed{\text{START}}$

↓

Define functions at times t_k along trajectory

Routines: See Table D.1

↓

Spline functions over time

Routine: Function. NAG E01BAF

↓

Extract value of functions at $\bar{t}_l$, storing in $F_{ij}(y_i; \bar{t}_l)$

↓

$\boxed{\text{RETURN}}$

D.3 Average of Function F

Form the average of a function F at a specific time $\bar{t}_l$. F being any one of $\gamma^{(0)}_{\bar{t}_l}(O)$, $\gamma^{(2)}_{\bar{t}_l}(O)$, $\partial_p^2 \gamma^{(0)}_{\bar{t}_l}(O)$ for an observable O.

$\boxed{\text{BEGIN}}$

↓

Define potential constants, mass, velocity.

Function	Routine	Time (s)
∇H	fcnchdham	0.02
$\nabla\nabla H$	fcnchddham	0.03
V, L_3, HL_3, L^2, HL^2	fcnavtch0	0.36
g_i	fcnavtime1	0.13
$g_i g_i$	fcnavtime2	0.17

Table D.1:

The functions for which average values are calculated. The times reported are the times that it takes to obtain values for the functions at all the $\bar{t}_l$. The last three entries have each component split into three parts, $\gamma^{(0)}, \gamma^{(2)}$, and $\partial_p^2 \gamma^{(0)}$. The first two entries determine only the $\gamma^{(0)}$ part.

Define times $\bar{t}_l$ for which averages are to be calculated

Routine: Main

↓

Define impact parameter grid on interval [0,5]

Routine: Main

↓

$b_i = 0$

↓

$\boxed{1}$

↓

Define Bessel function Ω

Routines: X2SUB, X4SUB, NAG S18AEF, NAG S18AFF

↓

Determine y_{center} and y_{range} that require
extra points for y integration
Routine: YPARAM

↓

Define y grid on $[y_{min} : y_{max}]$
Routine: Main

↓

$y_j = y_{max}$

↓

$\boxed{2}$

↓

Calculate TRAJECTORIES

↓

Define FUNCTIONS

↓

Next y_j
If $y_j < y_{min} \xrightarrow{F} \boxed{2}$

↓ T

Integrate $F_y(y_j : \bar{t}_l)$ over y: Store in $F_b(b_i : \bar{t}_l)$
Routines: Main, NAG D01GAF
Method: Finite Difference

↓

Next b_i
If $b_i > 5 \xrightarrow{F} \boxed{1}$

↓ T

Integrate $F_b(b_i : \bar{t}_l)$ over b: Store in $F(\bar{t}_l)$

Routines: Main, NAG D01GAF

Method: Finite Difference

↓

Define Gaussian quadrature weights and grid for b in [5,150]

Routines: Main, NAG D01BCF

↓

$b_i = 5$

↓

$\boxed{3}$

↓

Define Bessel function Ω

Routines: X2SUB, X4SUB, NAG S18AEF, NAG S18AFF

↓

Determine y_{center} and y_{range} that require

extra points for y integration

Routine: YPARAM

↓

Define y grid on $[y_{min} : y_{max}]$

Routine: Main

↓

$y_j = y_{max}$

↓

$\boxed{4}$

↓

Calculate TRAJECTORIES

↓

Define FUNCTIONS

$\downarrow$

Next y_j

If $y_j < y_{min} \xrightarrow{F} \boxed{4}$

$\downarrow$ T

Integrate $F_y(y_j;\bar{t}_l)$ over y: Store in $F_b(b_i;\bar{t}_l)$

Routines: Main. NAG D01GAF

Method: Finite Difference

$\downarrow$

Next b_i

If $b_i > 150 \xrightarrow{F} \boxed{3}$

$\downarrow$ T

Integrate $F_b(b_i;\bar{t}_l)$ over b: Store in $F(\bar{t}_l)$

Routines: Main

Method: Gauss Legendre Quadrature

$\downarrow$

Output $F(\bar{t}_l)$

$\downarrow$

$\boxed{\text{STOP}}$

Bibliography

[1] Alber, G., and Cooper, J. (1986) *Phys. Rev. A* **33**, 3084.

[2] Allard, N., and Kielkopf, J. (1982) *Rev. Mod. Phys.* **54**, 1103.

[3] Bejar, J., and Gush, H.P. (1974) *Can. J. Phys.* **52**, 1669.

[4] Bézard, B., Gautier, D., and Marten, A. (1986) *Astron. & Astrophys.* **161**, 387.

[5] Bishop, D., and Cheung, L. (1978) *Chem. Phys. Lett.* **55**, 598.

[6] Borysow, A., Frommhold, L., and Meyer, W. (1988) *J. Chem. Phys.* **88**, 4855.

[7] Bowman, F. (1958) *Introduction to Bessel Functions*, Dover, New York.

[8] Braunss, G., and Rompf, D. (1993) *J. Phys. A.* **26**, 4107.

[9] Buckingham, A.D. (1967) *Adv. Chem. Phys.* **12**, 107.

[10] Bunker, P.R. (1968) *J. Mol. Spectrosc.* **28**, 422.

[11] Burnett, K. (1985) *Phys. Rep.* **118**, 339.

[12] Carruthers, P., and Zachariasen, F. (1983) *Rev. Mod. Phys.* **55**, 245.

[13] Child. M.S. (1974) *Molecular Collision Theory*. Academic Press. New York.

[14] de Boer. J. and Michels. A. (1938) *Physica* **5**. 945.

[15] Drakopoulos. P.G.. and Tabisz. G.C. (1987a) *Phys. Rev. A* **36**. 5556.

[16] Drakopoulos. P.G.. and Tabisz. G.C. (1987b) *Phys. Rev. A* **36**. 5566.

[17] Estrada. R.. Gracia-Bondía. J.M.. and Várilly. J.C. (1989) *J. Math. Phys.* **30**. 2789.

[18] Fender. B.E.F.. and Halsey Jr.. G.D. (1962) *J. Chem. Phys.* **36**. 1881.

[19] Ford. A.L.. and Browne. J.C. (1977) *Phys. Rev. A* **16**. 1992.

[20] Ford. K.W.. and Wheeler. J.A. (1959a) *Annals of Physics* **7**. 259.

[21] Ford. K.W.. and Wheeler. J.A. (1959b) *Annals of Physics* **7**. 287.

[22] Gao. B.. Cooper. J.. and Tabisz. G.C. (1992) *Phys. Rev. A* **46**. 5781.

[23] Gao. B.. Tabisz. G.C.. Trippenbach. M.. and Copper. J. (1991) *Phys. Rev. A* **44**. 7379.

[24] Gautier. D.. and Owen. T. (1983) *Nature* **302**. 215.

[25] Geiss. J.. and Reeves. H. (1972) *Astron. & Astrophys.* **18**. 126.

[26] Goldstein. H. (1981) *Classical Mechanics. 2nd. Ed.*. Addison-Wesley Publishing Company. New York.

[27] Green. S. (1974) *Physica* **76**. 609.

[28] Groenewold. H.J. (1946) *Physica* **12**. 405.

[29] Herman, R.M. (1979) *Phys. Rev. Lett.* **42**, 1206.

[30] Herman, R.M., Tipping, R.H., and Poll, J.D. (1979) *Phys. Rev. A* **20**, 2006.

[31] Herzberg, G. (1949) *Nature* **163**, 170.

[32] Herzberg, G. (1950) *Spectra of Diatomic Molecules, 2nd Ed.*, D. Van Nostrand Company, Inc., New York.

[33] Hirschfelder, J.O., Curtis, C.F., and Bird, R.B. (1954) *Molecular Theory of Gases and Liquids*, John Wiley & Sons, New York.

[34] Hörmander, L. (1979) *Comm. Pure Appl. Math.* **32**, 359.

[35] Kolos, W. (1973) *J. Mol. Struct.* **19**, 93.

[36] Kolos, W., and Wolniewicz, L. (1963) *Rev. Mod. Phys.* **35**, 473.

[37] Kreek, H., and Le Roy, R.J. (1975) *J. Chem. Phys.* **63**, 338.

[38] Le Roy, R.J., and Hutson, J.M. (1987) *J. Chem. Phys.* **86**, 837.

[39] London, R. (1983) *The Quantum Theory of Light, 2nd Ed.*, Clarendon Press, Oxford.

[40] Lu, Z. (1991) Ph.D. Thesis (unpublished), University of Manitoba.

[41] Lu, Z., Tabisz, G.C., and Ulivi, L. (1993) *Phys. Rev. A* **47**, 1159.

[42] Ma, Q., Tipping, R.H., and Poll, J.D. (1988) *Phys. Rev. A* **38**, 6185.

[43] McKellar, A.R.W. (1973) *Can. J. Phys.* **51**, 389.

[44] McKellar, A.R.W. (1974) *J. Chem. Phys.* **61**, 4636.

[45] McKellar, A.R.W. (1986) *Can. J. Phys.* **64**, 227.

[46] McKellar, A.R.W., Goetz, W., and Ramsay, D.A. (1976) *Astrophys. J.* **207**, 663.

[47] McKellar, A.R.W., Johns, J.W.C., Majewski, W., and Rich, N.H. (1984) *Can. J. Phys.* **62**, 1673.

[48] McKellar, A.R.W., and Rich, N. (1984) *Can. J. Phys.* **62**, 1665.

[49] McQuarrie, B., Tabisz, G.C., Gao, B., and Cooper, J. (1995) *Phys. Rev. A* **52**, 1976.

[50] Meinander, N. (1995) in *Collision- and Interaction-Induced Spectroscopy*, edited by G.C. Tabisz and M.N. Neuman, Kluwer Academic Publishers, Dordrecht, 507.

[51] Merzbacher, E. (1970) *Quantum Mechanics, 2nd. Ed.*, John Wiley & Sons, New York.

[52] Molzahn, F.H., and Osborn, T.A. (1994) *Annals of Physics* **230**, 343.

[53] Moyal, J.E. (1949) *Proc. Cambridge Philos. Soc.* **45**, 99.

[54] Mulder, F., Avoird, A.V.D., and Wormer, P.E.S. (1979) *Mol. Phys.* **37**, 159.

[55] Nelson, J.B., and Tabisz, G.C. (1982) *Phys. Rev. Lett.* **48**, 1398.

[56] Nelson, J.B., and Tabisz, G.C. (1983) *Phys. Rev. A* **28**, 2157.

[57] Osborn, T.A., and Molzahn, F.H. (1995) *Annals of Physics* **241**, 79.

[58] Poll, J.D., and Hunt, J.L. (1976) *Can. J. Phys.* **54**, 461.

[59] Poll, J.D., and Karl, G. (1973) *Can. J. Phys.* **51**, 594.

[60] Poll, J.D., Tipping, R.H., Prasad, R.D.G., and Reddy, S.P. (1976) *Phys. Rev. Lett.* **36**, 248.

[61] Poll, J.D., and Van Kranendonk, J. (1961) *Can. J. Phys.* **39**, 189.

[62] Prosser, R.T. (1983) *J. Math. Phys.* **24**, 548.

[63] Rich, N.H., and McKellar, A.R.W (1983) *Can. J. Phys.* **61**, 1648.

[64] Rose, M.E. (1957) *Elementary Theory of Angular Momentum*, John Wiley and Sons, Inc., New York.

[65] Sakurai, J.J. (1985) *Modern Quantum Mechanics*, Addison-Wesley Publishing Company, Inc., Don Mills.

[66] Schaefer, J., and Monchick, L. (1987) *J. Chem. Phys.* **87**, 171.

[67] Stefanov, B. (1992) *J. Phys. B: At. Mol. Opt. Phys.* **25**, 4519.

[68] Stogryn, D.E., and Hirschfelder, J.O. (1959) *J.Chem. Phys.* **31**, 1531.

[69] Tabisz, G.C., and Nelson, J.B. (1985) *Phys. Rev. A* **31**, 1160.

[70] Tipping, R.H., Poll, J.D., and McKellar, A.R.W. (1978) *Can. J. Phys.* **56**, 75.

[71] Tipping, R.H., and Poll, J.D. (1985) in *Molecular Spectroscopy: Modern Research, Vol. III*, edited by K.N. Rao, Academic Press, New York, 421.

[72] Trafton, L. (1978) *Astrophys. J.* **222**, 740.

[73] Trauger, J.T., Roesler, F.L., Carleton, N.P., and Traub, W.A. (1973) *Astrophys. J. Lett.* **184**, L137.

[74] Trefler. M.. and Gush. H.P. (1968) *Phys.Rev. Lett.* **20**. 703.

[75] Ulivi. L.. Lu. Z.. and Tabisz. G.C. (1989) *Phys. Rev. A* **40**. 642.

[76] Van Kranendonk. J. (1968) *Can. J. Phys.* **46**. 1173.

[77] Voros. A. (1978) *J. Functional Analysis* **29**. 104.

[78] Weyl. H. (1927) *Z.Phys.* **46**. 1.

[79] Wick. G.C. (1935) *Atti. Reale. Accad. Naz. Lincei.* (Ser 6). **21**. 708.

[80] Wigner. E.P. (1932) *Phys.Rev.* **40**. 749.

[81] Wolniewicz. L. (1976) *Can. J. Phys.* **54**. 672.

[82] Wolniewicz. L.. and Kowalski. T. (1973) *Chem. Phys. Lett.* **18**. 55.

[83] Zare. R.N. (1988) *Angular Momentum.* John Wiley & Sons. New York.

IMAGE EVALUATION
TEST TARGET (QA-3)

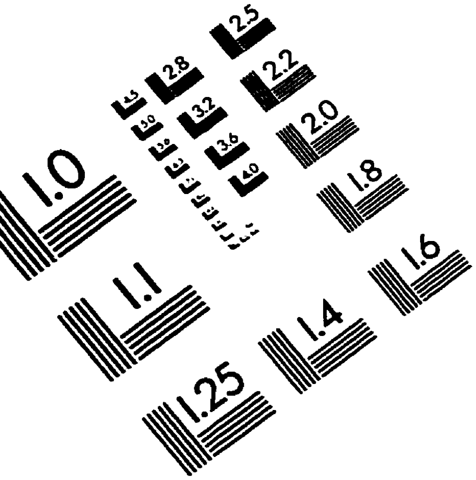

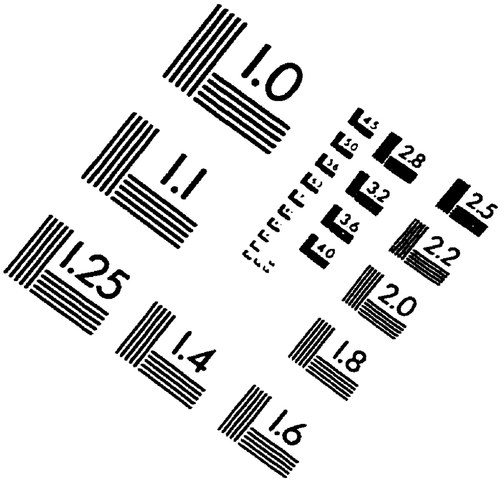

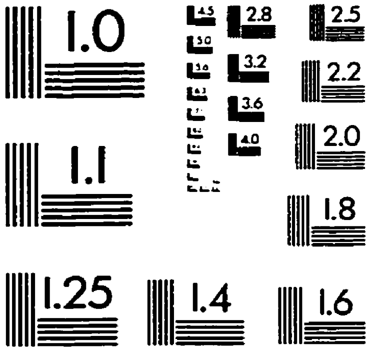

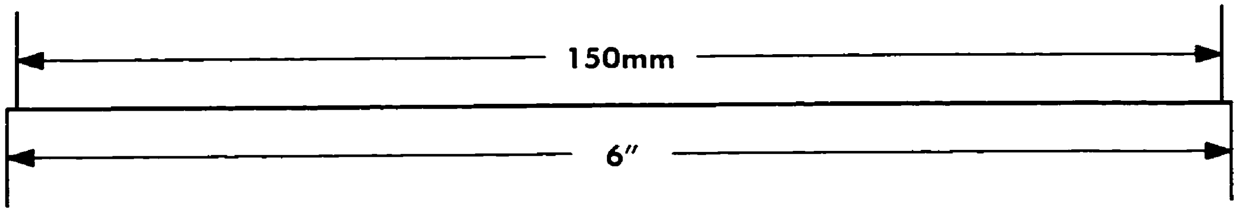

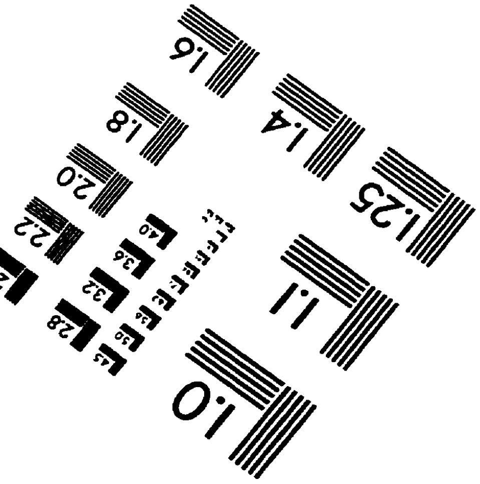

APPLIED IMAGE . Inc
1653 East Main Street
Rochester, NY 14609 USA
Phone: 716/482-0300
Fax: 716/288-5989